MODERN METHODS
FOR
SELECTED ELECTROMAGNETIC FIELD PROBLEMS

MAREK ZIÓŁKOWSKI

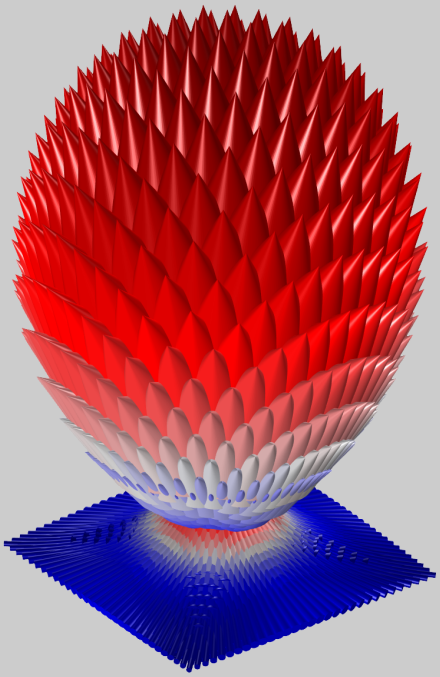

Szczecin 2015

West Pomeranian University of Technology, Szczecin, Poland

Marek Ziółkowski

MODERN METHODS FOR SELECTED ELECTROMAGNETIC FIELD PROBLEMS

Szczecin 2015

Reviewers
Hartmut Brauer
Stanisław Gratkowski

Cover project
Marek Ziółkowski

Published with the permission of the Rektor of
West Pomeranian University of Technology, Szczecin, Poland

ISBN 978-83-7663-198-1

Wydawnictwo Uczelniane Zachodniopomorskiego Uniwersytetu Technologicznego w Szczecinie
70-311 Szczecin, al. Piastów 48, tel. 091 449-47-60, e-mail: wydawnictwo@zut.edu.pl
Druk PPH Zapol, Sobczyk Sp.j., 71-062 Szczecin, al. Piastów 42, tel. 091 434-10-21
e-mail: zarzad@zapol.com.pl

To M...

CONTENTS

I'm not promising the moon,
I'm not promising a rainbow,
... Just a practical solution

— Sting & Rob Mathes

PREFACE

This monograph presents selected results of several years of work the author conducted at the Technical University of Szczecin (now West Pomeranian University of Technology, Szczecin) and the Technische Universität Ilmenau. The monograph consists of five chapters and describes some methods applicable in the analysis of selected problems of the electromagnetic field.

The first two chapters of monograph have been written to Recall memory of my friend Modest Gramz. Thus, these chapters have more or less historical character.

Chapter 1 is devoted to the finite element method. It does not describe the method itself but presents only some shape functions which can be used in the FEM, namely, vector shape functions for brick finite elements. Nodal, edge, and face implementations are discussed in details.

Chapter 2 presents an analysis of a general 3D magnetostatic field problem using the finite element method with various magnetic field formulations. The analysis by means of scalar potentials together with modeling of 3D windings is described at first. Next, magnetic field descriptions using the magnetic vector potential $\mathbf{A}$ and the direct $\mathbf{H}$ formulation are discussed. Their implementations in the FEM with separated $\mathbf{A}/\mathbf{H}$ components using edge finite elements are also shown.

Chapter 3 deals with a problem of reconstruction of the interface between two oscillating electrically conducting immiscible fluids through which flows direct current. Using the magnetic tomography concept the system based on magnetic field measurements around the cell with fluids has been developed for the interface identification. In the chapter, first, the methods for calculation of the magnetic field outside the cell are described. Then, some algorithms for an identification of the dominant mode in the oscillating interface are presented, namely, simple genetic algorithm, direct search technique, and cross-correlation approach.

Chapter 4 describes analytical methods suitable for modeling Lorentz eddy current testing (LET) problems. The chapter presents 2D and 3D LET models for which calculation of Lorentz forces, defect response signals, and modeling of permanent magnets are analyzed.

The last chapter, Chapter 5, is dedicated to the 3D visualization of objects and scalar and vector fields which is an important element of any numerical/analytical 3D simulation.

ACKNOWLEDGMENTS

This monograph would not have been possible without help of several people who supported and motivated me in one or another way in writing and finishing this work.

Two of them are for sure the most important, Prof. Stanislaw Gratkowski and Dr. Hartmut Brauer to whom I owe my deepest gratitude.

I would also like to thank Prof. Stefan Domek, the dean of the Electrical Engineering Faculty at the West Pomeranian University of Technology, Szczecin for his trust.

Warmest thanks to all my colleagues of the FG Theoretische Elektrotechnik for stimulating discussions and friendly atmosphere.

I would also like to express my love and gratitude to my Martina - without her endless daily support all this work would have been impossible to complete.

LIST OF FIGURES

LIST OF TABLES

LIST OF SYMBOLS AND ABBREVIATIONS

$[\sigma]$	diagonal conductivity tensor [S/m]
$[\mathbb{S}]$	global stiffness matrix (FEM)
χ_{DCF}	dipolar correction factor
$\Delta\mathbf{F}^{(n)}$	defect response signal [N]
$\delta(\cdot)$	Dirac function
$\delta_c^{\%}$	total relative error for c-component
η	interface elevation [m]
η_{mn}	single mode amplitude of the oscillating interface
Γ	domain boundary
$\Im(\cdot)$	imaginary part operator
$\mathbf{1}_k$	local unit vectors
$\mathbf{F}^{(n)}$	force profile [N]
$\mathbf{F}_{LF}$	Lorentz force [N]
$\mathbf{F}_{PM}$	force exerted on PM [N]
$\mathbf{m}$	magnetic dipole moment [A/m^2]
$\mathbf{m}_l$	magnetic moment of l-dipole [Am]
$\mathbf{n}$	normal unit vector
$\mathbf{p}$	current dipole moment [Am]
$\mathbf{w}$	vector test function
μ	magnetic permeability [H/m]
μ_0	permeability of free space [$= 4\pi \times 10^{-7}$H/m]
∇	nabla operator
ν	magnetic reluctivity [m/H]
ω	relaxation factor

Ω	simulation domain
ω_{mn}	eigen frequency [1/s]
$\overline{x}$	mean value of x
Φ	scalar velocity potential [m^2/s]
ϕ, φ	electric scalar potential [V]
$\Pi(\cdot)$	rectangle function
$\Re(\cdot)$	real part operator
ρ	density [kg/m^3]
σ	electrical conductivity [S/m]
σ_m	density of magnetic charges [Vs/m^2]
$\underline{X}[k]$	complex discrete Fourier transform
φ, ψ	magnetic scalar potentials [A]
$\widehat{\mathbf{F}}$	spatial Fourier transform
$\widetilde{C}_F$	spectral cost function
$\{\mathbb{R}\}$	load vector (FEM)
$C(\cdot)$	generalized complete elliptic integral
C_F	cost function
f_N	Nyquist frequency
$G_0^{(k)}$	equivalent ellipsoid goodness factor
$J_m(\cdot)$	Bessel function of the first kind of order m
p	fluid pressure [N/m^2]
p_c	crossover probability (GA)
p_m	mutation probability (GA)
$r_{ij,k}^{(m)}$	linear cross-correlation coefficient
R_m	magnetic Reynolds number
T_h	threshold
$x[k]$	discrete signal

A	magnetic vector potential [Vs/m]
B	magnetic flux density [T]
D	electric flux density [C/m^2]
E	electric field intensity [V/m]
g	gravitational acceleration ($= 9.81$ [m/s^2])
H	magnetic field intensity [A/m]
J	electric current density [A/m^2]
M	magnetization density [A/m]
T	electric vector potential [A/m]
v	velocity vector [m/s]
ASCII	American Standard Code for Information Interchange
BEM	Boundary Element Method
CAD	Computer Aided Design
CC	Cross-Correlation
CCW	Counter ClockWise
COG	Center Of Gravity
CPU	Central Processing Unit
CR(C)U	Column-wise Representation, Complete, Unordered (matrix)
CS	Coordinate System
CT	Computer Tomograp
DC	Direct Current
DCF	Dipolar Correction Factor
DFT	Discrete Fourier Transform
DRS	Defect Response Signal
EAA	Extended Area Approach
ECG	ElectroCardioGraphy
ECT	Eddy Current Testing
EEG	ElectroEncephaloGraphy

EqE	Equivalent Ellipsoid
ERP	Event-Related Potentials
FEM	Finite Element Method
FFTW	Fastest Fourier Transform in the West
GA	Genetic Algorithm
GBVP	General Boundary Value Problem
GNU	GNU's Not Unix
GUI	Graphical User Interface
LET	Lorentz force Eddy current Testing
MCG	MagnetoCardioGraphy
MDM	Magnetic Dipoles Model
MDS	Modified Direct Search algorithm
MDS-AS	Modified Direct Search algorithm with Amplitude Spectra
MEG	MagnetoEncephaloGraphy
MFT	Magnetic Field Tomography
MRI	Magnetic Resonance Imaging
Nd-Fe-B	Neodymium-Iron-Boron
NMDE	Normalized Maximum Difference Error
NRMSD	Normalized Root Mean Square Deviation
NRMSE	Normalized Root Mean Square Error
OOGL	Object Oriented Graphics Library
PAM	Partition Around Medoids
PCA	Principal Component Analysis
PCGM	Preconditioned Conjugate Gradient Method
PFR	Parametric Fourier Representation
PM	Permanent Magnet
RAM	Random-Access Memory
RR(C)O	Row-wise Representation, Complete and Ordered (matrix)

SGA	Simple Genetic Algorithm
SLAP	Sparse Linear Algebra Package
STL	STereoLithography
SVD	Singular Value Decomposition
VRML	Virtual Reality Meta Language
WRA	Weak Reaction Approach
WWW	World Wide Web

1

VECTOR SHAPE FUNCTIONS

1.1. INTRODUCTION

In the finite element method (FEM) , choice of shape functions which are used for description of the behavior of the electromagnetic field in a finite element, strongly affects the process of solving the analyzed boundary value problem [52]. For scalar problems, an approximation of unknown field function (scalar potential) is usually limited to a specification of the order of polynomial defining shape functions in a finite element. For vector problems, however, the following important properties should be also taken into account:

- the continuity of tangential (or normal) components of the approximate vector field on common faces of adjacent finite elements,
- the continuity of normal (or tangential) components of the curl of the approximate vector field on borders between finite elements,
- zero divergence (or zero curl) of the approximate vector field inside finite elements.

The above properties (or the lack of them) have a strong influence on the applicability of specific boundary value formulations used in 3D magnetostatic problems as well as in 3D quasi-static eddy-current problems.

The goal of this chapter is to present three types of the vector field approximation using brick finite elements as a simple example. According to [12], the following terms (related to finite element geometric parts such as nodes, edges, and faces) will be used to describe the analyzed approximation, namely: nodal, edge, and facet approximation. For each type of approximation, finite element matrices used in the FEM will be determined. They can be directly applied to various problems of technical electrodynamics.

1.2. SAMPLE VECTOR PROBLEM OF TECHNICAL ELECTRODYNAMICS

To avoid unnecessary repetitions in the further analysis of various vector formulations, a general boundary value problem (GBVP) of electrodynamics is defined.

First, the vector function $\mathbf{F}$ is introduced. It can be interpreted as one of the following electromagnetic fields: the electric/magnetic field intensity $\mathbf{E}/\mathbf{H}$, the electric/magnetic

flux density $\mathbf{D}/\mathbf{B}$, the electric current density $\mathbf{J}$, or the magnetic/electric vector potential $\mathbf{A}/\mathbf{T}$.

Then, the vector GBVP (static, quasi-static) is defined as follows: in a certain region Ω is seeking to vector function $\mathbf{F}$. The function $\mathbf{F}$ satisfies the equation:

$$\nabla \times (\nu \nabla \times \mathbf{F}) - \kappa \nabla (\nu \nabla \cdot \mathbf{F}) + \beta \mathbf{F} = \mathbf{Q} \tag{1.1}$$

and the appropriate boundary conditions:

$$\nu \nabla \times \mathbf{F} \times \mathbf{n} = \mathbf{P} \quad \text{and} \quad \kappa \mathbf{n} \cdot \mathbf{F} = p, \quad \text{on } \Gamma_P \tag{1.2}$$

$$\mathbf{n} \times \mathbf{F} = \mathbf{D} \quad \text{and} \quad \nu \nabla \cdot \mathbf{F} = q, \quad \text{on } \Gamma_D \tag{1.3}$$

where Γ_P and Γ_D are non-overlapping parts of boundary Γ of the analyzed region Ω; $\mathbf{Q}$, $\mathbf{P}$; $\mathbf{D}$ are given vector functions; p, q are known scalar functions; coefficients ν, κ, β depend on material parameters and type of the problem (static, quasi-static).

Applying Galerkin's method, the following equivalent integral formulation can be obtained:

$$\begin{aligned} &\int_\Omega \nu (\nabla \times \mathbf{w}) \cdot (\nabla \times \mathbf{F}) d\Omega + \kappa \int_\Omega \nu (\nabla \cdot \mathbf{w})(\nabla \cdot \mathbf{F}) d\Omega + \beta \int_\Omega \mathbf{w} \cdot \mathbf{F} d\Omega = \\ &= \int_\Omega \mathbf{w} \cdot \mathbf{Q} d\Omega + \int_{\Gamma_P} \mathbf{w} \cdot \mathbf{P} d\Gamma + \kappa \int_{\Gamma_P} q \mathbf{w} \cdot \mathbf{n} d\Gamma \end{aligned} \tag{1.4}$$

The vector test function $\mathbf{w}$ in (1.4) has to satisfy homogeneous principal boundary conditions:

$$\kappa \mathbf{w} \cdot \mathbf{n} = 0 \quad \text{on } \Gamma_P \tag{1.5}$$

$$\mathbf{n} \times \mathbf{w} = 0 \quad \text{on } \Gamma_D \tag{1.6}$$

Non-homogeneous boundary conditions (1.2) and (1.3) have to be fulfilled similarly as for scalar problems [51].

In order to solve (1.4) by means of the finite element method, it is necessary to determine finite element matrices for actually used approximation of the vector field $\mathbf{F}$. The vector field $\mathbf{F}$ in any finite element is approximated using vector shape functions $\mathbf{w}_k = w_k \mathbf{1}_k, k = 1 \dots K$ as:

$$\tilde{\mathbf{F}} = \sum_{k=1}^{K} F_k \mathbf{w}_k = \sum_{k=1}^{K} F_k w_k \mathbf{1}_k \tag{1.7}$$

where coefficients F_k can be interpreted as the components of $\mathbf{F}$ at selected points of the finite element (nodes, middle of element edges, or faces), $\mathbf{1}_k$ are local unit vectors, and K is equal to the number of selected points. Substituting (1.7) into (1.4), the following set of algebraic equations is obtained:

$$[\mathbb{S}]\{\tilde{\mathbb{F}}\} = \{\mathbb{R}\} \tag{1.8}$$

where $[\mathbb{S}]$ is the global stiffness matrix and $\{\mathbb{R}\}$ is the load vector.

Assuming that coefficients ν, κ and β are constant inside finite elements, the global stiffness matrix $[\mathbb{S}]$ can be constructed as a sum of the following matrices:

$$[\mathbb{S}] = \nu[\mathbb{E}] + \kappa\nu[\mathbb{G}] + \beta[\mathbb{H}] \tag{1.9}$$

with elements D_{kn}, E_{kn}, and G_{kn} calculated as volume integrals over the appropriate finite element:

$$E_{kn} = \int_{\Omega^e} (\nabla \times \mathbf{w}_k) \cdot (\nabla \times \mathbf{w}_n) d\Omega \tag{1.10}$$

$$G_{kn} = \int_{\Omega^e} (\nabla \cdot \mathbf{w}_k)(\nabla \cdot \mathbf{w}_n) d\Omega \tag{1.11}$$

$$H_{kn} = \int_{\Omega^e} \mathbf{w}_k \cdot \mathbf{w}_n d\Omega \tag{1.12}$$

The right hand side vector $\{\mathbb{R}\}$ of the global system (1.8) is obtained using source terms from (1.1) - (1.3) and the corresponding integrals in (1.4). Under the assumption that the functions Q, P and q are constant in the considered finite element, elements of the load vector $\{R\}$ can be calculated as:

$$R_k = Q_k \int_{\Omega^e} w_k d\Omega + P_k \int_{\Gamma_P^e} w_k d\Gamma + q\kappa n_k \int_{\Gamma_D^e} w_k d\Gamma \tag{1.13}$$

where $Q_k = \mathbf{Q} \cdot \mathbf{1}_k, P_k = \mathbf{P} \cdot \mathbf{1}_k, n_k = \mathbf{n} \cdot \mathbf{1}_k$, and Γ_P^e, Γ_D^e are element parts belonging to the boundary Γ_P or Γ_D, respectively. In next sections, the above matrices for the brick finite element using nodal and edge approximations will be presented in details.

1.3. THE BRICK FINITE ELEMENT

The first order brick finite element is a special type of 8-node isoparametric finite elements where the element edges are parallel to the axes of global coordinate system. The analysis presented here is restricted to the brick elements because of problems with a construction of general isoparametric finite elements having the properties described in Section 1.1.. In the paper [129], the author has tried to define such general elements but the assumptions which he has used are in fact fulfilled only for the brick element. Tetrahedral elements with various approximations of vector fields have been already described in [8, 12, 13, 97].

The normalized brick finite element to be analyzed is shown in Fig. 1.1. It is assumed that the axes of the local coordinate system (ξ, η, ζ) are parallel to the axes of the global coordinate system (x, y, z). In that case, the local coordinate system is given as:

$$(\xi, \eta, \zeta) = \left(\frac{2}{l_x}(x - x_m), \frac{2}{l_y}(y - y_m), \frac{2}{l_z}(z - z_m) \right) \tag{1.14}$$

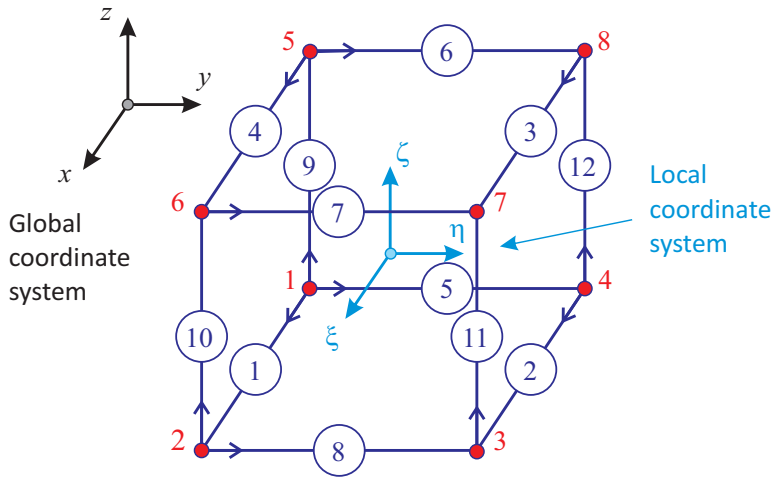

Fig. 1.1: Normalized brick element with node and edge numbering scheme

where x_m, y_m, z_m are coordinates of the center of gravity of the analyzed element and l_x, l_y, l_z are lengths of element edges, respectively. Additionally, the following auxiliary parameters are introduced:

$$\begin{aligned}
\alpha_{1x} &= \tfrac{1}{2}(1-\xi), \quad \alpha_{2x} = \tfrac{1}{2}(1+\xi), \\
\alpha_{1y} &= \tfrac{1}{2}(1-\eta), \quad \alpha_{2y} = \tfrac{1}{2}(1+\eta), \\
\alpha_{1z} &= \tfrac{1}{2}(1-\zeta), \quad \alpha_{2z} = \tfrac{1}{2}(1+\zeta)
\end{aligned} \tag{1.15}$$

The classical 3D nodal shape functions for the brick finite element are given as:

$$\begin{aligned}
N_1 &= \alpha_{1x}\alpha_{1y}\alpha_{1z}, \quad N_5 = \alpha_{1x}\alpha_{1y}\alpha_{2z}, \\
N_2 &= \alpha_{2x}\alpha_{1y}\alpha_{1z}, \quad N_6 = \alpha_{2x}\alpha_{1y}\alpha_{2z}, \\
N_3 &= \alpha_{2x}\alpha_{2y}\alpha_{1z}, \quad N_7 = \alpha_{2x}\alpha_{2y}\alpha_{2z}, \\
N_4 &= \alpha_{1x}\alpha_{2y}\alpha_{1z}, \quad N_8 = \alpha_{1x}\alpha_{2y}\alpha_{2z}
\end{aligned} \tag{1.16}$$

Two additional types of shape functions can be introduced for the brick finite element, namely, edge shape functions:

$$\begin{aligned}
N_1^e &= N_{1x}^e = \alpha_{1y}\alpha_{1z}, \quad N_7^e = N_{3y}^e = \alpha_{2x}\alpha_{2z}, \\
N_2^e &= N_{2x}^e = \alpha_{2y}\alpha_{1z}, \quad N_8^e = N_{4y}^e = \alpha_{2x}\alpha_{1z}, \\
N_3^e &= N_{3x}^e = \alpha_{2y}\alpha_{2z}, \quad N_9^e = N_{1z}^e = \alpha_{1x}\alpha_{1y}, \\
N_4^e &= N_{4x}^e = \alpha_{1y}\alpha_{2z}, \quad N_{10}^e = N_{2z}^e = \alpha_{2x}\alpha_{1y}, \\
N_5^e &= N_{1y}^e = \alpha_{1x}\alpha_{1z}, \quad N_{11}^e = N_{3z}^e = \alpha_{2x}\alpha_{2y}, \\
N_6^e &= N_{2y}^e = \alpha_{1x}\alpha_{2z}, \quad N_{12}^e = N_{4z}^e = \alpha_{1x}\alpha_{2y}
\end{aligned} \tag{1.17}$$

and facet shape functions:

$$N_1^f = \alpha_{1x}, \quad N_3^f = \alpha_{1y}, \quad N_5^f = \alpha_{1z},$$
$$N_2^f = \alpha_{2x}, \quad N_4^f = \alpha_{2y}, \quad N_6^f = \alpha_{2z} \tag{1.18}$$

The relationships between above shape functions and their derivatives are presented in Table 1.1.

Table 1.1: Shape functions and their derivatives

	Node		
	$l_x \frac{\partial}{\partial x}$	$l_y \frac{\partial}{\partial y}$	$l_z \frac{\partial}{\partial z}$
N_1	$-N_1^e$	$-N_5^e$	$-N_9^e$
N_2	N_1^e	$-N_8^e$	$-N_{10}^e$
N_3	N_2^e	N_8^e	$-N_{11}^e$
N_4	$-N_2^e$	N_5^e	$-N_{12}^e$
N_5	$-N_4^e$	$-N_6^e$	N_9^e
N_6	N_4^e	$-N_7^e$	N_{10}^e
N_7	N_3^e	N_7^e	N_{11}^e
N_8	$-N_3^e$	N_6^e	N_{12}^e

	Face		
	$l_x \frac{\partial}{\partial x}$	$l_y \frac{\partial}{\partial y}$	$l_z \frac{\partial}{\partial z}$
N_1^f	-1	0	0
N_2^f	1	0	0
N_3^f	0	-1	0
N_4^f	0	1	0
N_5^f	0	0	-1
N_6^f	0	0	1

	Edge		
	$l_x \frac{\partial}{\partial x}$	$l_y \frac{\partial}{\partial y}$	$l_z \frac{\partial}{\partial z}$
$N_1^e = N_{1x}^e$	0	$-N_5^f$	$-N_3^f$
$N_2^e = N_{2x}^e$	0	N_5^f	$-N_4^f$
$N_3^e = N_{3x}^e$	0	N_6^f	N_4^f
$N_4^e = N_{4x}^e$	0	$-N_6^f$	N_3^f
$N_5^e = N_{1y}^e$	$-N_5^f$	0	$-N_1^f$
$N_6^e = N_{2y}^e$	$-N_6^f$	0	N_1^f
$N_7^e = N_{3y}^e$	N_6^f	0	N_2^f
$N_8^e = N_{4y}^e$	N_5^f	0	$-N_2^f$
$N_9^e = N_{1z}^e$	$-N_3^f$	$-N_1^f$	0
$N_{10}^e = N_{2z}^e$	N_3^f	$-N_2^f$	0
$N_{11}^e = N_{3z}^e$	N_4^f	N_2^f	0
$N_{12}^e = N_{4z}^e$	$-N_4^f$	N_1^f	0

1.4. VECTOR SHAPE FUNCTIONS - NODAL REALIZATION

The most popular approach in the finite element method to problems described by vector field functions is the independent approximation of every global vector field component by means of the classic 3D nodal shape functions (1.16) (nodal approximation). As a global vector field component, we understand the component received from

the projection of the vector field on one of the axes of the global Cartesian coordinate system. It should be noted that in the paper [28], the authors have proposed the approximation using local vector components (components which are covariant with respect to the local coordinate system received from the isoparametric transformation) but the realization of their approach is very complicated and therefore it is not considered in this work. According to the previously formulated assumptions (Section 1.1.), the first order vector shape functions for the brick finite elements are defined using the bi-linear form of shape functions (1.16). In this case, the respective test functions (1.7) take the following form:

$$\mathbf{w}_k = \begin{cases} N_k \mathbf{1}_x & k = 1,\ldots,8 \\ N_{k-8} \mathbf{1}_y & k = 9,\ldots,16 \\ N_{k-16} \mathbf{1}_z & k = 17,\ldots,24 \end{cases} \tag{1.19}$$

with the coefficients F_k defined as:

$$F_k = \begin{cases} F_k^x & k = 1,\ldots,8 \\ F_{k-8}^y & k = 9,\ldots,16 \\ F_{k-16}^z & k = 17,\ldots,24 \end{cases} \tag{1.20}$$

Figure 1.2 shows the nodal vector shape functions in a normalized brick element related to the corresponding element node. The shape functions are visualized as combined vectors $\mathbf{w}_k + \mathbf{w}_{k+8} + \mathbf{w}_{k+16}, k = 1,\ldots,8$, where k denotes the node index.

The nodal approximation of the vector field $\mathbf{F}$ has the following properties:

- all components of the approximate vector function $\tilde{\mathbf{F}}$ are continuous on faces of adjacent elements,
- the normal component of the curl of $\tilde{\mathbf{F}}$ $(\nabla \times \tilde{\mathbf{F}})$ is continuous on faces of adjacent elements in contrast to its tangential components which are discontinuous,
- the divergence $\nabla \cdot \tilde{\mathbf{F}}$ is not equal to 0 inside finite elements except for the case where components F_k $(k = x,y,z)$ are constant with respect to the appropriate coordinates.

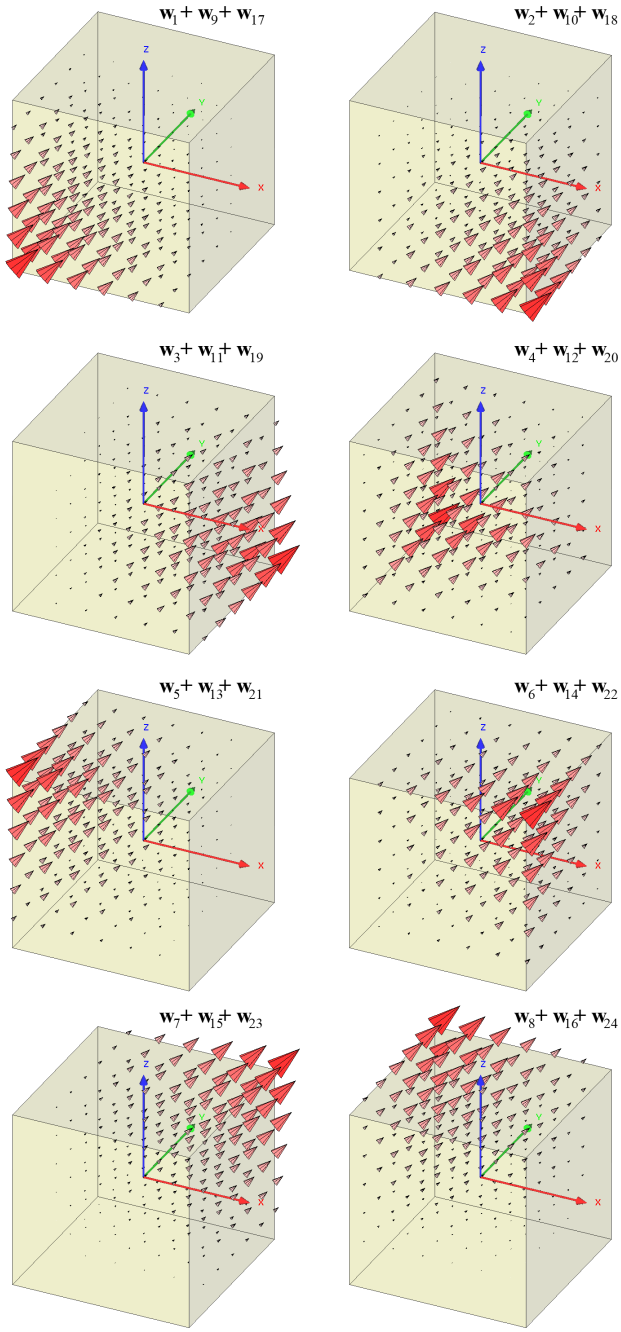

Fig. 1.2: Nodal approximation - vector shape functions in a normalized brick element visualized as combined vectors: $\mathbf{w}_k + \mathbf{w}_{k+8} + \mathbf{w}_{k+16}, k = 1, \ldots, 8$

Elements of the stiffness matrix $[\mathbb{S}]$ are calculated according to (1.9), with the elements (1.10) - (1.12) of $[\mathbb{E}]$, $[\mathbb{G}]$, and $[\mathbb{H}]$ expressed as follows:

$$E_{kn} = \begin{cases} d_1 A_{y,k,n} + d_2 A_{z,k,n} & k = 1\dots 8; \quad n = 1\dots 8 \\ -d_6 B_{xy,(n-8),k} & k = 1\dots 8; \quad n = 9\dots 16 \\ -d_5 B_{xz,(n-16),k} & k = 1\dots 8; \quad n = 17\dots 24 \\ -d_6 B_{xy,(k-8),n} & k = 9\dots 16; \quad n = 1\dots 8 \\ d_3 A_{x,(k-8),(n-8)} + & \\ +d_2 A_{z,(k-8),(n-8)} & k = 9\dots 16; \quad n = 9\dots 16 \\ -d_4 B_{yz,(n-16),(k-8)} & k = 9\dots 16; \quad n = 17\dots 24 \\ -d_5 B_{xz,(k-16),n} & k = 17\dots 24; \quad n = 1\dots 8 \\ -d_4 B_{yz,(k-16),(n-8)} & k = 17\dots 24; \quad n = 9\dots 16 \\ d_3 A_{x,(k-16),(n-16)} + & \\ +d_1 A_{y,(k-16),(n-16)} & k = 17\dots 24; \quad n = 17\dots 24 \end{cases} \tag{1.21}$$

$$G_{kn} = \begin{cases} d_3 A_{x,k,n} & k = 1\dots 8; \quad n = 1\dots 8 \\ d_6 B_{xy,k,(n-8)} & k = 1\dots 8; \quad n = 9\dots 16 \\ d_5 B_{xz,k,(n-16)} & k = 1\dots 8; \quad n = 17\dots 24 \\ d_6 B_{xy,n,(k-8)} & k = 9\dots 16; \quad n = 1\dots 8 \\ d_2 A_{y,(k-8),(n-8)} & k = 9\dots 16; \quad n = 9\dots 16 \\ d_4 B_{yz,(k-8),(n-16)} & k = 9\dots 16; \quad n = 17\dots 24 \\ d_5 B_{xz,n,(k-16)} & k = 17\dots 24; \quad n = 1\dots 8 \\ d_4 B_{yz,(n-8),(k-16)} & k = 17\dots 24; \quad n = 9\dots 16 \\ d_1 A_{z,(k-16),(n-16)} & k = 17\dots 24; \quad n = 17\dots 24 \end{cases} \tag{1.22}$$

$$H_{kn} = \begin{cases} d_7 C_{k,n} & k = 1\dots 8; \quad n = 1\dots 8 \\ 0 & k = 1\dots 8; \quad n = 9\dots 16 \\ 0 & k = 1\dots 8; \quad n = 17\dots 24 \\ 0 & k = 9\dots 16; \quad n = 1\dots 8 \\ d_7 C_{(k-8),(n-8)} & k = 9\dots 16; \quad n = 9\dots 16 \\ 0 & k = 9\dots 16; \quad n = 17\dots 24 \\ 0 & k = 17\dots 24; \quad n = 1\dots 8 \\ 0 & k = 17\dots 24; \quad n = 9\dots 16 \\ d_7 C_{(k-16),(n-16)} & k = 17\dots 24; \quad n = 17\dots 24 \end{cases} \tag{1.23}$$

where constants d_i are defined as

$$d_1 = \frac{l_x l_z}{36 l_y},\ d_2 = \frac{l_x l_y}{36 l_z},\ d_3 = \frac{l_y l_z}{36 l_z},\ d_4 = \frac{l_x}{24},\ d_5 = \frac{l_y}{24},\ d_6 = \frac{l_z}{24}, d_7 = \frac{l_x l_y l_z}{216}$$

and the elements $A_{x,i,j}, A_{y,i,j}, A_{z,i,j}, B_{xy,i,j}, B_{xz,i,j}, B_{yz,i,j}, C_{i,j}$ are given as the following matrices

$$[\mathbb{A}_{x,i,j}] = \begin{bmatrix} 4 & -4 & -2 & 2 & 2 & -2 & -1 & 1 \\ & 4 & 2 & -2 & -2 & 2 & 1 & -1 \\ & & 4 & -4 & -1 & 1 & 2 & -2 \\ & & & 4 & 1 & -1 & -2 & 2 \\ & & & & 4 & -4 & -2 & 2 \\ & & & & & 4 & 2 & -2 \\ & & & & & & 4 & -4 \\ sym & & & & & & & 4 \end{bmatrix} \tag{1.24}$$

$$[\mathbb{A}_{y,i,j}] = \begin{bmatrix} 4 & 2 & -2 & -4 & 2 & 1 & -1 & -2 \\ & 4 & -4 & -2 & 1 & 2 & -2 & -1 \\ & & 4 & 2 & -1 & -2 & 2 & 1 \\ & & & 4 & -2 & -1 & 1 & 2 \\ & & & & 4 & 2 & -2 & -4 \\ & & & & & 4 & -4 & -2 \\ & & & & & & 4 & 2 \\ sym & & & & & & & 4 \end{bmatrix} \tag{1.25}$$

$$[\mathbb{A}_{z,i,j}] = \begin{bmatrix} 4 & 2 & 1 & 2 & -4 & -2 & -1 & -2 \\ & 4 & 2 & 1 & -2 & -4 & -2 & -1 \\ & & 4 & 2 & -1 & -2 & -4 & -2 \\ & & & 4 & -2 & -1 & -2 & -4 \\ & & & & 4 & 2 & 1 & 2 \\ & & & & & 4 & 2 & 1 \\ & & & & & & 4 & 2 \\ sym & & & & & & & 4 \end{bmatrix} \tag{1.26}$$

$$[\mathbb{B}_{xy,i,j}] = \begin{bmatrix} 2 & 2 & -2 & -2 & 1 & 1 & -1 & -1 \\ -2 & -2 & 2 & 2 & -1 & -1 & 1 & 1 \\ -2 & -2 & 2 & 2 & -1 & -1 & 1 & 1 \\ 2 & 2 & -2 & -2 & 1 & 1 & -1 & -1 \\ 1 & 1 & -1 & -1 & 2 & 2 & -2 & -2 \\ -1 & -1 & 1 & 1 & -2 & -2 & 2 & 2 \\ -1 & -1 & 1 & 1 & -2 & -2 & 2 & 2 \\ 1 & 1 & -1 & -1 & 2 & 2 & -2 & -2 \end{bmatrix} \tag{1.27}$$

$$[\mathbb{B}_{xz,i,j}] = \begin{bmatrix} 2 & 2 & 1 & 1 & -2 & -2 & -1 & -1 \\ -2 & -2 & -1 & -1 & 2 & 2 & 1 & 1 \\ -1 & -1 & -2 & -2 & 1 & 1 & 2 & 2 \\ 1 & 1 & 2 & 2 & -1 & -1 & -2 & -2 \\ 2 & 2 & 1 & 1 & -2 & -2 & -1 & -1 \\ -2 & -2 & -1 & -1 & 2 & 2 & 1 & 1 \\ -1 & -1 & -2 & -2 & 1 & 1 & 2 & 2 \\ 1 & 1 & 2 & 2 & -1 & -1 & -2 & -2 \end{bmatrix} \tag{1.28}$$

$$[\mathbb{B}_{yz,i,j}] = \begin{bmatrix} 2 & 1 & 1 & 2 & -2 & -1 & -1 & -2 \\ 1 & 2 & 2 & 1 & -1 & -2 & -2 & -1 \\ -1 & -2 & -2 & -1 & 1 & 2 & 2 & 1 \\ -2 & -1 & -1 & -2 & 2 & 1 & 2 & 2 \\ 2 & 1 & 1 & 2 & -2 & -1 & -1 & -2 \\ 1 & 2 & 2 & 1 & -1 & -2 & -2 & -1 \\ -1 & -2 & -2 & -1 & 1 & 2 & 2 & 1 \\ -2 & -1 & -1 & -2 & 2 & 1 & 2 & 2 \end{bmatrix} \tag{1.29}$$

$$[\mathbb{C}_{i,j}] = \begin{bmatrix} 8 & 4 & 2 & 4 & 4 & 2 & 1 & 2 \\ & 8 & 4 & 2 & 2 & 4 & 2 & 1 \\ & & 8 & 4 & 1 & 2 & 4 & 2 \\ & & & 8 & 2 & 1 & 2 & 4 \\ & & & & 8 & 4 & 2 & 4 \\ & & & & & 8 & 4 & 2 \\ & & & & & & 8 & 4 \\ sym & & & & & & & 8 \end{bmatrix} \tag{1.30}$$

Integrals used for the calculation of right hand side vector elements R_k (1.13) are equal respectively:

$$\int_{\Omega^e} N_i d\Omega = \frac{V_e}{8}, \quad \int_{\Gamma^e} N_i d\Gamma = \frac{S_e}{4} \tag{1.31}$$

where V_e denotes the volume of the corresponding finite element and S_e is the area of the appropriate element face.

1.5. VECTOR SHAPE FUNCTIONS - EDGE APPROXIMATION

The edge approximation introduced to electromagnetic field calculations in the paper [13] can be implemented using tetrahedral elements [8, 10, 11, 97, 131] as well as brick elements. Linear edge shape functions for the brick finite element shown in Fig. 1.1 have the following form:

$$\mathbf{w}_k = N_k^e \mathbf{1}_k, \quad k = 1 \ldots 12 \tag{1.32}$$

where N_k^e is given by (1.17) and unit vectors $\mathbf{1}_k$ are defined as:

$$\mathbf{1}_k = \begin{cases} \mathbf{1}_x & k = 1 \ldots 4 \\ \mathbf{1}_y & k = 5 \ldots 8 \\ \mathbf{1}_z & k = 9 \ldots 12 \end{cases} \tag{1.33}$$

The coefficient F_k in (1.7) is the projection of the vector field $\mathbf{F}$ on the brick edge k at its center. Figure 1.3 shows the edge shape functions attached to the corresponding element edge in the normalized brick element.

The approximation of the vector field $\mathbf{F}$ by means of edge shape functions has the following properties:

- the tangential components of $\tilde{\mathbf{F}}$ on common faces of adjacent finite elements are continuous whereas normal components are discontinuous (except for the case where the function $\mathbf{F}$ is constant in the normal direction to the considered face),
- the normal component of the curl of $\tilde{\mathbf{F}}$ ($\nabla \times \tilde{\mathbf{F}}$) is continuous on faces of adjacent finite elements while the tangential components of curl are discontinuous,
- the divergence $\nabla \cdot \tilde{\mathbf{F}}$ equals zero inside brick finite elements.

The above features of the edge approximation cause that edge elements are particularly interesting in the calculation of electromagnetic fields. Since the edge approximation satisfies the condition $\nabla \cdot \tilde{\mathbf{F}} = 0$, it can be assumed $\kappa = 0$ in the general boundary problem (Section 1.2.), which considerably simplifies the equation (1.1) and the corresponding boundary conditions as well.

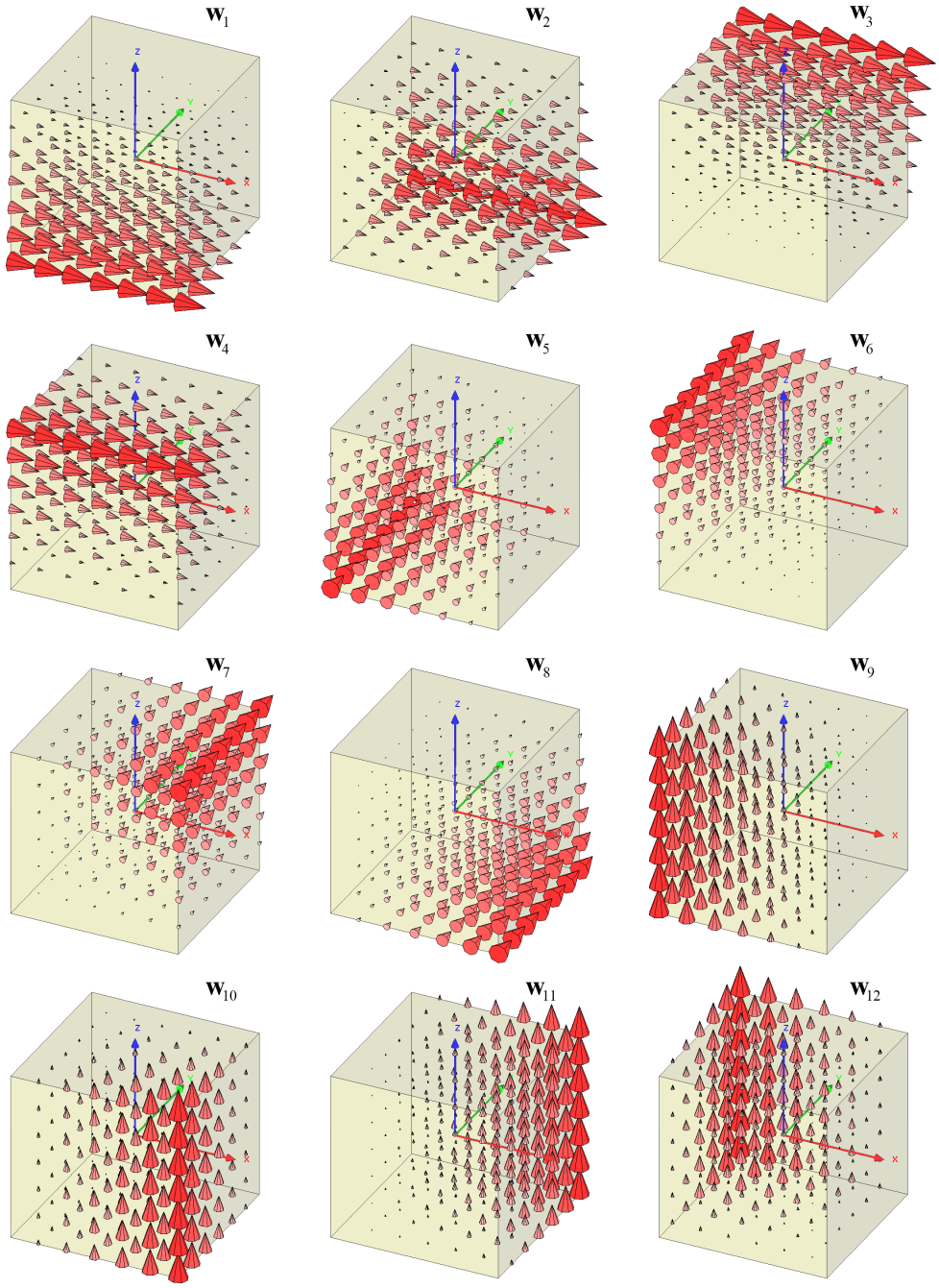

Fig. 1.3: Edge approximation - vector shape functions in a normalized brick element

The continuity of tangential components of the approximate vector field $\tilde{\mathbf{F}}$ and the normal components of its curl, and at the same time, discontinuity of the remaining components is beneficial because it allows the FEM easily integrating materials heterogeneity in the domain under consideration. It should be noted that the continuity of all components of the vector field $\tilde{\mathbf{F}}$, which was the characteristic feature of nodal aproximation, limits the possibilities. This is also one of the reasons of a growing popularity of edge approximation.

Elements (1.10) - (1.12) of $[\mathbb{E}], [\mathbb{G}]$, and $[\mathbb{H}]$ for the edge approximation have the following form:

$$E_{kn} = \begin{cases} e_1 A_{k,n} + e_2 B_{k,n} & k = 1\ldots4; \quad n = 1\ldots4 \\ -e_6 C_{k,(n-4)} & k = 1\ldots4; \quad n = 5\ldots8 \\ -e_5 C_{(n-8),k} & k = 1\ldots4; \quad n = 9\ldots12 \\ -e_6 C_{n,(k-4)} & k = 5\ldots8; \quad n = 1\ldots4 \\ e_2 A_{(k-4),(n-4)} + e_3 B_{(k-4),(n-4)} & k = 5\ldots8; \quad n = 5\ldots8 \\ -e_4 C_{(k-4),(n-8)} & k = 5\ldots8; \quad n = 9\ldots12 \\ -e_5 C_{(k-8),n} & k = 9\ldots12; \quad n = 1\ldots4 \\ -e_4 C_{(n-4),(k-8)} & k = 9\ldots12; \quad n = 5\ldots8 \\ e_3 A_{(k-8),(n-8)} + e_1 B_{(k-8),(n-8)} & k = 9\ldots12; \quad n = 9\ldots12 \end{cases} \tag{1.34}$$

$$G_{kn} = 0 \tag{1.35}$$

$$H_{kn} = \begin{cases} e_7 D_{k,n} & k = 1\ldots4; \quad n = 1\ldots4 \\ 0 & k = 1\ldots4; \quad n = 5\ldots8 \\ 0 & k = 1\ldots4; \quad n = 9\ldots12 \\ 0 & k = 5\ldots8; \quad n = 1\ldots4 \\ e_7 D_{(k-4),(n-4)} & k = 5\ldots8; \quad n = 5\ldots8 \\ 0 & k = 5\ldots8; \quad n = 9\ldots12 \\ 0 & k = 9\ldots12; \quad n = 1\ldots4 \\ 0 & k = 9\ldots12; \quad n = 5\ldots8 \\ e_7 A_{(k-8),(n-8)} & k = 9\ldots12; \quad n = 9\ldots12 \end{cases} \tag{1.36}$$

where constants e_i are defined as

$$\begin{aligned} &e_1 = \frac{l_x l_z}{6 l_y}, \quad e_2 = \frac{l_x l_y}{6 l_z}, \quad e_3 = \frac{l_y l_z}{6 l_z}, \\ &e_4 = \frac{l_x}{6}, \quad e_5 = \frac{l_y}{6}, \quad e_6 = \frac{l_z}{6}, \quad e_7 = \frac{l_x l_y l_z}{36} \end{aligned} \tag{1.37}$$

and the elements $A_{i,j}, B_{i,j}, C_{i,j}, D_{i,j}$ are described by the matrices

$$[\mathbb{A}_{i,j}] = \begin{bmatrix} 2 & -2 & -1 & 1 \\ & 2 & 1 & -1 \\ & & 2 & -2 \\ sym & & & 2 \end{bmatrix}, \quad [\mathbb{B}_{i,j}] = \begin{bmatrix} 2 & 1 & -1 & -2 \\ & 2 & -2 & -1 \\ & & 2 & 1 \\ sym & & & 2 \end{bmatrix},$$
$$[\mathbb{C}_{i,j}] = \begin{bmatrix} 2 & 1 & -1 & -2 \\ -2 & -1 & 1 & 2 \\ -1 & -2 & 2 & 1 \\ 1 & 2 & -2 & -1 \end{bmatrix}, \quad [\mathbb{D}_{i,j}] = \begin{bmatrix} 4 & 2 & 1 & 2 \\ & 4 & 2 & 1 \\ & & 4 & 2 \\ sym & & & 4 \end{bmatrix} \tag{1.38}$$

Elements R_k of the load vector in (1.13) are calculated using the following integrals:

$$\int_{\Omega^e} N_i d\Omega = \frac{V_e}{4}, \quad \int_{\Gamma^e} N_i d\Gamma = \frac{S_e}{2} \tag{1.39}$$

where V_e denotes the volume of the corresponding finite element and S_e is the area of the appropriate element face.

1.6. VECTOR SHAPE FUNCTIONS - FACET APPROXIMATION

The first order facet approximation for the brick finite element shown in Fig. 1.1 is introduced using facet shape functions N_k^f given by (1.18). In this case, the test functions (1.7) have the following form:

$$\mathbf{w}_k = N_k^f \mathbf{1}_k \tag{1.40}$$

where $\mathbf{1}_k$ is a unit vector defined as

$$\mathbf{1}_k = \begin{cases} \mathbf{1}_x & k = 1,2 \\ \mathbf{1}_y & k = 3,4 \\ \mathbf{1}_z & k = 5,6 \end{cases} \tag{1.41}$$

The coefficient F_k in (1.7) is interpreted in this approximation as a projection of the vector field $\tilde{\mathbf{F}}$ on normal located in the center of the k^{th} brick face. Figure 1.4 presents linear facet vector shape functions in a normalized brick element associated with the corresponding brick face.

The facet approximation is characterized by the following properties:

- tangential components of the approximate vector field $\tilde{\mathbf{F}}$ are discontinuous on common faces of adjacent brick finite elements,
- the curl of $\tilde{\mathbf{F}}$ equals zero inside brick finite elements.

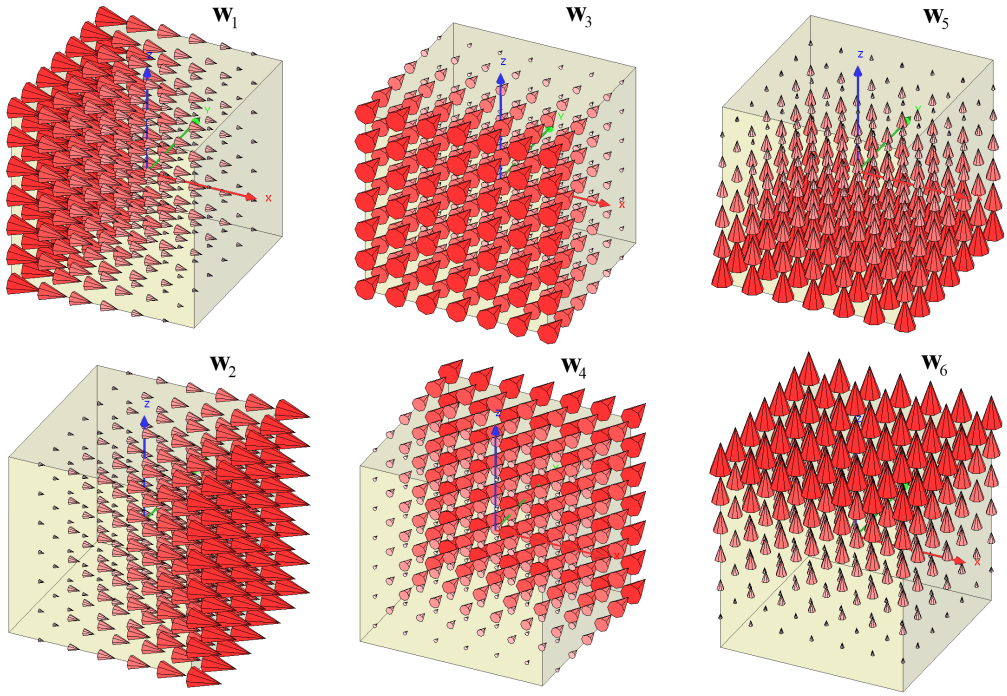

Fig. 1.4: Linear facet shape functions in a normalized brick element

The above properties show that the linear facet approximation is of little use in the calculation of electromagnetic fields. It can not be used as a basis for the approximation of the vector field $\mathbf{F}$. However, it is worth noting that the curl of the vector field $\tilde{\mathbf{F}}$ in the edge approximation is in fact expressed by the facet shape functions. Thus, the facet elements are an important complement to the nodal and edge approximation.

1.7. SUMMARY

In this chapter, various vector shape functions used in the 3D finite element method applied to the technical electrodynamics are presented. At the beginning, the general boundary value problem (including both static and quasi-static vector fields) is defined. Then, a normalized brick finite element together with corresponding shape functions of the first order is introduced. Using the normalized brick finite element as a simple example, three approximations of vector fields in a finite element are presented and discussed, namely, nodal, edge and facet approximation. For the nodal and edge approximation the complete stiffness matrices and load vectors are given. The characteristic features of all approximations are also discussed showing reasons for the popularity of edge approximation and inability to use of facet approximation in the calculation of electromagnetic fields.

2

ANALYSIS OF 3D MAGNETOSTATIC FIELDS

2.1. INTRODUCTION

The purpose of this chapter is to compare the essential features of solutions of 3D linear magnetostatic boundary value problems obtained by the finite element method using the brick finite element introduced in Chapter 1. In this chapter the following formulations for the description of the magnetic field are used:

- magnetic scalar potential φ or two, reduced and total, magnetic scalar potentials $\varphi - \psi$,
- magnetic vector potential $\mathbf{A}$,
- magnetic field intensity $\mathbf{H}$.

In the next section, a general 3D magnetostatic boundary value problem is formulated. Additionally, a simple benchmark example which is further used for comparisons of the above formulations is introduced. For each formulation, boundary conditions and the implementation of material heterogeneity in the considered region are explained in details.

The magnetostatic boundary value problem is formulated in such a way that it could also be applicable in an iterative process of fulfilling continuity conditions on boundaries between conducting and non-conducting regions in eddy current problems. In addition, to explain more completely specific features of 3D magnetostatic problems, the following issues are also discussed: (1) the formulation φ-ψ for a ferromagnetic block in an external magnetic field, (2) the application of the electric vector potential $\mathbf{T}$ for description of windings leading direct current, (3) calculations of the magnetic field produced by a sample electromagnet, and (4) the formulation $\mathbf{A}$-$\mathbf{M}$ applicable to the analysis of nonlinear problems.

2.2. GENERAL 3D MAGNETOSTATIC BOUNDARY VALUE PROBLEM

Let Ω be a non-conductive region in 3D space surrounded by the boundary Γ. The static magnetic intensity field $\mathbf{H}$ in the region Ω is described by Maxwell's equations:

$$\nabla \times \mathbf{H} = 0, \quad (\nabla \times \mathbf{H} = \mathbf{J}_s, \quad \mathbf{J}_s = 0) \tag{2.1}$$

$$\nabla \cdot \mathbf{B} = 0, \quad \mathbf{B} = \mu \mathbf{B} \tag{2.2}$$

where $\mathbf{J}_s$ is a source current density in a certain region $\Omega_s \subset \Omega$. The assumption $\mathbf{J}_s = 0$ does not narrow the analysis because in any case the magnetic field $\mathbf{H}_s$ produced by source currents of known distribution can be calculated using the Biot-Savart law and then included in boundary conditions. The other method of taking into account the source field $\mathbf{H}_s$ is shown in Section 2.3.2.. In Section 2.3.2., the effective method of modeling the magnetic field produced by 3D current windings using the magnetic scalar potential φ and the electric vector potential $\mathbf{T}$ is described.

Additionally, it is assumed that the magnetic permeability μ is constant in every part of the region Ω. To complete the definition of the boundary value problem, it is presumed that the boundary Γ of the region Ω consists of two parts:

Γ_H, with the following boundary condition:

$$\mathbf{H} \times \mathbf{n} = \mathbf{K}_0 \tag{2.3}$$

and Γ_B, where the normal component of the magnetic flux density is defined:

$$\mathbf{n} \cdot \mathbf{B} = B_{n0} \tag{2.4}$$

To illustrate problems which appear during numerical simulations of the above boundary value problem, a simple test problem shown in Fig. 2.1 is defined. For the

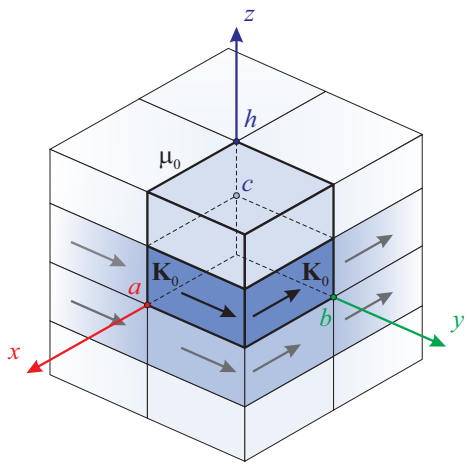

Fig. 2.1: Simple test problem - surface currents $\mathbf{K}_0$ flowing on the walls of air cavity

problem shown in Fig. 2.1 it is necessary to find the distribution of magnetic field $\mathbf{H}$ produced by the surface current $\mathbf{K}_0$ flowing on the walls of air cavity $2a \times 2b \times 2h$ ($\mu = \mu_0$) located in an ideal ferromagnetic material ($\mu \to \infty$).

Because of symmetry, only one eighth of the cavity region is analyzed. The following boundary conditions are set on symmetry planes and cavity walls:

$$\mathbf{n} \cdot \mathbf{B} = 0 \quad \text{for} \begin{cases} x = 0, & 0 \leqslant y \leqslant b, \quad 0 \leqslant z \leqslant h \\ y = 0, & 0 \leqslant x \leqslant a, \quad 0 \leqslant z \leqslant h \end{cases} \tag{2.5}$$

$$\mathbf{H} \times \mathbf{n} = \mathbf{K}_0 \quad \text{elsewhere} \tag{2.6}$$

Surface currents $\mathbf{K}_0$ are defined as:

$$\mathbf{K}_0 = \begin{cases} K_0\mathbf{1}_y & x = a, \quad 0 \leqslant y \leqslant b, \quad 0 \leqslant z \leqslant c \\ 0 & x = a, \quad 0 \leqslant y \leqslant b, \quad c < z \leqslant h \\ -K_0\mathbf{1}_x & y = b, \quad 0 \leqslant x \leqslant a, \quad 0 \leqslant z \leqslant c \\ 0 & y = b, \quad 0 \leqslant x \leqslant a, \quad c < z \leqslant h \\ 0 & z = 0, \quad 0 \leqslant x \leqslant a, \quad 0 \leqslant y \leqslant b \\ 0 & z = h, \quad 0 \leqslant x \leqslant a, \quad 0 \leqslant y \leqslant b \end{cases} \tag{2.7}$$

The above problem can be solved analytically using the method of separation of variables [52]. Applying $\alpha \to 0$ to the solution given in [52], p. 74, components of the magnetic field intensity $\mathbf{H}$ can be described by the following expressions:

$$H_x = \frac{4}{\pi} \sum_{m=1}^{\infty} w_m r_m \sin r_m z \sum_{n=1}^{\infty} \frac{(-1)^{n+1}}{(2n-1)\beta_{xmn}} \frac{\sinh \beta_{xmn} x}{\cosh \beta_{xmn} a} \cos q_n y \tag{2.8}$$

$$H_y = \frac{4}{\pi} \sum_{m=1}^{\infty} w_m r_m \sin r_m z \sum_{n=1}^{\infty} \frac{(-1)^{n+1}}{(2n-1)\beta_{ymn}} \frac{\sinh \beta_{ymn} y}{\cosh \beta_{ymn} b} \cos p_n x \tag{2.9}$$

$$\begin{aligned} H_z = &\frac{4}{\pi} \sum_{m=0}^{\infty} w_m \cos r_m z \sum_{n=1}^{\infty} \frac{(-1)^{n+1}}{2n-1} \cdot \\ &\cdot \left(\frac{\cosh \beta_{xmn} x}{\cosh \beta_{xmn} a} \cos q_n y + \frac{\cosh \beta_{ymn} y}{\cosh \beta_{ymn} b} \cos p_n x \right) \end{aligned} \tag{2.10}$$

where

$$\begin{aligned} r_m &= \frac{m\pi}{h}, \quad q_n = \frac{(2n-1)\pi}{2b}, \quad p_n = \frac{(2n-1)\pi}{2a}, \\ \beta_{xmn} &= \sqrt{q_n^2 + r_m^2}, \quad \beta_{ymn} = \sqrt{p_n^2 + r_m^2} \\ w_m &= \begin{cases} \dfrac{2K_0}{m\pi} \sin(m\pi \dfrac{c}{h}) & , m \neq 0 \\ K_0 \dfrac{c}{h} & , m = 0 \end{cases} \end{aligned}$$

Results of the analytical solution (further used as the reference in comparisons of various formulations) are shown in Fig. 2.2. Calculations have been performed for the following dimensionless parameters: $a = b = h = 1$, $c/h = 0.6$, and $K_0 = 0.5$.

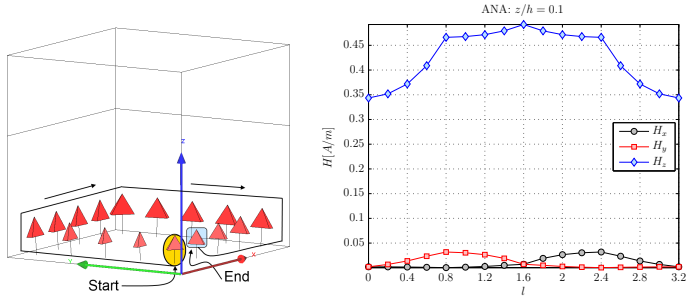

(a) Line l_1

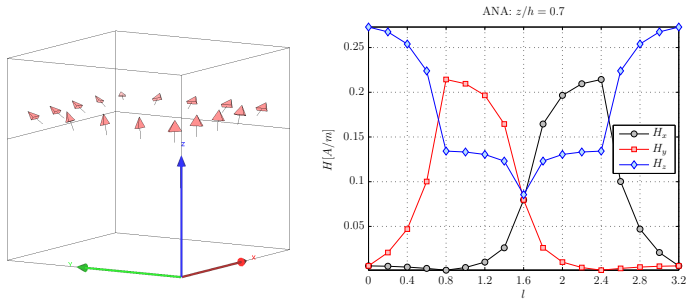

(b) Line l_2

Fig. 2.2: Magnetic field intensity **H** in a cubic hole, (ANA - analytical solution)

The magnetic field intensity **H** is calculated in a set of points $\mathbf{P}_i$ located on two lines l_1 and l_2. Positions of points on the line l_k are defined as follows:

$$l_k : \tilde{\mathbf{P}}_i \begin{cases} x/a = \begin{bmatrix} \tilde{x}_0, & i = 1 \dots N_y - 1 \\ \tilde{x}_0 + (i-1)\Delta\tilde{x}, & i = 1 \dots N_x - 1 \\ \tilde{x}_0 + N_x \Delta\tilde{x} & i = 1 \dots N_y - 1 \\ \tilde{x}_0 + (N_x - i)\Delta\tilde{x}, & i = 1 \dots N_x - 1 \end{bmatrix} \\ y/b = \begin{bmatrix} \tilde{y}_0 + (i-1)\Delta\tilde{y}, & i = 1 \dots N_y - 1 \\ \tilde{y}_0 + N_y \Delta\tilde{y}, & i = 1 \dots N_x - 1 \\ \tilde{y}_0 + (N_y - i)\Delta\tilde{y}, & i = 1 \dots N_y - 1 \\ \tilde{y}_0, & i = 1 \dots N_x - 1 \end{bmatrix} \\ z/h = \begin{bmatrix} \tilde{z}_k, & i = 1 \dots N_y - 1 \\ \tilde{z}_k, & i = 1 \dots N_x - 1 \\ \tilde{z}_k, & i = 1 \dots N_y - 1 \\ \tilde{z}_k, & i = 1 \dots N_x - 1 \end{bmatrix} \end{cases} \tag{2.11}$$

where N_x, N_y are numbers of observation points along x and y axis, respectively; $\tilde{x}_0 = x_0/a$, $\tilde{y}_0 = y_0/b$, $\tilde{z}_k = z_k/h$; $\Delta\tilde{x} = \Delta x/a$, $\Delta\tilde{y} = \Delta y/b$ are normalized distances between

adjacent points. Figure 2.2 shows the results for $\tilde{z}_1 = 0.1$ (line l_1) and $\tilde{z}_2 = 0.7$ (line l_2). Other settings, namely $N_x = N_y = 5$, $\Delta\tilde{x} = \Delta\tilde{y} = 0.2$, and $\tilde{x}_0 = \tilde{y}_0 = 0.1$ are the same for both lines.

Results of calculations are presented as 3D arrows located at points $\tilde{\mathbf{P}}_i$. The size of arrows is proportional to the magnetic field $\mathbf{H}$ at the hook points $\tilde{\mathbf{P}}_i$. Additionally, plots of magnetic field components $\mathbf{H} = [H_x, H_y, H_z]^T$ against a normalized distance from the point $\tilde{\mathbf{P}}_0 = [\tilde{x}_0, \tilde{y}_0, \tilde{z}_k]^T$ calculated along the l_k line are presented.

2.3. 3D ANALYSIS OF MAGNETOSTATIC FIELD BY MEANS OF SCALAR POTENTIALS

First, the boundary value problem described in Section 2.2. is solved by means of the finite element method using the scalar potential formulation φ. Because the region Ω is magnetically homogeneous and does not contain source currents it is enough to apply only one magnetic scalar potential defined as $\mathbf{H} = -\nabla\varphi$. The equation

$$\nabla \cdot (\mu \nabla \varphi) = 0 \tag{2.12}$$

results from equations (2.1) and (2.2) after substitution $\mathbf{H} = -\nabla\varphi$. (2.12) has a unique solution if Dirichlet/Neumann boundary conditions are set on the boundary Γ. Neumann boundary condition follows directly from (2.4) and has the form:

$$\frac{\partial \varphi}{\partial n} = -\frac{1}{\mu} B_{n0} \quad \text{on } \Gamma_B \tag{2.13}$$

In general, it is difficult to obtain Dirichlet boundary conditions directly from equation (2.3). In fact, they can be found if the vector function $\mathbf{n} \times \mathbf{K}_0$ can be expressed as a gradient of a certain scalar function. Fortunately, in the test problem (Section 2.2.), Dirichlet condition on boundary Γ_H is obvious. If $\varphi = 0$ is assumed on the wall $z = 0$ then on walls $x = 0$ and $y = b$ in the interval $z \in (0, c)$, the scalar potential φ varies linearly with z and takes the constant value φ_0 on the rest part of the boundary Γ_H ($\varphi_0 = -cK_0$):

$$\varphi = \left\{ \begin{array}{ll} -cK_0 z, & 0 \leqslant z \leqslant c \\ -cK_0, & c \leqslant z \leqslant h \end{array} \right\} \quad \text{for } x = 0 \text{ or } y = b \tag{2.14}$$

The solution of equation (2.12) with Dirichlet and Neumann boundary conditions (2.13) and (2.14) by means of FEM with classical node finite elements using scalar potential φ formulation is shown in Fig. 2.3. Details of a weak formulation of the problem and an approximation of the scalar potential in a finite element as well as calculations of element matrices are omitted because they can easily be found in the literature e.g. [116, 147, 148].

For each component H_p of the magnetic intensity $\mathbf{H}$, the normalized local error $\epsilon^i_{k,p}$ at point $\tilde{\mathbf{P}}_i$ located on line l_k (2.11) is calculated as:

$$\epsilon^i_{k,p} = \frac{H^i_{p,FEM} - H^i_{p,ANA}}{H^i_{ANA}} 100\%, \qquad p \in \{x, y, z\} \tag{2.15}$$

where $H^i = \sqrt{(H_x^i)^2 + (H_y^i)^2 + (H_z^i)^2}$, and subscripts *FEM*, *ANA* denote fields obtained from the finite element method and the reference analytical method (2.8) - (2.10), respectively.

Normalized root mean square deviation (NRMSD) δ_k along the line l_k is defined as:

$$\delta_k = \sqrt{\delta_{k,x}^2 + \delta_{k,y}^2 + \delta_{k,z}^2} \tag{2.16}$$

where

$$\delta_{k,p} = \frac{\sqrt{\frac{1}{N}\sum_{i=1}^{N}\left(H_{p,FEM}^i - H_{p,ANA}^i\right)^2}}{\max\limits_{i=1\ldots N}(H_{p,ANA}^i) - \min\limits_{i=1\ldots N}(H_{p,ANA}^i)} 100\%, \quad p \in \{x, y, z\} \tag{2.17}$$

and $N = 2(N_x + N_y - 2)$ is the number of computational points along the line l_k (2.11).

Figure 2.3 shows results and the normalized local error ϵ_k^i along lines l_k for the FEM analysis using the magnetic scalar potential φ formulation. The calculations have been

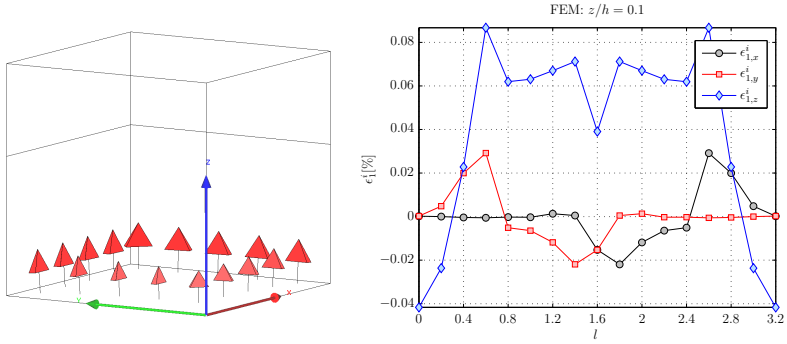

(a) Line l_1: $\delta_1 = 0.29\%$

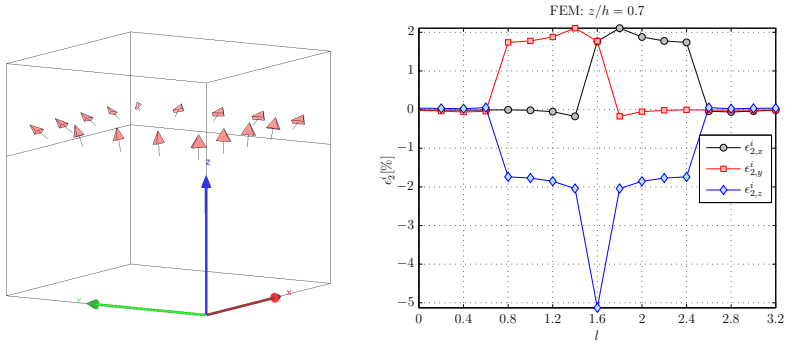

(b) Line l_2: $\delta_2 = 2.44\%$

Fig. 2.3: Test problem - magnetic intensity **H** and normalized error ϵ_k^i calculated using magnetic scalar potential φ (FEM mesh: $15 \times 15 \times 15$ scalar linear node brick elements)

performed for a uniform mesh of $15 \times 15 \times 15$ linear node brick finite elements. It can be observed that the largest local error ($\epsilon^i_{2,z} = -5.1\%$) occurs for H_z component on the line l_2 in the vicinity of the corner where the wrap-current ends and at the same time $\mathbf{K}_0$ changes direction ($l_2 = 1.6$). Increasing the density of the finite element mesh reduces the global NRMSD of the $\mathbf{H}$ field determination according to $\mathcal{O}(h)$, where h is the mesh density. The maximum normalized local error on the line l_2 decreases even faster as $\mathcal{O}(h^2)$. The relatively large local error near the corner where the surface current changes direction is not related to the formulation used in the FEM, but is the result of the specificity of the test problem. In summary, it can be concluded that the FEM formulation using the magnetic scalar potential φ is an effective approach to modeling the magnetic field in homogeneous magnetic non-conductive domains.

2.3.1. 3D ANALYSIS BY MEANS OF TWO SCALAR POTENTIALS

In the previous section, the 3D magnetostatic analysis for magnetically homogeneous domain has been described. For this case, the source magnetic field $\mathbf{H}_s$ was taken into account by setting appropriate non-homogeneous boundary conditions (2.3) and (2.4). In this section, the region Ω restricted by the boundary Γ, consisting of two parts Ω_{air} (empty air space, $\mu = \mu_0$) and Ω_{Fe} (ferromagnetic material, $\mu = \mu_{Fe}$) is considered. It is assumed that the source field $\mathbf{H}_s$ is known. In the empty air space Ω_{air}, the magnetic field $\mathbf{H}_t$ can be expressed as a sum of the source (external) field $\mathbf{H}_s$ and the induced field $\mathbf{H}$:

$$\mathbf{H}_t = \mathbf{H}_s + \mathbf{H} \tag{2.18}$$

The induced magnetic field $\mathbf{H}$ can be described by the so-called reduced magnetic scalar potential φ ($\mathbf{H} = -\nabla\varphi$). Thus, the magnetic field $\mathbf{H}_t$ in the air region is given as:

$$\mathbf{H}_t = \mathbf{H}_s - \nabla\varphi \tag{2.19}$$

The total magnetic field in the ferromagnetic region can be described by the magnetic scalar potential ψ as

$$\mathbf{H}_t = -\nabla\psi \tag{2.20}$$

The introduction of two different potentials (φ and ψ) is motivated by the need to avoid large computational errors which arise in the case of using decomposition (2.18) also in the ferromagnetic region [108, 121]. Another reason for applying this approach is the loss of symmetry of the Jacobi matrix in the FEM in the case when the magnetic field analysis in the nonlinear ferromagnetic region uses only reduced potential φ.

The advantage of using two potentials is a possibility to take into account the external source magnetic field $\mathbf{H}_s$ directly in the equation describing the magnetic field as

$$\nabla \cdot (\mu_0 \nabla\varphi) = \nabla \cdot (\mu_0 \mathbf{H}_s) \tag{2.21}$$

In addition, the two potential approach allows the use of special techniques for modeling unbounded regions (e.g. infinite elements [53]) which significantly reduces the global number of finite elements in the analyzed region, and thus also the computation time.

Because the magnetic field is source free ($\nabla \cdot \mathbf{B} = 0$), the right side of equation (2.21) is equal to zero in Ω_{air} except the interface boundary Γ_{Fe} between the air and the ferromagnetic region. Thus, the magnetic field in Ω_{air} and Ω_{Fe} is described by equations

$$\begin{cases} \nabla \cdot (\mu_0 \nabla \varphi) = 0 & \text{in } \Omega_{air} \\ \nabla \cdot (\mu_{Fe} \nabla \psi) = 0 & \text{in } \Omega_{Fe} \end{cases} \tag{2.22}$$

Continuity conditions at the interface Γ_{Fe} have the following form:

$$-\mu_{Fe} \frac{\partial \psi}{\partial n} = \mu_0 \left(H_{sn} - \frac{\partial \varphi}{\partial n} \right) \tag{2.23}$$

and

$$-\mathbf{n} \times \nabla \psi = \mathbf{n} \times (\mathbf{H}_s - \nabla \varphi) \tag{2.24}$$

where $\mathbf{n}$ is a unit normal vector to the interface Γ_{Fe} directed outside the ferromagnetic region.

The condition (2.23) can be included in the weak formulation of (2.22) using the Galerkin's method for both regions Ω_{air} and Ω_{Fe} together:

$$\begin{aligned} &\int_{\Omega_{Fe}} \mu_{Fe} \nabla w_i \nabla \psi d\Omega - \int_{\Gamma_{Fe}} \mu_{Fe} w_i \frac{\partial \psi}{\partial n} d\Gamma + \\ &+ \int_{\Omega_{air}} \mu_0 \nabla w_i \nabla \varphi d\Omega + \int_{\Gamma_{Fe}} \mu_0 w_i \frac{\partial \varphi}{\partial n} d\Gamma = 0, \qquad \forall w_i \end{aligned} \tag{2.25}$$

where w_i denotes a scalar test function. The change of the leading sign of the second boundary integral results from the direction of the unit vector $\mathbf{n}$ directed into the air region. After substitution of (2.23) into (2.25), it takes the form:

$$\int_{\Omega_{air}} \mu_0 \nabla w_i \nabla \varphi d\Omega + \int_{\Omega_{Fe}} \mu_{Fe} \nabla w_i \nabla \psi d\Omega = -\mu_0 \int_{\Gamma_{Fe}} H_{sn} w_i d\Gamma \tag{2.26}$$

To include this approach in the finite element procedure the following vector has to be calculated for every boundary element Γ^e_{Fe} located on interface Γ_{Fe}:

$$\{B\}^e = -\mu_0 \int_{\Gamma^e_{Fe}} H_{sn} [\mathbb{N}] d\Gamma \tag{2.27}$$

where $[\mathbb{N}]$ is a matrix of finite element node shape functions. Vector $\{\mathbb{B}\}^e$ has to be added to the right side of the global system of algebraic equations (load vector) resulting from the finite element method.

The boundary condition (2.24) can be integrated along any curve C lying on the interface Γ_{Fe} and connecting the analyzed point $\mathbf{P}_i$ with the selected point $\mathbf{P}_0$ for which $\varphi(\mathbf{P}_0) = \psi(\mathbf{P}_0)$ is assumed:

$$\psi(\mathbf{P}_i) = \varphi(\mathbf{P}_i) - \int_{C(\mathbf{P}_i,\mathbf{P}_0)} \mathbf{H}_s d\mathbf{l} \tag{2.28}$$

The equation (2.28) indicates that the nodes lying on the Γ_{Fe} interface should be assigned to two different potential values differing by the following constant:

$$\varphi_0 = \int_{C(\mathbf{P}_i,\mathbf{P}_0)} \mathbf{H}_s d\mathbf{l} \tag{2.29}$$

In the finite element method, in order to ensure the uniqueness of the potential description it is assumed that the nodes on the boundary Γ_{Fe} are assigned to the potential φ. Fulfillment of the condition (2.28) is ensured by a suitable correction of the global load vector, i.e., by adding the following vector:

$$\{\mathbb{F}_c\}^e = [\mathbb{S}_R]\{\varphi_0\}^e \tag{2.30}$$

where $\{\mathbb{F}_c\}^e$ is the vector calculated for elements belonging to Ω_{Fe}, and touching the interface Γ_{Fe}, $[\mathbb{S}_R]$ is a reduced boundary stiffness matrix, and $\{\varphi_0\}^e$ is the vector of potential differences on Γ_{Fe} (2.29).

In the presented method, the information about the external magnetic field is moved from the external boundary Γ to the interface Γ_{Fe} between air and the ferromagnetic region. The conditions (2.3) and (2.4) on boundary Γ result from the symmetry or/and from the cuts of the region Ω.

As an example, the problem shown in Fig. 2.4 is analyzed. The ferromagnetic block $2a \times 2b \times 2c$ is placed in a uniform magnetic field $\mathbf{H}_s = H_0\mathbf{1}_y$. It is assumed that the magnetic permeability of the block is constant and equal to μ_{Fe}. Due to symmetry

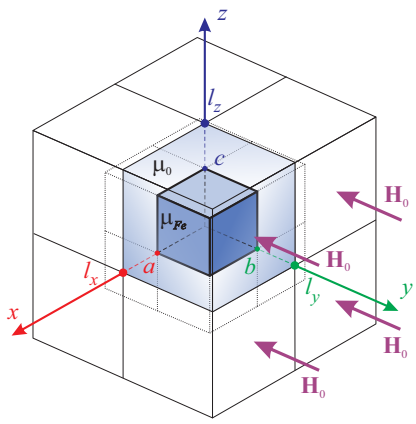

Fig. 2.4: Ferromagnetic block in external uniform magnetic field

of the problem, the analysis is sufficient to perform only for $1/8^{th}$ part of the whole region. The appropriate boundary and continuity conditions have the following form:

$\varphi = \psi = 0$	for $y = 0$ (symmetry)
$\frac{\partial \varphi}{\partial n} = \frac{\partial \psi}{\partial n} = 0$	for $x = 0$ and $z = 0$ (symmetry)
$H_{sn} = H_0$	in equation (2.26) for $y = b$
$\varphi_0 = H_0 y$	in equation (2.30) for $x = a$ and $z = c$
infinite elements [53]	for $x = l_x$, $y = l_y$, and $z = l_z$.

Calculations have been performed using the finite element mesh consisting of $20 \times 20 \times 20$ 8-node linear brick elements. Results for two different values of magnetic permeability μ_{Fe} are shown in Fig. 2.5 in a form of arrows representing magnetic flux density distribution in the analyzed region.

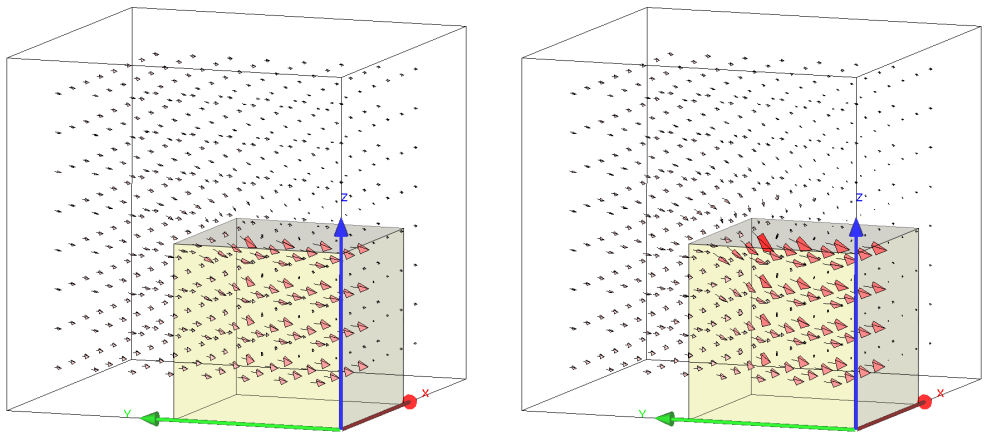

(a) $\mu_{Fe} = 10\mu_0$ (b) $\mu_{Fe} = 1000\mu_0$

Fig. 2.5: Ferromagnetic block in a uniform magnetic field - distribution of magnetic flux density **B** for different values of μ_{Fe}

2.3.2. MODELING OF 3D AIR COILS

In most systems of practical application, the magnetic field should be analyzed not only in the non-conductive regions, but also in regions (coils) in which the predetermined current flows. If the coils can not be removed outside the region analyzed, the methods described in Sections 2.3. and 2.3.1. can not be used.

Subregion in which electric current flows can always be separated by wrapping it in a smooth surface. However, in this case, the analyzed domain starts to be multi-connected, and to ensure the uniqueness of the scalar potential, suitable cuts of the region have to be performed. This approach has been described in many publications,

e.g. [22, 57, 71, 72]. These works, however, are purely theoretical and the proposed algorithms are difficult to implement in the general case.

This section presents the analysis limited to the coil windings lying on mutually parallel planes. This assumption enables the use of only one component of the electric vector potential $\mathbf{T}$ ($\mathbf{J} = \nabla \times \mathbf{T}$) to the description of the source currents flowing in the coil [98]. The application of the potential $\mathbf{T}$ to describe more complex coil systems, for example the end zone windings of electrical machines, it is also possible, but requires the use of at least two components of the potential $\mathbf{T}$ [120]. In such cases, ensuring the continuity of the magnetic field on the borders between different region (conductive, non-conductive) is an important point that should be carefully analyzed.

Taking into account the previous comments, the magnetic field of the coil of finite dimensions is calculated as follows. The density of the electric source current $\mathbf{J}_s$ flowing through the coil is described by the electric vector potential $\mathbf{T}$ as:

$$\mathbf{J}_s = \nabla \times \mathbf{T} \tag{2.31}$$

For example, the distribution of the electric vector potential $\mathbf{T} = T_z(x, y)\mathbf{1}_z$ for the

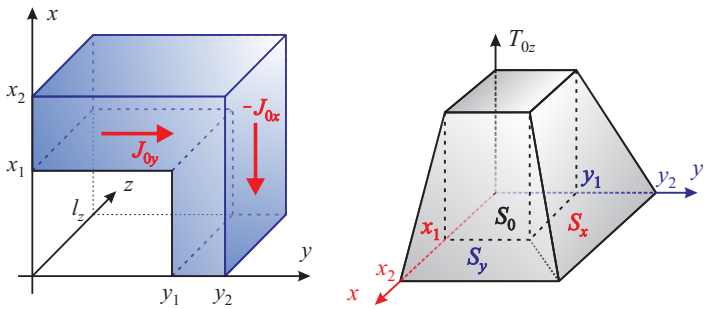

(a) Rectangular coil (b) Electric vector potential $\mathbf{T}$

Fig. 2.6: Model of a rectangular coil with current and distribution of electric vector potential (one eighth part)

coil with electric current density $\mathbf{J}_0$ shown in Fig. 2.6a takes the form:

$$T_z = \begin{cases} T_{0z}\dfrac{y_2 - y}{y_2 - y_1} & \text{in } S_x \times [0, l_z] \\ T_{0z}\dfrac{x_2 - x}{x_2 - x_1} & \text{in } S_y \times [0, l_z] \\ T_{0z} & \text{in } S_0 \times [0, l_z] \\ 0 & \text{outside} \end{cases}$$

where $T_{0z} = J_{0x}(y_2 - y_1) - J_{0y}(x_2 - x_1)$, l_z is half the height of the coil, and the condition $J_{0x}(y_2 - y_1) = J_{0y}(x_2 - x_1)$ must be satisfied because of the continuity of the electric current in the coil. Due to the symmetry of the coil, only one eighth of the entire system is shown.

Determination of potential $\mathbf{T}$ distribution is a task which has to be solved in the definition of the problem. For typical coil systems, it is usually a relatively easy task. It is interesting to focus attention on the continuity of the electric vector potential $\mathbf{T}$. It is appropriate to ensure the continuity of the potential $\mathbf{T}$ on the side walls of the coil. This leads to the assumption of non-zero constant potential inside the coil (see, for example $S_0 \times [0, l_z]$ region in Fig. 2.6b). Discontinuity of the potential $\mathbf{T}$ occurs only at the end walls of the coil (plane $z = l_z$ in Fig. 2.6a), but this kind of discontinuity can be easily included in the weak integral formulation.

Using the Ampére law:

$$\nabla \times \mathbf{H}_t = \mathbf{J}_s \tag{2.32}$$

the total magnetic field $\mathbf{H}_t$ in the coil region can be described by the electric vector potential $\mathbf{T}$ and the scalar potential φ as

$$\mathbf{H}_t = \mathbf{T} - \nabla\varphi, \quad \text{in } \Omega_c \tag{2.33}$$

where Ω_c denotes the coil region itself together with the interior air area inside the coil. The magnetic field $\mathbf{H}_t$ in the air region Ω_e outside Ω_c can be described by the scalar potential ψ

$$\mathbf{H}_t = -\nabla\psi, \quad \text{in } \Omega_e \tag{2.34}$$

The assumptions about the continuity of the electric vector potential $\mathbf{T}$ also ensure the continuity of scalar potentials at the boundary of Ω_c

$$\varphi(\mathbf{P}) = \psi(\mathbf{P}), \quad \text{for } \mathbf{P} \in \Gamma_c \tag{2.35}$$

where Γ_c denotes the boundary of Ω_c.

Only at the end walls of the coil (part of the boundary Γ_c for $z = l_z$, Fig. 2.6) must be satisfied in addition the following condition resulting from the continuity of the normal component of the magnetic flux density:

$$\mu_c \left(T_n - \frac{\partial\varphi}{\partial n} \right) = -\mu_e \frac{\partial\psi}{\partial n} \tag{2.36}$$

where μ_c and μ_e are magnetic permeabilities in Ω_c and Ω_e, respectively.

The equations describing the magnetic field by means of potentials $\mathbf{T}$, φ, and ψ take the form:

$$\nabla \cdot (\mu_c \nabla\varphi) = \nabla \cdot (\mu_c \mathbf{T}), \quad \text{in } \Omega_c \tag{2.37}$$

$$\nabla \cdot (\mu_e \nabla\psi) = 0, \quad \text{in } \Omega_e \tag{2.38}$$

Using Galerkin's method, equations (2.37) and (2.38) can be transformed to the equivalent integral weak form as

$$\int_{\Omega_c} w_i \left[\nabla \cdot (\mu_c \nabla\varphi) - \nabla \cdot (\mu_c \mathbf{T}) \right] d\Omega + \int_{\Omega_e} w_i \nabla \cdot (\mu_e \nabla\psi) d\Omega = 0, \quad \forall w_i \tag{2.39}$$

After applying the vector identity $\nabla \cdot (w\mathbf{v}) = w\nabla \cdot \mathbf{v} - \mathbf{v} \cdot \nabla w$ and the *Gauss'* theorem yields the equation

$$\int_{\Omega_c} \mu_c \nabla w_i \nabla \varphi d\Omega - \int_{\Gamma_c} \mu_c w_i \frac{\partial \varphi}{\partial n} d\Gamma - \int_{\Omega_c} \mu_c \mathbf{T} \cdot \nabla w_i d\Omega + \\ + \int_{\Gamma_c} \mu_c w_i T_n d\Gamma + \int_{\Omega_e} \mu_e \nabla w_i \nabla \psi d\Omega + \int_{\Gamma_c} \mu_e w_i \frac{\partial \psi}{\partial n} d\Gamma = 0 \tag{2.40}$$

where $\mathbf{n}$ is the normal unit vector directed outside region Ω_c (notice the leading sign changing in the last boundary integral).

Under the condition (2.36), it can be shown that the sum of boundary integrals in (2.40) equals zero. Thus, the condition (2.36) is automatically satisfied and (2.40) obtains the form:

$$\int_{\Omega_c} \mu_c \nabla w_i \nabla \varphi d\Omega + \int_{\Omega_e} \mu_e \nabla w_i \nabla \psi d\Omega = \int_{\Omega_c} \mu_c \mathbf{T} \cdot \nabla w_i d\Omega \tag{2.41}$$

Application of the finite element method to solve the system of equations (2.37) - (2.38) with the continuity conditions (2.35) and (2.36) is reduced, therefore, to the determination of the element stiffness matrix (using the left side of (2.41)) and to calculate the load vector $\{F\}$ for elements of the region Ω_c:

$$\{\mathbb{F}\}^e = \int_{\Omega_c^e} \mu_c \mathbf{T} \cdot \nabla[\mathbb{N}] d\Omega \tag{2.42}$$

The process of creating the global matrices and taking into account the boundary conditions at the outer boundary of the region Ω_e is similar to that described in the previous sections.

Modeling coils whose dimensions are small compared to other dimensions of the analyzed system forces using a large density of the finite element mesh surrounding the coil and the coil itself. In such cases, replacement of the coil by 3D current wraps or a single turn with current is often better solution.

Figure 2.7 shows one eighth of an infinitely thin solenoid with rectangular cross-section. As in the case of thick solenoids, analyzed region is divided into subregion Ω_c lying inside the coil and an external air subregion Ω_e. In the region Ω_c, the magnetic field is described by the scalar potential φ and constant magnetic intensity $\mathbf{H}_0 = H_0 \mathbf{1}_z$:

$$\mathbf{H}_c = \mathbf{H}_0 - \nabla \varphi \tag{2.43}$$

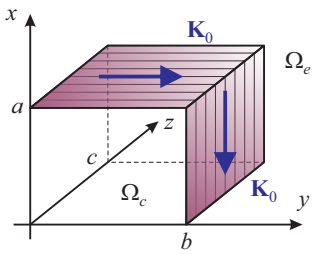

Fig. 2.7: Infinitely thin rectangular solenoid (one eighth part)

In the external air region Ω_e, the magnetic field is depicted by $\mathbf{H} = -\nabla\psi$. The following continuity conditions have to be satisfied at the side faces of the solenoid:

$$\mathbf{n} \times (-\nabla\psi - \mathbf{H}_0 + \nabla\varphi) = \mathbf{K}_0 \tag{2.44}$$

where $\mathbf{n}$ is the normal unit vector directed outside the region Ω_c and $\mathbf{K}_0$ denotes the surface current density vector. If one assumes $\mathbf{n} \times \mathbf{H}_0 = -\mathbf{K}_0$ then the condition (2.44) is satisfied when the scalar potentials are continuous at the boundary Γ_c, i.e., $\varphi(\mathbf{P}) = \psi(\mathbf{P}),\ \mathbf{P} \in \Gamma_c$. It is therefore enough to assume

$$H_0 = K_0 = \frac{NI}{2c}$$

where N is the number of solenoid turns, I is the current in the coil, and $2c$ is the length of the solenoid. Then the vector $\mathbf{H}_0$ performs the same function as the electric vector potential $\mathbf{T}$ for thick coils. For elements in Ω_c, the load vector $\{F\}^e$ is calculated according (2.42) where instead of the electric vector potential $\mathbf{T}$ the vector $\mathbf{H}_0$ is used.

In the case of an infinitely thin current loop located on a plane parallel to the $X0Y$ plane, the region Ω_c is reduced to the surface S_c (Fig. 2.8). The Ampére law indicates

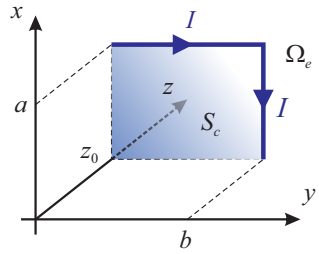

Fig. 2.8: Infinitely thin rectangular current loop (one fourth part)

that the potential ψ is discontinuous on the surface S_c and fulfills the following condition:

$$\psi^+(\mathbf{P}) - \psi^-(\mathbf{P}) = I, \quad \mathbf{P} \in S_c \tag{2.45}$$

In order to distinguish the potentials ψ^+ and ψ^-, the orientation of the surface S_c must be defined. It is assumed that the direction of the normal unit vector of the surface S_c is determined using a right-handed screw rule in relation to the direction of current I. To satisfy the condition (2.45) in the finite element method, two elements (one on the negative side, and one on the positive side of surface S_c) with a common face belonging to the surface S_c are considered. Ascribing the potential ψ_i^+ to the nodes on the surface S_c, the potential ψ_i^- can be eliminated in the following way

$$[\mathbb{S}]^-\{\psi^-\}^e = [\mathbb{S}]^-\{\psi^+\}^e - [\mathbb{S}]^-\{\mathbb{I}\}^e \tag{2.46}$$

where $[\mathbb{S}]^-$ is the stiffness matrix of the element located on the negative side of surface S_c and $\{\mathbb{I}\}^e$ is the vector which is equal to I in positions corresponding to the nodes

located on the surface S_c and zero elsewhere. In fact, this procedure is analogous to the procedure taking into account the Dirichlet boundary conditions in the FEM. It is obvious that the calculation of the magnetic field in the finite element lying on the negative side of the surface S_c must take into account the actual value of the potential ψ^- equal to $\psi^+ - I$. In the particular case where the infinitely thin current loop is located in the symmetry plane $z = 0$ where $\mathbf{n} \times \mathbf{H} = 0$ the potential ψ^- is equal to potential ψ^+ and $\psi^+ = I/2$. This case can be treated as classical Dirichlet problem for the Laplace equation.

In order to illustrate the method, sample results of calculations of the magnetic field produced by the infinitely thin rectangular current loop and the thick rectangular air coil are shown in Fig. 2.9a and Fig. 2.9b, respectively.

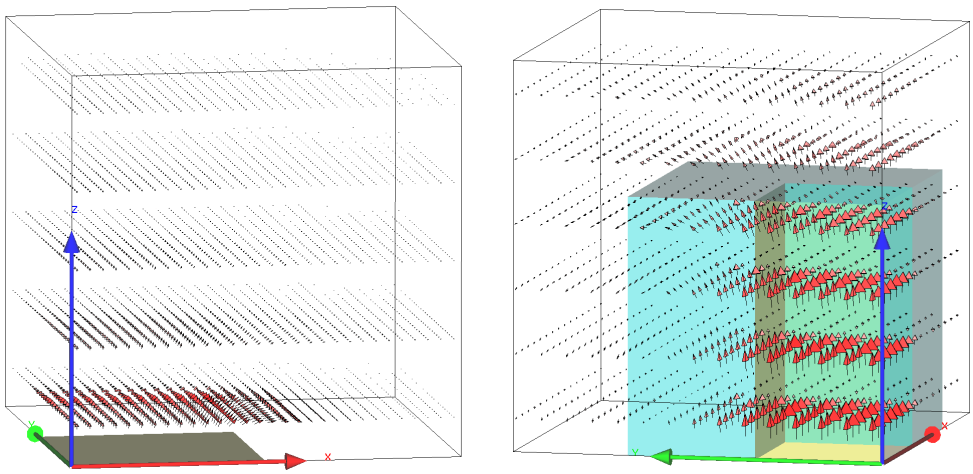

(a) Infinitely thin rectangular current loop

(b) Thick air coil

Fig. 2.9: Magnetic flux density produced by rectangular air coils calculated using scalar potentials (one eighth view)

2.3.3. MODELING OF 3D COILS WITH IRON-CORES

Determination of the magnetic field using an electric vector potential $\mathbf{T}$ to describe the iron-core coil, whose shape satisfies the conditions set out in the previous section is also possible. This requires the use of an appropriate assembly of the magnetic field descriptions in the analyzed regions. As a basic rule should be assumed that the description associated with the coil region Ω_c is dominant. Due to the fact that the region Ω_c includes also the interior of the winding it usually contains a part of the iron-core. In other words, the iron-core is divided by the surface Γ_c in a subregion where the magnetic field is described by the electric vector potential $\mathbf{T}$ and scalar potential φ, and the subregion where the scalar potential ψ is sufficient to use. The consequence of this

approach is the need to define different material codes for the same iron-core (Fig. 2.10). An alternative approach, based on the assumption of dominance of the magnetic field description applicable to the iron-core, makes it necessary to take into account the condition (2.28) on the surface of the core contained in Ω_c. However, this method of analysis of the magnetic field is much more complicated in terms of organization of data input and calculations.

Figure 2.10 shows the magnetic flux density distribution in the iron-core of a sample rectangular coil calculated using the dominance of the description of the magnetic field in the region Ω_c.

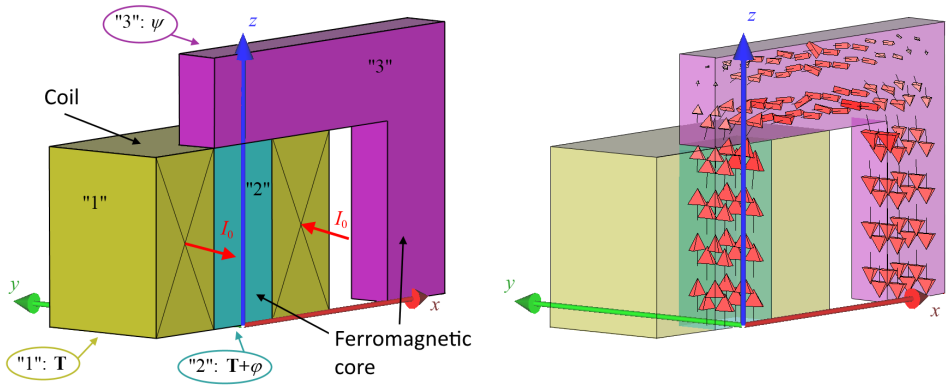

(a) Calculation setup

(b) Magnetic flux density

Fig. 2.10: Magnetic flux density in the iron-core of the rectangular coil (one fourth view)

2.4. 3D MAGNETOSTATIC ANALYSIS USING MAGNETIC VECTOR POTENTIAL

The introduction of magnetic vector potential $\mathbf{A}$ defined as $\mathbf{B} = \nabla \times \mathbf{A}$ to the description of the three-dimensional magnetic field creates additional difficulties associated with the uniqueness of this potential [29, 58, 61, 73, 94]. In addition to equation:

$$\nabla \times (\nu \nabla \times \mathbf{A}) = 0, \quad \text{in } \Omega \tag{2.47}$$

resulting from (2.1) and (2.2) ($\nu = 1/\mu$ is the magnetic reluctivity), the potential $\mathbf{A}$ has to satisfy the gauge condition which in magnetostatics is typically the Coulomb condition:

$$\nabla \cdot \mathbf{A} = 0, \quad \text{in } \Omega \tag{2.48}$$

There are several ways to fulfill the condition (2.48) in weak formulations used in the finite element method (see the overview in [61]). In this section, the analysis is focused on the use of edge finite elements and the case in which $\mathbf{A}$ vector components can be separated, i.e., for each of them can be formulated an independent boundary

value problem. It should be noted that the inclusion of the source current directly in the equation (2.47) does not create additional difficulties. Omission of source current arises only from the chosen way of comparing the presented methods.

2.4.1. EDGE ELEMENTS IN A-FORMULATION

The use of edge finite elements to determine the distribution of the magnetic vector potential $\mathbf{A}$ is the most simple and direct way to satisfy the gauge condition (2.48). The properties of edge elements described in Section 1.5. show that the condition $\nabla \cdot \mathbf{A} = 0$ is fulfilled in the whole region Ω including the boundary Γ. The continuity of the normal component of magnetic flux density $\mathbf{B}$ between finite elements is satisfied automatically. The discontinuity of tangential components of $\mathbf{B}$ allows to take into account the heterogeneity of the environment.

The boundary condition (2.3) on Γ_H has the form:

$$(\nu \nabla \times \mathbf{A}) \times \mathbf{n} = \mathbf{K}_0 \tag{2.49}$$

It can be easily included in the weak formulation (1.4) as:

$$\int_\Omega \nu(\nabla \times \mathbf{w}) \cdot (\nabla \times \mathbf{A}) d\Omega = \int_{\Gamma_H} \mathbf{w} \cdot \mathbf{K}_0 d\Gamma \tag{2.50}$$

On the boundary part Γ_B, the essential condition for $\mathbf{A} \times \mathbf{n}$ has to be set. This condition, together with the condition $\nabla \cdot \mathbf{A} = 0$ should be based on (2.4). Unfortunately, it was not possible to find a general algorithm for determining this condition for any function B_{n0}. In the simplest but also the most frequent case when $B_{n0} = 0$ (usually due to the symmetry of the problem) the following setting can be used:

$$\mathbf{A} \times \mathbf{n} = 0, \quad \text{on } \Gamma_B \tag{2.51}$$

In the test problem defined in Section 2.2., (2.49) and (2.51) can be fulfilled without any problems.

Figure 2.11 presents results of magnetic field calculations for the test problem. The comparison with the analytical results (2.10) and as well with the results received by means of the scalar potential φ (Section 2.3.) shows that the errors ϵ_1^i at points lying on the line l_1 are negligible for both formulations (errors are below 0.15%, see also Fig. 2.3). The greatest errors appear for the component H_z on line l_2 $(z/h = 0.7)$ just above the line where the condition (2.3) starts to be discontinuous (max relative error 5%). It should be noted that the values of H_z component calculated using the scalar potential φ are less than the exact values while those obtained from the vector calculation ($\mathbf{A}$ with edge elements) are greater than the exact solution.

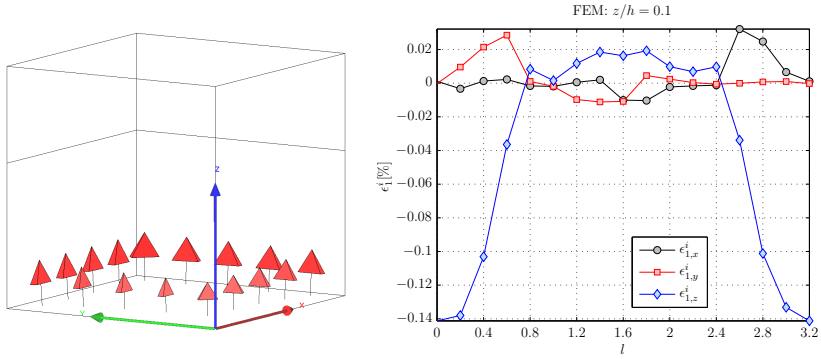

(a) Line l_1: $\delta_1 = 0.26\%$

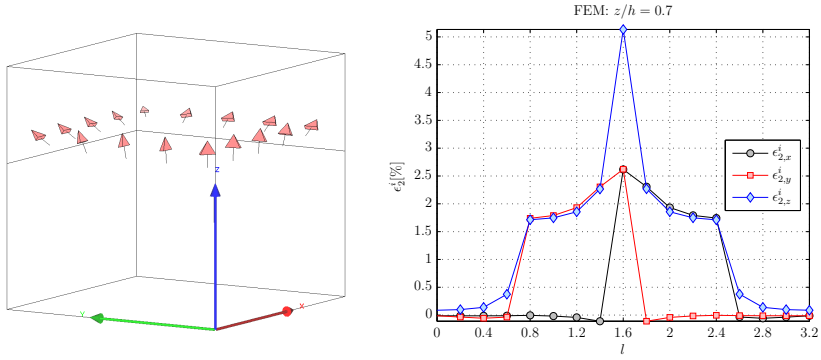

(b) Line l_2: $\delta_2 = 2.54\%$

Fig. 2.11: Test problem - magnetic field **H** and normalized error ϵ_k^i calculated using magnetic vector potential **A** (FEM mesh: $15 \times 15 \times 15$ linear edge brick elements)

2.4.2. MAGNETIC VECTOR POTENTIAL - SEPARATION OF COMPONENTS

If the nodal vector shape functions (Section 1.4.) are applied to calculations of the magnetic field in the finite element method, the gauge condition (2.48) has to be directly inserted into the solved equation. This can be realized by adding to the equation (2.47) the additional term $-\nabla(\nu\nabla \cdot \mathbf{A}) = 0$ as it is shown below

$$\nabla \times (\nu\nabla \times \mathbf{A}) - \nabla(\nu\nabla \cdot \mathbf{A}) = 0 \tag{2.52}$$

Integral, weak form of this equation takes the form:

$$\int_\Omega \nu(\nabla \times \mathbf{w}) \cdot (\nabla \times \mathbf{A}) d\Omega + \int_\Omega \nu(\nabla \cdot \mathbf{w})(\nabla \cdot \mathbf{A}) d\Omega = \int_{\Gamma_H} \mathbf{w} \cdot \mathbf{A} d\Gamma \tag{2.53}$$

In order to obtain a unique solution of (2.52), in addition to the boundary conditions mentioned in the previous section, the following conditions must also be taken into account:

$$\mathbf{n} \cdot \mathbf{A} = 0, \quad \text{on } \Gamma_H \tag{2.54}$$

$$\nabla \cdot \mathbf{A} = 0, \quad \text{on } \Gamma_B \tag{2.55}$$

In general, conditions (2.54) and (2.55) can be non-homogeneous. However, taking this into account in the analyzed problems would be only an unnecessary complication.

Further, a special case of the equation (2.52) with the accompanying boundary conditions is considered. When the magnetic permeability μ is constant throughout the region under consideration, then using the vector identity:

$$\nabla \times (\nabla \times \mathbf{A}) = \nabla(\nabla \cdot \mathbf{A}) - \nabla^2 \mathbf{A}$$

equation (2.52) can be replaced by the following system of scalar partial differential equations:

$$\nabla^2 A_x = 0, \quad \nabla^2 A_y = 0, \quad \nabla^2 A_z = 0 \tag{2.56}$$

Remark: separation of the components of the vector potential $\mathbf{A}$ is also possible in heterogeneous regions, and even for nonlinear problems, as it will be shown in the next section.

In order to complete the formulation of the problem, it is necessary to define the Dirichlet or Neumann boundary conditions for each component of the vector $\mathbf{A}$. This task is relatively simple when considered part of the boundary lies on the plane perpendicular to one of the coordinate axes. For the arbitrary oriented plane the suitable expressions may be found in [66].

As an example, the definition of boundary conditions for the components of potential $\mathbf{A}$ on parts of Γ_H and Γ_B lying on the plane $z = \text{const}$ with $\mathbf{n} = \mathbf{1}_z$ is presented. Boundary conditions on Γ_H have the form:

$$A_z = 0 \qquad \text{from (2.54)} \tag{2.57}$$

$$\frac{\partial A_x}{\partial z} = \mu K_{0x} \quad \text{and} \quad \frac{\partial A_y}{\partial z} = \mu K_{0y} \qquad \text{from (2.49) and (2.54)} \tag{2.58}$$

For the boundary of Γ_B-type, boundary conditions take the form:

$$A_x = 0 \quad \text{and} \quad A_y = 0 \qquad \text{from (2.51)} \tag{2.59}$$

$$\frac{\partial A_z}{\partial z} = 0 \qquad \text{from (2.55) and (2.51)} \tag{2.60}$$

As it can be seen, the partial derivatives in (2.58) and (2.60) correspond to normal derivatives to the respective boundary surfaces. In an analogous way, the boundary conditions on the planes $x = \text{const}$ and $y = \text{const}$ can be defined. Boundary conditions for the test problem are summarized in Table 2.1.

The solution of the test problem using the finite element mesh consisting of $15 \times 15 \times 15$ linear brick elements is presented in Fig. 2.12.

Table 2.1: Boundary conditions for test problem (magnetic vector potential **A**)

	A_x	$\partial A_x/\partial n$	A_y	$\partial A_y/\partial n$	A_z	$\partial A_z/\partial n$
$x = 0$	–	0	0	–	0	–
$x = a,\ z \leqslant c$	0	–	–	$-\mu K_0$	–	0
$x = a,\ z > c$	0	–	–	0	–	0
$y = 0$	0	–	–	0	0	–
$y = b,\ z \leqslant c$	–	$-\mu K_0$	0	–	–	0
$y = b,\ z > c$	–	0	0	–	–	0
$z = 0$	–	0	–	0	0	–
$z = h$	–	0	–	0	0	–

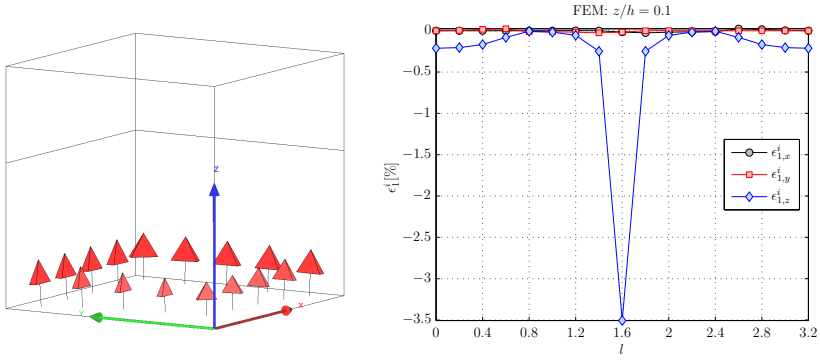

(a) Line l_1: $\delta_1 = 2.94\%$

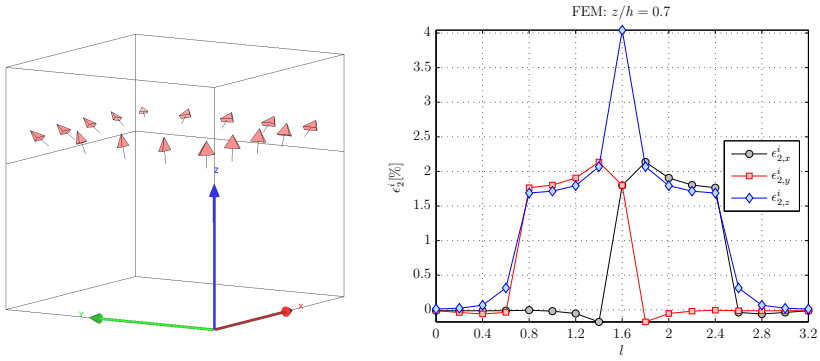

(b) Line l_2: $\delta_2 = 2.36\%$

Fig. 2.12: Test problem - magnetic intensity **H** and normalized error ϵ_k^i calculated using potential **A** with separated components (FEM mesh: $15 \times 15 \times 15$ linear brick elements)

The greatest normalized local errors ϵ_k^i are observed for the component H_z near the corner $x = a$, $y = b$, regardless of the position of the line l_k. Increasing the density of the finite element mesh reduces the local error (although not as significant as for

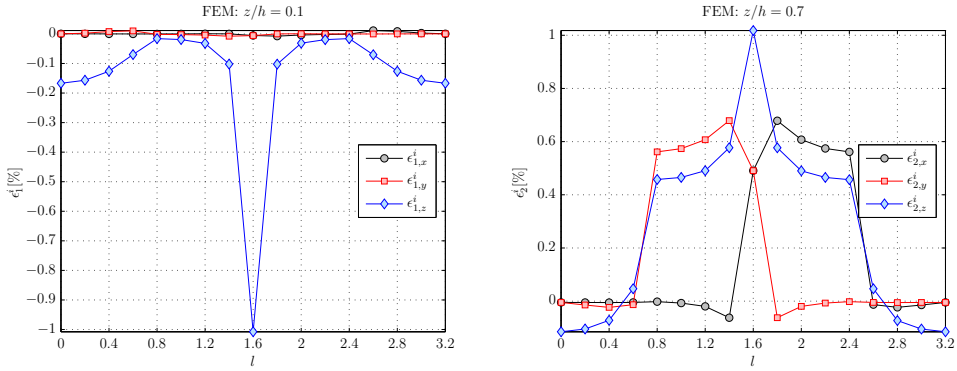

(a) Line l_1: $\delta_1 = 0.87\%$ (b) Line l_2: $\delta_2 = 0.69\%$

Fig. 2.13: Test problem - potential **A** with separated components - normalized error ϵ_k^i for FEM mesh consisting of $25 \times 25 \times 25$ linear brick elements

the previous formulations) but the location of its maximum near the corner remains unchanged (Fig. 2.13).

2.4.3. FORMULATION A-M FOR NONLINEAR MAGNETOSTATIC PROBLEMS

In the previous sections the analysis was limited to linear problems. In this section, the three-dimensional nonlinear magnetostatics problems are considered. The idea of applying in the finite element method the formulation of the field equations using the magnetic vector potential **A** and the magnetization vector **M** is presented. Similarly to the previous section, the components of the magnetic vector potential are analyzed separately, which significantly reduces the requirements on the size of computer's memory. In [66], the authors have proposed the formulation **A-M** for linear problems. The idea presented below is therefore a generalization of work [66].

The magnetic state of the environment may be characterized by three vectors: **B** (magnetic flux density), **H** (magnetic intensity) and **M** (magnetization density), connected with each other by the following relation:

$$\mathbf{H} = \frac{\mathbf{B}}{\mu_0} - \mathbf{M} \tag{2.61}$$

where μ_0 is the magnetic permeability of free space. It is enough to use any pair of the above three vectors for a unique description of the magnetic environment state at any point of the magnetic field generated by source currents or residual polarization of the environment. Applying the magnetic vector potential **A** and having (2.61), the first Maxwell equation takes the following form:

$$\nabla \times (\frac{1}{\mu_0} \nabla \times \mathbf{A} - \mathbf{M}) = \mathbf{J} \tag{2.62}$$

which after applying the Coulomb gauge can be split into three equations corresponding to three components of the magnetic vector potential:

$$\frac{1}{\mu_0}\left(\frac{\partial^2 A_x}{\partial x^2}+\frac{\partial^2 A_x}{\partial y^2}+\frac{\partial^2 A_x}{\partial z^2}\right)+\left(\frac{\partial M_z}{\partial y}-\frac{\partial M_y}{\partial z}\right)+J_x=0 \tag{2.63}$$

$$\frac{1}{\mu_0}\left(\frac{\partial^2 A_y}{\partial x^2}+\frac{\partial^2 A_y}{\partial y^2}+\frac{\partial^2 A_y}{\partial z^2}\right)+\left(\frac{\partial M_x}{\partial z}-\frac{\partial M_z}{\partial x}\right)+J_y=0 \tag{2.64}$$

$$\frac{1}{\mu_0}\left(\frac{\partial^2 A_z}{\partial x^2}+\frac{\partial^2 A_z}{\partial y^2}+\frac{\partial^2 A_z}{\partial z^2}\right)+\left(\frac{\partial M_y}{\partial x}-\frac{\partial M_x}{\partial y}\right)+J_z=0 \tag{2.65}$$

The following set of conditions results from the continuity of the magnetic field and the gauge (2.48) on the interface Γ_i between regions of different magnetic properties (indicated by indices I and II):

$\Gamma_i:\quad x=\text{const},\ \mathbf{n}=\mathbf{1}_x$

$$\begin{cases} A_x^I=A_x^{II},\ A_y^I=A_y^{II},\ A_z^I=A_z^{II} \\ \dfrac{\partial A_x^I}{\partial x}=\dfrac{\partial A_x^{II}}{\partial x} \\ \dfrac{1}{\mu_0}\dfrac{\partial A_y^I}{\partial x}-M_z^I=\dfrac{1}{\mu_0}\dfrac{\partial A_y^{II}}{\partial x}-M_z^{II} \\ \dfrac{1}{\mu_0}\dfrac{\partial A_z^I}{\partial x}+M_y^I=\dfrac{1}{\mu_0}\dfrac{\partial A_z^{II}}{\partial x}+M_y^{II} \end{cases} \tag{2.66}$$

$\Gamma_i:\quad y=\text{const},\ \mathbf{n}=\mathbf{1}_y$

$$\begin{cases} A_x^I=A_x^{II},\ A_y^I=A_y^{II},\ A_z^I=A_z^{II} \\ \dfrac{1}{\mu_0}\dfrac{\partial A_x^I}{\partial y}+M_z^I=\dfrac{1}{\mu_0}\dfrac{\partial A_x^{II}}{\partial y}+M_z^{II} \\ \dfrac{\partial A_y^I}{\partial y}=\dfrac{\partial A_y^{II}}{\partial y} \\ \dfrac{1}{\mu_0}\dfrac{\partial A_z^I}{\partial y}-M_x^I=\dfrac{1}{\mu_0}\dfrac{\partial A_z^{II}}{\partial y}-M_x^{II} \end{cases} \tag{2.67}$$

$\Gamma_i:\quad z=\text{const},\ \mathbf{n}=\mathbf{1}_z$

$$\begin{cases} A_x^I=A_x^{II},\ A_y^I=A_y^{II},\ A_z^I=A_z^{II} \\ \dfrac{1}{\mu_0}\dfrac{\partial A_x^I}{\partial z}-M_y^I=\dfrac{1}{\mu_0}\dfrac{\partial A_x^{II}}{\partial z}-M_y^{II} \\ \dfrac{1}{\mu_0}\dfrac{\partial A_y^I}{\partial z}+M_x^I=\dfrac{1}{\mu_0}\dfrac{\partial A_y^{II}}{\partial z}+M_x^{II} \\ \dfrac{\partial A_z^I}{\partial z}=\dfrac{\partial A_z^{II}}{\partial z} \end{cases} \tag{2.68}$$

Applying Galerkin's method to equation (2.63) yields:

$$-\frac{1}{\mu_0}\int_\Omega \nabla w_i \nabla A_x d\Omega + \oint_{\Gamma_i} w_i \left[\frac{1}{\mu_0}\frac{\partial A_x}{\partial n} + (M_z \mathbf{1}_y - M_y \mathbf{1}_z)\cdot \mathbf{n}\right] d\Gamma = \\ = \int_\Omega \left(\frac{\partial w_i}{\partial y} M_z - \frac{\partial w_i}{\partial z} M_y\right) d\Omega - \int_\Omega w_i J_x d\Omega \tag{2.69}$$

The surface integral in (2.69) can be written for any finite element as:

$$\oint_{\Gamma_i^e} w_i \left[\frac{1}{\mu_0}\frac{\partial A_x}{\partial n} + (M_z \mathbf{1}_y - M_y \mathbf{1}_z)\cdot \mathbf{n}\right] d\Gamma = \\ = \sum_{p=1}^{N_f} \int_{\Gamma_{i,p}^e} w_i \left[\frac{1}{\mu_0}\frac{\partial A_x}{\partial n_p} + (M_z \mathbf{1}_y - M_y \mathbf{1}_z)\cdot \mathbf{n}_p\right] d\Gamma \tag{2.70}$$

where N_f is the number of element faces . Integrands in expression (2.70) for the respective unit vectors have the form:

$$w_i \left[\frac{1}{\mu_0}\frac{\partial A_x}{\partial n_p} + (M_z \mathbf{1}_y - M_y \mathbf{1}_z)\cdot \mathbf{n}_p\right] = \begin{cases} w_i \dfrac{1}{\mu_0}\dfrac{\partial A_x}{\partial x}, & \mathbf{n}_p = \mathbf{1}_x \\ w_i \left(\dfrac{1}{\mu_0}\dfrac{\partial A_x}{\partial y} + M_z\right), & \mathbf{n}_p = \mathbf{1}_y \\ w_i \left(\dfrac{1}{\mu_0}\dfrac{\partial A_x}{\partial z} - M_y\right), & \mathbf{n}_p = \mathbf{1}_z \end{cases} \tag{2.71}$$

It should be noted the similarity of the above formulas to the conditions of continuity of the component A_x (second equations in (2.66), (2.66), and (2.68)). If the face $\Gamma_{i,p}^e$ is in the area under consideration, the omission of the surface integral in a summation process automatically ensures fulfillment of the continuity conditions of the field component. This is due to the fact that the surface integrals of the elements adjacent to the face $\Gamma_{i,p}^e$ are identical but have opposite signs thereby deleting each other. If $\Gamma_{i,p}^e$ is a part of the exterior surface, the omission of the surface integral leads to the homogeneous Neumann condition on this surface (assuming that the external region is free air space). Analogous equations can be obtained for components A_y and A_z.

Since the components of the magnetization $\mathbf{M}$ only appear in the element load vector, this method is particularly well suited to the analysis of nonlinear systems. The global stiffness matrix has to be calculated only once at the beginning of the calculation process. In addition, the stiffness matrix is the same for all components of the magnetic vector potential $\mathbf{A}$ which significantly speeds up the calculation. Although the correction of magnetization vector in a nonlinear iterative process requires at the same time all three components of the magnetic vector potential, the increase of computational complexity is associated only with the presence of various load vectors for each component. The iterative calculation algorithm is shown in Fig. 2.14.

It is necessary to explain in more details how to correct the magnetization vector $\mathbf{M}$ in the successive steps of an iterative process. After determination of the components

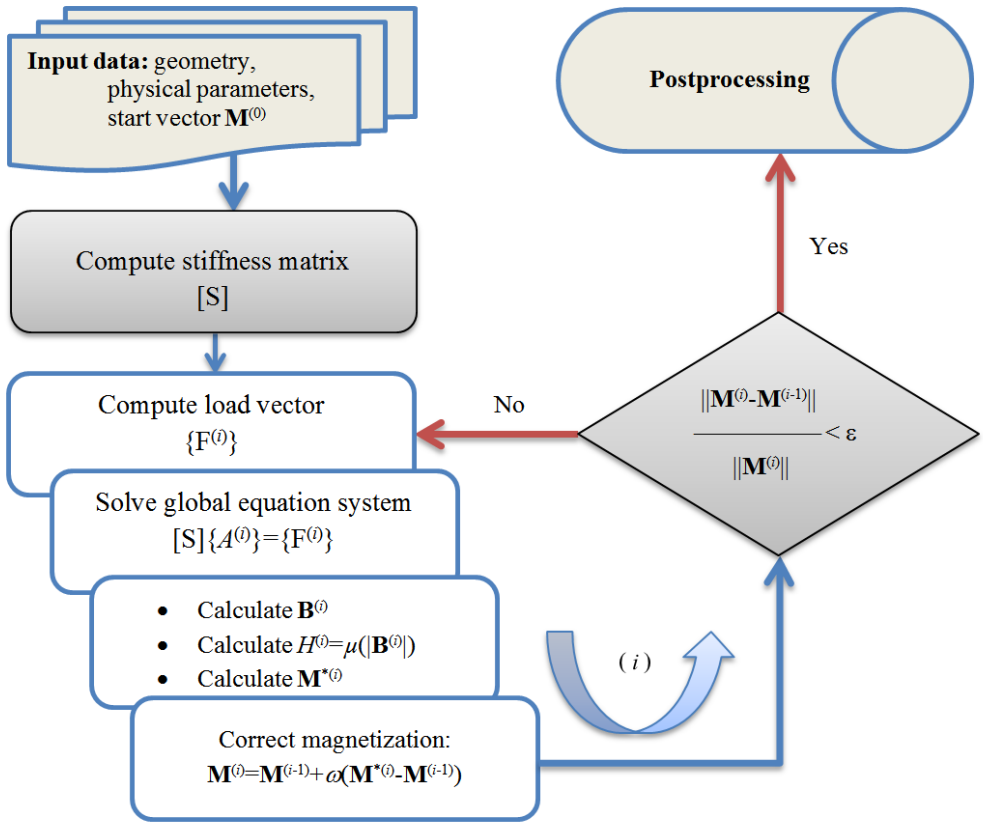

Fig. 2.14: Flowchart of solving nonlinear problems with **A**-**M** formulation

of the magnetic flux density $\mathbf{B} = \nabla \times \mathbf{A}$ inside finite elements, the components of the magnetic intensity vector (H_x, H_y, H_z) have to be found using the magnetization BH-curve $\mu(|\mathbf{B}|)$. The new values of the magnetization vector $\mathbf{M}^*$ are calculated as:

$$M_x^* = \frac{1}{\mu_0} B_x - H_x, \quad M_y^* = \frac{1}{\mu_0} B_y - H_y, \quad M_z^* = \frac{1}{\mu_0} B_z - H_z \tag{2.72}$$

In order to accelerate the convergence of an iterative process, the magnetization vector $\mathbf{M}$ in the subsequent iterative steps is modified according to the following formula:

$$\mathbf{M}^{(i)} = \mathbf{M}^{(i-1)} + \omega(\mathbf{M}^{*(i)} - \mathbf{M}^{(i-1)}) \tag{2.73}$$

where ω is a relaxation factor chosen on the basis of numerical experiment, e.g. $\omega = 0.5$.

2.5. 3D MAGNETOSTATIC ANALYSIS - DIRECT H FORMULATION

Direct application of the magnetic intensity $\mathbf{H}$ in calculations of the magnetic field in the finite element method is subject to significant restrictions. The main limitation is the inability to take into account the heterogeneity of the environment in such a simple way as in the case of scalar or vector potential formulations. The second limitation is the difficulty in including regions with source currents. However, the proposed method may be useful in certain special cases, for example, in the analysis of some Lorentz force eddy current testing systems (Section 4.4.).

The analysis presented in this section assumes homogeneity of the magnetic environment. Under this assumption, (2.2) can be replaced by the equation:

$$\nabla \cdot \mathbf{H} = 0 \tag{2.74}$$

Using parameter λ and the following equation

$$\nabla \times \nabla \times \mathbf{H} - \lambda \nabla(\nabla \cdot \mathbf{H}) = 0 \tag{2.75}$$

two formulations of the boundary value problem can be introduced, namely: (1) $\mathbf{H}$ with separated components for $\lambda = 1$, and (2) $\mathbf{H}$ approximated by the edge finite elements with the condition (2.74) for $\lambda = 0$.

2.5.1. DIRECT H-FORMULATION WITH SEPARATED COMPONENTS

Similarly to the magnetic vector potential $\mathbf{A}$ formulation, equation (2.75) ($\lambda = 1$) may be replaced by three scalar Laplace equations associated with the corresponding component of magnetic intensity $\mathbf{H}$. Boundary conditions on Γ_H-type boundary lying in the plane $z = \text{const}$ with $\mathbf{n} = \mathbf{1}_z$ have the form:

$$H_x = -K_{0y} \quad \text{and} \quad H_y = K_{0x} \qquad \text{from (2.3)} \tag{2.76}$$

$$\frac{\partial H_z}{\partial z} = -\frac{\partial K_{0x}}{\partial x} + \frac{\partial K_{0y}}{\partial y} \qquad \text{from (2.74) and (2.3).} \tag{2.77}$$

Boundary conditions on Γ_B-type boundary take the form:

$$H_z = \frac{1}{\mu} B_{z0} \qquad \text{from (2.4)} \tag{2.78}$$

$$\frac{\partial H_y}{\partial z} = \frac{1}{\mu}\frac{\partial B_{z0}}{\partial y} \quad \text{and} \quad \frac{\partial H_x}{\partial z} = \frac{1}{\mu}\frac{\partial B_{z0}}{\partial x} \qquad \text{from (2.1) and (2.4)} \tag{2.79}$$

It should be noted that the determination of the conditions (2.76) - (2.79) is relatively simple, in contrast to the potential formulations (scalar or vector, see previous sections) which may be important when the functions $\mathbf{K}_0$ and B_{n0} are functions of complex shapes. All boundary conditions for the test problem (Section 2.2.) are presented in Table 2.2.

Integration of the Dirac function over the element edge located on the boundary surface produces an additional term. The term is equal to half the length of the element

Table 2.2: Boundary conditions for test problem (direct **H** formulation)

	H_x	$\partial H_x/\partial n$	H_y	$\partial H_y/\partial n$	H_z	$\partial H_z/\partial n$
$x = 0$	0	–	–	0	–	0
$x = a,\ z \leqslant c$	–	$K_0\delta(c)$	0	–	K_0	–
$x = a,\ z > c$	–	0	0	–	0	–
$y = 0$	–	0	0	–	–	0
$y = b,\ z \leqslant c$	0	–	–	$K_0\delta(c)$	K_0	–
$y = b,\ z > c$	0	–	–	0	0	–
$z = 0$	0	–	0	–	–	0
$z = h$	0	–	0	–	–	0

$\delta(c)$ is the Dirac function for $z = c$

edge lying on the segment $z = c$, $x = a$, $y \in (0, b)$ or $z = c$, $y = b$, $x \in (0, a)$ multiplied by K_0. This term should be added to the right side vector of the global finite element algebraic equations system in positions corresponding to the nodes of the edge element. Results of calculations for the FEM mesh consisting of $15 \times 15 \times 15$ linear brick finite elements based on the direct **H** formulation are shown in Fig. 2.15. The components H_x and H_y are calculated with a high accuracy while for the component H_z errors are much greater (e.g. $\epsilon^i_{2,z} = -18.6\%$ for $l = 1.6$).

The refinement of the finite element mesh improves the quality of results (see Fig. 2.16 for the FEM mesh with $25 \times 25 \times 25$ elements). The normalized root mean square deviation as well as the normalized local relative errors decrease for all components of the magnetic field, e.g. $\epsilon^i_{2,z} = -11.6\%$ for $l = 1.6$.

It can be concluded that the poor accuracy of the component H_z is a result of the specific features of the test problem, i.e., discontinuity of the Dirichlet boundary condition at $z = c$, but not the applied **H**-formulation.

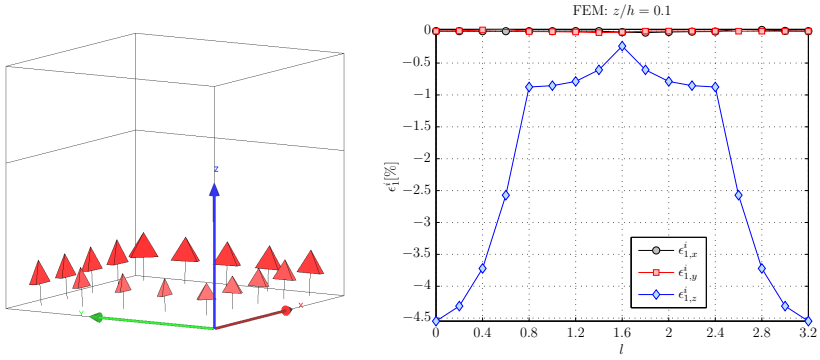

(a) Line l_1 - NRMSD: $\delta_1 = 1.90\%$

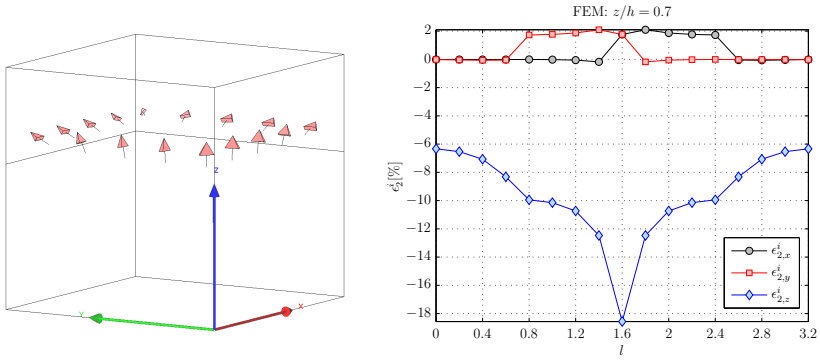

(b) Line l_2 - NRMSD: $\delta_2 = 4.64\%$

Fig. 2.15: Test problem - magnetic intensity **H** and normalized error ϵ_k^i calculated using **H** formulation with separated components (FEM mesh: $15 \times 15 \times 15$ linear brick elements)

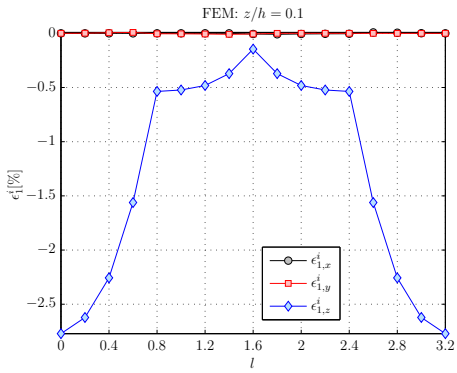

(a) Line l_1 - NRMSD: $\delta_1 = 1.14\%$

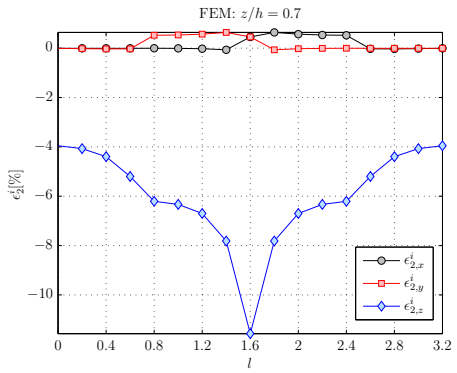

(b) Line l_2 - NRMSD: $\delta_2 = 2.83\%$

Fig. 2.16: Test problem - **H** formulation with separated components - normalized error ϵ_k^i for FEM mesh of $25 \times 25 \times 25$ linear brick elements

2.5.2. EDGE ELEMENTS IN DIRECT H-FORMULATION

An attempt was made to use the edge finite elements in **H** formulation to solve the boundary value problem for equation (2.75) ($\lambda = 0$) with the boundary condition (2.3) on Γ_H and homogeneous natural boundary conditions on the walls $x = 0$ and $y = 0$.

Figure 2.17 shows a comparison between the analytical solution and the solution received from the direct **H** formulation using edge elements.

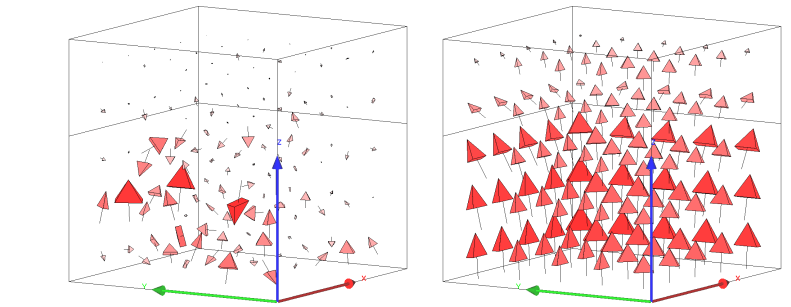

(a) FEM solution (b) Analytical solution

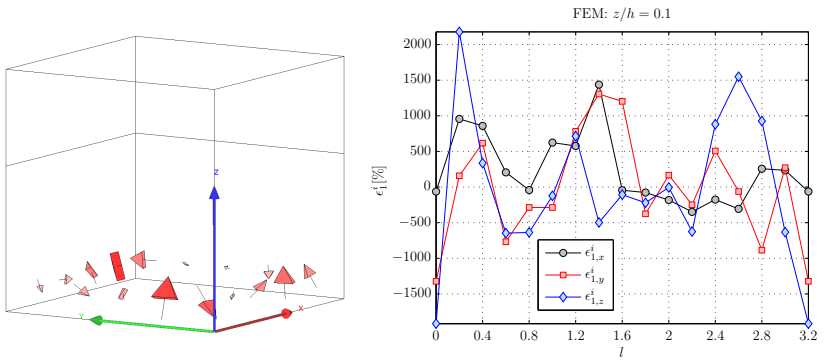

(c) Line l_1 - NRMSD: $\delta_1 = 2396\%$

Fig. 2.17: Test problem - magnetic intensity **H** and normalized error ϵ_k^i calculated using **H** formulation with edge elements - spurious solution (FEM mesh: $15 \times 15 \times 15$ linear edge brick elements)

The solution obtained by the numerical method has a non-physical nature which in fact confirms earlier reports given in [107] and [134]. The presence of non-physical solutions in the formally correct formulated boundary value problem is due to the fact that on Γ_B-type boundary, instead of the stronger essential boundary condition (2.4) is set the weaker natural condition resulting from the applied edge approximation (Section 1.5.). The method discussed in this section should be rejected as not suitable for the calculation of magnetic fields.

2.6. SUMMARY

In this chapter the comparison of various formulations used in the analysis of 3D magnetostatic fields is presented. First, a general 3D magnetostatic boundary value problem has been formulated. Next, the simple benchmark problem having the analytical solution has been introduced. The analysis of 3D magnetostatic fields starts with the approach using two magnetic scalar potentials (total and reduced). Sample results have been presented. Modeling of 3D windings without and with a ferromagnetic core by means of the electric vector potential $\mathbf{T}$ together with two examples have been described in details. An application of edge elements in the magnetic vector potential formulation has been shown. Further, it has been demonstrated how to separate components of the magnetic vector potential in the $\mathbf{A}$ formulation. The formulation $\mathbf{A} - \mathbf{M}$ has been introduced to solve nonlinear magnetostatic problems. The corresponding iterative algorithm for such problems is also formulated. At the end, the direct formulation using the magnetic intensity $\mathbf{H}$ has been presented. Negative attempt to apply edge elements in this formulation has also been discussed.

3

INTERFACE BETWEEN TWO ELECTRICALLY CONDUCTING FLUIDS IN CYLINDRICAL CELL

3.1. INTRODUCTION

The work presented in this chapter is based on the research project entitled "*Detection of interface movements with the help of magnetic field tomography: Part 1: Experiment and sensor systems, Part 2: Numerical treatment of inverse problems*," realized at Technical University of Ilmenau and supported by DFG (Deutsche Forschungsgemeinschaft) in years 2001 - 2007. In the frame of this project, the author was a member of group responsible for developing algorithms and numerical simulations. The experimental part of the project has been realized by the other group of researchers.

There is a variety of problems in material processing where it is useful to know time-dependent distributions of the electrical conductivity of a single fluid or a multiphase flow. For instance, knowledge of the position of the interface between highly conducting molten aluminum and poorly conducting liquid cryolite is important to prevent unwelcome instabilities in aluminum reduction cells [32]. Other examples of such problems can include the identification of electrical conductivity distributions in glass melting furnaces, metal-slag interfaces in steel and iron making as well as on-line detection of various inclusions in molted metals. The liquids involved in material processing such as molten metals, semiconductors, and glass melts are mostly hot and highly aggressive. Therefore, conventional measurement techniques employing local probes face serious difficulties. The purpose of this chapter is to demonstrate that a concept of magnetic field tomography (MFT) which was previously applied to a variety of problems in biomagnetism [15], can be successfully used to identify the interface between two current carrying fluids with different electrical conductivities [31, 40]. According to the idea of the MFT, the magnetic field is measured by a finite number of sensors placed around the tank with two immiscible electrically conducting fluids to reconstruct the moving interface between them.

If typical figures of aluminum electrolysis cells are considered it must be noticed that the cross section has usually a length of a few meters, whereas the interface displacement is very small compared to the lateral extent of the system (Fig. 3.1). The applied high electrical currents (about 100 kA) result in interface displacements of the order of several centimeters. From industrial practice it is known that already such small interface displacements can disturb significantly the operation of the cell. This

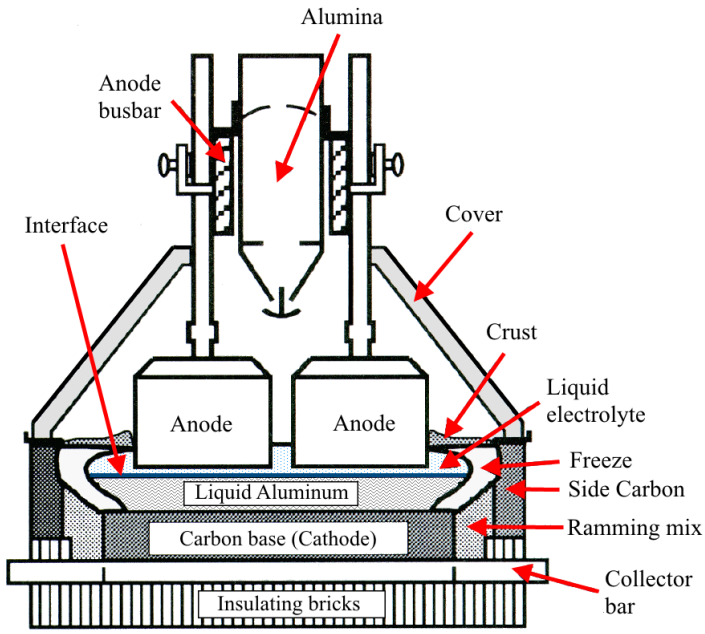

Fig. 3.1: Sample aluminum reduction cell

is the reason why the estimation of such surface deformations as well as contactless methods for their observation are of particular interest. The basic idea of the proposed approach is to exploit to the greatest possible extent the magnetic field produced by electrical currents which are already present in material processing operations such as aluminum reduction or electrical glass melting rather than the field due to injection of an additional artificial electrical current. In particular, it is demonstrated that the external magnetic field generated by the electrical current flowing through a highly simplified model of an aluminum reduction cell provides sufficient information for the reconstruction of the unknown interface shape.

3.2. PHYSICAL MODEL AND FORMULATION OF THE PROBLEM

Figure 3.2 shows the simplified model of the electrolytic bath used in the study. The model consists of a long cylindrical tank of radius R and height h in which two immiscible fluids with different constant electrical conductivities σ_1 and σ_2 are placed. It is also assumed that the temperature of the fluids is equal to the ambient temperature. Although this model is far away from the real aluminum reduction cell, its simplicity allows to demonstrate important features of methods applied to the identification of interface shapes between fluids. Another reason for introducing this model is its relatively easy implementation in the laboratory to enable experimental verification of the identification methods.

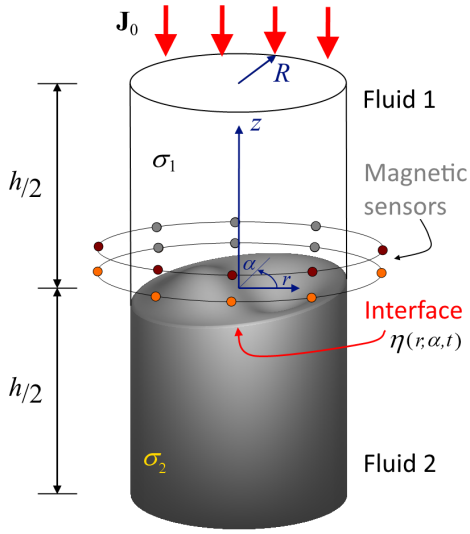

Fig. 3.2: Highly simplified physical model of an aluminum reduction cell

It is assumed that $\sigma_1 \ll \sigma_2$ which corresponds to the real situation in the reduction cell. The wall of the cylinder is non-conductive. At the top of the cylinder a homogeneous direct current of density $\mathbf{J}_0$ is imposed. In the case of a flat interface between the fluids (equilibrium state), the distribution of current density $\mathbf{J}$ throughout the cylinder is homogeneous. As soon as the interface is deformed, e.g. due to gravitational waves or an external forcing, the current density distribution near the interface becomes inhomogeneous (Fig. 3.3). The inhomogeneity of $\mathbf{J}$ can be represented by the perturbation current density $\mathbf{j}$.

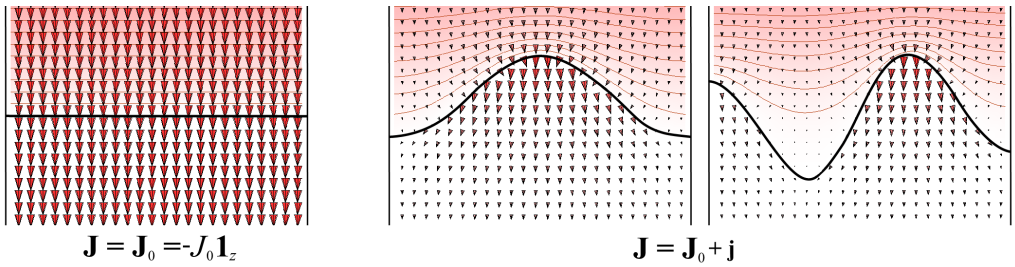

Fig. 3.3: Current density distribution for fluids in the equilibrium state (*left*), near axisymmetric (*middle*) and near non-axisymetric oscillating interfaces (*right*)

The question is now whether the interface shape can be reconstructed from the magnetic flux density $\mathbf{B}$ measured outside the cylindrical cell. Generally, the interface shapes in the cylindrical cell can be split into two group of shapes: (1) axisymmetric, and (2) non-axisymmetric. Axisymmetric interfaces lead to axisymmetric current den-

sity distributions which produce magnetic fields with only one azimuthal component B_α. This means that there is observed no differences between the distributions of the magnetic fields generated by currents flowing through the various axisymmetric interfaces (consequence of the Biot-Savart law). In conclusion, the axisymmetric interface shapes cannot be identified using magnetic field measurements outside the cylinder. Such configurations can only be analyzed using electrical potential measurements [81]. However, if the perturbation of the fluid interface is not axisymmetric, it leads to the non-axisymmetric current density distribution which produces a perturbation of the magnetic field observed as B_r and B_z components outside the cylinder. This fact can be used for the interface reconstructions.

Using the concept of the magnetic field tomography, a general problem of the interface reconstruction (inverse problem) is formulated as follows: having two immiscible free oscillating conducting fluids in the cylindrical cell supplied with direct current reconstruct the interface shape using the magnetic flux density distribution measured by the sensors located around the cell. In the investigated problem, the construction of the MFT system is restricted in such a way that it measures only two components of the magnetic field, i.e., the radial component B_r and the axial one B_z, because they are directly connected with the interface perturbation and have the similar order of magnitude. The azimuthal component B_α, despite of the part related to the interface perturbation contains also the main magnetic field produced by the impressed current $\mathbf{J}_0$. The magnitude of the measured B_α is much greater in this case and requires the use of sensors with different sensitivity range.

In next sections, the interface between two immiscible free oscillating fluids is defined and the methods for calculation of the magnetic field outside the cylindrical cell (forward problem) are presented.

3.2.1. DESCRIPTION OF THE INTERFACE SHAPE

An exact solution of the flow field of two immiscible fluids with the interface free oscillating along z-axis in the cylindrical container is practically impossible. Therefore, for simplification, it is assumed that the flow field is frictionless, irrotational, and incompressible [82] and only small interface oscillations are considered to avoid instabilities due to drops formation. Additionally, the influence of the external magnetic field on the oscillating fluid is neglected. The configuration of the analyzed problem is shown in Fig. 3.4.

To determine the shape of the free oscillating interface, the Euler equation describing motion of fluids is used [83]. The fluid moving in a gravitational field is described by:

$$\frac{\partial \mathbf{v}}{\partial t} + (\mathbf{v} \cdot \nabla)\mathbf{v} = -\frac{\nabla p}{\rho} + \mathbf{g} \tag{3.1}$$

where $\mathbf{v}$ is the fluid velocity, $\partial \mathbf{v}/\partial t$ is the local acceleration of the flow, $(\mathbf{v} \cdot \nabla)\mathbf{v}$ is the convective acceleration for a fluid particle drifting with the stream at the velocity $\mathbf{v}$ in the flow direction, p is the fluid pressure, ρ is the fluid density, and $\mathbf{g}$ is the gravitational acceleration. Equation (3.1) is one of the fundamental equations of fluid dynamics.

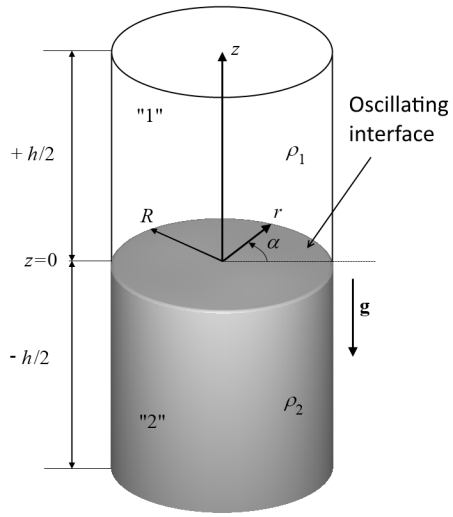

Fig. 3.4: Cylindrical container with two immiscible oscillating fluids

Additionally, the equation of continuity [83] for an incompressible ideal fluid has the following form:

$$\nabla \cdot \mathbf{v} = 0 \tag{3.2}$$

Because of the assumption of irrotational flow, the velocity $\mathbf{v}$ of the flow field can be expressed as gradient of the velocity potential $\Phi = \Phi(\mathbf{r}, t)$, where $\mathbf{r}$ is a position vector. Hence, the equation (3.2) takes the form

$$\mathbf{v} = -\nabla\Phi \quad \rightarrow \quad \nabla^2\Phi = 0 \tag{3.3}$$

which in the cylindrical coordinate system (r, α, z) can be written as:

$$\frac{1}{r}\frac{\partial}{\partial r}\left(r\frac{\partial\Phi}{\partial r}\right) + \frac{1}{r^2}\frac{\partial^2\Phi}{\partial\alpha^2} + \frac{\partial^2\Phi}{\partial z^2} = 0 \tag{3.4}$$

The boundary condition at $r = R$ is given as:

$$\frac{\partial\Phi}{\partial r} = 0 \tag{3.5}$$

which follows from the request of vanishing of the normal component of the fluid velocity at the container side wall ($v_n = 0_{|r=R}$). Additionally, taking into account $h >> R$ (long cylinder), boundary conditions for Φ at bottom and top boundaries of the container can be set as:

$$\Phi \rightarrow 0, \quad |z| \rightarrow \infty \tag{3.6}$$

Using the separation of variables method and the Fourier cosine expansion, the general solution of (3.4) with boundary conditions (3.5) and (3.6) for the interface free oscillating about a state of equilibrium can be written as an infinite double sum of terms (modes) oscillating with eigen frequencies ω_{mn}:

$$\Phi_1(r,\alpha,z,t) = \sum_{m=0}^{\infty}\sum_{n=1}^{\infty} C_1^{mn} \cos m\alpha \, \mathrm{J}_m\left(q_{mn} r\right) e^{-q_{mn} z} \cos \omega_{mn} t, \quad z \geqslant 0 \tag{3.7}$$

$$\Phi_2(r,\alpha,z,t) = \sum_{m=0}^{\infty}\sum_{n=1}^{\infty} C_2^{mn} \cos m\alpha \, \mathrm{J}_m\left(q_{mn} r\right) e^{q_{mn} z} \cos \omega_{mn} t, \quad z \leqslant 0 \tag{3.8}$$

where $\mathrm{J}_m(\cdot)$ is the Bessel function of the first kind of order m, and q_{mn} is the n_{th} root of $\mathrm{J}'_m\left(q_{mn} r\right) = \mathrm{J}'_m\left(\xi_{mn} r/R\right) = 0|_{r=R}$. Table 3.1 shows the roots ξ_{mn} for the first 25 modes.

Table 3.1: n_{th} roots of $\mathrm{J}'_m\left(\xi_{mn}\right) = 0$

ξ_{mn}		m				
		0	1	2	3	4
n	1	3.8317	1.8412	3.0542	4.2012	5.3176
	2	7.0156	5.3314	6.7061	8.0152	9.2824
	3	10.1735	8.5363	9.9695	11.3459	12.6819
	4	13.3237	11.7060	13.1704	14.5858	15.9641
	5	16.4706	14.8636	16.3475	17.7887	19.1960

Using the following vector identity:

$$\nabla(\mathbf{a}\cdot\mathbf{b}) = (\mathbf{a}\cdot\nabla)\mathbf{b} + (\mathbf{b}\cdot\nabla)\mathbf{a} + \mathbf{a}\times(\nabla\times\mathbf{b}) + \mathbf{b}\times(\nabla\times\mathbf{a}) \tag{3.9}$$

and substituting $\mathbf{a} = \mathbf{b} = \mathbf{v}$ and $\nabla\times\mathbf{v} = 0$ for the irrotational fluid, the second term in (3.1) takes the form:

$$(\mathbf{v}\cdot\nabla)\mathbf{v} = \frac{1}{2}\nabla(v^2) \tag{3.10}$$

Introducing (3.10) and $\mathbf{v} = -\nabla\Phi$ into equation (3.1) gives

$$\nabla\left(-\frac{\partial\Phi}{\partial t} + \frac{1}{2}v^2 + \frac{p}{\rho} + gz\right) = 0 \tag{3.11}$$

After integration of (3.11) one can obtain:

$$-\frac{\partial\Phi}{\partial t} + \frac{1}{2}v^2 + \frac{p}{\rho} + gz = F(t) \tag{3.12}$$

where $F(t)$ is an arbitrary function of time. Equation (3.12) is a general form of the Bernoulli equation for unsteady incompressible fluid flows. Equation (3.12) can be

linearized for free interface oscillations and small displacements by neglecting the squared velocity term. Additionally, because only the spatial derivatives of potential Φ have a physical meaning ($\mathbf{v} = -\nabla\Phi$), a constant or even any function of time can be added to Φ whenever it is convenient. This allows inclusion of the integration constant $F(t)$ (3.12) into the definition of Φ. Finally, the linearized form of (3.12) is given by:

$$-\frac{\partial\Phi}{\partial t} + \frac{p}{\rho} + gz = 0 \tag{3.13}$$

Let $\eta = \eta(r, \alpha, t)$ denotes the elevation of the oscillating interface at time t above the equilibrium state. The elevation η can be determined from the condition for continuity of pressure ($p_1 = p_2$) at the interface $z = \eta$. According to (3.13), the pressure continuity can be written as

$$\rho_1 \frac{\partial\Phi_1}{\partial t} - \rho_1 g\eta = \rho_2 \frac{\partial\Phi_2}{\partial t} - \rho_2 g\eta \tag{3.14}$$

Finally, the elevation can be expressed as

$$\eta = \frac{1}{g}\frac{1}{\rho_2 - \rho_1}\left(\rho_2 \frac{\partial\Phi_2}{\partial t} - \rho_1 \frac{\partial\Phi_1}{\partial t}\right) \tag{3.15}$$

Before calculation of the interface shape, it is necessary to find the relation between C_1^{mn} and C_2^{mn} in (3.7) and (3.8). The normal component of the fluid velocity is continuous at the interface for the equilibrium state

$$\frac{\partial\Phi_1}{\partial z} = \frac{\partial\Phi_2}{\partial z}\bigg|_{z=0} \tag{3.16}$$

hence

$$-q_{mn}C_1^{mn} = q_{mn}C_2^{mn} \quad \Rightarrow \quad -C_1^{mn} = C_2^{mn} = C_{mn} \tag{3.17}$$

The eigen frequencies ω_{mn} in (3.7) - (3.8) are determined as follows. For small interface displacements, the kinematic condition at the interface $z = \eta$ can be approximately replaced by a linearized condition at $z = 0$:

$$\frac{\partial\eta}{\partial t} = -\frac{\partial\Phi_i}{\partial z}\bigg|_{z=0} \tag{3.18}$$

which comes from the assumption that the normal component of velocity for points on the interface is simply the time derivative of the elevation $\eta(r, \alpha, t)$. Substitution of (3.15) into (3.18) gives:

$$-g(\rho_2 - \rho_1)\frac{\partial\Phi_i}{\partial z} = \rho_2 \frac{\partial^2\Phi_2}{\partial t^2} - \rho_1 \frac{\partial^2\Phi_1}{\partial t^2}\bigg|_{z=0} \tag{3.19}$$

Inserting (3.7), (3.8), and (3.16) into (3.19) results in the following formula for the eigen frequency of the mode mn :

$$\omega_{mn} = \sqrt{g q_{mn}\frac{\rho_2 - \rho_1}{\rho_2 + \rho_1}} \tag{3.20}$$

Finally, the elevation η of the free oscillating interface can be generally expressed as:

$$\eta(r,\alpha,t) = \sum_{m=0}^{\infty}\sum_{n=1}^{\infty} A_{mn}\cos m\alpha\, \mathrm{J}_m\left(q_{mn}r\right)\cos\omega_{mn}t \tag{3.21}$$

where $A_{mn} = C_{mn}\omega_{mn}(\rho_2+\rho_1)/[g(\rho_2-\rho_1)]$. The equilibrium state described by $\eta = 0|_{m=n=0}$ as a trivial solution is excluded from (3.21).

Two types of interface shapes can be distinguished from equation (3.21), namely:

1. Axisymmetric interface shapes

$$\eta(r,\alpha,t) = \sum_{n=1}^{\infty} A_{mn}\,\mathrm{J}_0\left(q_{0n}r\right)\cos\omega_{0n}t = \sum_{n=1}^{\infty}\eta_{0n}\cos\omega_{0n}t \tag{3.22}$$

2. Non-axisymmetric interface shapes

$$\eta(r,\alpha,t) = \sum_{m=1}^{\infty}\sum_{n=1}^{\infty} A_{mn}\,\mathrm{J}_m\left(q_{mn}r\right)\cos m\alpha\cos\omega_{mn}t = \sum_{m=1}^{\infty}\sum_{n=1}^{\infty}\eta_{mn}\cos\omega_{mn}t \tag{3.23}$$

where $\eta_{mn} = \eta_{mn}(r,\alpha)$ denotes the single mode amplitude, m and n are called the azimuthal and the radial mode number, respectively. Sample snapshots of interfaces at the moment of maximum elevation described by a single stable mode and oscillating with the corresponding eigen frequency are shown in Fig. 3.5 (simulations).

Although the number of modes in (3.22) and (3.23) is infinite, usually, the higher modes can be neglected in a practical analysis because their amplitudes are much smaller than the amplitudes of modes with low radial and azimuthal numbers [35]. Therefore, instead of (3.23), the following approximation of interface shapes is used further:

$$\eta(r,\alpha,t) = \sum_{m=1}^{M}\sum_{n=1}^{N} A_{mn}\cos m\alpha\,\mathrm{J}_m\left(q_{mn}r\right)\cos\omega_{mn}t = \sum_{m=1}^{M}\sum_{n=1}^{N}\eta_{mn}\cos\omega_{mn}t \tag{3.24}$$

where M and N are the highest available azimuthal and radial mode numbers, respectively. Axisymmetric modes are excluded due to remarks in the previous section.

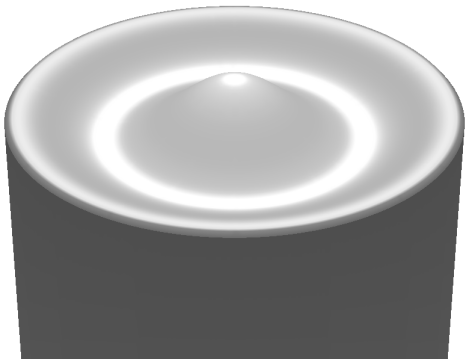

(a) Mode η_{02}.

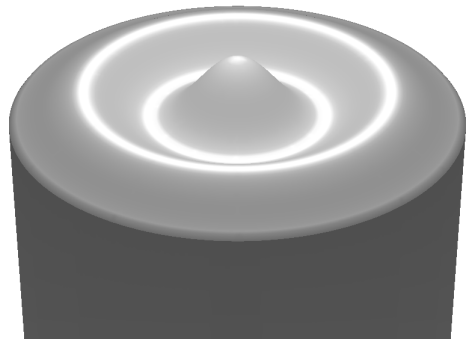

(b) Mode η_{03}.

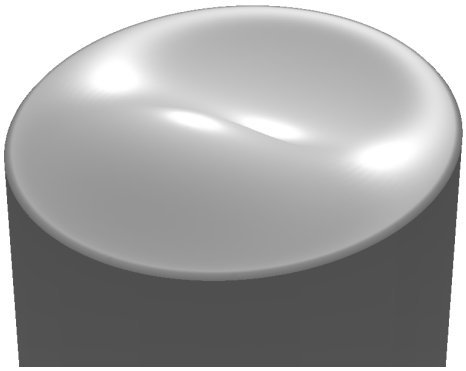

(c) Mode η_{12}.

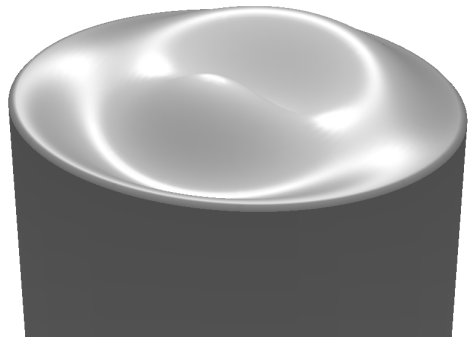

(d) Mode η_{13}.

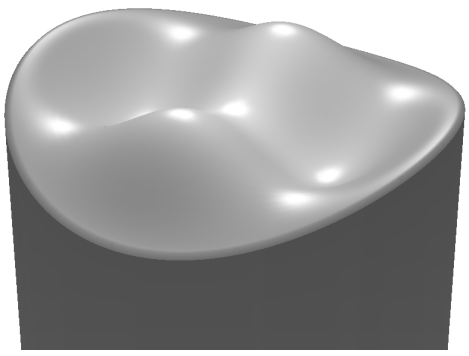

(e) Mode η_{22}.

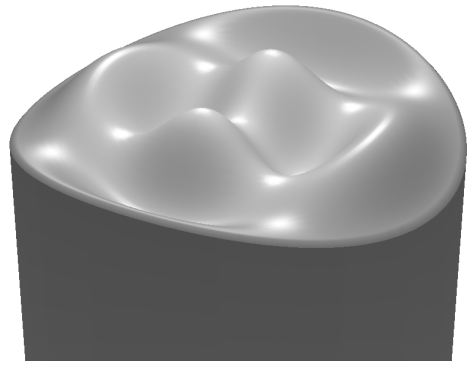

(f) Mode η_{23}.

Fig. 3.5: Sample normalized interfaces at the moment of maximum elevation - axisymmetric modes: η_{02}, η_{03}, non-axisymmetric modes: η_{12}, η_{13}, η_{22}, η_{23}

3.2.2. MAGNETIC FIELD OUTSIDE CYLINDRICAL CELL - ANALYTICAL APPROACH

The supply current flowing in the cell is a direct current. Additionally, the frequency of oscillating interface η is relatively small. These two facts allows to neglect eddy currents effects in conducting fluids ($\nabla \times \mathbf{E} = 0$) and in consequence the electrical current in the cylinder can be described by means of the quasi-static total electric potential V. Under above assumptions, the procedure for determining the magnetic field around the cylinder (Fig. 3.2) is obvious. First, the distribution of electric potential V has to be determined inside the cylinder. Next, using formula $\mathbf{J} = -\sigma \nabla V$, the current density $\mathbf{J}$ is calculated. At the end, the magnetic field density outside the cylinder can be calculated according the Biot-Savart law:

$$\mathbf{B} = \frac{\mu_0}{4\pi} \int_{\Omega} \frac{\mathbf{J} \times \mathbf{1}_r}{r^2} d\Omega, \tag{3.25}$$

where Ω denotes the cylinder region.

Any deformation of the interface changes the internal current density distribution in the cylinder and thus the external magnetic field. Using the quasi-static electric potential formulation this effect can be described by means of the electric potential φ corresponding to the interface perturbation. The potential φ can be found by solving Laplace equations in the respective fluids:

$$\nabla^2 \phi_1 = 0, \ z \geqslant \eta \tag{3.26}$$

$$\nabla^2 \phi_2 = 0, \ z \leqslant \eta \tag{3.27}$$

where η is the interface elevation and

$$\phi_{1,2} = J_0 \frac{z}{\sigma_{1,2}} + \varphi_{1,2} \tag{3.28}$$

J_0 is the impressed constant current density at the top of cylinder. To simplify the analysis, the height of the cylinder h is assumed to be much greater than the radius R ($h \gg R$). The following boundary conditions can now be formulated:

$$\frac{\partial \varphi_{1,2}}{\partial r} = 0, \ r = R \tag{3.29}$$

$$\frac{\partial \varphi_{1,2}}{\partial z} = 0, \ z \to \pm\infty \tag{3.30}$$

which correspond to the facts that the wall of the cylinder is an electrical insulator and the distribution of current density vector $\mathbf{J}$ should be homogeneous at the top and the base of the cylinder, i.e., the influence of current perturbation is vanishing far away from the interface. The perturbation potential φ in the respective fluids can be found by means of the separation of variables method as:

$$\varphi_1 = \sum_{m=1}^{\infty} \sum_{n=1}^{\infty} C_1^{mn} \, \mathrm{J}_m(q_{mn} r) \cos m\alpha e^{-q_{mn} z}, \ z \geqslant 0 \tag{3.31}$$

$$\varphi_2 = \sum_{m=1}^{\infty} \sum_{n=1}^{\infty} C_2^{mn} \, \mathrm{J}_m(q_{mn} r) \cos m\alpha e^{q_{mn} z}, \quad z \leqslant 0 \tag{3.32}$$

where $\mathrm{J}_m(\cdot)$ is the Bessel function of the first kind of order m and q_{mn} is the n_{th} root of $\mathrm{J}'_m(q_{mn}r) = \mathrm{J}'_m(\xi_{mn}r/R) = 0|_{r=R}$ (see Table 3.1).

In general case, it is not possible to find the analytical solution of (3.26) - (3.27) in the form of (3.31) because the following continuity conditions cannot be fulfilled at the interface:

$$\phi_1 = \phi_2, \quad z = \eta, \tag{3.33}$$

$$\mathbf{n} \cdot (\mathbf{J}_1 - \mathbf{J}_2) = 0, \quad z = \eta \tag{3.34}$$

However, the approximate analytical solution can be found for infinitesimal perturbations of the interface ($\eta \ll R, h$) by introducing at $z = 0$ the following jump condition [32, 70] instead of the potential continuity at $z = \eta$:

$$\varphi_1 - \varphi_2 = J_0 \eta \left(\frac{1}{\sigma_2} - \frac{1}{\sigma_1} \right), \quad z = 0 \tag{3.35}$$

The continuity of the normal component of the current density at $z = 0$ is defined as:

$$\sigma_1 \frac{\partial \varphi_1}{\partial z} = \sigma_2 \frac{\partial \varphi_2}{\partial z}, \quad z = 0 \tag{3.36}$$

because $\mathbf{n} \approx \mathbf{1}_z$, for small perturbations. Now, using (3.23), the constants $C_{1,2}^{mn}$ can be obtained as:

$$C_1^{mn} = A_{mn}^t J_0 \frac{1}{\sigma_1} \frac{\sigma_1 - \sigma_2}{\sigma_1 + \sigma_2} \tag{3.37}$$

$$C_2^{mn} = A_{mn}^t J_0 \frac{1}{\sigma_2} \frac{\sigma_2 - \sigma_1}{\sigma_1 + \sigma_2} \tag{3.38}$$

where $A_{mn}^t = A_{mn} \cos \omega_{mn} t$ denotes the time dependent amplitude of the oscillating interface.

Current density components of the current flowing in the cell regions can be found from $\mathbf{J} = -\sigma \nabla V$ as:

$$J_r^{1,2} = \mp J_0 \frac{\sigma_1 - \sigma_2}{\sigma_1 + \sigma_2} \sum_{m=1}^{\infty} \sum_{n=1}^{\infty} A_{mn}^t \underbrace{q_{mn} \frac{\mathrm{J}_{m-1}(q_{mn}r) - \mathrm{J}_{m+1}(q_{mn}r)}{2}}_{d\,\mathrm{J}_m(q_{mn}r)/dr} \cos m\alpha e^{-q_{mn}|z|} \tag{3.39}$$

$$J_\alpha^{1,2} = \pm J_0 \frac{\sigma_1 - \sigma_2}{\sigma_1 + \sigma_2} \sum_{m=1}^{\infty} \sum_{n=1}^{\infty} A_{mn}^t \frac{m}{r} \mathrm{J}_m(q_{mn}r) \sin m\alpha e^{-q_{mn}|z|} \tag{3.40}$$

$$J_z^{1,2} = -J_0 \mp J_0 \frac{\sigma_1 - \sigma_2}{\sigma_1 + \sigma_2} \sum_{m=1}^{\infty} \sum_{n=1}^{\infty} A_{mn}^t q_{mn} \mathrm{J}_m(q_{mn}r) \cos m\alpha e^{-q_{mn}|z|} \tag{3.41}$$

The magnetic field outside the cylinder can be calculated using the Biot-Savart law (3.25) and (3.39) - (3.41). The integral (3.25) is computed numerically as follows. First, a mesh of tetrahedral elements inside the cylinder is created. Next, it is assumed that the current density in every tetrahedral element is constant and is equal to the value calculated at the center of gravity (COG) of the element using analytical formulas

(3.39) - (3.41). Further, assuming that elements of created mesh are sufficiently small comparing a distance where the magnetic field is calculated (magnetic sensor positions) the integral (3.25) can be replaced by the following sum:

$$\mathbf{B}_0 = \frac{\mu_0}{4\pi} \sum_{i=1}^{N_e} \frac{\mathbf{J}_i \times (\mathbf{r}_i - \mathbf{r}_0)}{r_i^3} \Delta\Omega_i, \tag{3.42}$$

where N_e is the total number of tetrahedral elements, $\mathbf{J}_i$ is the current density vector in i^{th}-element, $\mathbf{r}_i$ is COG-position of i^{th}-element, $\mathbf{r}_0$ is the magnetic sensor position, and $\Delta\Omega_i$ is the volume of i^{th}-element.

Further, results of calculations of B_r and B_z component using (3.42) around the cylindrical cell are presented as field distributions over the evolved appropriate sensors array. The construction principle of the evolved arrays is shown in Fig. 3.6.

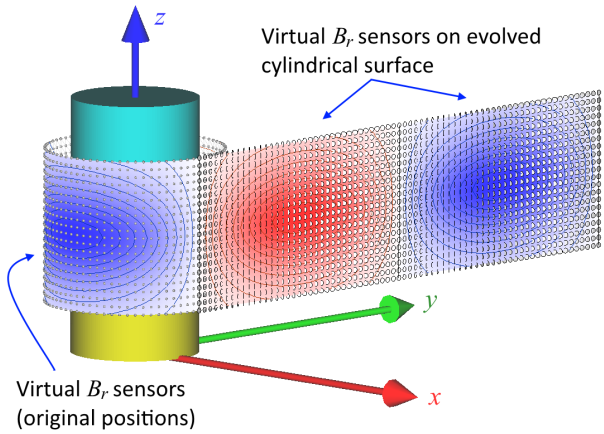

Fig. 3.6: Construction principle of evolved sensors array together with B_r distribution

The following parameters of the cell model are applied: $h = 100\,\text{mm}$ (cylinder height), $R = 25\,\text{mm}$ (cylinder radius), $\sigma_1 = 100\,\text{S/m}$ (upper fluid conductivity), $\sigma_2 = 3.46\,\text{MS/m}$ (lower fluid conductivity), and $J_0 = 509.3\,\text{A/m}^2 = 1\,\text{A}\,/(\pi R^2)$ (impressed current density at $z = h/2$). The magnetic field around the cylinder is calculated at the distance $d = 10\,\text{mm}$ from the cylinder wall in the range of $z \in [-30\,\text{mm}, 30\,\text{mm}]$. Figure 3.7 shows distributions of the radial (B_r) and axial (B_z) components of the magnetic field for the interface perturbation amplitude equals $A = 2.5\,\text{mm} \ll R$. The snapshots are taken for the instant when the interface perturbation reaches the maximum elevation. It should also be noticed that the maximums of radial and axial components are over 30 times smaller than the maximum of the azimuthal component $B_\alpha^{max} = 4770\,\text{nT}$ calculated for the undisturbed interface at the equilibrium state.

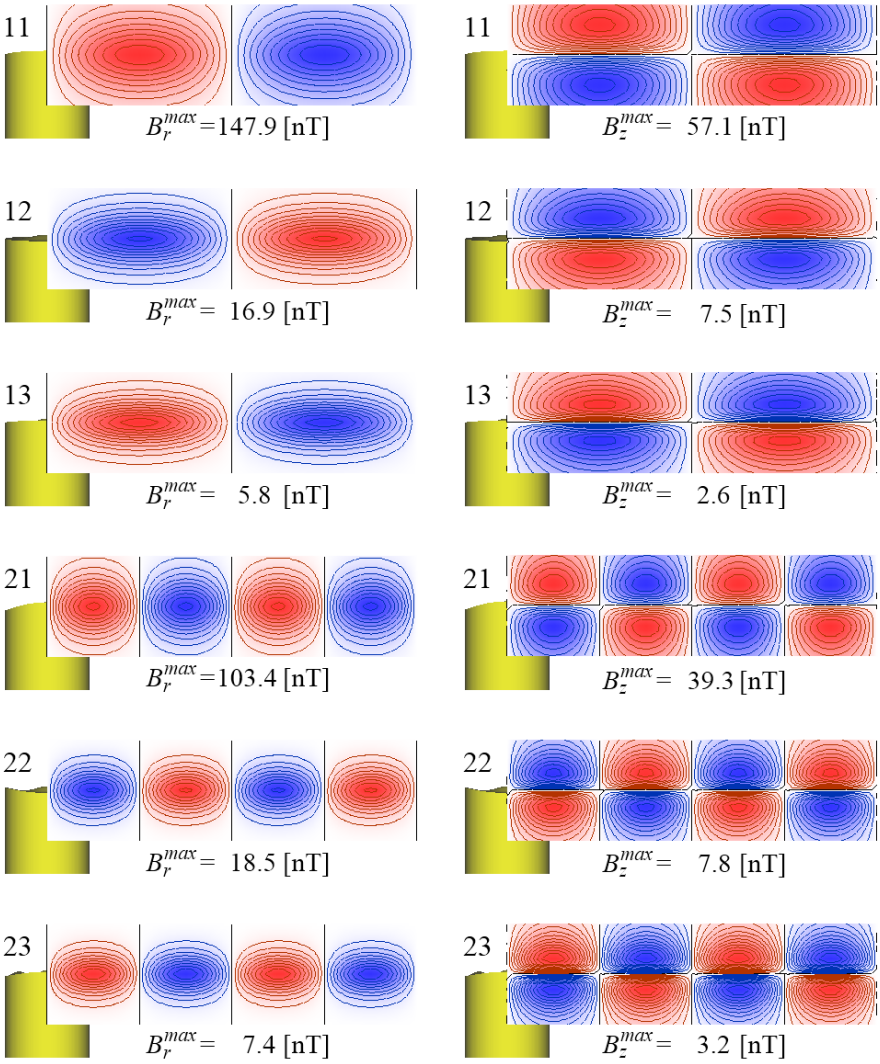

Fig. 3.7: Analytical solution for interface modes $11-12$ and $21-23$ - distributions of B_r and B_z around cylinder at $r = R + d = 35\,\text{mm}$ for the moment of maximum interface elevation ($A = 2.5\,\text{mm}$)

3.2.3. VERIFICATION OF THE ANALYTICAL APPROACH

An important part of every stage in a solving process of any technical problem is a verification of the applied method. It is important to find how close are simulation results to the physical model and to check if there are not any principal errors in the applied method (method validity) or in its implementation. The verification, in the

simplest case, can be performed by applying to the same problem a different method which better describes the real model. Of course, ultimately the best verification is the comparison between simulations and measurements. However, this type of verification is beyond the scope of the monograph. The goal of this section is to present a comparison of magnetic field calculated by analytical methods described in Section 3.2.2. with results of simulations performed with the help of the finite element method (FEM).

Application of the finite element method requires, in principle, to replace only one procedure in the algorithm for calculating the magnetic field around the cylindrical cell. Namely, the procedure that determines the electric potential and current density distribution in the cell. The rest of the algorithm remains unchanged. The main advantage of using the finite element method is to eliminate the problem of continuity conditions fulfillment (3.33) - (3.34) at the interface which could not be accurately resolved in the analytical approach. The continuity conditions are automatically fulfilled in any FEM implementation using the electric scalar potential.

Using assumptions from Section 3.2.2., the problem of finding the current density distribution in the oscillating fluids is reduced to the static analysis of the cylindrical cell with two homogeneous conducting regions at the moment when the interface between regions reaches the maximum elevation. In principle, such problem can be solved by any commercial FEM software with an electromagnetic module. In the analyzed problem, an important factor which has to be taken into account during a selection of suitable FEM software is the answer to the question: how easy the interface geometry given by (3.21) can be modeled. Unfortunately, it was not possible to find any commercial FEM program which enables the modeling surface patches defined by Bessel functions directly in a graphical user interface (GUI). Usually, the user has to prepare the separate external procedure which generates geometry data of the surface patch and then to import it into GUI. How easily this can be accomplished is the fundamental question. After thorough analysis of all the pros and cons of available FEM programs, COMSOL Multiphysics® (earlier known as FEMLAB®) was selected for further use.

COMSOL Multiphysics® is an engineering, design, and finite element analysis software environment for the modeling and simulation of any physics-based system [26]. COMSOL® can be integrated with Matlab® which is a high-level technical computing language and interactive environment for algorithm development, data visualization, data analysis, and numeric computation [88]. COMSOL® and Matlab® together, create powerful numerical environment with a seldom flexibility which enables to solve a lot of technical problem.

As an example of using COMSOL® package, cylindrical cell model described in the previous section is presented. The model implemented in COMSOL® together with the applied finite element mesh are shown in Fig. 3.8. Figure 3.9 presents the electric scalar potential at cross-sections $x = 0$ and $y = 0$ together with the current density distribution calculated in the analyzed cell.

An alternative to commercial software are packages specifically adapted to the analyzed problem and self-developed by the user. Using such approach, the user, in the first phase, spends more time for the software preparation but as a result he receives

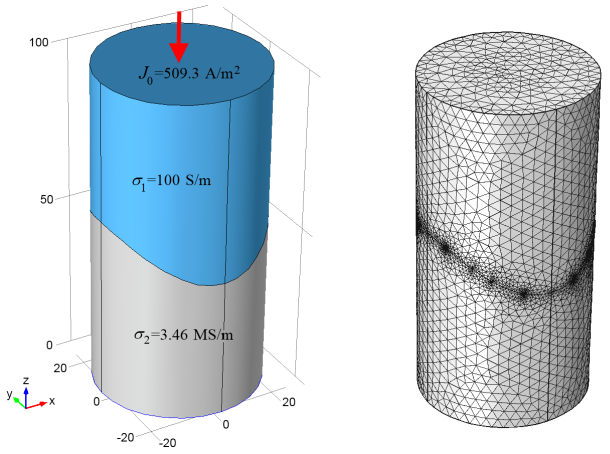

(a) Physical model. (b) Sample finite element mesh.

Fig. 3.8: Cylindrical cell with two conducting fluids - mode η_{21} for the moment of maximum interface elevation ($A = 7.0\,\mathrm{mm}$)

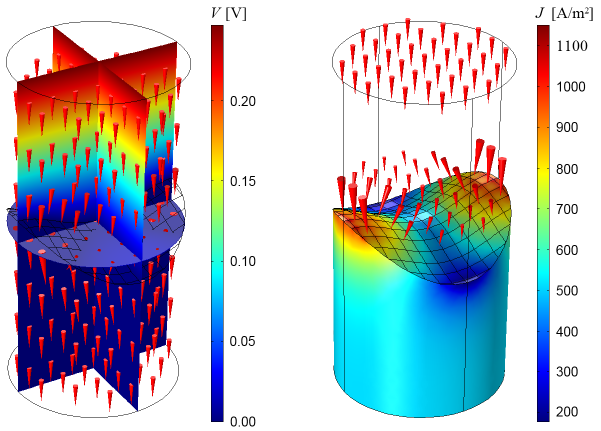

(a) **J** and V at $x = 0$ and $y = 0$. (b) **J** and $|\mathbf{J}|$ near interface.

Fig. 3.9: Results of FEM calculations in a cylindrical cell - current density **J** (*cones*) and electric scalar potential V distributions

potentially more flexibility for implementation specific features of the problem and has full control over the implemented code. Usually, if the code is properly optimized, the developed program can also run faster than the commercial one. Using this approach, the author has developed the TFEM3D routine. The TFEM3D routine based on the finite element method allows calculations of current density distributions in the cylindrical cell filled with two conducting fluids. Additionally, procedures for calcula-

tions of magnetic flux density components outside the cylinder for predefined sensor configurations are integrated in TFEM3D.

The main structure of the finite element part of TFEM3D is based on SONMAP2D [51], a general system for numerical analysis of 2D electrodynamic problems. It was necessary to rewrite completely the pre- and post-processing routines to adopt them to the cylindrical cell problem. The method of solving large, sparse systems of linear algebraic equations used in SONMAP2D had also to be changed. In the first version of TFEM3D, the Yale sparse matrix package containing direct solvers for symmetric and non-symmetric systems of linear equations [36, 37] has been implemented. An important problem that must be considered when a new solver is implemented, is the storage scheme of matrix data structures used by the solver because this directly influences routines creating and assembling global stiffness and load matrices in the finite element method. The Yale package uses a special storage scheme for storing sparse matrices. The Yale scheme has minimal storage requirements and is very convenient for sparse matrix operations. In this scheme, the values of the nonzero elements of the sparse matrix $[\mathbb{A}]$ are stored by rows, together with their corresponding indexes which are located in two vector arrays $\{\mathbb{AN}\}$ and $\{\mathbb{JA}\}$, respectively. The third vector array $\{\mathbb{IA}\}$ contains pointers to the first element in each row of the matrix $[\mathbb{A}]$, e.g.:

$$[\mathbb{A}] = \begin{bmatrix} 11 & 0 & 13 & 14 \\ 0 & 22 & 0 & 24 \\ 31 & 0 & 33 & 0 \\ 0 & 42 & 0 & 44 \end{bmatrix} \quad \begin{aligned} \{\mathbb{AN}\} &= [11\ \ 13\ \ 14\ \ 22\ \ 24\ \ 31\ \ 33\ \ 42\ \ 44]^T \\ \{\mathbb{JA}\} &= [1\ \ 3\ \ 4\ \ 2\ \ 4\ \ 1\ \ 3\ \ 2\ \ 4]^T \\ \{\mathbb{IA}\} &= [1\ \ 4\ \ 6\ \ 8\ \ 10]^T \end{aligned}$$

This representation is complete because the entire matrix is represented, and ordered, and because the elements of each row are stored in the ascending order of their column indexes. Following [109], it is assigned as RR(C)O, which states for Row-wise Representation, (C)omplete and Ordered.

Unfortunately, the direct solvers are fast enough for systems up to, roughly saying, 100000 unknowns which is enough for most of 2D problems but it is usually too less for 3D cases. For 3D problems, the iterative solvers have to be considered. For this reason, in the second version of TFEM3D, it was decided to implement a part of free-available public domain Common Mathematical Library (SLATEC CML) [130], namely, Sparse Linear Algebra Package (SLAP) which contains a set of several iterative solvers of linear algebraic systems. SLATEC is the acronym for the Sandia, Los Alamos, Air Force Weapons Laboratory Technical Exchange Committee. This organization was formed in 1974 to foster the exchange of technical information. The SLATEC CML is written in FORTRAN 77 and contains general purpose mathematical and statistical routines. The sparse linear algebra package uses two storage schemes of sparse matrices: 1) the SLAP Triad format, and 2) the SLAP Column format. In the SLAP Triad format only the nonzero elements are stored. They may appear in any order. The user must supply three

vector arrays: $\{\mathbb{AN}\}$ with non-zero elements of matrix $[\mathbb{A}]$ and their locations given in $\{\mathbb{IA}\}$, $\{\mathbb{JA}\}$ with the row and column indexes, respectively, e.g.:

$$[\mathbb{A}] = \begin{bmatrix} 11 & 0 & 13 & 14 \\ 0 & 22 & 0 & 24 \\ 31 & 0 & 33 & 0 \\ 0 & 42 & 0 & 44 \end{bmatrix} \quad \begin{aligned} \{\mathbb{AN}\} &= [22\ \ 14\ \ 31\ \ 42\ \ 44\ \ 13\ \ 33\ \ 24\ \ 11]^T \\ \{\mathbb{JA}\} &= [2\ \ 4\ \ 1\ \ 2\ \ 4\ \ 3\ \ 3\ \ 3\ \ 1]^T \\ \{\mathbb{IA}\} &= [2\ \ 1\ \ 3\ \ 4\ \ 4\ \ 1\ \ 3\ \ 2\ \ 1]^T \end{aligned}$$

The SLAP Triad scheme is very easy to generate and it can directly be obtained from the Yale scheme but on the other hand it is not very efficient for the iterative solution of linear systems especially on vector computers. In fact, SLAP changes internally this format to the SLAP Column format in the iteration solvers which is much more effective. The SLAP Column format is very similar to the Yale scheme but instead of row-wise representation it uses column-wise one. Additionally, it is unordered because non-zero elements of matrix $[\mathbb{A}]$ must not be ordered in the column. According to [109], it can be classified as CR(C)U scheme (Column-wise Representation, (C)omplete, Unordered), e.g.:

$$[\mathbb{A}] = \begin{bmatrix} 11 & 0 & 13 & 14 \\ 0 & 22 & 0 & 24 \\ 31 & 0 & 33 & 0 \\ 0 & 42 & 0 & 44 \end{bmatrix} \quad \begin{aligned} \{\mathbb{AN}\} &= [11\ \ 31\ \ 42\ \ 22\ \ 13\ \ 33\ \ 44\ \ 14\ \ 24]^T \\ \{\mathbb{JA}\} &= [1\ \ 3\ \ 4\ \ 2\ \ 1\ \ 3\ \ 4\ \ 1\ \ 2]^T \\ \{\mathbb{IA}\} &= [1\ \ 3\ \ 5\ \ 7\ \ 10]^T \end{aligned}$$

A valuable feature of the SLAP package is that for symmetric problems, the Yale storage scheme can be directly used in it without applying any additional conversion routines.

Several tests have been carried out to compare COMSOL Multiphysics® 3.5a with TFEM3D using CPU time of FEM calculations as a test criterion. Tests run on PC computer equipped with Intel Core i7 Extreme 975 processor and 24GB RAM under 64 bit Windows 7 Professional. In all comparisons, the same models were used, i.e., first, the model of the cylindrical cell was created and calculated in COMSOL® and then, after conversion, the model was imported and calculated by TFEM3D. In all simulations, the first order tetrahedral finite elements have been applied. It was found that for COMSOL® as well as for TFEM3D choosing a preconditioned conjugate gradient method as a solver gave results in the fastest way. The preconditioned conjugate gradient method (PCGM) is suitable for the symmetric, positive definite linear systems. In all tests, the diagonal scaling (DS) has been used as the preconditioning routine. This routine performs left preconditioning using the main diagonal of the stiffness matrix.

Table 3.2 presents CPU times of solving linear systems of algebraic equations with N_p unknowns in COMSOL® and in TFEM3D; N_e denotes the number of tetrahedral elements of the corresponding finite element meshes. It can be observed that TFEM3D solves the FEM task about 30% faster than COMSOL®.

In the TFEM3D preprocessor, a simple finite element mesh generator of tetrahedral elements is implemented. It works on a slice principle and depends only on two parameters: the predefined maximum size of element edge d_E, used during generation

Table 3.2: CPU time of FEM calculations (Solver: PCGM+DS)

			COMSOL V.3.5a	TFEM3D
	N_e	N_p	CPU [s]	CPU [s]
1	206779	37623	0.72	0.39
2	819797	153568	4.37	2.57
3	2631993	488359	18.74	12.01
4	8428313	1535399	81.97	53.27

of a regular 2D triangular mesh of the cylinder base, and the number of slices N_{SL}, which determines the mesh density in the z-direction. TFEM3D slice generator works as follows: first, a uniform slice distribution throughout the cylinder is created, then it is rescaled relative to $z = 0$ using the exponential scaling function to receive more dense mesh in the vicinity of the interface (EXP-mesh). At the end, the deformed interface shape is calculated according to (3.23) and applied to modify z-coordinates of all nodes of the exponential mesh where $|z| < h/2$ (Fig. 3.10). The slice generator imple-

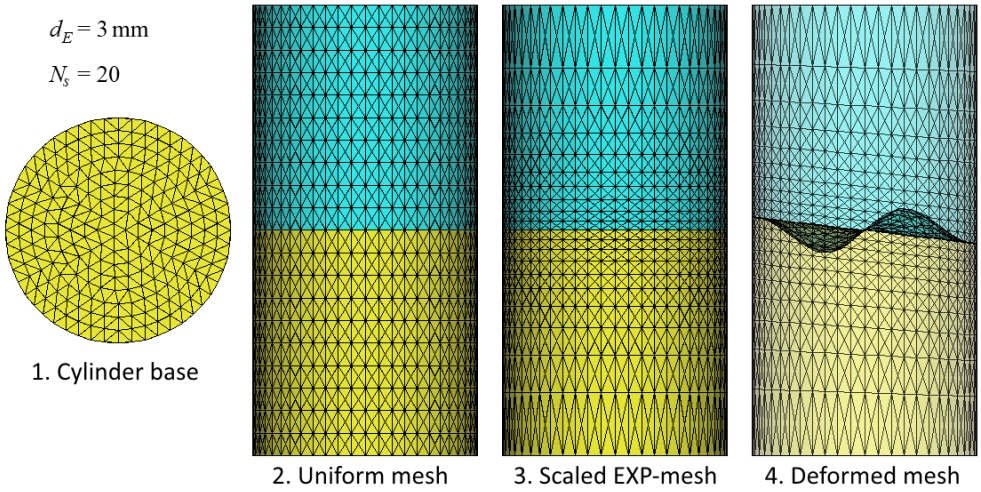

Fig. 3.10: Cylindrical cell - four steps of finite element mesh construction

mented in TFEM3D works faster than the general finite element mesh generator based on 3D Delaunay triangulation used in COMSOL® . It eliminates also not necessary overloading of elements in regions where the interface touches the cylinder wall (see Fig. 3.8).

Now, the verification of analytical results presented in the previous section will be shown using the FEM calculations carried out with the TFEM3D routine. As previously, the same cell model is used, i.e., $h = 100\,\text{mm}$ (cylinder height), $R = 25\,\text{mm}$

(cylinder radius), $\sigma_2 = 3.46\,\mathrm{MS/m}$ (lower fluid conductivity), $\sigma_1 = 100\,\mathrm{S/m}$ (upper fluid conductivity), and $J_0 = 509.3\,\mathrm{A/m^2} = 1\,\mathrm{A}/(\pi R^2)$ (impressed current density at $z = h/2$). The magnetic field around the cylinder is calculated at a distance $d = 10\,\mathrm{mm}$ from the wall of the cylinder in the range of $z \in [-30\,\mathrm{mm}, 30\,\mathrm{mm}]$. The FEM model is generated using the maximum 2D edge size equals $d_E = 1\,\mathrm{mm}$ and the number of slices $N_{SL} = 50$ which gives the FE mesh with the total number of tetrahedral elements equals $N_e = 3131100$ and the number of nodes equals $N_p = 681166$. Figure 3.11

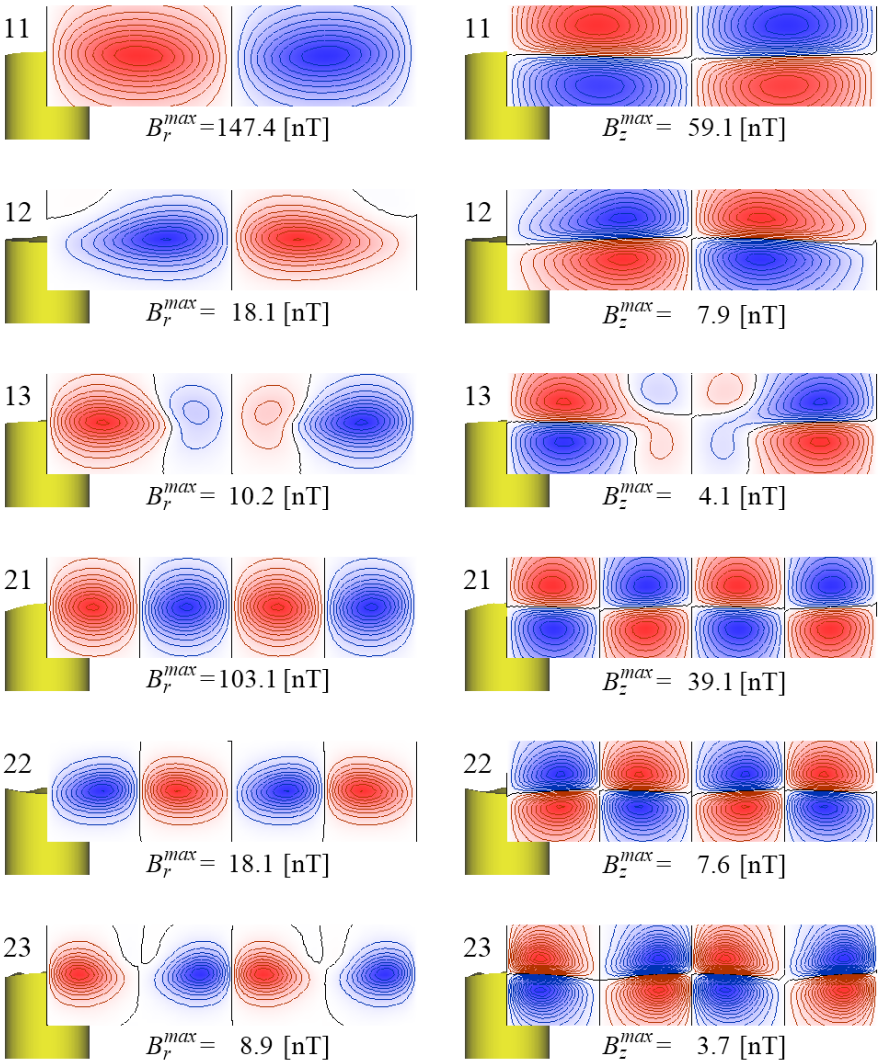

Fig. 3.11: FEM solution for interface modes $11 - 12$ and $21 - 23$ - B_r and B_z around cylinder at $r = R + d = 35\,\mathrm{mm}$ for the moment of maximum interface elevation ($A = 2.5\,\mathrm{mm}$)

shows distributions of radial (B_r) and axial (B_z) components of the magnetic field for interface perturbations oscillating with the amplitude equals $A = 2.5\,\text{mm}$. Results are presented in a form of equi-level plots over evolved cylindrical surface The snapshots are taken for the time instant which corresponds to the interface perturbation with the maximum elevation. After a visual inspection of calculated distributions it can be found significant differences between the analytical solution and the FEM one, especially for higher radial modes although the amplitude of the oscillating interface fulfills $A \ll R$ condition. It can also be noticed that the magnetic field distribution received from the analytical solution does not follow the interface distortion as it is in the FEM case. To verify the analytical results quantitatively, the rectangular array of $N_a \times N_z$ evenly distributed magnetic sensors is constructed around the cylinder at the distance $d = 10\,\text{mm}$ in the range of $z \in [-30\,\text{mm}, 30\,\text{mm}]$, where N_a is the number of sensors in one azimuthal row and N_z is the number of rows in z-direction. The following total relative error indicators are defined:

$$\delta_r^{\%} = \sqrt{\frac{\sum_{j=1}^{N_r}\sum_{i=1}^{N_a}\left(B_r^{ANA} - B_r^{FEM}\right)_{ij}^2}{\sum_{j=1}^{N_r}\sum_{i=1}^{N_a}\left(B_r^{FEM}\right)_{ij}^2}}100\% \tag{3.43}$$

$$\delta_z^{\%} = \sqrt{\frac{\sum_{j=1}^{N_r}\sum_{i=1}^{N_a}\left(B_z^{ANA} - B_z^{FEM}\right)_{ij}^2}{\sum_{j=1}^{N_r}\sum_{i=1}^{N_a}\left(B_z^{FEM}\right)_{ij}^2}}100\% \tag{3.44}$$

where indices ANA and FEM stand for the magnetic field calculated with the help of the analytical and the FEM solution at ij sensor position, respectively.

Table 3.3 shows relative total errors calculated for various amplitudes of the interface distortion when the sensor array is defined on $N_a \times N_z = 72 \times 21$ rectangular grid of points. It can be seen that the calculated errors are very large for almost all modeled

Table 3.3: Analytical solution - total relative errors

Mode	$\delta_r^{\%}$ $A[\text{mm}]$			$\delta_z^{\%}$ $A[\text{mm}]$		
	1.0	2.5	7.0	1.0	2.5	7.0
11	1.0	2.4	6.7	2.1	4.9	14.0
12	14.1	35.5	99.4	22.5	56.8	165.0
13	43.0	73.7	89.6	68.5	129.0	170.7
21	0.9	2.2	6.8	1.7	4.3	13.5
22	6.6	17.4	69.0	11.1	29.1	111.3
23	18.8	40.5	65.8	30.7	68.3	119.8

interfaces (except interfaces defined by modes η_{11} and η_{21}). Sample 1D distributions of

magnetic field components around the distorted interface described by the mode η_{13} are plotted at one sensor row located at $z = 0$ and $r = 35\,\text{mm}$ (Fig. 3.12 and 3.13).

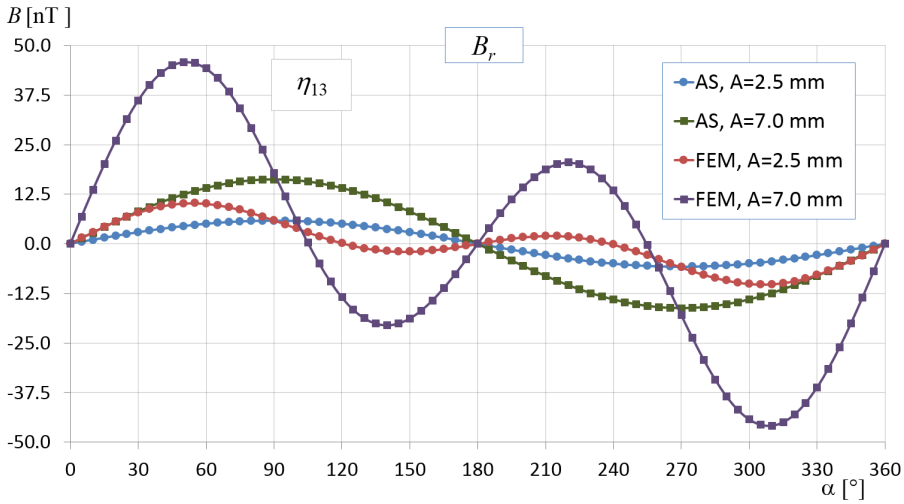

Fig. 3.12: Analytical (AS) versus FEM solution for interface mode η_{13} - distribution of B_r around cylinder in one row of sensors located at $r = R + d = 35\,\text{mm}$ and $z = 0$

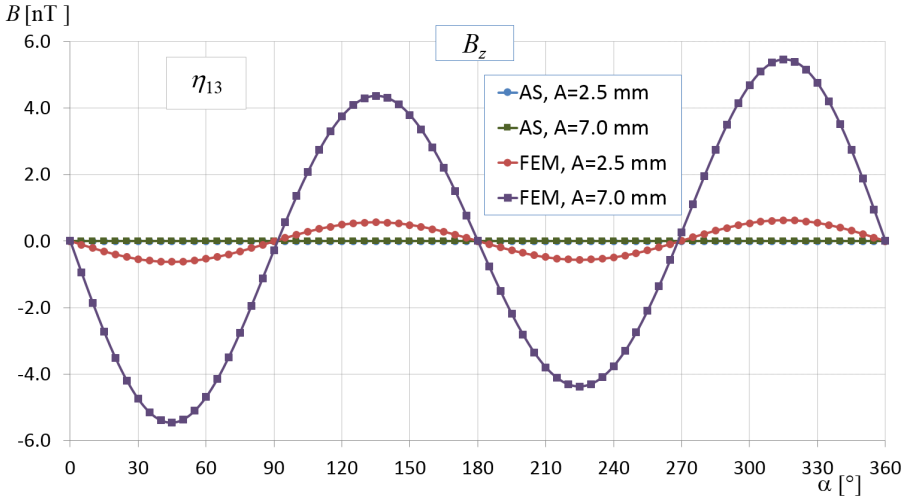

Fig. 3.13: Analytical (AS) versus FEM solution for interface mode η_{13} - distribution of B_z around cylinder in one row of sensors located at $r = R + d = 35\,\text{mm}$ and $z = 0$

The first are analyzed distributions of magnetic field for cases when formulas (3.39) - (3.41) are applied (analytical solution). It is perceived that 1D distributions of the magnetic field are sinusoidal with a spacial period $2\pi/m$, where m is the azimuthal mode number of the oscillating interface. The amplitudes of these distributions linearly

dependent on the maximum elevation of distorted interfaces, i.e when the maximum elevation of the analyzed interface is p times greater than the maximum elevation of the reference distortion then, the corresponding magnetic field values are also p times greater than the reference one, respectively. The similar effect can be observed for the relative total error at low order interface modes where the total error almost linearly rises with the elevation amplitude (see Table 3.3). Another feature of magnetic field distributions based on the analytical solution is the lack of z component of the magnetic flux density at the equilibrium plane $z = 0$. All above features are the consequence of flattening of the interface distortion to the equilibrium position and applying conditions (3.35) and (3.36) in the analytical approach. On the other hand, in FEM results, magnetic field distributions follow the outline of the distorted interface on the cylinder wall, i.e., positions of magnetic flux density components maximums depend on the interface elevation amplitude and are located outside $z = 0$. This is the reason why no linear relation can be found between magnetic field distributions for the same interface mode but with a different elevation amplitude. Additionally, it can be observed the non-zero B_z component at sensors placed in one row corresponding to the interface equilibrium position $z = 0$ (Fig. 3.12). The modified analytical approach has been proposed in [156] to improve results the quality of the analytical method. In the modified approach, some additional terms are added to the original analytical solution corresponding to harmonics found in the spatial Fourier analysis of magnetic flux density distributions received from the FEM calculations. Although the modified approach reduces errors of calculated magnetic field distributions, it is still restricted to small elevation amplitudes $A < 2.5\,\text{mm}$.

Finally, it can be concluded that if a large range of elevation amplitudes of distorted interfaces is considered the only procedure which can be applied for the interface reconstruction algorithm is the routine based on the finite element method because the analytical approaches give magnetic field distributions far away from the reality.

3.3. INTERFACE SHAPE RECONSTRUCTION - DOMINANT MODE IDENTIFICATION

In this section, some methods applicable to the solution of the interface reconstruction problem formulated in Section 3.2. are presented. First, the problem is defined in more details. It is assumed that the elevation of the interface between two immiscible fluids located in the cylindrical tank can be fully described by (3.24). Therefore, the general interface reconstruction problem can be reduced in fact to the identification of coefficients A_{mn} in (3.24). The choice of the highest azimuthal (M) and radial (N) mode numbers in the expression (3.24) used during the reconstruction process depends strongly on a configuration of applied magnetic sensor system. If only simulations are considered, this choice is not critical because any configuration of sensors can be applied as it is necessary. In consequence, M and N are assigned to relatively high values. However, in the reality, as the construction of the real measurement system has to be taken into account it is not possible to use so many sensors as necessary because of the design constrains and the cost of system implementation. Above limitations restrict significantly the possible choice of the highest mode numbers in the expression (3.24). In the

analyzed implementation, the system consists of 8×2 magnetometer sensors evenly distributed around the cylindrical cell which enables to measure two components of the magnetic flux density at one measurement point, i.e., the radial, B_r and the axial, B_z component.

Figure 3.14 shows the configuration of 2D-magnetometer sensors used in the analysis with sensors schematically represented by two perpendicular solenoids.

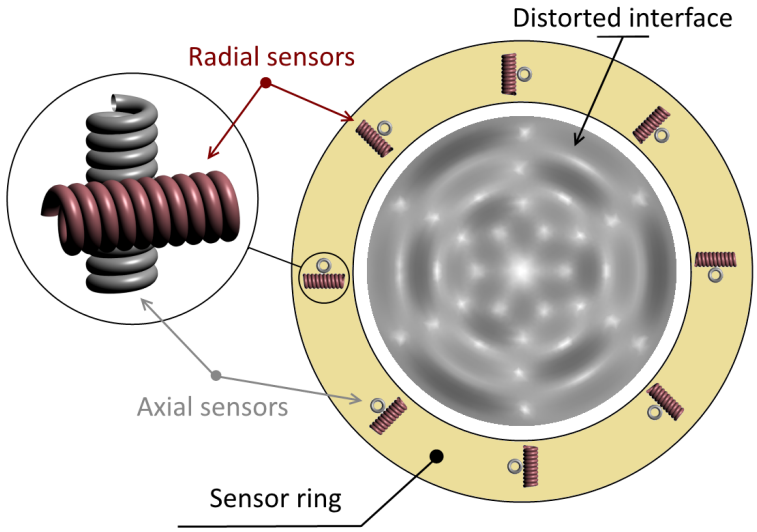

Fig. 3.14: Configuration of evenly distributed magnetometer sensors mounted on the sensor ring used during simulations (average distance of sensors COG to z-axis equals $r = 40\,\text{mm}$)

In order to simplify the analysis even more, the general problem of the interface shape reconstruction between two conducting fluids is reduced to the identification of the interface dominant mode. In other words, the only one coefficient in (3.24) which corresponds to the dominant mode in the oscillating interface is searched. The algorithm of full interface reconstruction based on genetic algorithms can be found in [76]. The dominant mode identification approach can be treated as a first shot method of finding the general shape of the interface and can be further connected with the method presented in [76]. All methods which are presented here have one common feature, they are non-gradient methods, i.e., they are not using descent derivatives in the successive minimization steps. Additionally, they reach the solution much faster as the general reconstruction algorithm [76]. Three methods will be presented: the first one based on a simple genetic algorithm [49], the second one using the direct search approach [157], and the third one applying the correlation between measured/simulated signal and signals stored in the previously calculated data-base [151].

Before describing the methods, the analysis of magnetic flux density profiles recorded or simulated by the measuring system shown in Fig. 3.14 is presented to determine the limitations of the applied system.

3.3.1. SIGNAL PROFILES AND LIMITS OF MEASUREMENT SYSTEM

Because the oscillating interface at the maximum elevation moment produces the maximum distorted magnetic field, it is enough to analyze profiles of magnetic flux density distributions for this moment only. The magnetic sensors are evenly distributed around the cylinder and fixed on a printed board which has a ring form (Fig. 3.14 and 3.15). The axial and azimuthal position of the ring are controlled by two parameters: z_0−distance and α_0−angle relative to the coordinate system used in the interface modeling.

Figure 3.15 shows a sample distribution of the radial component of magnetic flux density calculated for the maximum elevation of the oscillating interface described by mode η_{13} with the amplitude $A = 7\,\text{mm}$. The sensor ring is located in the middle of the

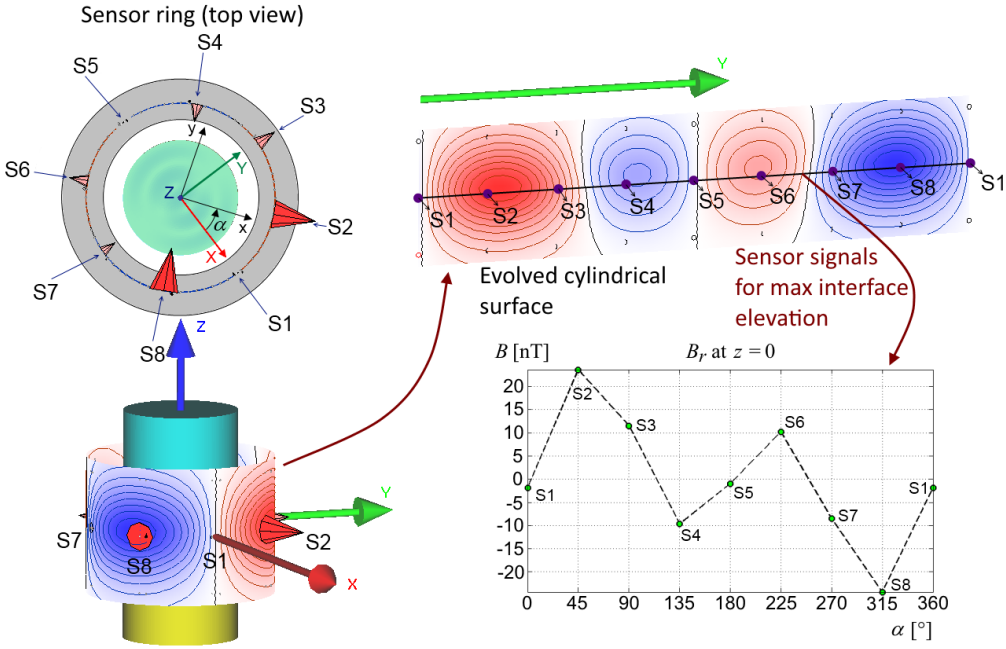

Fig. 3.15: Sample B_r signal simulated at $z = 0$ for the moment of maximum interface elevation described by the mode η_{13} ($A = 7\,\text{mm}$). Relative angular position of the sensor ring in relation to the cell coordinate system equals $\alpha_0 = 0$

cell ($z_0 = 0$) and the coordinate system of the sensor ring coincides with the coordinate system of the cell ($\alpha_0 = 0$).

Determination of characteristic features of B_r, B_z signals based on a direct analysis of signal profiles is not straightforward especially if you notice significant changes of the profile with a variation of the azimuthal position of the sensor ring.

Figure 3.16 shows a sample distribution of the radial component of the magnetic flux density calculated for two azimuthal positions of the sensor ring, $\alpha = 0$ and $\alpha = 20°$, produced in the vicinity of the oscillating interface and corresponding to the maximum

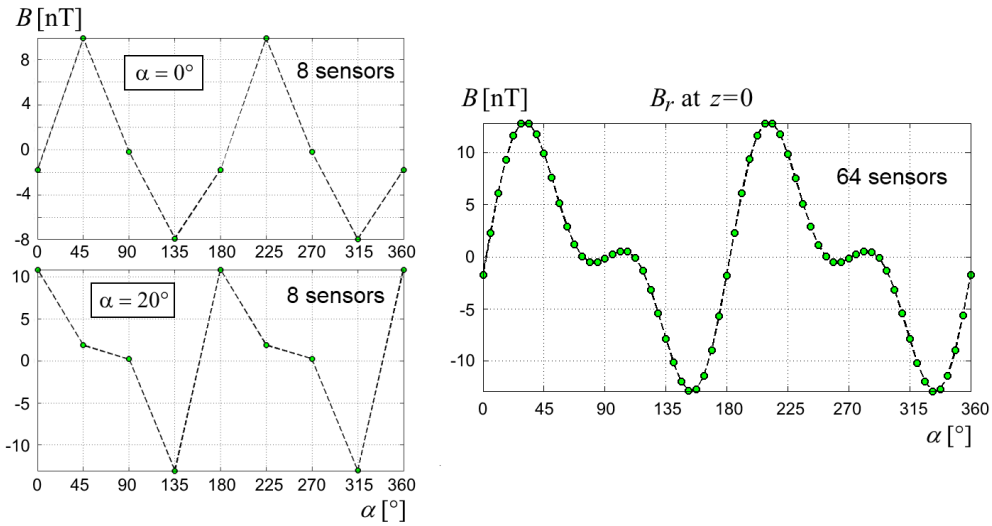

Fig. 3.16: Signal profiles of radial component B_r simulated at $z_0 = 0$ for the moment of maximum interface elevation defined by the mode η_{23} ($A = 7\,\text{mm}$). Ring with 8 sensors at two azimuthal positions: $\alpha_0 = 0$ and 20° (*left*), ring with 64 virtual sensors at $\alpha_0 = 0$ (*right*)

elevation of mode η_{23} with the amplitude equals $A = 7\,\text{mm}$. The distribution of B_r component simulated for the sensor ring with 64 virtual sensors is also shown for comparison.

The features of used signals can be identified much easier if the analysis is performed in a spatial frequency domain. Switching to the spatial frequency domain can be realized by applying the spatial Fourier transform to simulated/recorded distributions of magnetic flux densities around the cylindrical cell. Because all signal profiles are periodic with a spatial period equals $T_0 = 2\pi/m$, resulting Fourier transforms are given as series of complex coefficients describing discrete harmonics of the signal that are an integer multiple of the fundamental frequency $f_0 = 1/T_0$.

In fact, instead of continuous Fourier transform, only a spatial discrete Fourier transform (DFT) can be performed using a sequence of magnetic flux densities calculated at N_s sensor positions located on the sensor ring and treated as discrete samples representing the original signal. In this sense, the spatial sampling frequency is defined by the number of sensors N_s and is equal to $f_s = N_s f_0$. Using the Nyquist-Shannon sampling theorem [100, 118] the upper bound for harmonics of the signal is determined to allow its perfect reconstruction as $f < f_s/2$. The upper bound of the perfect signal reconstruction is called the Nyquist frequency and is denoted as $f_N = f_s/2$. In the analyzed case, the number of sensors and the Nyquist frequency are equal to $N_s = 8$ and $f_N = 4f_0$, respectively. It means that only signals with frequency spectrum limited to the first three harmonics can be perfectly reconstructed by the system. As an ideal signal reconstruction it is understood the inverse Fourier transformation which gives

correct real signals at sensors from calculated discrete Fourier transforms independent on the used azimuthal position of the sensor ring.

To study frequency contents of signal profiles produced by various interface shapes defined by single interface modes, the amplitude spectra are calculated for the following interface modes: η_{ij} where $i = 1 \ldots 3$, $j = 1 \ldots 3$. In calculations of signal spectra, the `fftw_plan_dft_r2c_1d` procedure (1D DFT for real input and complex output) from FFTW library is used. The FFTW library is a collection of fast C-routines for computing the discrete Fourier transform [38]. The real-input ($r2c$) DFT in FFTW of a 1D real array x of size N computes a forward Fourier transform $\underline{X}$ according to:

$$\underline{X}[k] = \sum_{n=0}^{N-1} x[n] e^{2\pi njk/N}, \quad j = \sqrt{-1} \tag{3.45}$$

FFTW computes an unnormalized transform, where is no coefficient in front of the summation in the DFT. In other words, applying the forward and the backward transform sequentially will multiply the input by N. The output complex array $\underline{X}$ posses the Hermitian symmetry:

$$\underline{X}[k] = \underline{X}^*[N-k] \tag{3.46}$$

where $\underline{X}$ is assumed to be periodic so that $\underline{X}[N] = \underline{X}[0]$. As a result of this symmetry, half of the output is redundant (being the complex conjugate of the other half), and therefore the FFTW calculates only output elements $0 \ldots N/2$ of $\underline{X}$ ($N/2+1$ complex numbers), where the division by 2 is rounded down, saving computation time and used memory. Moreover, the Hermitian symmetry implies that $\underline{X}[0]$ and, if N is even, the $\underline{X}[N/2]$ elements are purely real [38].

First, 64 virtual sensors are used to assure that all significant harmonics of the analyzed signals are found. Figures 3.17 and 3.18 show calculated amplitude spectra for radial and axial components of the magnetic flux density using the virtual 64-sensor ring located at $z_0 = 0$. It can be observed that the index of the dominant harmonic in B_r amplitude spectrum corresponds to the azimuthal index i of the analyzed interface mode. However, this is not the case for B_z amplitude spectra, where the index of the dominant harmonic follows a multiple of the azimuthal index i, generally. Using the Nyquist frequency equals $f_N = 4f_0$, it can be stated that for the 8-sensor ring the perfect reconstruction of signal profiles is only possible for the following modes: η_{11}, η_{12}, η_{13}, η_{21}, and η_{31} for B_r component and η_{11}, η_{12}, η_{13} for B_z component. Figures 3.19 and 3.20 depict amplitude spectra of the same signals as above but calculated using the 8-sensor ring. It can be observed that the spectra of signals where the perfect reconstruction with 8 sensors is possible remain unchanged whereas the spectra of signals for which the perfect reconstruction is not possible are quite different. Especially, the spectra of signals for the interface described by modes η_{2x} are quite similar because for all these modes, frequencies of some significant harmonics are located at or above the Nyquist frequency and therefore they are eliminated when the analysis is carried out using only 8 sensors. This also explains why the distinction of some modes in the process of the dominant mode identification is very difficult.

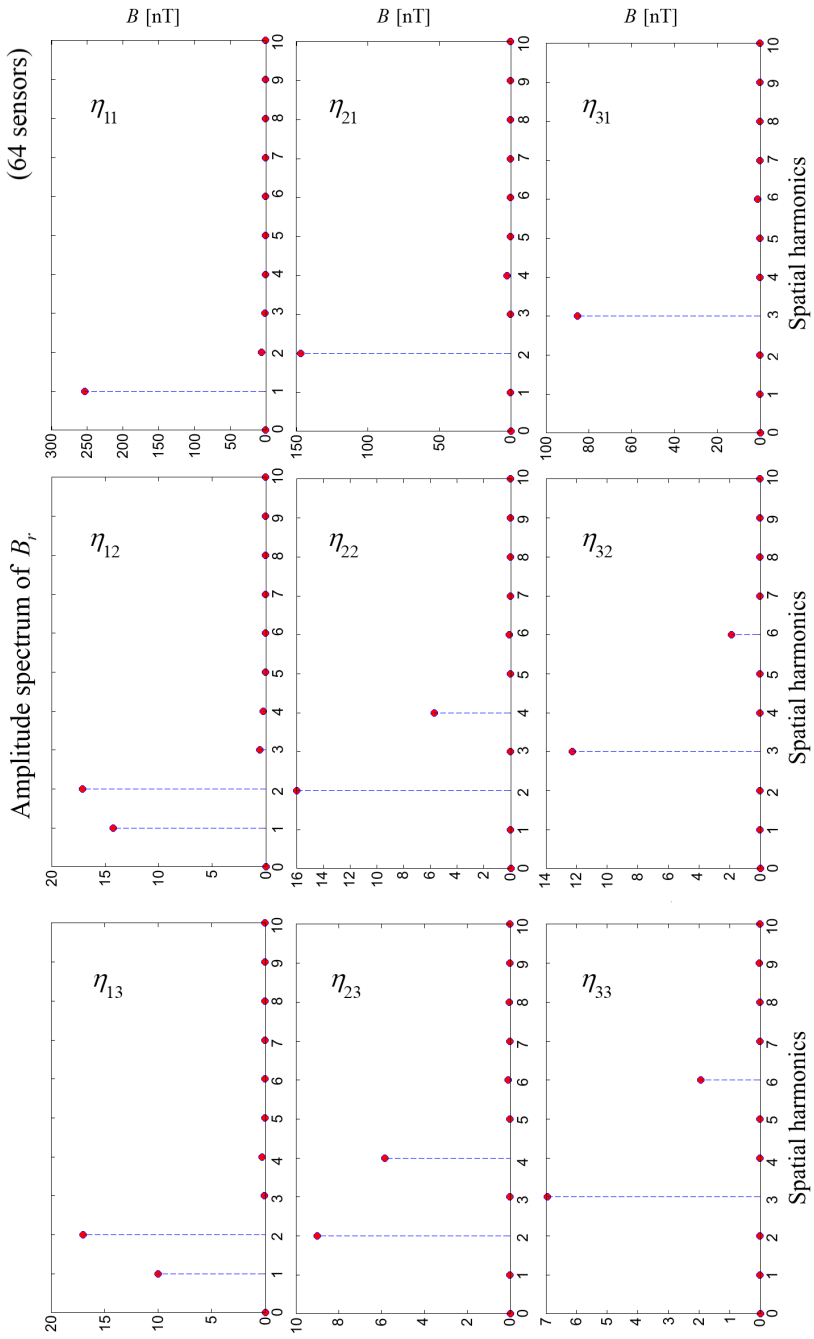

Fig. 3.17: Modes η_{11} - η_{33}: amplitude spectra of radial component of magnetic flux density for 64 virtual sensors evenly distributed around the cylinder at $z_0 = 0$ and $r = R + d = 40\,\text{mm}$

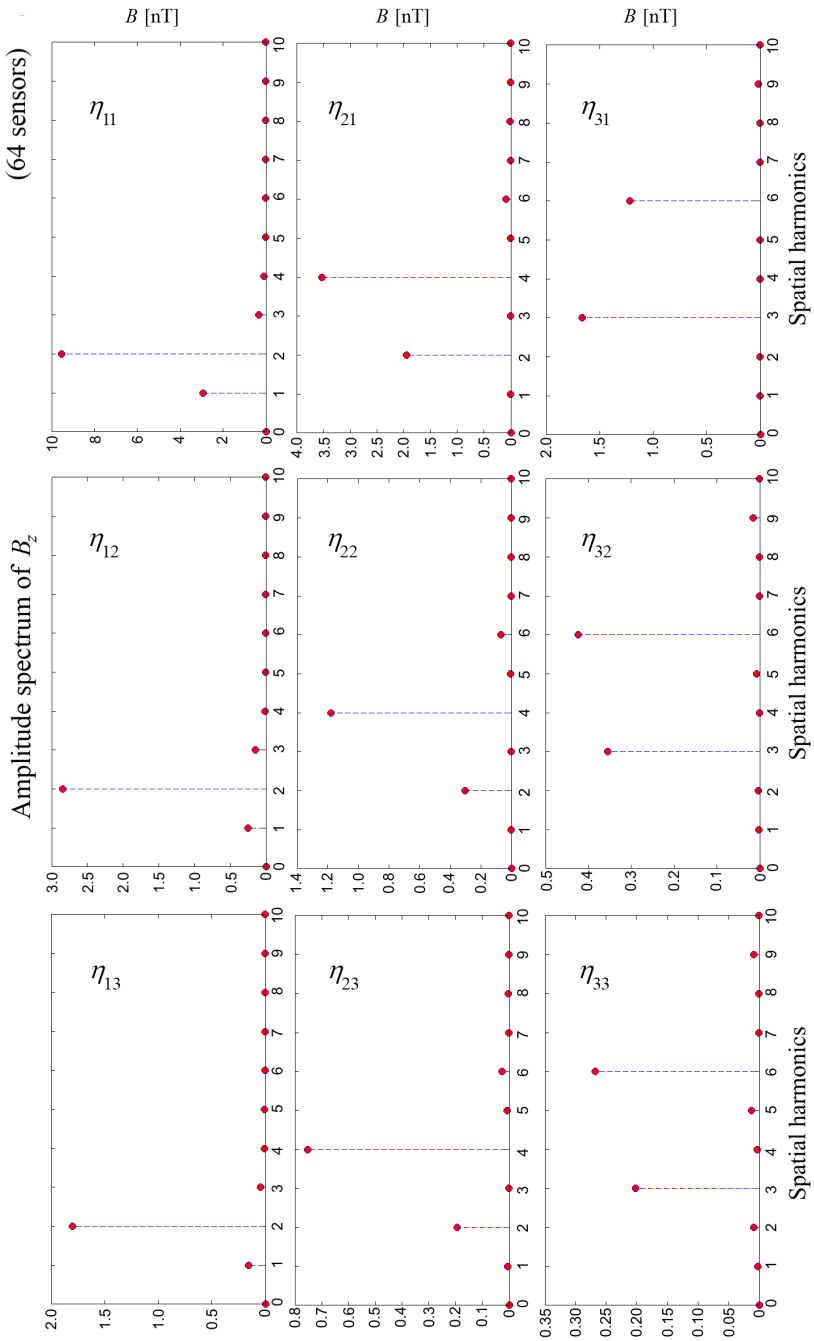

Fig. 3.18: Modes η_{11} - η_{33}: amplitude spectra of axial component of magnetic flux density for 64 virtual sensors evenly distributed around the cylinder at $z_0 = 0$ and $r = R + d = 40\,\text{mm}$

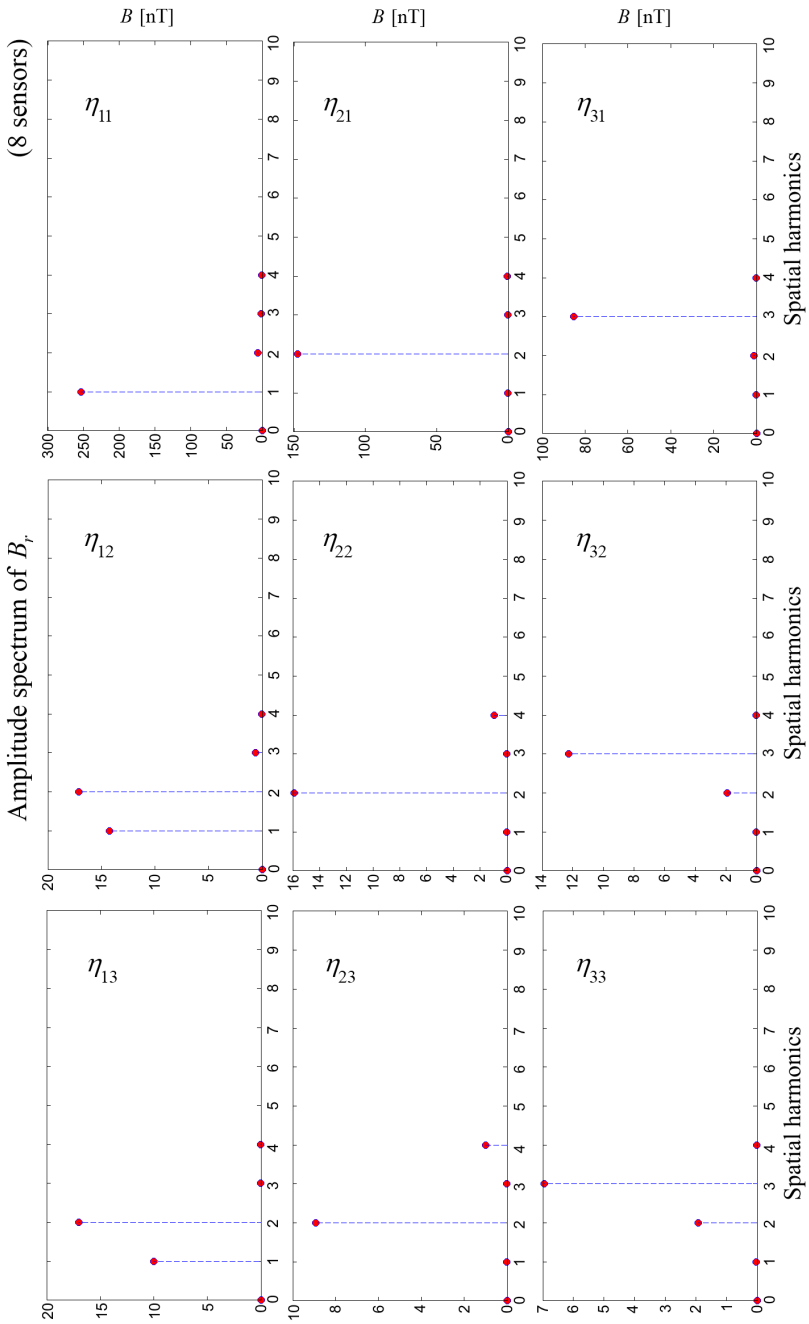

Fig. 3.19: Modes η_{11} - η_{33}: amplitude spectra of radial component of magnetic flux density for 8 sensors evenly distributed around the cylinder at $z_0 = 0$ and $r = R + d = 40\,\text{mm}$

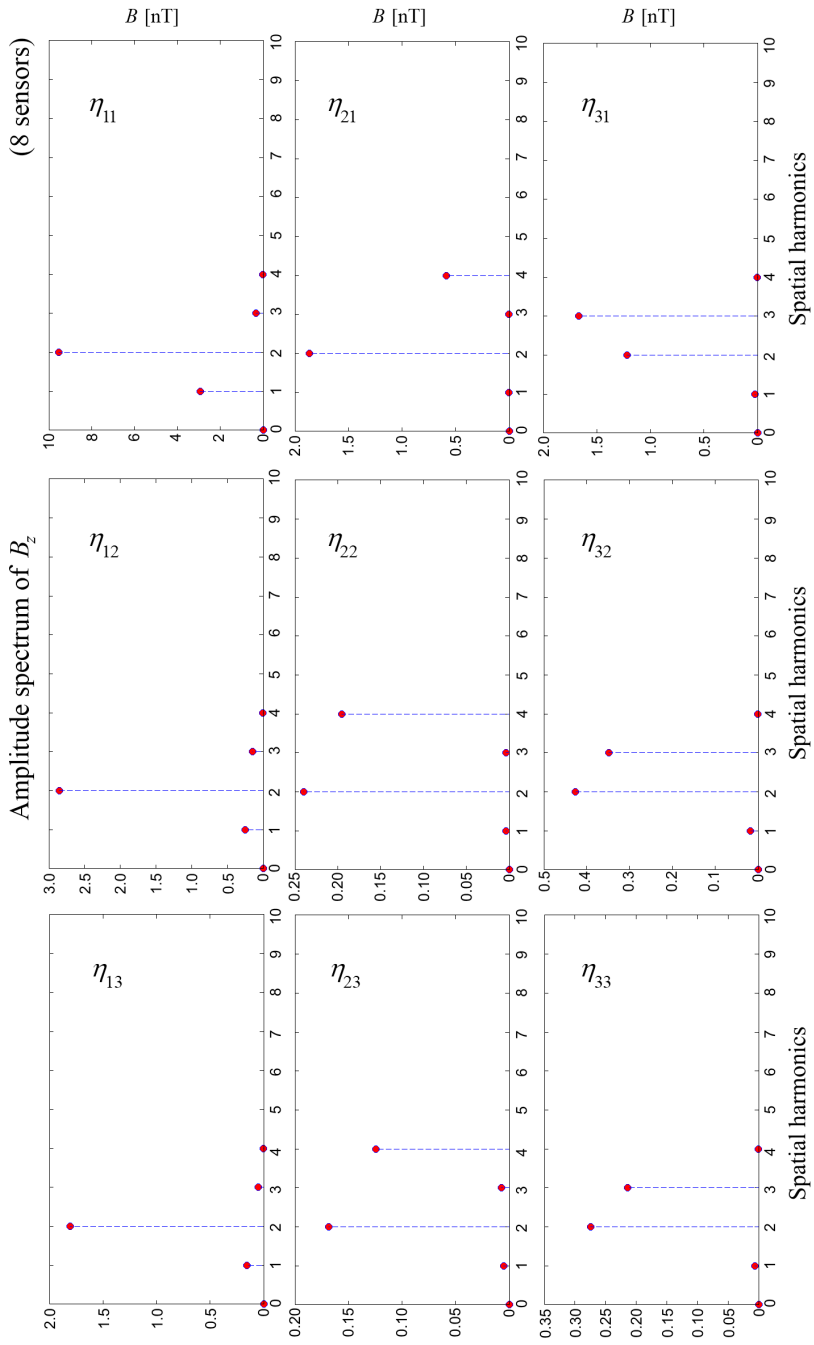

Fig. 3.20: Modes η_{11} - η_{33}: amplitude spectra of axial component of magnetic flux density for 8 sensors evenly distributed around the cylinder at $z_{=}0$ and $r = R + d = 40\,\text{mm}$

It can also be noticed an interesting feature of the DFT for modes η_{32} and η_{33}. The original spectra of the signals corresponding to these modes contain sixth harmonic which cannot be detected in the case of using the ring with 8 sensors. Instead of the sixth harmonic, the second one is observed which in fact does not exist in the original spectra! The appearance of spurious frequencies as mirror reflections with respect to the Nyquist frequency is called aliasing or folding back effect, e.g., if $f_N = 4f_0$ is the Nyquist frequency, then the sixth harmonic reflects against f_N with a frequency difference $\Delta f = f_6 - f_N = 2f_0$ and is visible in the spectrum as the second harmonic. Generally, the folding back effect should be eliminated because spurious harmonics can influence real harmonics for more complex signals. However, if the problem deals only with signals corresponding to the oscillating interface described by pure modes one can try to use the folding back effect in the reconstruction process. Nevertheless, this procedure should be applied with a special care because the risk of wrong signal reconstruction is relatively high.

3.3.2. SIMPLE GENETIC ALGORITHM

Although a genetic algorithm (GA) is not the fastest method which can be applied to the identification of the dominant mode in the oscillating interface it is presented here to show its main idea and important steps of its implementation. A specific terminology associated with genetic algorithms is also clarified , e.g. genome/chromosome, population, generation, etc.

The genetic algorithm is a method for solving optimization problems that tries to simulate natural selection, the process that drives biological evolution. The genetic algorithm repeatedly modifies a population of individual solutions. At each step, the genetic algorithm selects individuals at random way from the current population (parents) and uses them to produce the next generation (children). Over successive generations, the population evolves toward the best solution defined as the minimum/maximum of predefined cost function. The genetic algorithm uses three main operators at each step to create the next generation from the current population:

- *Selection* operator, which selects the individuals that contribute to the population at the next generation,
- *Crossover* operator, which combines two parents to form children for the next generation,
- *Mutation* operator, that applies random changes to individual parents to form children.

To apply genetic algorithms it is necessary to think first about the genome/chromosome representation which corresponds to the problem. Each genome/chromosome instance represents a single solution of the problem so it is up to the user to define which parameters should be included in the representation and how they should be coded. Next, genetic operators listed above have to be defined to determine how the

evolution should run. At the end, the objective/cost function must be defined to determine how good or bad is the individual solution (genome/chromosome) in the evolution process. Usually, cost functions are not used in the genetic algorithm directly. Instead of direct using of cost values delivered by cost functions, GA uses so called fitness function which scales raw costs to find the fitness of genomes for mating. There are many types of genetic algorithms. In the analysis, a standard simple genetic algorithm (SGA) described in [49] is applied. The simple genetic algorithm uses non-overlapping populations and optional elitism. Elitism ensures the propagation of the best genome (solution) between generations without disruption by crossover or mutation operator. The default selection operator in SGA is the roulette wheel selection where the probability of selection is proportional to a fitness score of the individual genome. In the standard SGA the genome is represented as a string of bits. SGA uses a single point crossover operator, i.e., a single crossover point on two genome strings (parents) is selected and all data beyond that point is swapped between them producing two new genome strings (children). The crossover operator is defined by crossover probability.p_c Typical values of p_c are in the range between 0.4 and 0.9. If $p_c = 0.5$ then half of the new population is formed by selection and crossover and half by selection only. The mutation operator checks every bit position in the genome, reversing the bit value depending on the mutation probability p_m. Typical value of the mutation probability is of the order 0.001, but as all parameters in GA it is problem dependent. Other typical values of p_m can be estimated as $p_m \sim 1/L$ or $p_m \sim 1/N\sqrt{L}$ taking into account the bitwise genome length L and the number of genomes N in the population [25].

In the proposed implementation of SGA, a C++ library of genetic algorithms GAlib created at the Mechanical Engineering Department of MIT [133] is applied. GAlib includes tools for using genetic algorithms to do optimization in any C++ program using any representation and any genetic operators. The GAlib source code is not in the public domain, but it is available at no cost for non-profit purposes.

To solve the identification problem of the dominant mode in the oscillating interface between two conducting fluids using the simple genetic algorithm it is necessary to define the genome corresponding to a single solution of the forward problem described in Section 3.2.3.. The genome must contain enough information about the interface and the sensors so that the forward problem can be solved by means of TFEM3D. In the considered problem, a simple generic binary genome `GABin2DecGenome` from GAlib is applied. The genome implements the traditional method of converting binary strings to decimal values based on binary-to-decimal mapping. To use this genome, it is necessary to specify how many bits will be used for the representation of chosen parameter together with the range of mapped parameter values.

The representation of various dominant interface modes in SGA can be expressed through their indexes (radial and azimuthal) and corresponding amplitudes. In fact, it is not necessary to code both mode indexes independently. It is more effective to substitute the double index of the mode η_{ij} with the single index $k = (i-1)N + j - 1$, where N is the number of available interface radial modes, and then use it in SGA. The index k is mapped on a binary string with a length L of 4 bits. It allows to code an index for maximum 16 interface modes. In the analysis, according to the previous

section, the range of interface modes is restricted to the first 3 azimuthal and the first 4 radial numbers, i.e., $\eta_{ij} : i = 1 \ldots 3, j = 1 \ldots 4$. The range of mapped index k in this case is set to $[0, 11]$. The elevation amplitude of the interface is coded in a binary string of the same binary length as the string used for the index k. The amplitude range is defined as $[A_{min}, A_{max}] = [4.0\,\text{mm}, 16.0\,\text{mm}]$ to cover all expected amplitudes of the oscillating interface. The amplitude resolution δA is equal to $\delta A = (A_{max} - A_{min})/(2^L - 1) = (16 - 4)/15 = 0.8\,\text{mm}$. As it can be seen, the amplitude resolution is not very high. The reason for choosing so short binary string for the amplitude representation is the fact that the identification of the dominant mode should be done as quickly as possible even at the expense of the amplitude estimation accuracy. The precise value of the amplitude can be estimated later by a different method when the dominant mode of the interface is already found e.g. by the direct searching method.

To illustrate a structure of applied genomes, the sample genome for the interface mode η_{13} oscillating with the amplitude $A_{13} = 7.2\,\text{mm}$ is shown. The index k of mode η_{13} is equal to $k = (1 - 1)4 + 3 - 1 = 2$ and is coded as '`0010`' binary string. This is the first part of the used genome. The binary code of the amplitude is calculated using formula: $\texttt{int}[(A_{13} - A_{min})/\delta A] = \texttt{int}[(7.2 - 4.0)/0.8] = 4 = 0100_2$ and is stored as '`0100`' binary string. This is the second part of the genome. After concatenation of both strings, the binary genome '`0010 0100`' representing the mode η_{13} is ready to use in SGA. It is obvious how to construct the reverse decoding procedure of the interface mode indexes ij and the corresponding amplitude from the binary genome representation.

After construction of the genome, a cost function (objective function) has to be defined to evaluate a goodness of individual solutions, i.e., the function for which smaller values correspond to better fitting solutions. The following example will show how important is to select the appropriate definition of the cost function.

Two cost functions C_{F1} and C_{F2} with different way to take account of the magnetic flux density components are defined, namely:

$$C_{F1} = \sqrt{\sum_{c=r,z} \frac{\sum_{i=1}^{N_s} (B_{ci} - B_{ci}^0)^2}{\sum_{i=1}^{N_s} (B_{ci}^0)^2}} 100\% \tag{3.47}$$

$$C_{F2} = \sqrt{\frac{\sum_{c=r,z} \sum_{i=1}^{N_s} (B_{ci} - B_{ci}^0)^2}{\sum_{c=r,z} \sum_{i=1}^{N_s} (B_{ci}^0)^2}} 100\% \tag{3.48}$$

where index c denotes radial (r) or axial (z) component, N_s is the number of used sensors, and B_{ci}, B_{ci}^0 are calculated and reference components of the magnetic flux density at sensor positions, respectively. B_{ci} values correspond to the actual genome and are calculated using TFEM3D program described in Section 3.2.3.. The reference magnetic flux components B_{ci}^0 are simulated or measured and relate to the maximum

elevation of the oscillating interface which should be identified. In the cost function C_{F1}, the influence of all components of the magnetic flux density is taken into account with equal weights regardless of their absolute values. In the cost function C_{F2} the impact of individual components is reduced by grouping them together in the numerator and denominator.

Table 3.4 shows sample signals measured by 8 sensors evenly distributed around the cylindrical cell (Fig. 3.15) produced by the oscillating interface defined by one dominant mode and corresponding to its maximal elevation. The reference signal is calculated for the interface mode η_{33} and the amplitude $A = 7\,\text{mm}$ using the fine FEM cell model ($d_E = 1\,\text{mm}$). Signals in simulation 1 (mode η_{32}, $A = 5.2\,\text{mm}$) and 2 (mode η_{33}, $A = 7\,\text{mm}$) are calculated applying the fast FEM cell model ($d_E = 3\,\text{mm}$).

Table 3.4: Signals at sensors positions for sample dominant modes corresponding to the maximum interface elevation (in nT)

Sensor	*Mode 33* *Reference*		*Mode 32* *Simulation 1*		*Mode 33* *Simulation 2*	
	B_r	B_z	B_r	B_z	B_r	B_z
1	-1.39	-0.09	-1.55	-0.05	-1.24	-0.04
2	3.66	0.13	6.92	0.03	3.58	-0.16
3	-6.38	0.27	-10.00	0.15	-6.33	0.24
4	6.15	-0.43	7.06	-0.24	5.31	-0.19
5	0.41	-0.04	1.04	-0.01	0.38	-0.09
6	-7.38	0.41	-8.89	0.23	-6.60	0.17
7	7.37	-0.14	10.50	-0.08	7.19	-0.22
8	-2.43	-0.10	-5.07	-0.01	-2.28	0.21
	$C_{F1}[\%]$		65.8		79.7	
	$C_{F2}[\%]$		46.0		9.0	

Cost functions for signals obtained in the simulation 1 and 2 are calculated according (3.47) and (3.48). The received results (Table 3.4) show that the use of the cost function C_{F1} may lead to the elimination of the correct mode in the identification process because $C_{F1}^{32} < C_{F1}^{33}$ whereas the use of the cost function C_{F2} performs a correct validation of the analyzed modes $C_{F2}^{32} > C_{F2}^{33}$. For this reason, in further considerations, the equation (3.48) will be used as the basic definition of the cost function in the validation procedures.

Since the cost function C_F has to be calculated many times during the evaluation of SGA, the execution time of all procedures involved in that process, mainly TFEM3D, has to be extremely minimized. In the simplest way, this can be achieved by using appropriate FEM models of the cylindrical cell. If the finite element mesh is too dense,

the number of unknowns of the global equation system will grow up and this will result in increasing of the execution time of TFEM3D. On the other hand, if the finite element mesh is too simple, the results are received fast but with a low accuracy. In TFEM3D, the generation of finite element mesh is controlled using two parameters (see Section 3.2.3.): d_E, which defines the maximum size of 2D elements used in a generation of 2D cylindrical base slices and N_{SL}, the number of slices which determines density of 3D finite elements in the axial direction. The parameter d_E can be estimated if you notice that in the modeling of interface shapes, the approximation of Bessel functions in (3.24) is more critical than the approximation of azimuthal trigonometric functions. Using this fact, first, it is calculated the distance of the first maximum of the highest radial interface mode used in the SGA to the z-axis, i.e., the r-position of the first maximum of η_{ij} for $j = 4$. Then, under assumption that at least 3 finite elements are necessary to cover this distance, the limit value of d_E can be estimated. The limit value of d_E found for the cylindrical cell of radius $R = 25\,\text{mm}$ and the interface radial mode of order 4 is equal to $d_E \approx 2.4\,\text{mm}$. The necessary number of slices N_{SL} can be estimated from numerical experiments by observation how the quality of simulated magnetic signals is changing with decreasing of N_{SL}. It is found that using a combination of $N_{SL} = 16$ and $d_E = 3\,\text{mm}$ assures good compromise between the quality and the speed of calculations. For these parameters, the finite element mesh used in SGA consists of $N_e = 98560$ tetrahedral elements of the first order and $N_p = 22215$ nodes which results in average calculation time of the cost function for a single genome of around $0.2\,\text{s}$.

Before the first start of the SGA, the size of genetic material subjected to the evolution has to be defined, in other words, the number of genomes included in the population has to be given. If the population size is too small, the genetic algorithm may not explore enough of the solution space to find good solutions. Increasing the population size enables the genetic algorithm to search more variants and thereby obtain better results. However, the larger the population size, the longer the genetic algorithm takes to analyze each generation. Following [49], the appropriate population size N_{pop} for binary genomes can be estimated as:

$$N_{pop} \sim O\left(\frac{l}{m} 2^m\right) \tag{3.49}$$

where l is a binary length of applied genome string and m denotes an average number of bits per parameter. In the analyzed problem, l is equal to 8 (2×4 bits) and $m = l/2 = 4$ which results in the population size $N_{pop} = 2 \cdot 2^4 = 32$. Usually, the population size received from (3.49) is over-estimated and it can be reduced at least by factor 2.

Further, some results of the interface dominant mode identification performed by means of the simple genetic algorithm are presented. First, the reference data have been prepared by calculating components of the magnetic field at the sensor positions for the sensor ring with 8 2D-magnetometers (Fig. 3.14) located at $z = 0$ using the fine finite element model ($d_E = 1\,\text{mm}, N_{SL} = 50 : N_e = 3131100, N_p = 681166$). The following parameters of the cell model are used: $h = 100\,\text{mm}$ - cylinder height, $R = 25\,\text{mm}$ - cylinder radius, $\sigma_2 = 3.46\,\text{MS/m}$ - lower fluid conductivity, $\sigma_1 = 100\,\text{S/m}$ - upper fluid conductivity, and $J_0 = 509.3\,\text{A/m}^2 = 1\,\text{A}/(\pi R^2)$ - impressed current density at $z = h/2$. The radial and axial sensors are modeled as solenoids with the length of

15 mm and the radius equals 1.5 mm. The distance of solenoid centers to the wall of the cell is equal to 16 mm and 17 mm for radial and axial sensors, respectively. In all simulations, the azimuthal position of the sensor ring is set to $\alpha_0 = 0$.

Reference data have been prepared for a set of distorted interfaces described by various single modes ($\eta_{ij} : i = 1 \ldots 3, j = 1 \ldots 3$) with the same elevation amplitude equals $A_0 = 7$ mm. Additionally, the noisy data were simulated by adding a random white noise to the calculated magnetic flux density components with the level of 5% and 10% of the respective component maximum. During the SGA identification, cost function values (3.48) are calculated using TFEM3D and the reduced finite element model ($d_E = 3$ mm, $N_{SL} = 16$). After the identification of the dominant mode, to improve the accuracy of found amplitude, the precise amplitude tuning using a simple direct search method with a constant step equals $dA = 0.1$ mm is performed.

Tables 3.5, 3.6, and 3.7 show results of identifications for the following SGA parameters: $N_{pop} = 32/16/8$ - population size, $p_m = 0.125$ - mutation probability, $p_c = 0.8$ - crossover probability.

In all simulations, two components of the magnetic flux density (B_r, B_z) are used. Start populations in all simulations are chosen in a random way. To terminate the SGA process, two criteria are used: the maximum number of generations N_{gen} (set to 50) and the cost function threshold T_h (set to 10%). If the cost function value is below the defined threshold or the number of generations reaches the maximum, the SGA process is terminated.

In all tables, *RMode* denotes the reference dominant mode in the oscillating interface simulated by the fine finite element model whereas *IMode* is the mode identified by the SGA. A is the amplitude of the identified dominant mode. δA is the relative error of the estimated amplitude calculated as: $\delta A = 100\%(A - A_0)/A_0$. Values of the cost function C_F are calculated for estimated amplitudes after tuning according to (3.48). In columns CPU_{nn}, total time of SGA calculations including the amplitude tuning for the population size equals 32, 16 and 8 is presented, respectively.

Table 3.5: SGA dominant mode identifications - $Noise = 0\%$

RMode	*IMode*	A[mm]	δA[%]	C_F[%]	CPU_{32}[s]	CPU_{16} [s]	CPU_8[s]
11	11	7.0	0.0	0.36	19.7	16.2	9.2
12	12	7.1	1.4	2.50	56.6	14.6	14.7
13	13	7.2	2.8	2.85	37.8	14.3	58.2
21	21	7.1	1.4	0.37	10.2	19.3	18.7
22	22	7.9	12.9	2.46	14.8	10.1	7.2
23	23	7.8	11.4	5.32	75.6	16.1	52.4
31	31	7.1	1.4	0.48	75.5	84.4	12.3
32	32	7.6	8.6	2.42	20.2	67.4	13.3
33	33	7.6	8.6	6.41	20.3	89.9	36.1

Table 3.6: SGA dominant mode identifications - $Noise = 5\%$

RMode	*IMode*	A[mm]	δA[%]	C_F[%]	CPU_{32}[s]	CPU_{16}[s]	CPU_8[s]
11	11	7.0	0.0	2.28	19.7	16.2	9.2
12	12	7.1	1.4	3.24	102.8	14.6	14.7
13	13	7.2	2.8	2.95	65.9	14.3	58.1
21	21	7.1	1.4	1.81	10.2	19.3	18.7
22	22	8.1	15.7	2.80	14.2	9.5	7.8
23	23	7.9	12.9	6.32	94.1	46.6	52.1
31	31	7.2	2.8	2.32	19.2	61.9	57.8
32	32	7.5	7.1	2.98	19.9	43.9	13.6
33	33	7.6	8.6	5.85	20.3	87.3	36.1

Table 3.7: SGA dominant mode identifications - $Noise = 10\%$

RMode	*IMode*	A[mm]	δA[%]	C_F[%]	CPU_{32}[s]	CPU_{16}[s]	CPU_8[s]
11	11	7.1	1.4	4.91	19.6	15.4	14.7
12	12	7.0	0.0	5.09	47.8	16.0	12.8
13	13	7.3	4.3	4.80	38.0	14.8	58.6
21	21	7.2	2.8	3.56	9.9	24.2	32.8
22	22	8.0	14.3	5.15	14.5	10.0	7.5
23	23	7.9	12.9	7.13	130.8	69.0	28.7
31	31	6.8	-2.8	2.54	57.6	35.9	13.2
32	32	7.2	2.8	4.18	19.1	23.8	14.5
33	33	7.5	7.1	5.95	20.0	80.7	40.3

The results show that all performed SGA simulations were positive with a correct identified dominant mode. The elevation amplitude is estimated quite good (relative amplitude error $\delta A < 3\%$) for interfaces described by modes with spatial frequency spectra lying under Nyquist frequency (Section 3.3.1.), i.e., by modes η_{11}, η_{13}, η_{13}, η_{21}, and η_{31}. For interfaces described by remaining modes, found elevation amplitude is over-estimated which is, in fact, not so critical as the under-estimation. The correlation can also be observed between cost-functions values and the applied noise level, i.e., higher noise level results in higher minimum cost-functions values. Roughly, it can be said that the minimum values of the cost-function are equal to about 50% of the noise level for most identified dominant modes. However, this conclusion is only true for noisy signals in the presence of white noise.

Several other probability values of mutation and crossover have been tested with the elitism switched on or off. For the analyzed problem, the most significant was a suitable choice of the mutation probability. If the mutation probability is not big enough the diversity of genomes in successive generations is too small especially concerning mode indexes and results in a false dominant mode identification. Choosing the mutation probability according criterion: $p_m = 1/L$, where L is the bit length of used genomes, was the best choice. The choice of the crossover probability is less critical. It affects only the calculation time but not the correct identification of the dominant mode. Switching off the elitism, i.e., switching of the propagation of the best genome to the next generation has similar effect.

The analysis of the influence of the population size on the calculation time (CPU) shows that using criterion (3.49) provides over-estimated population size. In the analyzed problem, the population size can be chosen even 4 times smaller maintaining the positive identification of the dominant mode and reducing the calculation time. An average execution time of one identification of the interface dominant mode is calculated as the average time of all performed simulations ($Noise = 0, 5, 10\%$) and is equal to 39.0, 34.6, and 28.0 s for $N_{pop} = 32, 16$, and 8, respectively.

Using in the SGA only B_r component of the magnetic flux density instead of two components (B_r, B_z) does not change significantly the results presented in the above tables. Only minima of cost-functions reach smaller values which is obvious if you look at the position of the sensor ring located at $z = 0$. At this position, B_r component is much greater than B_z one (see Fig. 3.11), which means, its contribution to the cost function (3.48) is dominant. Thus, if the sensor ring is located at $z = 0$, it is enough to use only radial component of the magnetic flux density for identifying the dominant mode in the oscillating interface.

The presented implementation of the identification of the dominant mode in the oscillating interface has one restriction: the exact azimuthal position of the sensor ring in relation to the cylinder cell coordinate system has to be known. In numerical simulations, this is not a problem because the correct position of the sensor ring according to the simulated signals can always be set. However, in a real experiment it is not so easy to find the precise azimuthal position of the sensor ring. Genetic algorithm makes it possible to find the solution to the problem of finding the azimuthal position of the sensor ring in a quite simple way. Simply, the actually used genome has to be expanded about one additional parameter with the information about the azimuthal position of the sensor ring. For this purpose, the binary string of encoded azimuthal angle with a length of 4 bits is added to the actual genome. The range of azimuthal angles is set to $[0, 45°]$ which covers the angular distance between two successive sensors on the sensor ring with an angular resolution $\delta\alpha$ equals 3°.

Table 3.8 presents sample results of identifications of dominant modes for simulated noisy magnetic flux density signals ($Noise = 5\%$) calculated for the azimuthal position of the sensor ring equals $\alpha_0 = 20°$. The modified SGA described above has been applied with the following parameters: $N_{pop} = 8$, $p_m = 0.2$, $p_c = 0.8$, and $N_{gen} = 50$. In the column α, the azimuthal positions of the sensor ring found by the modified SGA are given.

Table 3.8: SGA identifications - unknown azimuthal position of sensors - $Noise = 5\%$

RMode	*IMode*	A[mm]	$\alpha[^\circ]$	C_F[%]	CPU_8[s]
11	11	7.0	21.0	1.77	30.0
12	12	7.1	21.0	4.00	51.6
13	13	7.3	21.0	3.88	120.7
21	21	7.1	21.0	2.78	31.0
22	22	7.3	21.0	4.30	56.2
23	23	7.7	18.0	9.25	120.5
31	31	7.1	21.0	5.09	118.8
32	32	7.5	21.0	4.88	73.1
33	33	7.3	21.0	8.39	120.8

All found azimuthal angles are close to the reference angle $\alpha_0 = 20^\circ$ within the accuracy of the azimuthal angle resolution $\delta\alpha = 3^\circ$. The average identification time is equal to about 80 s which is almost 3 times longer than the average time of identifications with known position of the sensor ring.

So far, after the SGA, the simple direct search method is additionally applied for the amplitude correction to find the amplitude with the minimum cost function (3.48). However, this procedure is not effective if the azimuthal position of the sensor ring is unknown. To improve the identification quality in a better way, the SGA has to be applied once more. It is enough to modify the structure of the genome, because in the second SGA run, the dominant mode is already known. Additionally, the resolution of searching parameters can be improved by narrowing ranges of the searching amplitude and the azimuthal angle. The genome consists now of two binary strings with the length of 4 bits each corresponding to the amplitude and the azimuthal angle. The ranges of parameters can be selected on the basis of identification results and set to $[6.5\,\text{mm}, 8\,\text{mm}]$ and $[18^\circ, 20^\circ]$ for the amplitude and the azimuthal angle, respectively. Narrowing SGA search scopes results in better resolution of sought parameters, i.e., $\delta A = 0.05\,\text{mm}$ and $\delta\alpha = 0.2^\circ$.

Table 3.9 presents results of amplitude and azimuthal position searching for sample set of oscillating interfaces with added 5% white noise using the above formulated SGA. It can be observed that all cost functions reach smaller values than in Table 3.8. For almost all modes, the rule saying that in the presence of white noise minimal values of the cost function are equal about 50% of the introduced noise can be applied. It can also be noticed that found amplitudes remain almost unchanged compared to the previous implementation of SGA whereas the azimuthal angles are closer to the reference azimuthal position of the sensor ring ($\alpha_0 = 20^\circ$).

Table 3.9: Precise SGA identifications of amplitude and azimuthal angle - *Noise* = 5%

IMode	A[mm]	$\alpha[^\circ]$	C_F[%]	CPU_8[s]
11	7.0	20.8	1.68	7.8
12	7.1	20.2	3.05	119.6
13	7.3	20.2	2.78	117.6
21	7.1	20.2	1.04	16.9
22	7.5	19.8	2.32	117.1
23	7.5	19.8	8.16	115.0
31	7.1	20.2	1.96	16.2
32	7.5	20.0	1.81	7.4
33	7.3	20.0	5.81	116.6

Parameters of test signals and signals found by the SGA together with the corresponding cost functions are presented in Table 3.10 to explain why the precise SGA finds other values than the reference parameters A_0 and α_0. Test signals are simulated for exactly the same parameters as in the case of reference signals using like in the SGA reduced finite element meshes ($d_E = 3\,\text{mm}$, $N_{SL} = 16$). Reference signals are calculated using fine finite element meshes ($d_E = 1\,\text{mm}$, $N_{SL} = 50$). As it can be seen, the values of the cost function C_F^0 are greater than zero for all test signals. This is the result of using different numerical models for the test and the reference signals. Since SGA is seeking for the minimum of the cost function, found combination of the interface am-

Table 3.10: FEM models - comparison of cost functions - without noise

Mode	Test			SGA		
	A_0[mm]	$\alpha_0[^\circ]$	C_F^0[%]	A[mm]	$\alpha[^\circ]$	C_F[%]
11	7.0	20.0	0.37	7.0	20.0	0.37
12	7.0	20.0	3.24	7.1	20.2	2.62
13	7.0	20.0	5.52	7.3	20.2	2.84
21	7.0	20.0	1.14	7.1	20.0	0.26
22	7.0	20.0	3.57	7.4	19.8	1.41
23	7.0	20.0	9.85	7.6	19.2	7.36
31	7.0	20.0	1.82	7.1	20.0	0.44
32	7.0	20.0	3.63	7.6	20.0	2.21
33	7.0	20.0	6.35	7.4	19.8	5.64

plitude and the azimuthal position of the sensor ring ensures that the corresponding cost function is lower or at least equal to C_F^0. Of course, if the resolution of the searching process is small enough. However, this does not mean that the found combination must be exactly the same as the combination applied in simulations of reference signals. In summary, it can be concluded that both the amplitude of the identified dominant mode and the azimuthal position of the sensor ring are determined fairly accurately despite of quite different numerical models used in the SGA and reference simulations.

Finally, the following three step strategy for the identification of the dominant mode identification in the oscillating interface between two conducting fluids by means of the simple genetic algorithm can be formulated:

1. Run SGA with the predefined genome and seeking parameters to identify the dominant mode.
2. Fix the found dominant mode, reduce the genome, and set new seeking parameters using rough results from the previous step.
3. Run SGA once more to find the accurate amplitude and the azimuthal position of the sensor ring.

At the end, it can be concluded that applied simple genetic algorithm accurately identifies dominant modes in the oscillating interface but the execution time of a single identification is relatively long.

3.3.3. DIRECT SEARCH METHOD

In this section, the direct search method (DS) adjusted to the identification of the dominant mode in the oscillating interface is presented [157]. For the known azimuthal position of the sensor ring relative to the oscillating interface, the idea of the direct search method is quite simple. First, a pool of interface dominant modes which should be analyzed has to be defined, e.g. $\{\eta_{ij} : i = 1 \dots M, j = 1 \dots N\}$, where M and N are the highest available azimuthal and radial mode indexes, respectively. Next, a range of possible amplitudes of the oscillating interface has to be determined: $A \in \langle A_{min}, A_{max} \rangle$. At the end, for every mode from the pool, the minimum of the cost function defined by (3.48) is searched in the predefined amplitude range using the golden section search [6, 68]. The golden section search is a technique which enables to find the extremum of a unimodal function of one variable by successively narrowing the intervals inside which the extremum is known to exist. Its name comes from the fact that the algorithm maintains the function values for triples of points whose distances form a golden ratio. After evaluation of all modes from the pool, the global minimum of all found cost function minimums is searched. The found global minimum defines the dominant mode of the oscillating interface and its amplitude. A straightforward implementation of this algorithm results unfortunately in longer execution times comparing to the SGA procedure presented in the previous section. The algorithm can be easiely accelerated after analyzing the typical distribution of the cost function (3.48) for all modes from the pool versus amplitudes of interface oscillations (Fig. 3.21). Instead of immediate searching

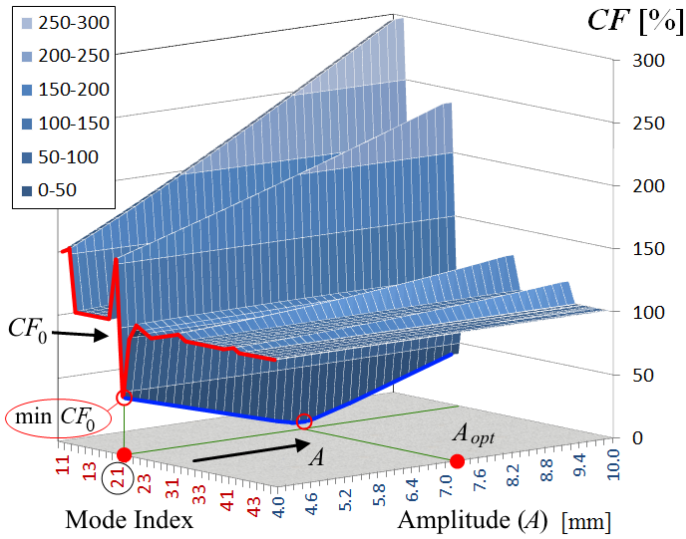

Fig. 3.21: Distribution of cost function for various interface modes versus amplitude

for the minimum of the cost function for all modes from the pool in the given range of amplitudes, the values of cost function C_{F0} are calculated for one predefined value of the amplitude only, e.g. for the lower limit of the amplitude range (see red line in Fig. 3.21). All calculated C_{F0} values are stored in a vector $\mathbf{V}$. Then, using the vector $\mathbf{V}$, modes from the pool are sorted in ascending order by placing at the first position of the list the mode with the smallest cost function ($V_1 : \eta_{mn} \rightarrow min\ C_{F0}$). Having sorted modes, for every mode from the list, the search for the minimum cost function can be started in the given range of amplitudes using the golden section approach (Fig. 3.22).

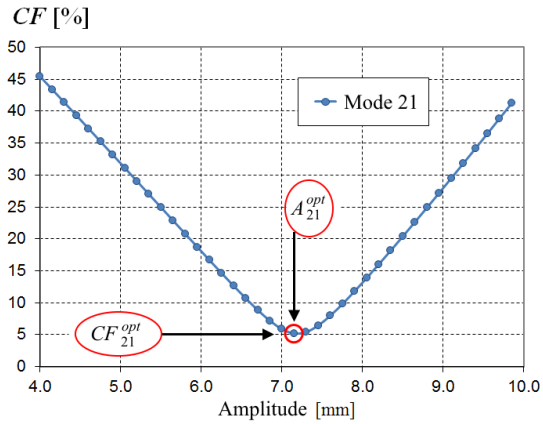

Fig. 3.22: Distribution of cost function versus amplitude for one mode

Additionally, using as a termination criterion the cost function threshold value C_F^{Th} below which the process of scanning over modes should be stopped, a modified direct search algorithm (MDS) is obtained. The MDS performance is in most cases much faster than the simple DS version. Selection of the appropriate value of C_F^{Th} is important because if the threshold value is too small the process will not be interrupted and in consequence the entire list of modes will be searched. In turn, the MDS process of finding of the dominant mode will not be accelerated. For simulated signals, the choice of the threshold is quite obvious because as it was stated in the previous section, the cost function values are correlated with the noise and it is enough to accept the value of the added noise level as the threshold value C_F^{Th}. In the case of measurement signals, the choice is not so obvious and usually requires a few additional simulations in order to find its proper value.

Tables 3.11, 3.12, and 3.13 show sample test results of dominant mode identifications in the oscillating interface by means of the MDS algorithm with the cost function threshold equals $C_F^{Th} = 10$ %. As the reference data, the simulated magnetic flux density signals are used. The signals are calculated by means of FEM at the sensors located on the sensor ring using the same model of the cylindrical cell as presented in the previous section and applying the fine FE mesh ($d_E = 1$ mm). For all simulations, the azimuthal position of the sensor ring is set to $\alpha_0 = 0^\circ$ while the amplitude of the oscillating interface is set to $A_0 = 7$ mm. In all tables *RMode* gives the reference dominant mode in the oscillating interface simulated by the fine finite element model whereas *IMode* is the identified dominant mode. A is the amplitude of the dominant mode found by the MDS and δA denotes the relative error of the estimated amplitude calculated as: $\delta A = 100\%(A - A_0)/A_0$. Results of all identifications found with the MDS are the same as the results received by means of the simple genetic algorithm described in the previous section (see Tables 3.5, 3.6, and 3.7 for comparison). From average computation time for both methods, it can be noticed that the modified direct search procedure is about 35% faster than the simple genetic algorithm.

Table 3.11: MDS dominant mode identifications - $Noise = 0\%$

RMode	*IMode*	A[mm]	δA[%]	C_F[%]	CPU[s]
11	11	7.03	0.38	0.09	11.8
12	12	7.06	0.93	2.42	11.9
13	13	7.21	2.95	2.85	21.8
21	21	7.07	1.04	0.08	11.8
22	22	7.93	13.22	2.46	11.8
23	23	7.84	11.96	5.30	24.3
31	31	7.13	1.88	0.19	11.7
32	32	7.62	8.86	2.42	11.7
33	33	7.56	8.02	6.40	15.9

Table 3.12: MDS dominant mode identifications - $Noise = 5\%$

RMode	*IMode*	A[mm]	δA[%]	C_F[%]	CPU[s]
11	11	6.99	-0.10	2.28	11.8
12	12	7.14	2.00	3.16	12.1
13	13	7.18	2.59	2.93	21.9
21	21	7.05	0.74	1.69	12.0
22	22	8.14	16.27	2.80	11.9
23	23	7.90	12.92	6.32	24.4
31	31	7.20	2.84	2.32	11.8
32	32	7.51	7.24	2.98	11.8
33	33	7.56	7.95	5.83	16.0

Table 3.13: MDS dominant mode identifications - $Noise = 10\%$

RMode	*IMode*	A[mm]	δA[%]	C_F[%]	CPU[s]
11	11	7.05	0.74	4.87	12.0
12	12	6.98	-0.29	5.08	12.1
13	13	7.27	3.84	4.76	21.9
21	21	7.17	2.48	3.54	11.9
22	22	8.04	14.84	5.15	11.9
23	23	7.88	12.62	7.13	24.6
31	31	6.85	-2.20	2.46	11.8
32	32	7.18	2.52	4.18	11.8
33	33	7.46	6.54	5.93	16.1

The MDS operates correctly only when the relative azimuthal location of the sensor ring in a relation to the coordinate system with the oscillating interface is known. If this location is unknown, the identification of the dominant mode in the oscillating interface usually fails, often leading to wrong mode recognition and wrong amplitude estimation. Generally, the elimination of this limitation in a signal domain is complicated and time consuming, so that the MDS method ceases to be competitive in relation to SGA. However, for a certain class of signals this limit can be relatively easy removed if the analysis is switched to the spatial frequency domain (see Section 3.3.1.) because the amplitude spectra of signals are insensitive to the angular shift of signals (shift theorem of Fourier transform [14]).

Further, the analysis is restricted to the class of signals which can be perfectly reconstructed from the Fourier spectrum calculated for N_s sensors (Section 3.3.1.). Some

additional signals with Fourier spectra significantly below the Nyquist frequency have also been added to this class, although the perfect reconstruction is not possible for them. For the system consisting of 8 sensors ($N_s = 8$), this class contains signals corresponding to the following modes: $\eta_{ij} \in \{\eta_{11}, \eta_{12}, \eta_{13}, \eta_{22}, \eta_{31}, \eta_{21}, \eta_{33}\}$ (see Fig. 3.19 and 3.20).

To apply effectively the MDS in the spatial frequency domain the cost function (3.48) has to be redefined by introducing directly the amplitude spectra of signals instead of the signals themselves. The following spectral cost function $\widetilde{C}_F$ is introduced:

$$\widetilde{C}_F = \sqrt{\frac{\sum\limits_{c=r,z}\sum\limits_{i=0}^{N_s/2}\left(\left|\underline{B}^i_c\right| - \left|\underline{B}^i_{c0}\right|\right)^2}{\sum\limits_{c=r,z}\sum\limits_{i=0}^{N_s/2}\left|\underline{B}^i_{c0}\right|^2}}100\% \tag{3.50}$$

where $\left|\underline{B}^i_c\right|$ and $\left|\underline{B}^i_{c0}\right|$ are amplitudes of i^{th} harmonics of measured and reference signals, respectively.

Tables 3.14, 3.15, and 3.16 show results of the dominant mode identifications by means of the modified direct search algorithm using amplitude spectra of signals (MDS-AS) performed for unknown azimuthal positions of the sensor ring. In calculations of the reference signals, the same FEM model of the cell as described above is used under assumption that the azimuthal position of the sensor ring is shifted by an angle $\alpha_0 = 20^\circ$ relative to the coordinate system of the oscillating interface. Noisy signals are created by adding to original signals a pseudo-random white noise of the level $N_{\%}$.

It can be noticed that in all simulations the dominant mode is correctly identified. In most cases, the amplitude of the oscillating interface is found with the error δA less than 10% and is usually overestimated. The largest amplitude errors occur for signals for which it is not possible to determine the correct amplitude spectrum, i.e., for signals corresponding to modes η_{32} and η_{33}.

Table 3.14: MDS-AS identifications - unknown azimuthal ring position - $Noise = 0\%$

RMode	*IMode*	A[mm]	δA[%]	$\alpha[^\circ]$	$\widetilde{C}_F$[%]	CPU[s]
11	11	7.03	0.38	20.0	0.10	8.9
12	12	7.06	0.93	19.9	2.54	8.9
13	13	7.21	2.95	19.9	3.04	14.0
21	21	7.04	0.60	19.9	2.45	8.9
31	31	7.13	1.86	20.0	0.20	8.7
32	32	7.61	8.75	20.0	2.15	8.8
33	33	7.55	7.90	20.0	5.71	13.0

Table 3.15: MDS-AS identifications - unknown azimuthal ring position - *Noise* = 5%

RMode	*IMode*	A[mm]	δA[%]	$\alpha[^\circ]$	$\widetilde{C}_F$[%]	CPU[s]
11	11	7.03	0.49	20.7	0.56	8.9
12	12	7.02	0.33	20.2	1.82	8.9
13	13	7.24	3.48	20.0	2.43	18.8
21	21	7.05	0.67	20.2	2.73	8.8
31	31	7.10	1.38	20.1	1.74	8.7
32	32	7.54	7.65	20.2	1.43	8.8
33	33	7.50	7.20	20.1	5.64	12.9

Table 3.16: MDS-AS identifications - unknown ring position - *Noise* = 10%

RMode	*IMode*	A[mm]	δA[%]	$\alpha[^\circ]$	$\widetilde{C}_F$[%]	CPU[s]
11	11	7.04	0.60	20.7	2.64	8.9
12	12	6.95	-0.65	20.6	2.59	8.9
13	13	7.26	3.73	19.9	4.70	14.0
21	21	6.98	-0.33	20.2	4.44	8.9
31	31	6.92	-1.10	20.6	2.47	8.7
32	32	7.80	11.37	20.2	1.27	8.8
33	33	7.50	7.13	19.9	6.36	13.0

The use of MDS-AS allows also to find easily the azimuthal position α of the sensor ring. The azimuthal position of the ring is simply equal to the subtraction of the phase shifts corresponding to the main Fourier harmonics found for the identified and the input signals. The phase shift α of the i^{th} harmonic is calculated as: $\alpha = \arctan(\Im(\underline{B}_r^i)/\Re(\underline{B}_r^i))$ using imaginary $\Im(\underline{B}_r^i))$ and real $\Re(\underline{B}_r^i))$ part of the harmonic $\underline{B}_r^i$ found during the spatial Fourier transform of the signal. It can be observed that all azimuthal positions of the sensor ring estimated in that way are close to the reference position equals 20°.

It is also noteworthy that the average identification time using the MDS-AS equal to 10.5 s is about 30% shorter than for the MDS (14.8 s).

In summary, it can be concluded that the direct search methods for problems with relatively small search space are tools that can be a competitive alternative to stochastic methods in terms of computation time.

3.3.4. CROSS-CORRELATION APPROACH

In this section, the approach using the cross-correlation of signals (CC approach) during the identification of dominant mode in the oscillating interface is presented [151].

The cross-correlation (CC) is a measure of similarity of two waveforms as a function of a shift applied to one of them. It is also known as a sliding dot product or sliding inner-product. The cross-correlation is commonly used for searching a long-duration signal for a shorter, known feature. To characterize a correlation between two discrete data sets $\mathbf{x} = \{x_1, \ldots, x_N\}$ and $\mathbf{y} = \{y_1, \ldots, y_N\}$ usually the linear correlation coefficient r (also called the product-moment correlation coefficient, or Pearson's r coefficient) is used [111]:

$$r = \frac{\sum_{i=1}^{N}(x_i - \overline{x})(y_i - \overline{y})}{\sqrt{\sum_{i=1}^{N}(x_i - \overline{x})^2}\sqrt{\sum_{i=1}^{N}(y_i - \overline{y})^2}} \tag{3.51}$$

where $\overline{x}$ and $\overline{y}$ are the mean values of the $\mathbf{x}$ and $\mathbf{y}$ respectively.

In the identification of the dominant mode, the cross-correlation applied to signals defined in a spatial domain around the cylindrical cell is used. The spatial shifting of signals is realized using their azimuthal periodicity. The cross-correlation is calculated between the signal produced by the analyzed interface and all reference signals collected in a pre-defined database. The database should contain signals corresponding to all possible dominant modes which can be expected in the oscillating interface, i.e., $\{\eta_{ij}: i = 1 \ldots M, j = 1 \ldots N\}$. As before, the signals correspond to the maximum elevation of the interface. For every mode from the database, the reference signals are calculated using a grid of virtual sensors regularly distributed around the cell (Fig. 3.23). The number of virtual sensors equals N_V in one grid row is not limited by the possibility of their physical implementation, so its choice should give signals with a high

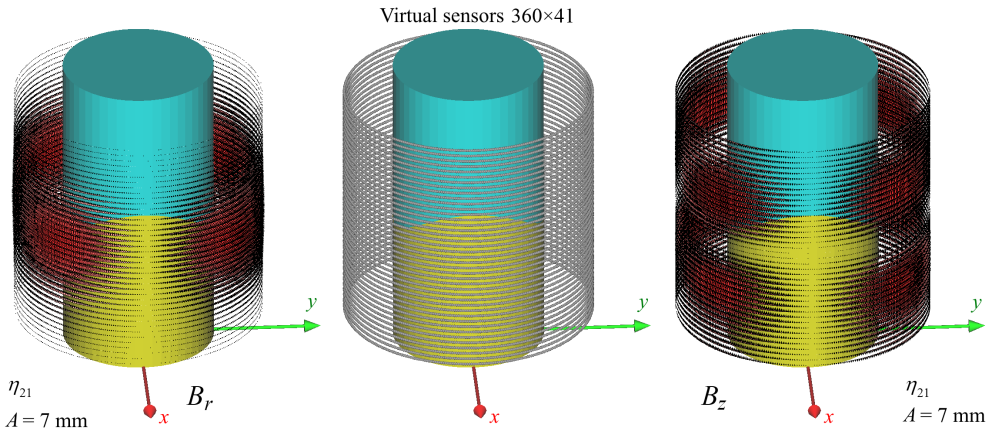

Fig. 3.23: Distribution of virtual sensors around the cell (360×41) and magnetic flux density components (B_r, B_z) calculated for the interface mode η_{21} and amplitude $A = 7\,\mathrm{mm}$

spatial resolution to enable precise azimuthal localization of shifted signals. In this case, the number of virtual sensors is defined as $N_V = 360$ what provides the resolution of shifting signal equal to $\Delta\alpha = 1/N_V = 1^\circ$.

The grid of virtual sensors should cover the interval of possible z-positions of the measuring system allowing its exact localization in the z-direction, which determines the number of grid rows N_R. In the implemented system, the range of z-positions of the sensor grid is set to $z \in < 10\,\text{mm}, 90\,\text{mm} >$ and the number of rows is equal to $N_R = 41$ which provides the resolution of the identification of the measurement system z-position equals $\Delta z = 2\,\text{mm}$.

Having the grid of virtual sensors, signals corresponding to all modes η_{ij} in the database are calculated using amplitudes from a predefined range $< A_{min}, A_{max} >$ and assumed amplitude resolution ΔA, e.g. $A_{min} = 2\,\text{mm}, A_{max} = 16\,\text{mm}, \Delta A = 1\,\text{mm}$. The number of various amplitudes N_A ascribed to every mode in the database is equal to $N_A = (A_{max} - A_{min})/\Delta A + 1$.

Figure 3.24 shows distributions of B_r and B_z components of the magnetic flux density around the cell calculated for sample interface modes η_{11} and η_{12}, and various amplitudes using the grid of virtual sensors defined above, i.e., $N_V \times N_R = 360 \times 41$. It can be noticed that field distribution patterns vary considerably with the increase of the oscillation amplitude, especially for modes with higher radial indexes.

In the first step of the cross-correlation approach, the index n_0 of the row with N_V sensors is localized in the virtual grid for which the position z_n is the closest to the actual position of the measurement ring (z_0):

$$n_0 \leftarrow \min \forall_{n=1\ldots N_R} |z_n - z_0| \tag{3.52}$$

In the second step, for every mode $\eta = \{\eta_{ij} : i = 1\ldots M, j = 1\ldots N\}$ and every amplitude $A = \{A_k : k = 1\ldots N_A\}$ from the database, the virtual signals $\mathbf{S}^V = \{S_i^V, i = 1\ldots N_V\}$ located at the row n_0 are extracted. If $z_n \neq z_0$, the linear interpolation of signals from adjacent rows is used, i.e., rows n_0 and $n_0 - 1$ for $z_n > z_0$, or rows n_0 and $n_0 + 1$ for $z_n < z_0$.

Next, for every signal found in the second step, the azimuthal shift angle $\alpha_m = m\Delta\alpha$ is searched ensuring the maximum value of the linear correlation coefficient $r_{ij,k}^{(m)}$ between the measured signal $\mathbf{S} = \{S_i, i = 1\ldots N_S\}$ and the shifted database signal $\mathbf{S}_m^V = \{S_i^V, i = 1 + m\ldots N_V + m\}$, where $m = 0\ldots N_V$ (Fig. 3.25). Cross-correlation coefficients $r_{ij,k}^{(m)}$ are calculated according to (3.51) using independently radial and axial components of magnetic flux density signals as: $r_{ij,k}^{(m)} = r_{ij,k}^{(m)}|_r \cdot r_{ij,k}^{(m)}|_z$.

All found maximums of cross-correlation coefficients together with the corresponding mode index, the amplitude and the shift angle are stored in a structure $\mathbf{C}$ of size $M \times N \times N_A$. At the end, the structure $\mathbf{C}$ is sorted in a descending order using CC coefficients. As a final result, the mode with the highest value of the cross-correlation coefficient is given at the first position of $\mathbf{C}$. This mode defines the signal from the database best matching to the measured signal together with its amplitude and the relative shift angle.

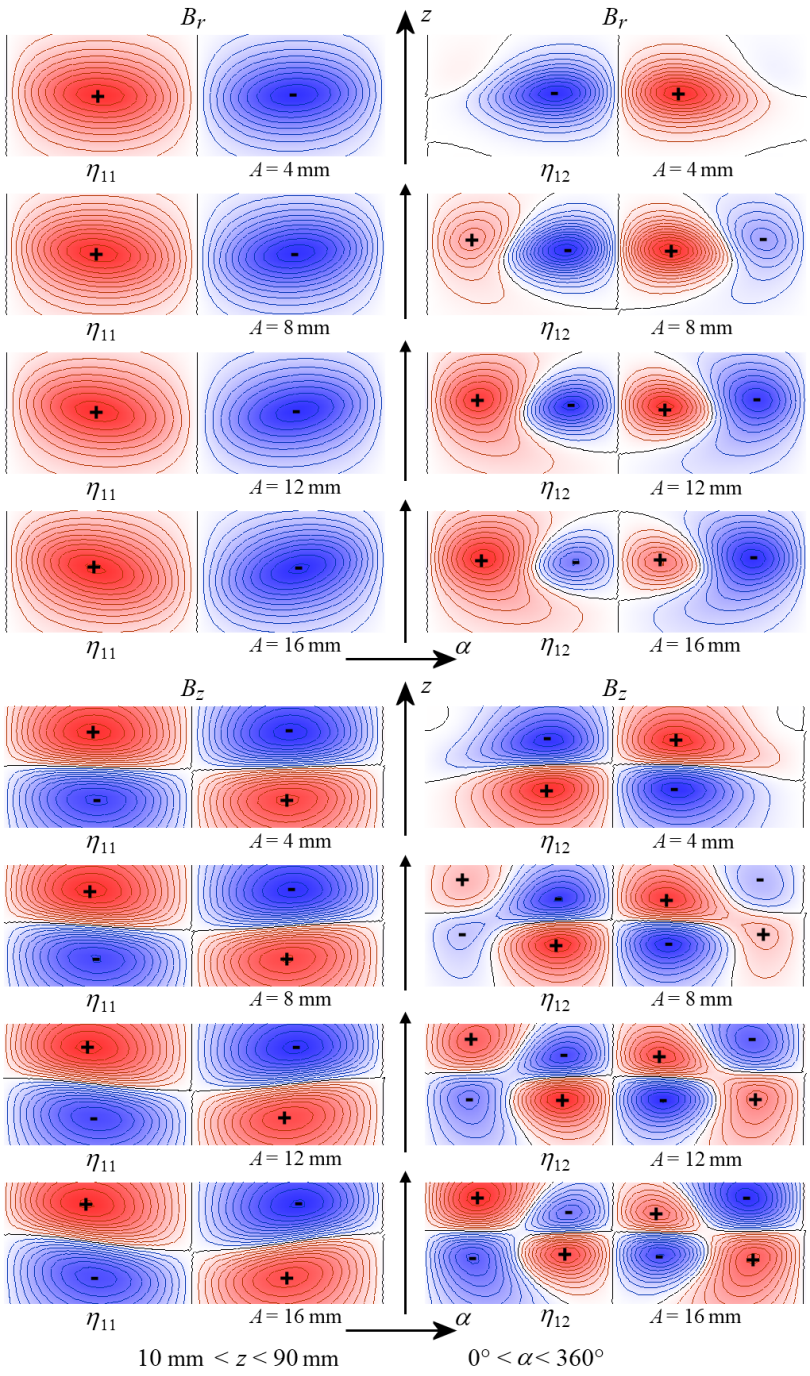

Fig. 3.24: Distributions of magnetic flux density components around the cylindrical cell for various amplitudes and interface dominant modes: η_{11}, η_{12}

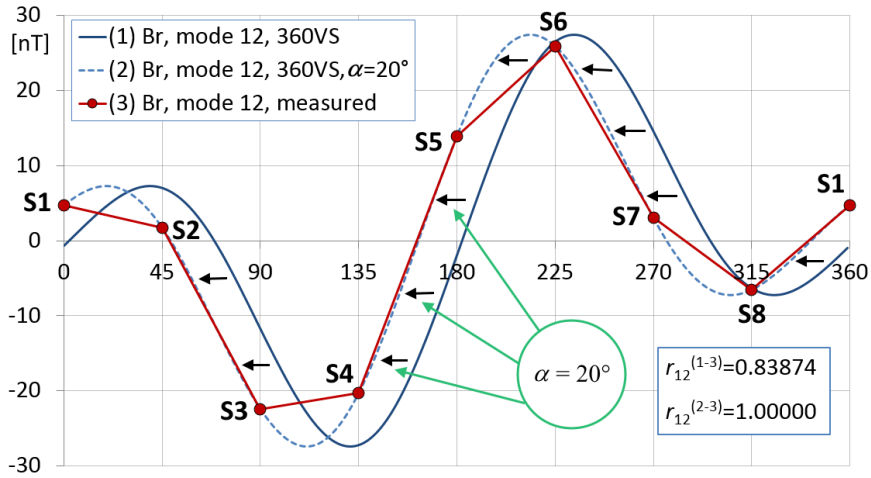

Fig. 3.25: The principle of matching signals using cross-correlation coefficient: (1) signal corresponding to the mode η_{12} and amplitude $A = 7\,\text{mm}$ read from the database, (2) best suited signal - signal (1) shifted by $\alpha = 20°$, (3) signal measured using 8-sensors system. CC calculated between signals (1) - (3): $r_{12}^{(1-3)} = 0.83874$, and between signals (2) - (3): $r_{12}^{(2-3)} = 1.00000$

Unfortunately, the use of cross-correlation coefficient only in the identification of dominant mode in the oscillating interface with 8 sensors does not always ensure the correct identification of the dominant mode, especially for interfaces defined by higher dominant modes. For example, let the signal $\mathbf{S} = \{S_i, i = 1 \ldots 8\}$ be produced by the interface described by the dominant mode η_{23} oscillating with the amplitude $A = 7\,\text{mm}$ and simulated using the fine FEM model ($d_E = 1\,\text{mm}$). The sensor ring is placed at $z_0 = 50\,\text{mm}$ and rotated in the azimuthal direction about angle $\alpha = 20°$. The cross-correlation coefficient of this signal and the signal corresponding to the mode η_{23} (amplitude $A = 7\,\text{mm}$, shift angle $\alpha = 20°$) stored in the database is equal to $r_{23} = 0.97512$. In this case, the cross-correlation coefficient is not equal to 1.0 because signals in the database are calculated using different FEM models, namely fast FEM models ($d_E = 3\,\text{mm}$). The CC coefficient of the signal $\mathbf{S}$ with the signal from the database corresponding to the mode η_{22} oscillating with the amplitude $A = 11mm$ and shifted by the angle $\alpha = 110°$ is equal to $r_{22} = 0.99857$, which is greater than in the previous case (Fig. 3.26). This means that during the identification process the false mode η_{22} must be selected instead of the correct one η_{23} because its correlation with the measured signal is higher! Additionally, it should be noticed that the cross-correlation coefficient is insensitive to absolute amplitudes of signals (compare signals in Fig. 3.26) what prevents the accurate identification of the amplitude of oscillating interface.

Problems mentioned above can be eliminated by increasing the number of sensors on the sensor ring. This results in the more accurate description of signals used during the identification. However, it is difficult to realize this approach in practice because of a small radius of the cylindrical cell ($R = 25\,\text{mm}$) and the actual physical sizes of sensors. An alternative way consists in adding a second co-axial sensors set parallel to

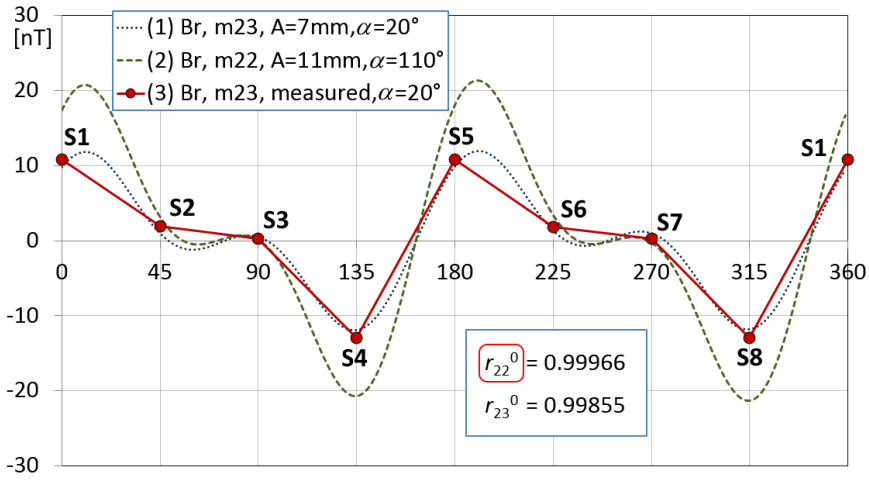

(a) B_r component.

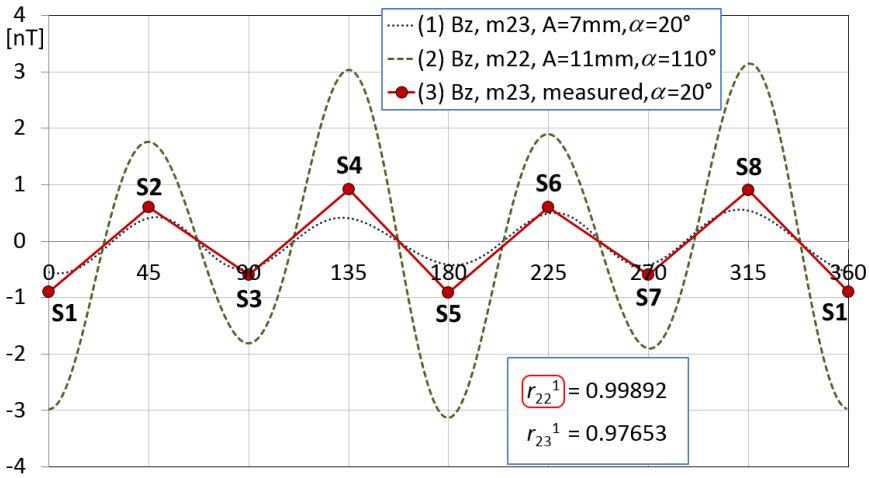

(b) B_z component.

Fig. 3.26: Example of false interface identification using the CC coefficient: (1) signals for the interface mode η_{23}, $A = 7\,\text{mm}$, and $\alpha = 20°$, (2) signals for the interface mode η_{22}, $A = 11\,\text{mm}$, and $\alpha = 110°$, (3) measured signals for the interface mode η_{23}, $A = 7\,\text{mm}$, and $\alpha = 20°$. Signals (1) and (2) are calculated using FEM models with $d_E = 3\,\text{mm}$, while signals (3) with $d_E = 1\,\text{mm}$. Found false mode η_{22} corresponds to $r_{22} = r_{22}^0 r_{22}^1 = 0.99857 > r_{23} = r_{23}^0 r_{23}^1 = 0.97512$

the first one and shifted in z direction by distance Δz. The choice of Δz is significant because the distance Δz cannot be too small due to the construction limits and also not too big due to the limited sensitivity of applied sensors. Choosing $\Delta z = 10\,\text{mm}$ is a good compromise as it is shown in [151].

Other approach for evaluation of database signals is to use cost functions (3.48) calculated for all signals stored in the structure **C** instead of CC coefficients directly. In this

case, calculation of cost functions is not so time consuming as in the previous methods because the signals already stored in the database are used and accordingly, there is no need to use FEM for their estimation. Using evaluated cost function values,the vector **C** is searched for the minimum of the cost function. The found minimum determines the dominant mode in the oscillating interface.

Tables 3.17 and 3.18 show dominant mode identifications results obtained by the cross-correlation approach using cost functions validation. Noisy test signals (noise level 10%) for appropriate modes were simulated assuming that the amplitude of oscillating interface is equal to $A_0 = 7$ mm. Azimuthal positions of the sensor ring are set to $\alpha = 0°$ (Table 3.17) and to $\alpha = 20°$ (Table 3.18). It can be observed that for all cases the

Table 3.17: CC dominant mode identifications - *Noise* = 10%

RMode	*IMode*	A[mm]	δA[%]	r	C_F[%]	CPU[s]
11	11	7.04	0.56	0.998135	4.87	3.7
12	12	7.00	0.00	0.998192	5.09	5.0
13	13	7.19	2.71	0.997657	4.99	4.9
21	21	7.12	1.68	0.998793	3.60	4.7
22	22	8.00	14.29	0.996398	5.15	4.7
23	23	8.00	14.29	0.917502	11.72	4.7
31	31	6.90	-1.37	0.998229	2.61	3.9
32	32	7.21	2.96	0.980606	4.00	3.8
33	33	7.33	4.70	0.677485	7.07	3.9

Table 3.18: CC identifications - unknown azimuthal ring position - *Noise* = 10%

RMode	*IMode*	A[mm]	δA[%]	$\alpha[°]$	r	C_F[%]	CPU[s]
11	11	7.03	0.39	20.0	0.998196	4.48	3.7
12	12	7.00	0.00	20.0	0.998108	5.45	4.5
13	13	7.25	3.55	20.0	0.997227	6.41	4.4
21	21	7.02	0.25	20.0	0.998939	3.63	3.9
22	22	7.57	8.11	20.0	0.997921	4.58	3.9
23	23	7.61	8.72	18.0	0.979056	8.53	3.9
31	31	6.95	-0.73	20.0	0.997758	4.22	3.9
32	32	7.88	12.62	20.0	0.987221	3.42	3.8
33	33	7.48	6.80	-39.0	0.664594	10.45	3.9

dominant mode is correctly identified ($RMode = IMode$). Amplitudes of modes lower than mode η_{22} are found with the relative error δA less than 4%. Errors for amplitudes of other modes ($\geq \eta_{22}$) are higher but less than 15%. The amplitudes of all modes, with the exception of the mode η_{13}, are overestimated.

CC coefficients for all but one identified interfaces are high ($r > 0.98$). Only for the interface described by the mode η_{33}, the CC coefficient is relatively small and equal to about 0.7.

Identification of unknown azimuthal sensor ring positions is mostly correct, except the mode η_{33}. Calculated values of the cost function fluctuate around 5%, excluding the modes η_{23} and η_{33}, for whom they are about 50% higher. A similar trend can be observed in the case of methods already presented, see Table 3.8 for SGA and Table 3.13 for MDS.

Average time to identify the dominant mode using CC approach with cost function validation is 4.0s, which is the best time of all the previously presented methods. This leads to the conclusion that although the CC require pre-build database (relatively time-consuming), in the identification phase, this method is a competitive alternative to MDS-AS.

3.4. SUMMARY

In this chapter, the problem of the interface identification between two stationary oscillating immiscible conducting fluids placed in a cylindrical cell and supplied with direct current has been presented. A simplified model of the interface based on eigen η-modes concept has been introduced. Magnetic field around the cylindrical cell with fluids has been calculated using the Biot-Savart law and approximate analytical method for a determination of current density distribution flowing in the cell. The found analytical description of current density in the cell has been verified with FEM using commercial and self-developed software (COMSOL®, TFEM3D). TFEM3D has been specially optimized to solve the problem fast and reliable. It includes a fast FEM mesh generator as well as some iterative solvers from SLATEC library.

Based on the magnetic field tomography concept the inverse problem of the interface reconstruction has been formulated. The inverse problem presented here has been restricted to the interface dominant mode identification only. It can be treated as a first stage for the full interface reconstruction. Magnetic signal profiles used in the identification process have been presented and limits of the implemented measurement system have been discussed. Three methods for the interface dominant mode identification have been introduced. The first method applies a simple genetic algorithm (SGA). The second one uses a modified direct search approach (MDS) and MDS associated with amplitude spectra analysis (MDS-AS). The third one employs the cross-correlation coefficient and the cost function validation together with solutions located in the pre-build database (CC). All three methods have been described in details and tested on simulated noisy data. Intentionally, the validation of the methods with measurement data is not presented here because its correct presentation demands also description of methods which are not strictly connected with field computation, e.g., signal data

processing, analysis of measurement system, etc. But this is out of scope of this monograph. In fact, the validation has been performed resulting in the positive evaluation of the proposed methods.

There are a number of publications written by a group with whom the author worked associated with the content of this chapter which can be considered as its supplement. The list (except publications already cited) sorted by date of publication is as follows: [19] forward simulations (FEM), [155] interface reconstruction (GA), [77] interface reconstruction (GA, FEM), [21] MFT - test experimental setup, rotating cylinder, electrolyte - metal interface, [80] rectangular aluminum cell, stability analysis, [91] measurements, test rotating distorted electrolyte - metal interface, [20] interface identification, improved GA, dominant mode, [158] interface reconstruction, modified GA, [149] experimental setup, feed electrode shape influence, [150] experimental setup, feed-wire problem, [89] experiment, reconstruction, mode η_{11}, [65] aluminum reduction cell, magnetic field profile, [78] evolution strategy, realistic post-processing, [115] MFT - experiment, mode η_{11}, [79] regularization technique, experimental data , [90] MFT - experiment, [152] MFT - system calibration, simulations, validation with experiment.

4

SEMI-ANALYTICAL METHODS IN LORENTZ FORCE EDDY CURRENT TESTING

4.1. INTRODUCTION

Lorentz force eddy current testing (LET) is a nondestructive technique which can be applied to systems where the source of magnetic field (e.g. permanent magnet) and the investigated conducting object are in relative movement. In such systems, due to induced eddy currents, a braking force (Lorentz force) acting on a conducting object appears. In LET, instead of measuring directly this force, the force having the same magnitude but opposite direction exerted on a permanent magnet is measured. LET can be applied to e.g. contactless velocity measurements in metallurgy [123], determination of conductivity [127], and detection/reconstruction of defects in conducting materials [105]. Numerical simulations of LET (forward and inverse) require precise calculations of forces existing in the LET system. In this chapter, some analytical and semi-analytical techniques applied to LET simulations are presented in details.

4.1.1. MOVING COORDINATE SYSTEMS - TRANSFORMATIONS

The principal postulates of special relativity are as follows [63]:

- *postulate of relativity*, the laws of physics are the same in all inertial systems,
- *postulate of a universal light speed*, the same speed of light is measured in all inertial systems.

Two inertial systems are considered, namely, stationary system O (reference frame) with coordinates (x, y, z, t) and the moving system O' (moving frame) with coordinates (x', y', z', t'). The system O' moves with a constant velocity $\mathbf{v}$ relatively to O (Fig. 4.1).

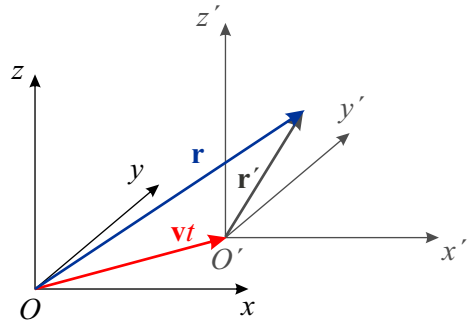

Fig. 4.1: The relative motion of two inertial systems

According to the first postulate, for problems when the displacement current ($\partial \mathbf{D}/\partial t = 0$) can be omitted, quasi-static magnetic Maxwell's equations take in both systems the following forms:

Reference frame O	Moving frame O'
$\nabla \times \mathbf{H} = \mathbf{J}$	$\nabla' \times \mathbf{H}' = \mathbf{J}'$
$\nabla \cdot \mathbf{B} = 0$	$\nabla' \cdot \mathbf{B}' = 0$
$\nabla \cdot \mathbf{J} = 0$	$\nabla' \cdot \mathbf{J}' = 0$
$\nabla \times \mathbf{E} = -\dfrac{\partial \mathbf{B}}{\partial t}$	$\nabla' \times \mathbf{E}' = -\dfrac{\partial \mathbf{B}'}{\partial t'}$
$\mathbf{B} = \mu_0(\mathbf{H} + \mathbf{M})$	$\mathbf{B}' = \mu_0(\mathbf{H}' + \mathbf{M}')$

(4.1)

where

$$\nabla = \frac{\partial}{\partial x}\mathbf{1}_x + \frac{\partial}{\partial y}\mathbf{1}_y + \frac{\partial}{\partial z}\mathbf{1}_z, \quad \nabla' = \frac{\partial}{\partial x'}\mathbf{1}_{x'} + \frac{\partial}{\partial y'}\mathbf{1}_{y'} + \frac{\partial}{\partial z'}\mathbf{1}_{z'}$$

From the second postulate, the Lorentz transformation of time and space coordinates is obtained as:

$$t' = \gamma\left(t - \frac{\mathbf{v}\cdot\mathbf{r}}{c}\right) \tag{4.2}$$

$$\mathbf{r}' = \gamma(\mathbf{r} - \mathbf{v}t) \tag{4.3}$$

where

$$\gamma = \frac{1}{\sqrt{1+\beta^2}}, \qquad \beta = \frac{v}{c} \tag{4.4}$$

and c is the speed of light in a vacuum. Taking into account $v \ll c$, (4.4) can be written as

$$\beta \simeq 0, \qquad \gamma \simeq 1 \tag{4.5}$$

and, in consequence, the Lorentz transformation reduces to the Galilean transformation:

$$t' = t \tag{4.6}$$

$$\mathbf{r}' = \mathbf{r} - \mathbf{v}t \tag{4.7}$$

It is necessary to find transformations between both inertial systems for the field equations (4.1) corresponding to the Galilean transformation (4.6) - (4.7) [135], [69], [42]. Considering the scalar function $f'(x', y', z', t')$ defined in the system O', spatial partial derivatives can be calculated as follows:

$$\frac{\partial f'}{\partial x} = \frac{\partial f'}{\partial x'}\frac{\partial x'}{\partial x} = \frac{\partial f'}{\partial x'} \tag{4.8}$$

Using (4.8), the following relation between nabla operators is received:

$$\nabla' f' = \nabla f' \tag{4.9}$$

The time derivative of f' is calculated using a chain rule as:

$$\begin{aligned}\frac{\partial f'}{\partial t} &= \frac{\partial f'}{\partial t'}\frac{\partial t'}{\partial t} - \frac{\partial f'}{\partial x'}\frac{\partial x'}{\partial t} - \frac{\partial f'}{\partial y'}\frac{\partial y'}{\partial t} - \frac{\partial f'}{\partial z'}\frac{\partial z'}{\partial t} = \\ &= \frac{\partial f'}{\partial t'} - v_x\frac{\partial f'}{\partial x'} - v_y\frac{\partial f'}{\partial y'} - v_z\frac{\partial f'}{\partial z'} = \\ &= \frac{\partial f'}{\partial t'} - (\mathbf{v}\cdot\nabla')f'\end{aligned} \tag{4.10}$$

Applying (4.9), (4.10) can written as

$$\frac{\partial f'}{\partial t} = \frac{\partial f'}{\partial t'} + (\mathbf{v}\cdot\nabla)f' \tag{4.11}$$

For vector functions, similar expressions can be derived. Let $\mathbf{F}(x', y', z', t')$ be a vector function in the O' system. It is easy to show that

$$\nabla'\cdot\mathbf{F}' = \nabla\cdot\mathbf{F}' \tag{4.12}$$

and

$$\nabla'\times\mathbf{F}' = \nabla\times\mathbf{F}' \tag{4.13}$$

For the time derivative, the following relation is valid:

$$\frac{\partial\mathbf{F}'}{\partial t} = \frac{\partial\mathbf{F}'}{\partial t'} + (\mathbf{v}\cdot\nabla)\mathbf{F}' \tag{4.14}$$

Using (4.12), (4.13), and the vector identity:

$$\nabla\times(\mathbf{A}\times\mathbf{B}) = (\mathbf{B}\cdot\nabla)\mathbf{A} - (\mathbf{A}\cdot\nabla)\mathbf{B} + \mathbf{A}(\nabla\cdot\mathbf{B}) - \mathbf{B}(\nabla\cdot\mathbf{A}) \tag{4.15}$$

The equation (4.14) can be rewritten as

$$\frac{\partial \mathbf{F}'}{\partial t} = \frac{\partial \mathbf{F}'}{\partial t'} + \mathbf{v}(\nabla \cdot \mathbf{F}') - \nabla \times (\mathbf{v} \times \mathbf{F}') \tag{4.16}$$

Finally, introducing (4.12), (4.13), and (4.15) into (4.1) for the moving frame O', the following set of equations is received:

$$\begin{aligned} \nabla \times \mathbf{H}' &= \mathbf{J}', \\ \nabla \cdot \mathbf{B}' &= 0, \\ \nabla \cdot \mathbf{J}' &= 0, \\ \nabla \times (\mathbf{E}' - \mathbf{v} \times \mathbf{B}') &= -\frac{\partial \mathbf{B}'}{\partial t} \end{aligned} \tag{4.17}$$

Comparing (4.1) with (4.17), the following field transformations can be found:

$$\begin{aligned} \mathbf{H}' &= \mathbf{H}, \\ \mathbf{B}' &= \mathbf{B}, \\ \mathbf{E}' &= \mathbf{E} + \mathbf{v} \times \mathbf{B}, \\ \mathbf{J}' &= \mathbf{J} \end{aligned} \tag{4.18}$$

The transformation for the magnetization density vector takes the form:

$$\mathbf{M}' = \mathbf{M} \tag{4.19}$$

The Ohm law has to be written as

$$\mathbf{J} = \sigma(\mathbf{E} + \mathbf{v} \times \mathbf{B}) \tag{4.20}$$

It can be concluded that this law applies to any frame of reference that moves across magnetic flux lines (or in which the body carrying the current $\mathbf{J}$ moves with respect to the magnetic field source) [69].

4.2. 2D LORENTZ EDDY CURRENT TESTING MODELS

4.2.1. PROBLEM DESCRIPTION

A long permanent magnet (PM) of a rectangular cross-section ($w \times h \times l$) is located at the lift-off distance h_0 above a conducting plate ($L \times D \times l$) of electrical conductivity σ_0 moving with a constant velocity v_0 along x-axis $\mathbf{v} = v_0 \mathbf{1}_x$ (Fig. 4.2).

The PM is magnetized along $0Y$-axis with magnetization vector $\mathbf{M} = M\mathbf{1}_y$. In the plate, an artificial, ideal ($\sigma_d = 0$) defect $c_x \times c_y \times l$ is drilled at the depth d. The center of the defect is located at $\mathbf{x}_0 = [x_0, y_0]^T = [x_n, -d - c_y/2]^T$.

In LET measurement systems, the force exerted on PM $\mathbf{F}_{PM}$ caused by relative motion of the PM and the conducting object is measured directly. However, in simulations, this force is calculated indirectly using the 3^{rd} Newton's axiom which says that the

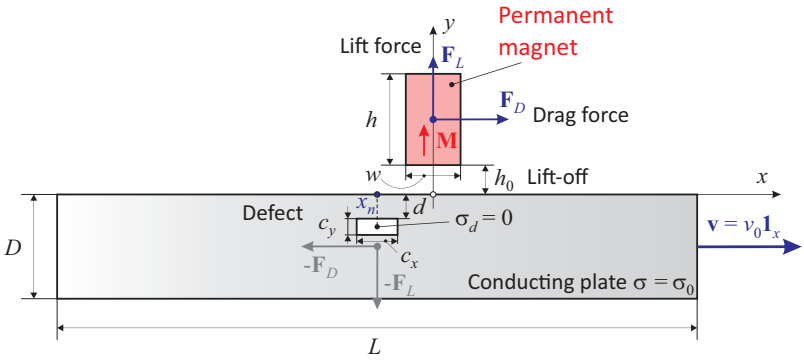

Fig. 4.2: The permanent magnet above the moving conducting plate with a defect

force exerted on the PM has the same magnitude as the Lorentz force acting on the conductor $\mathbf{F}_{LF}$ but the opposite direction ($\mathbf{F}_{PM} = -\mathbf{F}_{LF}$). The reason for this is the greater accuracy of the method of Lorentz force calculation than methods which can be applied for direct estimation of the force exerted on the PM, i.e., methods based on Maxwell's tensor or the virtual work principle. In 2D LET systems where $l \gg L, D$, the force exerted on PM has only two components $\mathbf{F}_{PM} = [F_x, F_y]^T$.

The force exerted on PM can be described in two equivalent coordinate systems (CS): (1) CS fixed to the PM, in which the conducting object (CO) is moving, and (2) CS fixed to the CO where the PM is moving (Fig. 4.3).

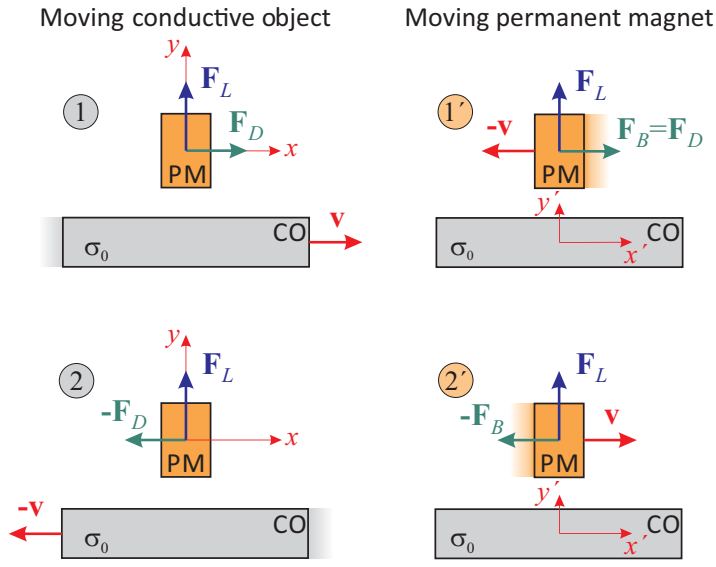

Fig. 4.3: The relative movement - forces exerted on the permanent magnet

In both CS, the component F_y exerted on the PM is always positive, regardless of the direction of the velocity vector and it is called the lift force (F_L). The sign of the F_x component depends on the direction of the velocity vector as well as on the used CS. In the CS fixed to the PM, the sign of F_x component follows the direction of the vector $\mathbf{v}$ and, in this case, F_x is called the drag force (F_D). In the CS fixed to the CO, the sign of F_x component is opposite to the direction of the vector $\mathbf{v}$ and the component is called the brake force (F_B).

Figure 4.4 shows typical distributions of force components exerted on the PM located above a moving aluminum block with a defect (see Fig. 4.2).

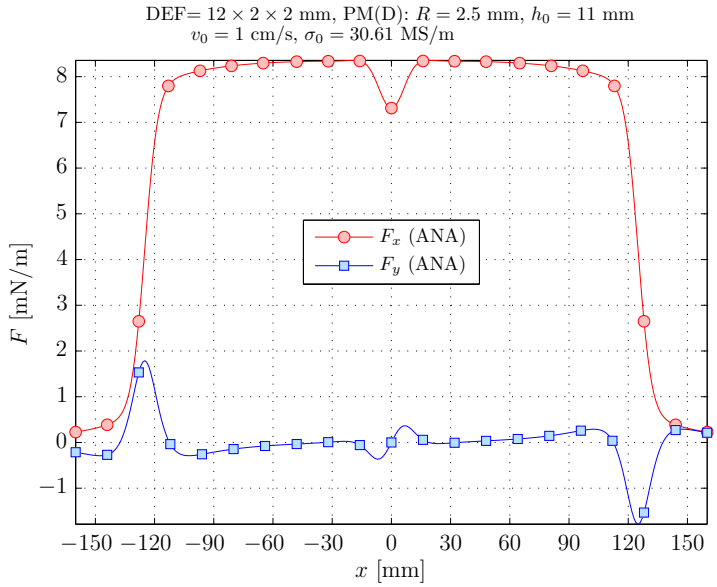

Fig. 4.4: Sample profiles of force components exerted on the permanent magnet hung at a lift-off distance h_0 above the moving aluminum block $L \times D = 250\,\text{mm} \times 50\,\text{mm}$ with $c_x \times c_y = 12\,\text{mm} \times 2\,\text{mm}$ defect located at a depth $d = 2\,\text{mm}$ ($\mathbf{v} = v_0\mathbf{1}_x$)

4.2.2. LORENTZ FORCES IN 2D LET SYSTEM

To calculate forces exerted on the PM above the moving conducting object with defect analytically, some simplifications must be introduced. First, it is assumed that the magnetic field produced by the PM is not affected by induced eddy currents in the conducting object, i.e., so-called weak reaction approach (WRA)[138, 142] can be applied. A necessary condition for the applicability of the WRA can be formulated as $R_m = v_0\mu\sigma_0 a \ll 1$, where R_m is the magnetic Reynolds number, a is the length parameter (specific for the analyzed problem), and v_0, σ_0, μ are the velocity, the electrical conductivity, and the magnetic permeability of the conducting object, respectively. The use of WRA allows to calculate the induced eddy currents $\mathbf{J}$ in a conducting object

directly by Ohm's law (4.20) for moving conductors. For 2D problems, the equation (4.20) is reduced to

$$\mathbf{J} = \sigma_0(\mathbf{E} + \mathbf{v} \times \mathbf{B}) = \sigma_0(-\nabla\phi + \mathbf{v} \times \mathbf{B}) = \sigma_0 \mathbf{v} \times \mathbf{B} = \sigma_0 v_0 B_y \mathbf{1}_z \tag{4.21}$$

because of $\nabla\phi = 0$. $\mathbf{B}$ denotes the magnetic flux density produced by the PM and σ_0, v_0 are the electrical conductivity and the velocity of the conducting object, respectively.

The force exerted on the 2D PM above the moving conductor can be calculated using the following formula of the Lorentz force acting on the conductor:

$$\begin{aligned} \mathbf{F}_{PM} = -\mathbf{F}_{LF} = -l \int_{S_0} \mathbf{J} \times \mathbf{B} dS = \\ = l\sigma_0 v_0 \left[\left(\int_{S_0} B_y^2 dS \right) \mathbf{1}_x - \left(\int_{S_0} B_x B_y dS \right) \mathbf{1}_y \right] \end{aligned} \tag{4.22}$$

where $\mathbf{J}$ denotes eddy currents density, $\mathbf{B}$ describes the magnetic flux density produced by the PM, $S_0 = L \times D$ is the cross-section area of the conductor, and l is the length of the system in the z-direction. It should be noted that directions of force components are independent from the direction of the magnetization vector $\mathbf{M}$. They depend only on the direction of the velocity vector. Due to anti-symmetry of B_x, the second integral in (4.22) disappears for $L \gg D$ and the conductor without defects, i.e., the lift force F_L calculated by the WRA always equals 0 if the PM is far away from the front/back walls of the conductor.

Let $\mathbf{F}_0^{(n)}$ and $\mathbf{F}^{(n)}$ denote profiles of forces exerted on the PM found for the conductor moving between x_1 and x_2 with velocity $\mathbf{v} = v_0 \mathbf{1}_x$ for the defect-free system and the system with a defect, respectively. The index n corresponds to the actual position of the conductor center $x_n \in < x_1, x_2 >$. The vector difference $\Delta\mathbf{F}^{(n)} = \mathbf{F}^{(n)} - \mathbf{F}_0^{(n)}$ describes the influence of the defect on Lorentz force component profiles and is called the defect response signal (DRS). In 2D LET problems eddy currents induced in the conductor have only y-component (4.21). For a conductor with an ideal defect ($\sigma_d = 0$) and the center located at x_n, induced eddy currents $\mathbf{J}^{(n)}$ can be described by the superposition $\mathbf{J}^{(n)} = \mathbf{J}_0^{(n)} + \mathbf{j}_D^{(n)}$, where $\mathbf{J}_0^{(n)}$ denotes eddy currents induced in the conductor without defect located at the same position x_n and $\mathbf{j}_D^{(n)}$ are eddy currents in the region covering the defect equal $\mathbf{j}_D^{(n)} = -\mathbf{J}_0^{(n)} \Big|_{S_D^{(n)}}$. Using above and (4.22), the DRS can be calculated as

$$\begin{aligned} \Delta\mathbf{F}^{(n)} = \mathbf{F}^{(n)} - \mathbf{F}_0^{(n)} = -l \int_{S_D^{(n)}} \mathbf{j}_D^{(n)} \times \mathbf{B}^{(n)} dS = l \int_{S_D^{(n)}} \mathbf{J}_0^{(n)} \times \mathbf{B}^{(n)} dS = \\ = l\sigma_0 v_0 \left\{ \left[- \int_{S_D^{(n)}} B_y^{(n)} B_y^{(n)} dS \right] \mathbf{1}_x + \left[\int_{S_D^{(n)}} B_x^{(n)} B_y^{(n)} dS \right] \mathbf{1}_y \right\} \end{aligned} \tag{4.23}$$

2D DRS calculations with WRA can be directly applied to conductors with more ideal defects because induced eddy currents in the plate flow only in the y-direction and currents in regions covering defects do not affect each other. The resultant DRS for

conductors containing more ideal defects is a simple superposition of single defect signals:

$$\Delta\mathbf{F}^{(n)} = \sum_{k=1}^{K} \Delta\mathbf{F}_k^{(n)} = l \sum_{k=1}^{K} \int_{S_{D_k}^{(n)}} \mathbf{J}_0^{(n)} \times \mathbf{B}^{(n)} dS \tag{4.24}$$

where K is the number of defects and $S_{D_k}^{(n)}$ denotes the region covering the k^{th} defect in the conductor with center located at x_n. The profile of the absolute force exerted on the PM above the moving conductor with K ideal defects calculated with the help of the WRA is given by

$$\begin{aligned}\mathbf{F}^{(n)} &= \mathbf{F}_0^{(n)} + \sum_{k=1}^{K} \Delta\mathbf{F}_k^{(n)} = \\ &= -l \int_{S_0^{(n)}} \mathbf{J}_0^{(n)} \times \mathbf{B}^{(n)} dS + l \sum_{k=1}^{K} \int_{S_{D_k}^{(n)}} \mathbf{J}_0^{(n)} \times \mathbf{B}^{(n)} dS\end{aligned} \tag{4.25}$$

In next sections, it will be shown how to calculate (4.23) - (4.25) using simple 2D models of the PM.

4.2.3. DIPOLAR MODEL OF 2D PERMANENT MAGNET

As the simplest model of a long PM of a rectangular cross-section $w \times h$ magnetized with the magnetization $\mathbf{M} = M\mathbf{1}_y$, an equivalent 2D magnetic line dipole (l-dipole) of the moment $\mathbf{m}_l = m_l\mathbf{1}_y = Mwh\mathbf{1}_y$ located at the center of gravity of the magnet is considered. The physical interpretation of the l-dipole is shown in Fig. 4.5. The l-dipole can be understood as two infinitely thin line currents flowing in opposite z-directions located at a distance d from each other. The formula for the magnetic field produced

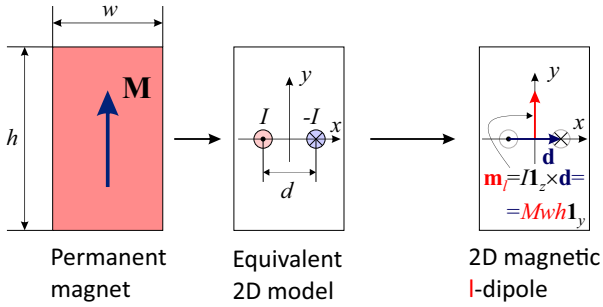

Fig. 4.5: Rectangular permanent magnet and the equivalent 2D magnetic line dipole (l-dipole)

by the l-dipole is easy to derive. The magnetic field produced by an infinitely thin line with current (Fig. 4.6a) can be described in the cylindrical coordinate system as

$$\mathbf{B} = -I\frac{\mu_0}{2\pi r}\mathbf{1}_\phi, \quad \mathbf{A} = I\frac{\mu_0}{2\pi}\ln r\mathbf{1}_z \tag{4.26}$$

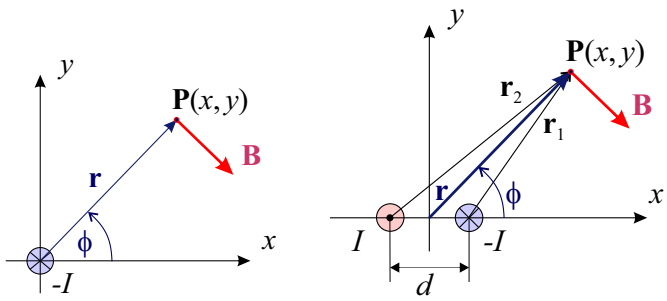

(a) One infinitely thin line (b) Two infinitely thin lines

Fig. 4.6: Configurations of line currents used to determine the magnetic flux density of l-dipole

where $\mathbf{A}$ is the magnetic vector potential ($\mathbf{B} = \nabla \times \mathbf{A}$). The magnetic vector potential $\mathbf{A}$ of two infinitely thin lines conducting opposite currents (Fig. 4.6b) is calculated as:

$$\mathbf{A} = I\frac{\mu_0}{2\pi}\ln\frac{r_1}{r_2}\mathbf{1}_z \tag{4.27}$$

where

$$r_1 = r\sqrt{1 - \frac{d}{r}\cos\phi + \left(\frac{d}{2r}\right)^2}, \qquad r_2 = r\sqrt{1 + \frac{d}{r}\cos\phi + \left(\frac{d}{2r}\right)^2}$$

For a magnetic l-dipole $d \ll r$ and the following expressions can substitute r_1 and r_2:

$$r_1 \cong r\sqrt{1 - \frac{d}{r}\cos\phi}, \qquad r_2 \cong r\sqrt{1 + \frac{d}{r}\cos\phi}$$

Equation (4.27) takes the form:

$$\mathbf{A} = I\frac{\mu_0}{4\pi}\ln\frac{1 - \frac{d}{r}\cos\phi}{1 + \frac{d}{r}\cos\phi}\mathbf{1}_z \tag{4.28}$$

Using the Taylor expansion

$$\ln\frac{1+x}{1-x} = 2\left(x + \frac{x^3}{3} + \ldots + \frac{x^{2i+1}}{2i+1} + \ldots\right), |x| < 1 \tag{4.29}$$

equation (4.28) is simplified to

$$\mathbf{A} = -\frac{\mu_0}{2\pi}Id\frac{\cos\phi}{r}\mathbf{1}_z \tag{4.30}$$

Finally, the magnetic flux density produced by 2D magnetic l-dipole of moment $\mathbf{m}_l = m_l\mathbf{1}_y = I\mathbf{1}_z \times \mathbf{d}$ shown in Fig. 4.7 is described in the cylindrical coordinate system as:

$$\mathbf{B} = \nabla \times \mathbf{A} = \frac{\mu_0}{2\pi r^2}m_l\left(\sin\phi\mathbf{1}_r - \cos\phi\mathbf{1}_\phi\right), \quad m_l = Id \tag{4.31}$$

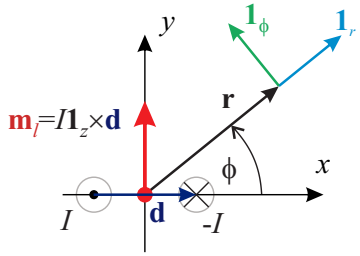

Fig. 4.7: 2D magnetic line dipole (l-dipole)

The following vector identity

$$\mathbf{m}_l = (\mathbf{m}_l \cdot \mathbf{1}_r)\mathbf{1}_r + (\mathbf{m}_l \cdot \mathbf{1}_\phi)\mathbf{1}_\phi = m_l \sin\phi \mathbf{1}_r + m_l \cos\phi \mathbf{1}_\phi$$

allows to rewrite (4.31) as

$$\mathbf{B} = \frac{\mu_0}{2\pi r^2}\left(2\frac{\mathbf{m}_l \cdot \mathbf{r}}{r^2}\mathbf{r} - \mathbf{m}_l\right) \tag{4.32}$$

regardless of the choice of the coordinate system.

The magnetic flux density $\mathbf{B}^{(n)}$ at any point $\mathbf{r} = [x, y]^T$ produced by 2D magnetic l-dipole $\mathbf{m}_l = m_l \mathbf{1}_y$ located at $\mathbf{r}_n = [x_n, y_n]^T$ is given by

$$\begin{aligned}\mathbf{B}^{(n)} &= m_l \frac{\mu_0}{2\pi}\frac{2(x-x_n)(y-y_n)}{[(x-x_n)^2+(y-y_n)^2]^2}\mathbf{1}_x + \\ &+ m_l \frac{\mu_0}{2\pi}\frac{(y-y_n)^2-(x-x_n)^2}{[(x-x_n)^2+(y-y_n)^2]^2}\mathbf{1}_y = B_x^{(n)}\mathbf{1}_x + B_y^{(n)}\mathbf{1}_y\end{aligned} \tag{4.33}$$

The DRS $\Delta\mathbf{F}^{(n)}$ of a single defect in a conducting plate moving along the x-axis below the magnetic l-dipole can be calculated using (4.23). In this case the defect is moving together with the plate from x_1 to x_2 (Fig. 4.2). In order to simplify the DRS calculations, the CS fixed to the conductor was chosen (Fig. 4.8) in which the position of the defect stays unchanged and the PM is moving from x_2 to x_1.

Having (4.33) in (4.23), the DRS takes the following form:

$$\begin{aligned}\Delta\mathbf{F}^{(n)} = l\sigma_0 v_0 \left(m_l \frac{\mu_0}{2\pi}\right)^2 \Bigg\{ &- \int_{S_D} \frac{\left[(y-y_n)^2-(x-x_n)^2\right]^2}{[(x-x_n)^2+(y-y_n)^2]^4} dxdy\mathbf{1}_x + \\ &+ 2\int_{S_D} (x-x_n)(y-y_n)\frac{(y-y_n)^2-(x-x_n)^2}{[(x-x_n)^2+(y-y_n)^2]^4} dxdy\mathbf{1}_y \Bigg\}\end{aligned} \tag{4.34}$$

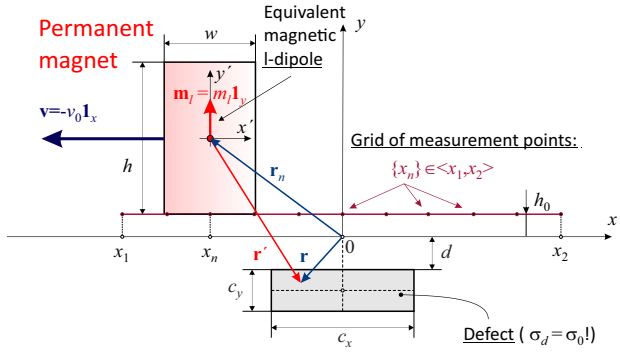

Fig. 4.8: General setup of the LET system used to calculate defect response signals

Indefinite integral terms in (4.34) can be calculated analytically and expressed by the following functions:

$$f_x(x,y,x_n,y_n) = \frac{(x-x_n)(y-y_n)}{6\left[(x-x_n)^2+(y-y_n)^2\right]^2} + \frac{1}{8(x-x_n)(y-y_n)} + \\ + \frac{1}{8(x-x_n)^2}\arctan\left(\frac{y-y_n}{x-x_n}\right) + \\ + \frac{1}{8(y-y_n)^2}\arctan\left(\frac{x-x_n}{y-y_n}\right) \tag{4.35}$$

$$f_y(x,y,x_n,y_n) = \frac{1}{12}\frac{(y-y_n)^2-(x-x_n)^2}{\left[(x-x_n)^2+(y-y_n)^2\right]^2} \tag{4.36}$$

Using (4.35) - (4.36), the analytical forms of DRS components for the rectangular defect $\{S_d : c_x \times c_y\}$ located at the depth d can easily be written as:

$$\Delta F_x^{(n)} = l\sigma_0 v_0 \left(m_l \frac{\mu_0}{2\pi}\right)^2 \times \\ \times \left[f_x\left(\frac{c_x}{2},-d,x_n,y_n\right) - f_x\left(\frac{c_x}{2},-d-c_y,x_n,y_n\right) - \right. \\ \left. - f_x\left(-\frac{c_x}{2},-d,x_n,y_n\right) + f_x\left(-\frac{c_x}{2},-d-c_y,x_n,y_n\right)\right] \tag{4.37}$$

$$\Delta F_y^{(n)} = l\sigma_0 v_0 \left(m_l \frac{\mu_0}{2\pi}\right)^2 \times \\ \times \left[f_y\left(\frac{c_x}{2},-d,x_n,y_n\right) - f_y\left(\frac{c_x}{2},-d-c_y,x_n,y_n\right) - \right. \\ \left. - f_y\left(-\frac{c_x}{2},-d,x_n,y_n\right) + f_y\left(-\frac{c_x}{2},-d-c_y,x_n,y_n\right)\right] \tag{4.38}$$

If the plate does not contain any defects and $L \gg |y_n + D|$ then, according to (4.25) and (4.37) - (4.38), Lorentz force exerted on the l-dipole located at y_n above the moving plate calculated by means of the WRA is equal to:

$$F_{x0} = l\sigma_0 v_0 \left(m_l \frac{\mu_0}{2\pi}\right)^2 \frac{\pi}{8} \left[\frac{1}{y_n^2} - \frac{1}{(y_n + D)^2}\right] \tag{4.39}$$

$$F_{y0} = 0 \tag{4.40}$$

The verification of the introduced approach of DRS calculations is performed by comparing them with results received from the finite element method (FEM) applied to the same models. FEM models and possible solution techniques were already described in details elsewhere, e.g. [154],[138].

Figure 4.9 shows the first test model consisting of an infinitely long cylindrical PM moving with a constant velocity above a conducting plate. It is easy to show that

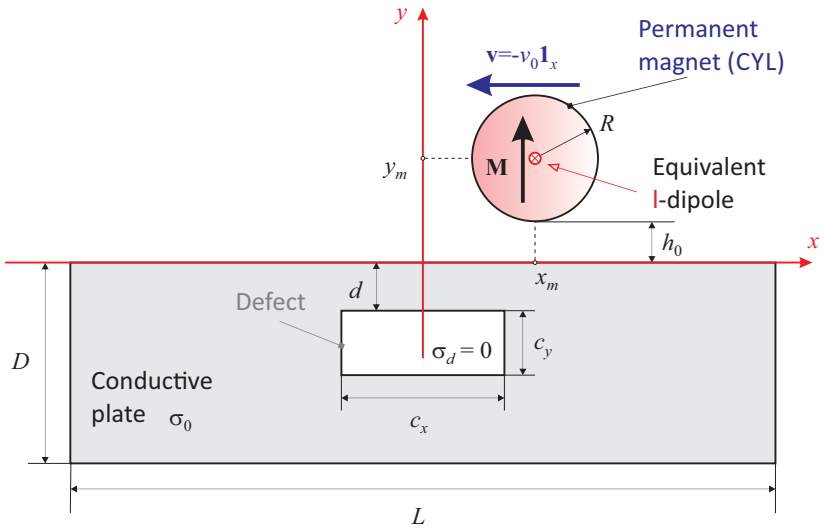

Fig. 4.9: Infinitely long, cylindrical permanent magnet of radius R, uniformly magnetized with the magnetization vector $\mathbf{M} = M\mathbf{1}_y$, moving with the constant velocity $\mathbf{v} = -v_0\mathbf{1}_x$ above a conducting plate with a rectangular defect

the magnetic flux density for $r \geqslant R$ produced by a uniformly, diametral magnetized infinitely long cylindrical PM of radius R is equal to the magnetic field (4.32) produced by the equivalent l-dipole of magnetic moment $\mathbf{m}_l = \pi R^2 \mathbf{M}$ localized at the center of the PM.

Figure 4.10 shows sample results of DRS calculations using dipolar model for the following LET configuration: (1) the PM: $R = 2.5\,\text{mm}$, $M = B_r/\mu_0 = 1.17\,\text{T}/\mu_0$, $h_0 = 11\,\text{mm}$ moving with the velocity $v_0 = 1\,\text{cm/s}$, (2) the conducting plate: $L \times D = 250\,\text{mm} \times 50\,\text{mm}$, electrical conductivity $\sigma_0 = 30.61\,\text{MS/m}$, (3) the rectangular defect: $c_x \times c_y = 12\,\text{mm} \times 2\,\text{mm}$ located at the depth $d = 2\,\text{mm}$. To validate the quality of

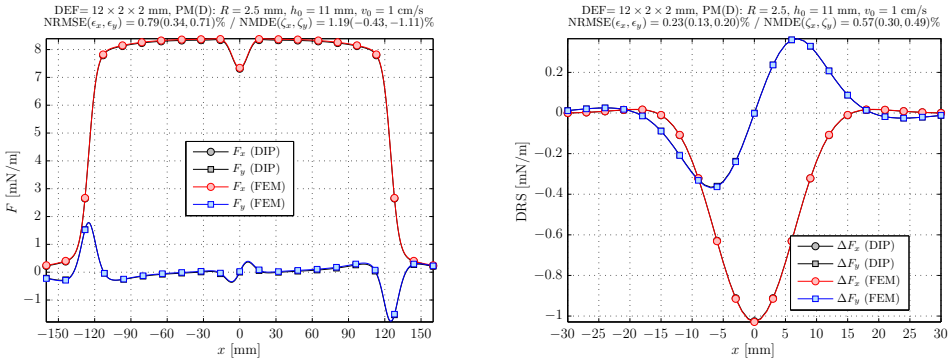

(a) Lorentz force profiles

(b) DRS near defect

Fig. 4.10: Cylindrical permanent magnet - comparison of the equivalent dipolar model with the reference FEM solution

dipolar models quantitatively, a normalized root mean square error ($NRMSE$) and a normalized maximum difference error ($NMDE$) are used. The errors are defined as:

$$NRMSE = \sqrt{\epsilon_x^2 + \epsilon_y^2}, \quad NMDE = \sqrt{\zeta_x^2 + \zeta_y^2} \tag{4.41}$$

where

$$\epsilon_c = \frac{\sqrt{\frac{1}{N}\sum_{n=1}^{N}\left[S_{c,DIP}^{(n)} - S_{c,FEM}^{(n)}\right]^2}}{\max\limits_{n=1\ldots N}\left[S_{c,FEM}^{(n)}\right] - \min\limits_{n=1\ldots N}\left[S_{c,FEM}^{(n)}\right]} 100\% \tag{4.42}$$

$$\zeta_c = \frac{S_c^{max}}{\max\limits_{n=1\ldots N}\left[S_{c,FEM}^{(n)}\right] - \min\limits_{n=1\ldots N}\left[S_{c,FEM}^{(n)}\right]} 100\% \tag{4.43}$$

$$S_c^{max} = \max_{n=1\ldots N}\left|S_{c,DIP}^{(n)} - S_{c,FEM}^{(n)}\right| \tag{4.44}$$

while index $c \in \{x, y\}$, N is a number of test points in the force/DRS profile S, and the subscript FEM denotes a reference solution calculated by FEM. Performed simulations show an excellent agreement between results received with help of the dipolar model and the FEM model. NRMS errors are less than 1% and 0.25% for Lorentz force and DRS profiles, respectively. It can be observed that the NRMSE for y-components is twice greater than errors for x-components.

The second test model is shown in Fig. 4.8. The equivalent l-dipole is located at the center of the rectangular PM moving above a conducting plate. The following LET configuration was used in test simulations: (1) the PM: $w \times h = 15\,\text{mm} \times 25\,\text{mm}$, $M = B_r/\mu_0 = 1.17\,\text{T}/\mu_0$, $h_0 = 1\,\text{mm}$, $v_0 = 1\,\text{cm/s}$, (2) the conducting plate: $L \times D = 250\,\text{mm} \times 50\,\text{mm}$, electrical conductivity $\sigma_0 = 30.61\,\text{MS/m}$, (3) the rectangular defect: $c_x \times c_y = 12\,\text{mm} \times 2\,\text{mm}$ located at the depth $d = 2\,\text{mm}$.

Results of simulations are presented in Fig. 4.11. In contrast to the first test, the use of simple, central equivalent l-dipole results in computation errors which are not acceptable, i.e., over 21% and 15% for Lorentz force and DRS, respectively.

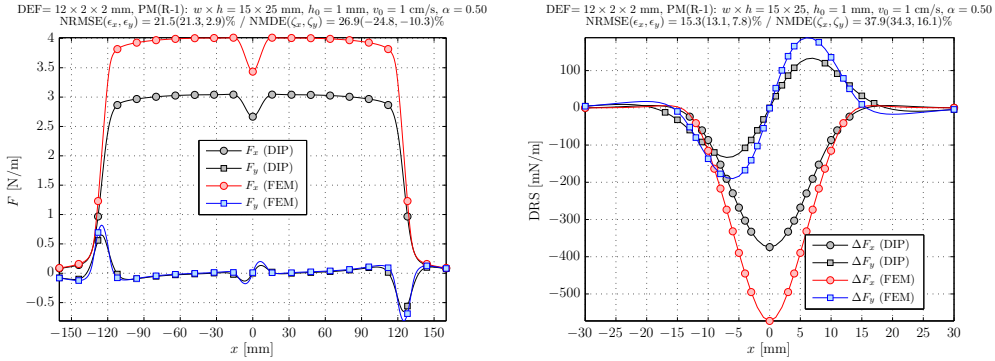

(a) Lorentz force (b) DRS

Fig. 4.11: Rectangular permanent magnet - Lorentz force and DRS profiles received from the central equivalent dipole model together with the reference FEM solution

The errors can be reduced if instead of the central l-dipole the α-model shown in Fig. 4.12 is used.

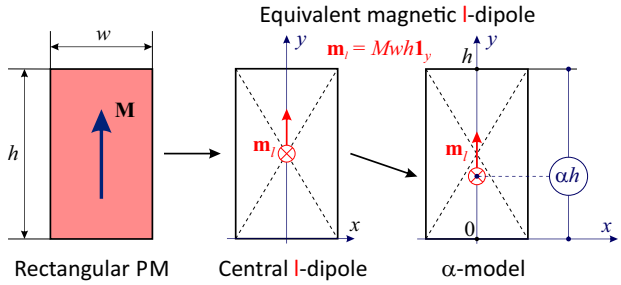

Fig. 4.12: Rectangular permanent magnet - equivalent l-dipole models

In the α-model, y-position of the equivalent l-dipole depends on the parameter α. The optimal value of the parameter $\alpha \in < 0,1 >$ can be easy found by a minimization procedure where the NRMSE of Lorentz force profiles received from the α-model comparing to the FEM model is minimized. The profiles used in the minimization procedure are calculated for the plate without any defects which means that the found value of α is not the best one for the plate with defects but ensures that the α-model gives better results than the central l-dipole model.

Figure 4.13 presents profiles for $\alpha = 0.433$. The corresponding NRMSE is equal to 1.26% and 2.39% for Lorentz force and DRS profiles, respectively.

In the current section, the simplest 2D model of a rectangular, infinitely long PM is presented, i.e., the l-dipole model. The use of a single l-dipole model together with

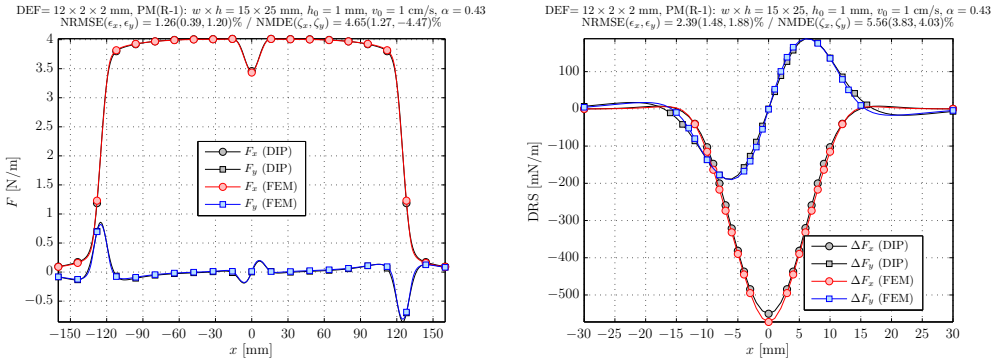

(a) Lorentz force (b) DRS

Fig. 4.13: Rectangular permanent magnet - Lorentz force and DRS profiles calculated using the α-MD model

the WRA in modeling LET system enables to find analytical formulas for Lorentz force profiles exerted on the PM above moving plate of finite width and depth with/ without defects (4.37) - (4.38). It was also shown that the use of α-model instead of the central l-dipole can significantly improve the accuracy of Lorentz force as well as the DRS calculations. In the next section, it will be shown how to calculate Lorentz force and DRS using exact magnetic field formulas for a rectangular PM.

4.2.4. 2D RECTANGULAR PERMANENT MAGNET - EXACT FIELD FORMULAS

Let the infinitely long, rectangular PM ($w \times h$) be magnetized with a constant magnetization density $\mathbf{M} = M\mathbf{1}_y$. In this case, the magnetic field produced by the rectangular PM can be calculated using an equivalent 2D current sheet model shown in Fig. 4.14. The surface sheet current densities $\mathbf{J}_S$ can be found from the cross product of $\mathbf{M}$ and the normal unit vector $\mathbf{n}$ emerging from the side bounds of the PM.

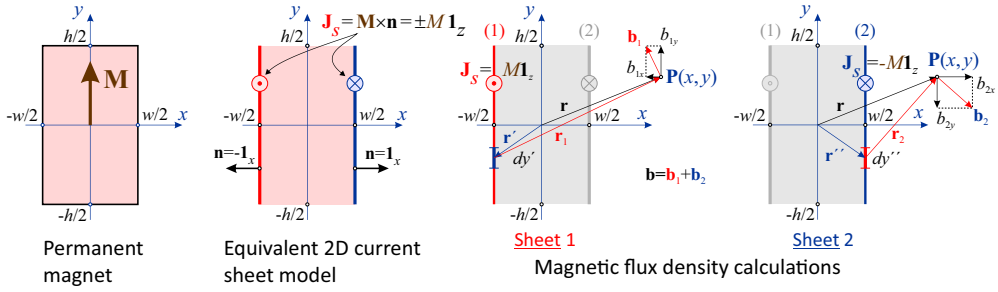

Fig. 4.14: Rectangular permanent magnet - the equivalent current sheet model

The magnetic flux density $\mathbf{B} = [B_x, B_y]^T$ at any point $\mathbf{P}$ outside the PM is calculated by a superposition of $\mathbf{B}_1$ and $\mathbf{B}_2$, the magnetic flux densities of the left and the right current bound layers as:

$$\mathbf{B} = \mathbf{B}_1 + \mathbf{B}_2 = \frac{\mu_0 M}{2\pi}\left(\int_{-h/2}^{h/2} \frac{\mathbf{1}_z \times \mathbf{r}_1}{r_1^2} dy' - \int_{-h/2}^{h/2} \frac{\mathbf{1}_z \times \mathbf{r}_2}{r_2^2} dy''\right) \tag{4.45}$$

where

$$r_1 = \sqrt{\left(x + \frac{w}{2}\right)^2 + (y - y')^2}, \qquad r_2 = \sqrt{\left(x - \frac{w}{2}\right)^2 + (y - y'')^2}$$

The integrals in (4.45) can be calculated analytically and expressed using elementary functions as:

$$B_x(x,y) = \frac{\mu_0 M}{4\pi} \ln\left[\frac{(x+\frac{w}{2})^2 + (y-\frac{h}{2})^2}{(x+\frac{w}{2})^2 + (y+\frac{h}{2})^2} \frac{(x-\frac{w}{2})^2 + (y+\frac{h}{2})^2}{(x-\frac{w}{2})^2 + (y-\frac{h}{2})^2}\right] \tag{4.46}$$

$$\begin{aligned} B_y(x,y) = \frac{\mu_0 M}{2\pi}\Bigg[&\arctan\left(\frac{y+\frac{h}{2}}{x+\frac{w}{2}}\right) - \arctan\left(\frac{y-\frac{h}{2}}{x+\frac{w}{2}}\right) + \\ &+ \arctan\left(\frac{y-\frac{h}{2}}{x-\frac{w}{2}}\right) - \arctan\left(\frac{y+\frac{h}{2}}{x-\frac{w}{2}}\right)\Bigg] \end{aligned} \tag{4.47}$$

In order to calculate DRS and Lorentz forces using the WRA, (4.46) - (4.47) were substituted into (4.23) - (4.25). Unfortunately, in this case, it was not possible to find appropriate analytical formulas as for the dipolar model. To overcome this problem, a concept of voxels grid is introduced (voxel = *vo*lume *x el*ement). It is assumed that any conducting region may be replaced by a uniform grid of conducting volumetric elements (voxels) $\Delta V_0 = l\Delta S = l\Delta x \Delta y$ of conductivity σ_0 (l is the length of the system in the z-direction, and Δx, Δy are the grid density in x- and y-direction, respectively). In each voxel flow induced eddy currents of current density $\mathbf{J}_0$. If the surface ΔS of voxels is sufficiently small, continuous distribution of eddy currents induced in the i^{th} voxel by the moving PM located at $\mathbf{r}_n$ can be approximated by a constant current density vector $\mathbf{J}_0^{(i,n)}$ calculated at $\mathbf{r}_i$, the center of the voxel. Taking above into account and using setup shown in Fig. 4.15, $\Delta\mathbf{F}^{(n)}$ given by (4.23) can be rewritten as:

$$\Delta\mathbf{F}^{(n)} = l\int_{S_d} \mathbf{J}_0 \times \mathbf{B} dS \simeq l\Delta S_1 \sum_{i=1}^{N_1} \mathbf{J}_0^{(i,n)} \times \mathbf{B}^{(i,n)} = \Delta\widetilde{\mathbf{F}}^{(n)} \tag{4.48}$$

and

$$\Delta\widetilde{\mathbf{F}}^{(n)} = l\Delta S_1 \sigma_0 v_0 \sum_{i=1}^{N_1} \left[-B_y^{(i,n)} B_y^{(i,n)} \mathbf{1}_x + B_x^{(i,n)} B_y^{(i,n)} \mathbf{1}_y\right] \tag{4.49}$$

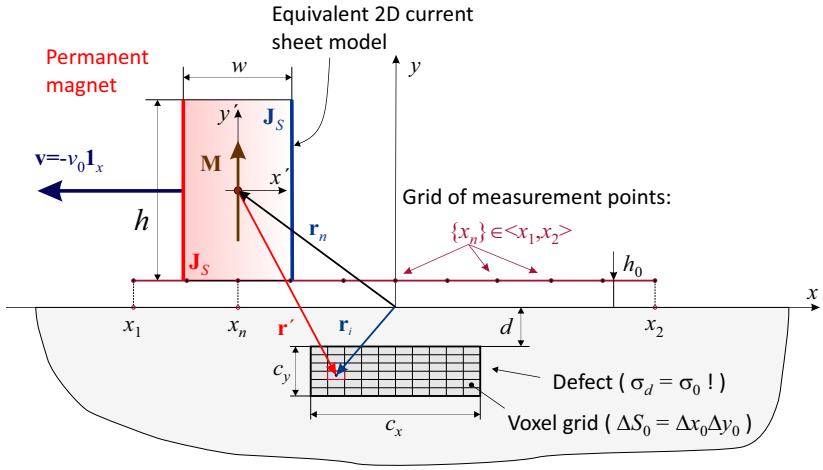

Fig. 4.15: LET system setup for DRS calculations - 2D current sheet model of the rectangular PM and the grid of voxels concept for a defect modeling

where N_1 is the total number of voxels in S_d region, $B_x^{(i,n)} = B_x(x_i - x_n, y_i - y_n)$, $B_y^{(i,n)} = B_y(x_i - x_n, y_i - y_n)$, $y_n = h_0 + h/2$, and $B_x(x,y)$, $B_y(x,y)$ are defined by (4.46) and (4.47), respectively. Similarly, the Lorentz force $\widetilde{\mathbf{F}}^{(n)}$ exerted on the rectangular PM moving above the conducting plate ($L \times D$) with K ideal defects can be calculated as:

$$\begin{aligned}\widetilde{\mathbf{F}}^{(n)} =& l\Delta S_0 \sigma_0 v_0 \sum_{i=1}^{N_0} \left[B_y^{(i,n)} B_y^{(i,n)} \mathbf{1}_x - B_x^{(i,n)} B_y^{(i,n)} \mathbf{1}_y \right] + \\ &+ l\sigma_0 v_0 \sum_{k=1}^{K} \Delta S_k \sum_{j=1}^{N_k} \left[-B_y^{(j,n)} B_y^{(j,n)} \mathbf{1}_x + B_x^{(j,n)} B_y^{(j,n)} \mathbf{1}_y \right]\end{aligned} \tag{4.50}$$

where $(N_0, \Delta S_0)$ and $(N_k, \Delta S_k)$ are total voxel numbers and voxel grid densities of the plate and defects voxel models, respectively.

Figure 4.16 shows results of sample simulations performed for the following LET configuration: (1) PM: $w \times h = 15\,\text{mm} \times 25\,\text{mm}$, $M = B_r/\mu_0 = 1.17\,\text{T}/\mu_0$, $h_0 = 1\,\text{mm}$, (2) conducting plate: $L \times D = 250\,\text{mm} \times 50\,\text{mm}$, $\sigma_0 = 30.61\,\text{MS/m}$, $v_0 = 1\,\text{cm/s}$, (3) rectangular defect: $c_x \times c_y = 12\,\text{mm} \times 2\,\text{mm}$, $d = 2\,\text{mm}$, and voxel grid densities $\Delta S_0 = \Delta S_1 = \Delta x \times \Delta y = 1\,\text{mm} \times 1\,\text{mm}$. The results of simulations are in excellent accordance with the results obtained by the reference FEM, i.e., the NRMSE given by (4.41) is equal to 0.65% and 0.16% for the Lorentz force and the DRS profiles, respectively.

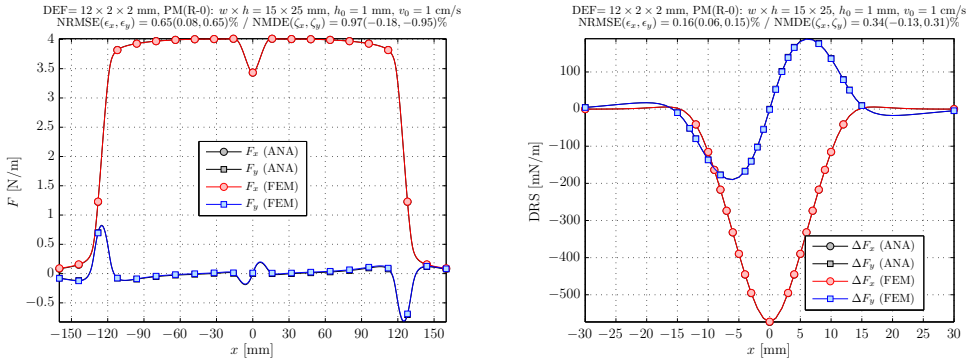

(a) Lorentz force

(b) DRS

Fig. 4.16: Rectangular PM - Lorentz force and DRS profiles calculated with exact magnetic field formulas for voxel grid density $\Delta x \times \Delta y = 1\,\text{mm} \times 1\,\text{mm}$

4.2.5. RÉSUMÉ

In Section 4.2., two analytical approaches of Lorentz force calculations in 2D LET systems are described. In both approaches, the weak reaction formulation of the LET problem is applied, i.e., the corresponding magnetic Reynolds number is much less than 1. Both approaches are based on the principle of superposition to calculate the defect response signals. In the first approach, the PM is replaced by a single equivalent magnetic l-dipole located inside the PM. This enables to find analytical formulas of DRSs for one or more rectangular defects as well as the global Lorentz force profile exerted on the PM above the moving plate. The position of the l-dipole can be found using procedure which minimizes the NRMSE between the Lorentz force profile calculated from the α-model and the reference solution. In the second approach, the exact analytical formulas describing the magnetic field generated by a rectangular PM are used. In this case, it was not possible to find analytical expressions for DRS. Therefore, a semi-analytical approach based on regular grids of voxels replacing the conductor as well as defects is introduced. Sample profiles of DRS and Lorentz forces calculated by both methods together with reference solutions obtained by FEM are also shown.

4.3. MODELING OF 3D PERMANENT MAGNETS

4.3.1. INTRODUCTION

An approximation of an arbitrary permanent magnet with one magnetic dipole provides sufficient solution for the magnetic field only at large distances [106]. Analytical description of the PM magnetic field is of great interest, but possibilities to derive an analytic solution and its integral are restricted and becomes a challenge for magnets of complex shapes. To overcome above limitations, it is introduced the magnetic

dipoles model (MDM) of a 3D permanent magnet in which the PM is substituted by an assembly of magnetic dipoles. The MDM allows to model PM of arbitrary shape by appropriate placing of magnetic dipoles in the PM volume. Optimal positions of magnetic dipoles can be found with help of the optimization procedure which minimizes the error between the magnetic field obtained from the MDM and the reference solution. An accuracy of MD models depends on a number of magnetic dipoles applied in the model. Further, an influence of the number of magnetic dipoles on the MDM accuracy is investigated. For simple shapes of 3D permanent magnets (e.g. cube, cylinder, cylinder rings, cylinder segments), it is possible to find analytical formulas describing the magnetic field produced by them [7, 27, 33, 41, 43, 44, 54, 112, 113, 117, 128]. Analytical formulas provide accurate modeling of the magnetic field at any point in space and can serve as reference solutions necessary for evaluation of the optimal MD models. The charge model enables to find an analytic solution of the magnetic field at each point outside rectangular PM in a form of elementary functions [2, 137]. For a cylindrical PM, the surface current model is applied [33, 44]. In the surface current model an axially magnetized with constant magnetization cylindrical PM is replaced by an equivalent surface current flowing in azimuthal direction on the lateral cylinder surface. In this case, the magnetic flux density outside the PM can be described with help of the generalized complete elliptic integrals [33].

4.3.2. MAGNETIC DIPOLES MODELS (MDM)

The idea of the magnetic dipoles model (MDM) consists in replacing the modeled PM by a regular grid of volumetric elements of identical volume (voxels). Shape of voxels depends on the PM shape, e.g. for a rectangular PM, voxels are small cuboids whereas for a cylindrical PM central voxels are small cylinders and the others are hollow cylinder sectors. It is assumed that only one magnetic dipole can be inserted into the voxel. Because all voxels have the same volume, magnetic moments of inserted magnetic dipoles are the same and equal $\mathbf{m} = \mathbf{M}V_0/N_D$, where $\mathbf{M}$ is the PM magnetization vector, V_0 is the volume of PM, and N_D denotes the number of magnetic dipoles used in the MDM. Positions of magnetic dipoles in voxels can be defined arbitrary, e.g. by using the center of gravity (COG) of the voxel. However, in the presented approach, the positions are determined with help of an optimization procedure which minimizes an error between the magnetic flux density obtained using MDM and the reference solution. The reference solution can be calculated analytically for simple PM shapes like cuboids, cylinders, or numerically for complicated forms of the PM.

4.3.3. α-MDM OF RECTANGULAR PERMANENT MAGNET

The permanent magnet in the form of rectangular cuboid with the base edge length a, the height h is located at the point $\mathbf{r}_0 = [x_0, y_0, z_0]^T$ corresponding to the COG of the PM base wall (Fig. 4.17). Edges of the PM are parallel to the axes of the global Cartesian coordinate system. The PM is magnetized along z-axis, where $\mathbf{M} = M\mathbf{1}_z$ denotes a magnetization vector. According to the idea of MDM, the rectangular PM

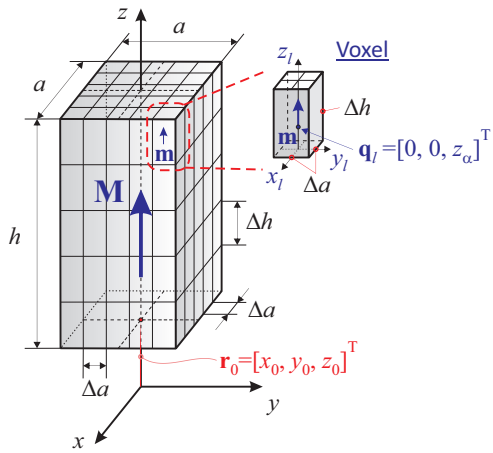

Fig. 4.17: Magnetic dipoles model α-MDM of a rectangular permanent magnet

is composed of a set of $N_D = N_a^2 N_h$ voxels, where N_a is a number of voxels along base edges and N_h is a number of voxels along height edges. Volume of each voxel is equal to $V_M = \Delta a^2 \Delta h = (a/N_a)^2 (h/N_h) = V_0/N_D$, where $V_0 = a^2 h$ denotes volume of the PM and N_D is the total number of magnetic dipoles in α-MDM. The moment of one magnetic dipole is given by $\mathbf{m} = m\mathbf{1}_z = \mathbf{M}V_M$. The magnetic flux density $\mathbf{B} = [B_x, B_y, B_z]^T$ at any point $\mathbf{r} = [x, y, z]^T$ outside the PM can be calculated as a superposition of magnetic flux densities of all dipoles in the α-MDM:

$$\mathbf{B}(x,y,z) = \sum_{m=1}^{N_D} \mathbf{b}_m(x,y,z) \tag{4.51}$$

where $\mathbf{b}_m(x,y,z)$ is the magnetic flux density of the m^{th} magnetic dipole located at $\mathbf{r}_m = [x_m, y_m, z_m]^T$ described by the formula

$$\mathbf{b}_m = V_M \frac{\mu_0}{4\pi} \left[3 \frac{\mathbf{M} \cdot (\mathbf{r} - \mathbf{r}_m)}{|\mathbf{r} - \mathbf{r}_m|^5} (\mathbf{r} - \mathbf{r}_m) - \frac{\mathbf{M}}{|\mathbf{r} - \mathbf{r}_m|^3} \right] \tag{4.52}$$

(4.52) can be written in the Cartesian coordinate system as

$$\mathbf{b}_m(x,y,z) = \begin{bmatrix} b_{x,m} \\ b_{y,m} \\ b_{z,m} \end{bmatrix} = M V_M \frac{\mu_0}{4\pi} \begin{bmatrix} 3\dfrac{(x-x_m)(z-z_m)}{r_m^5} \\ 3\dfrac{(y-y_m)(z-z_m)}{r_m^5} \\ 3\dfrac{(z-z_m)^2}{r_m^5} - \dfrac{1}{r_m^3} \end{bmatrix} \tag{4.53}$$

$r_m = \sqrt{(x-x_m)^2+(y-y_m)^2+(z-z_m)^2}$ is the distance between the observation point $\mathbf{r}$ and the position $\mathbf{r}_m$ of the m^{th} magnetic dipole. Positions $\mathbf{r}_m$ of magnetic dipoles in α-MDM are defined as

$$\mathbf{r}_m = \mathbf{r}_0 + \mathbf{q}_{ijk} + \mathbf{q}_l, \quad \begin{cases} x_m = x_0 - \dfrac{a}{2} + (i-\dfrac{1}{2})\Delta a, & i = 1,\ldots,N_a \\ y_m = y_0 - \dfrac{a}{2} + (j-\dfrac{1}{2})\Delta a, & j = 1,\ldots,N_a \\ z_m = z_0 + (k-1)\Delta h + z_\alpha, & k = 1,\ldots,N_h \end{cases} \tag{4.54}$$

where $m = i + (j-1)N_a + (k-1)N_a^2$ is the index of the m^{th} magnetic dipole, $\mathbf{r}_0 = [x_0, y_0, z_0]^T$ is the position of the center of the PM lower base and $z_\alpha = \alpha\Delta h$ defines the local z-position of the magnetic dipole in the corresponding voxel (Fig. 4.17). Selection of the parameter α as $\alpha \in <0,1>$ ensures that all magnetic dipoles are located inside respective voxels.

4.3.4. (α,β)-MDM OF CYLINDRICAL PERMANENT MAGNETS

The axially magnetized cylindrical permanent magnet ($\mathbf{M} = M\mathbf{1}_z$) of radius R and height H is placed at $\mathbf{r}_0 = [x_0, y_0, z_0]^T$ (Fig. 4.18). The magnetic field outside a cylin-

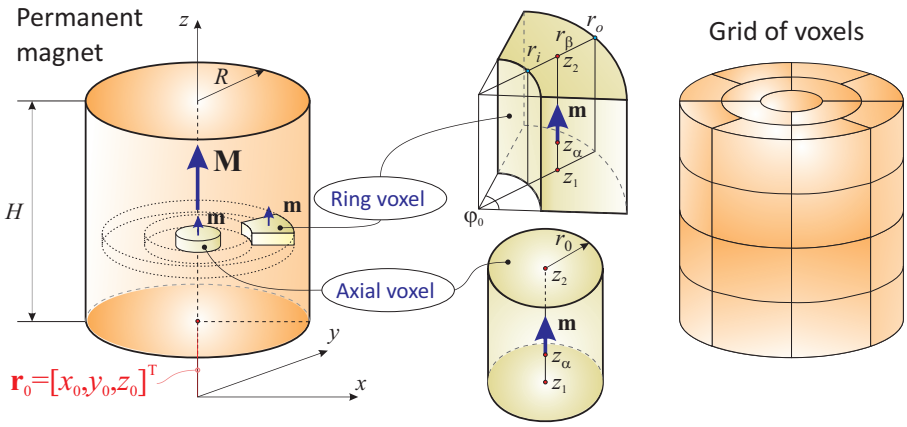

Fig. 4.18: Magnetic dipoles model (α,β)-MDM of a cylindrical permanent magnet

drical PM can be calculated using formulas (4.51) - (4.53) with different positions of magnetic dipoles in MDM. Magnetic dipoles of (α,β)-MDM are localized at a regular grid of voxels each having the same volume $V_M = V_0/N_D$, where $V_0 = \pi R^2 H$, and N_D is a total number of magnetic dipoles. The (α,β)-MDM grid consists of N_h slices. Each slice contains one central cylindrical voxel (axial voxel) of radius r_0 and height $\Delta h = H/N_h$, and N_R concentric rings with voxels of the form of a hollow cylinder

segment of inner radius r_i, outer radius r_o, segment angle φ_0, and the height Δh. The number of voxels (segments) N_S^i in the i^{th} ring is determined as follows:

$$N_S^i = 4\left\lfloor \frac{\pi}{2}\left(i - \frac{1}{2}\right)\right\rfloor \geqslant 4, \quad i = 1, \ldots, N_R \tag{4.55}$$

where $\lfloor \cdot \rfloor$ denotes the floor (greatest integer) function. N_S^i is always a multiple of 4 to ensure the symmetry of the (α, β)-MDM. The total number of magnetic dipoles N_D can be found as

$$N_D = N_H\left(1 + \sum_{i=1}^{N_R} N_S^i\right) \tag{4.56}$$

The radius r_0 of central voxels is given by

$$r_0 = \sqrt{\frac{V_M}{\pi \Delta h}} \tag{4.57}$$

The inner and outer radii of ring voxels are given by the following recurrence:

$$r_{i+1} = \sqrt{\frac{V_M N_S^i}{\pi \Delta h} + r_i^2}, \quad i = 1, \ldots, N_R - 1, \quad r_1 = r_0, r_{N_R} = R \tag{4.58}$$

Magnetic dipoles in ring voxels are located on a symmetry plane of the corresponding voxel (Fig. 4.18) while dipoles in axial voxels are placed on the cylinder main axis. Their positions in the slice are determined using the following formula

$$\begin{cases} r_\beta^i = \begin{cases} 0, & i = 0 \quad (axial\ voxel) \\ (1-\beta) r_i + \beta r_{i+1}, & i = 1, \ldots, N_R \quad (ring\ voxels) \end{cases} \\ z_\alpha = \alpha \Delta h \end{cases} \tag{4.59}$$

where parameters $(\alpha, \beta) \in < 0, 1 >$ ensure that dipoles are located inside corresponding voxels and are the same for voxels. The position $\mathbf{r}_m = [x_m, y_m, z_m]^T$ of the m^{th} magnetic dipole is defined in the global Cartesian coordinate system as

$$\mathbf{r}_m = \mathbf{r}_0 + \mathbf{q}_{ijk} = \begin{bmatrix} x_m = x_0 + r_\beta^i \cos\theta_j \\ y_m = y_0 + r_\beta^i \sin\theta_j \\ z_m = z_0 + (k-1)\Delta h + z_\alpha \end{bmatrix} \tag{4.60}$$

where $\mathbf{r}_0 = [x_0, y_0, z_0]^T$ is the position of the PM base center and θ_j is equal to

$$\theta_j = 2\pi \frac{j - \frac{1}{2}}{N_S^i}, \quad \begin{cases} i = 1, \ldots, N_R \\ j = 1, \ldots, N_S^i \\ k = 1, \ldots, N_H \end{cases} \tag{4.61}$$

Figure 4.19 shows sample grids of voxels for one slice of (α_o, β_o)-MDM together with magnetic dipoles obtained for $N_R = \{1, 6\}$ and $N_H = \{2, 18\}$, respectively. N_{D1} denotes the number of magnetic dipoles in one slice.

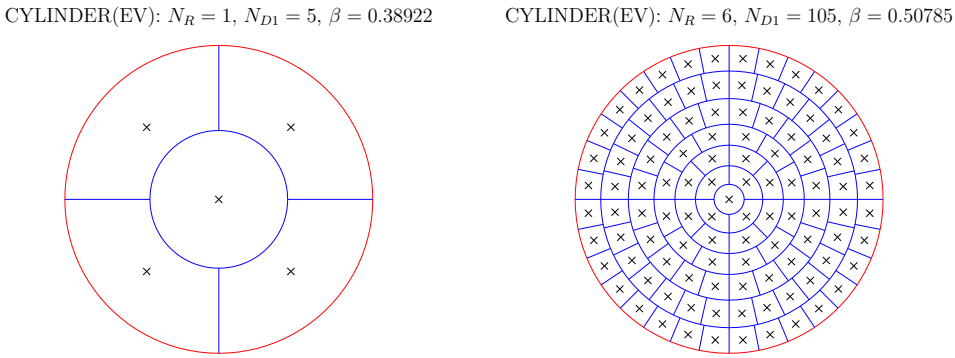

Fig. 4.19: Sample grids of voxels with magnetic dipoles (dipoles are marked with $\times$)

4.3.5. CUBOID/CYLINDER - ANALYTICAL FORMULAS OF MAGNETIC FLUX DENSITY

The magnetic flux density $\mathbf{B}$ at the point $\mathbf{r} = [x, y, z]^T$ outside a rectangular PM magnetized with the constant magnetization vector $\mathbf{M} = M\mathbf{1}_z$ shown in Fig. 4.20 can be found using the charge model [42] with fictitious magnetic charges of density $\sigma_m = \mu_0 \mathbf{M} \cdot \mathbf{n}$ placed on the top $(z = h + z_0, \mathbf{n} = \mathbf{1}_z)$ and the bottom $(z = z_0, \mathbf{n} = -\mathbf{1}_z)$ wall of PM.

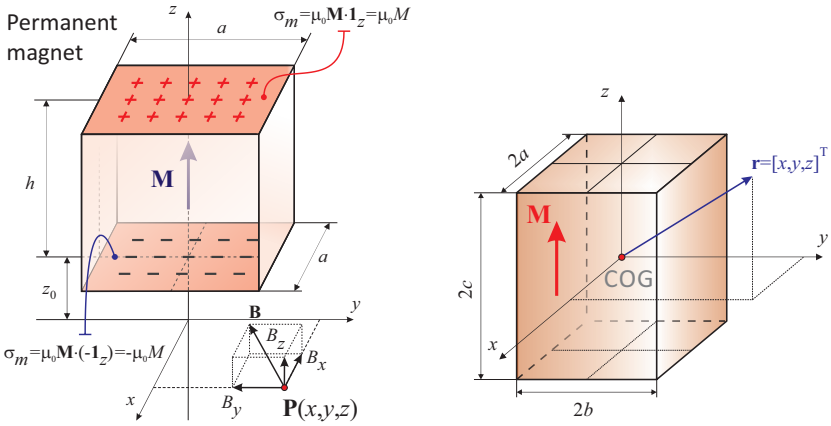

(a) Charge model (b) Calculation setup used in [137]

Fig. 4.20: Charge model of a rectangular permanent magnet

In this case, the magnetic flux density is described by the following formula

$$\mathbf{B}(\mathbf{r}) = \frac{1}{4\pi}\oint_S \frac{\sigma_m(\mathbf{r}')(\mathbf{r}-\mathbf{r}')}{|\mathbf{r}-\mathbf{r}'|^3}dS' = \\ = \frac{\mu_0 M}{4\pi}\int_{-a/2}^{a/2}\int_{-a/2}^{a/2}\left(\left.\frac{\mathbf{r}-\mathbf{r}'}{|\mathbf{r}-\mathbf{r}'|^3}\right|_{z'=z_0} - \left.\frac{\mathbf{r}-\mathbf{r}'}{|\mathbf{r}-\mathbf{r}'|^3}\right|_{z'=z_0+h}\right)dx'dy' \tag{4.62}$$

where $\mathbf{r} = [x,y,z]^T$, $\mathbf{r}' = [x',y',z']^T$,and $\mathbf{B} = [B_x, B_y, B_z]^T$.

Magnetic flux density components B_x, B_y and B_z at point $\mathbf{r} = [x,y,z]^T$ produced by the rectangular PM of dimensions $2a \times 2b \times 2c$ with the COG located at the origin of the coordinate system and all edges parallel to the coordinate axes, magnetized along z-axis with the constant magnetization $\mathbf{M} = M\mathbf{1}_z$ (Fig. 4.20b) are given according to [137] by

$$B_x(x,y,z) = \frac{\mu_0 M}{4\pi}\ln\frac{F_2(-x,y,-z)F_2(x,y,z)}{F_2(-x,y,z)F_2(x,y,-z)} \tag{4.63}$$

$$B_y(x,y,z) = \frac{\mu_0 M}{4\pi}\ln\frac{F_2(-y,x,-z)F_2(y,x,z)}{F_2(-y,x,z)F_2(y,x,-z)} \tag{4.64}$$

$$B_z(x,y,z) = \frac{\mu_0 M}{4\pi}[F_1(x,y,z) + F_1(-x,-y,-z)+ \\ + F_1(x,y,-z) + F_1(-x,-y,z)+ \\ + F_1(-x,y,z) + F_1(x,-y,-z)+ \\ + F_1(-x,y,-z) + F_1(x,-y,z)] \tag{4.65}$$

where functions $F_1(\cdot)$ and $F_2(\cdot)$ are defined as:

$$F_1(x,y,z) = \arctan\frac{(x+a)(y+b)}{(z+c)\sqrt{(x+a)^2+(y+b)^2+(z+c)^2}} \tag{4.66}$$

$$F_2(x,y,z) = \frac{\sqrt{(x+a)^2+(y-b)^2+(z+c)^2}+b-y}{\sqrt{(x+a)^2+(y+b)^2+(z+c)^2}-b-y} \tag{4.67}$$

The magnetic field generated by the cylindrical PM of radius R, height H, magnetized along main axis $\mathbf{1}_z$ with a constant magnetization vector $\mathbf{M} = M\mathbf{1}_z$ can be found using the surface current model (Fig. 4.21). In this model, the PM is replaced by an equivalent infinitely thin solenoid of radius R and height H defined by the surface current density $\mathbf{J}_S = \mathbf{M}\times\mathbf{n} = \mathbf{M}\times\mathbf{1}_r = M\mathbf{1}_\varphi$. Using the Biot-Savart law, the magnetic flux density of the PM can be calculated as:

$$\mathbf{B}(\mathbf{r}) = \frac{\mu_0}{4\pi}\oint_S \frac{\mathbf{J}_S(\mathbf{r}')\times(\mathbf{r}-\mathbf{r}')}{|\mathbf{r}-\mathbf{r}'|^3}dS' \tag{4.68}$$

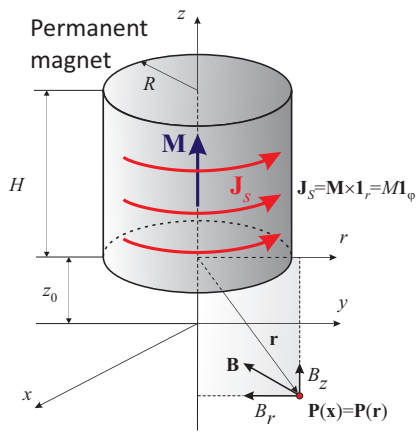

Fig. 4.21: Surface current model of a cylindrical permanent magnet

If the cylindrical permanent magnet $2R \times H$ is localized in the cylindrical coordinate system so that its COG coincides with the origin then the components B_r, B_z of the generated magnetic field are given by the following expressions [33]:

$$B_r(r,z) = \frac{\mu_0 M}{\pi}[\alpha_+ C(k_+,1,1,-1) - \alpha_- C(k_-,1,1,-1)] \tag{4.69}$$

$$B_z(r,z) = \frac{\mu_0 M}{\pi}\frac{R}{R+r}[\beta_+ C(k_+,\gamma^2,1,\gamma) - \beta_- C(k_-,\gamma^2,1,\gamma)] \tag{4.70}$$

where

$$\begin{aligned} z_\pm &= z \pm \frac{H}{2}, \quad \gamma = \frac{R-r}{R+r}, \quad k_\pm = \sqrt{\frac{z_\pm^2 + (R-r)^2}{z_\pm^2 + (R+r)^2}}, \\ \alpha_\pm &= \frac{R}{\sqrt{z_\pm^2 + (R+r)^2}}, \quad \beta_\pm = \frac{z_\pm}{\sqrt{z_\pm^2 + (R+r)^2}} \end{aligned} \tag{4.71}$$

The function $C(\cdot)$ denotes the generalized complete elliptic integral [33] defined as:

$$C(k_c,p,c,s) = \int_0^{\pi/2} \frac{c\cos^2\varphi + s\sin^2\varphi}{(\cos^2\varphi + p\sin^2\varphi)\sqrt{\cos^2\varphi + k_c^2\sin^2\varphi}} d\varphi \tag{4.72}$$

The magnetic field on the cylinder axis $(r = 0)$ is given by the following expression:

$$B_r(0,z) = 0, \quad B_z(0,z) = M\frac{\mu_0}{2}\left(\frac{z_+}{\sqrt{z_+^2 + R^2}} - \frac{z_-}{\sqrt{z_-^2 + R^2}}\right) \tag{4.73}$$

4.3.6. MAGNETIC DIPOLES MODELS - OPTIMAL PARAMETERS

Parameters α and β in (4.54) and (4.59) can be found using the following minimization procedure. First, a test region consisting of a regular grid of points positioned in the region below the PM is defined (Fig. 4.22).

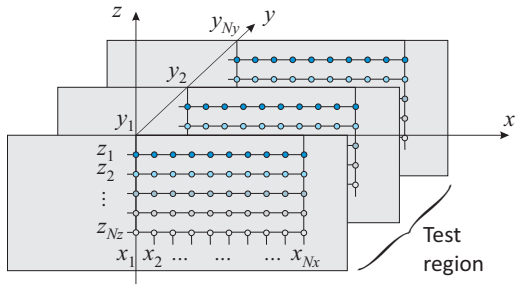

Fig. 4.22: Test region used in minimization procedures

The test region is composed of N_z XY-grid point layers $\mathbf{G}_k : \{x_i = (i-1)\Delta x,\, y_j = (j-1)\Delta y, i = 1,\ldots,N_x, j = 1,\ldots,N_y\}$ uniformly distributed along the z-axis at $\{z_k = -d_0 - (k-1)\Delta z, k = 1,\ldots,N_z\}$. Due to symmetry of analyzed permanent magnets, the test region is defined only in the first quadrant $(x \geqslant 0, y \geqslant 0)$. In the test region $\mathbf{G} = \{\mathbf{G}_k, k = 1,\ldots,N_z\}$, the average normalized root mean square error (NRMSE) is defined as follows:

$$NRMSE_G = \sqrt{\frac{1}{N_z}\sum_{k=1}^{N_z}\left[(\epsilon_x^k)^2 + (\epsilon_y^k)^2 + (\epsilon_z^k)^2\right]} \tag{4.74}$$

$$\epsilon_c^k = \frac{\sqrt{\frac{1}{N_x N_y}\sum_{i=1}^{N_x}\sum_{j=1}^{N_y}\left[B_c^{MDM}(x_i,y_j,z_k) - B_c^{REF}(x_i,y_j,z_k)\right]^2}}{(\max B_c^{REF} - \min B_c^{REF})|_{z=z_k}} 100\% \tag{4.75}$$

where $c \in \{x,y,z\}$, ϵ_c^k is the NRMSE of the k^{th} test layer, B_c^{MDM} is the c-component of the magnetic flux density calculated using the α- or (α,β)-MDM, B_c^{REF} is the c-component of the reference magnetic flux density found analytically or numerically.

To find optimal value α_o of the α-MDM (for given number of magnetic dipoles), the minimum of (4.74) is searched using golden section algorithm [111]. To find optimal values α_o and β_o in the (α,β)-MDM, the minimum of (4.74) is searched using the simplex search method [99]. In this case, $\alpha_o, \beta_o \in < 0, 1 >$ and the initial guess is set to $(\alpha_o = \beta_o = 1/2)$.

4.3.7. RECTANGULAR PERMANENT MAGNET - RESULTS OF SIMULATIONS

The rectangular permanent magnet under investigation with $a = 15\,\text{mm}, h = 25\,\text{mm}$, the magnetization $\mu_0 M = 1.17\,\text{T}$ is located at the lift-off distance $z_0 = h_0 = 1\,\text{mm}$

above $X0Y$ plane (see benchmark problems in [142]). The evaluated test region $\mathbf{G}$ in the optimization procedure (Section 4.3.6.) consists of $N_z = 5$ layers $z = z_k$ with $d_0 = -1\,\text{mm}$ and $\Delta z = 1\,\text{mm}$, i.e., the closest test layer $\mathbf{G}_1$ is about 2 mm from the bottom base of the cuboid. In each layer, a grid of $N_x \times N_y = 31 \times 31$ points with grid step $\Delta x = \Delta y = 1\,\text{mm}$ in the first quadrant of $X0Y$ is generated. The accuracy of the α-MD models is investigated at test planes $(z = z_k)$ by calculating the NRMSE of magnetic flux density produced by the optimal α_o-MDM and using the analytic charge model.

Figure 4.23 shows results calculated for various number of magnetic dipoles used in the α_o-MD models. Results are collected in groups using N_a (number of voxels

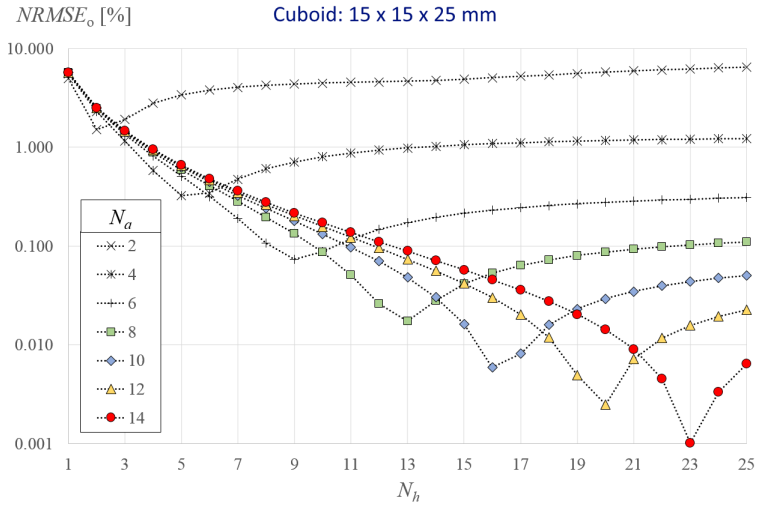

Fig. 4.23: NRMS errors of optimal α_o-MD models versus a number of slices N_h

along a-edges) as a leading constant parameter and N_h (number of slices) as a varying parameter. Figure 4.23 shows that for each N_a group, the optimal number of slices (i.e. the total number of dipoles) related to the minimum of NRMSE can be found, e.g., for $N_a = \{2 : 2 : 14\}$, the optimal numbers of slices equal $N_h = \{2, 5, 9, 13, 16, 20, 23\}$ which correspond to minimum errors $NMRSE_{opt} = \{1.52, 0.32, 0.07, 0.02, 0.006, 0.002, 0.001\}\%$, respectively. The following conclusion can be formulated: more dipoles is defined in one slice the higher is the optimal number of slices in the α-MDM corresponding to the minimum of NRMSE.

Figure 4.24 presents NRMSE calculated for 0.5-MD models with dipoles located at centers of voxels and the same N_a groups as previously. Although shapes of NRMSE group curves are similar to curves for α_o-MD models, minimums of NRMSE for small N_a are located at higher number of slices, i.e., minimum errors $NRMSE_{0.5} = \{1.91, 0.36, 0.09, 0.02, 0.01, 0.003, 0.002\}\%$ correspond to $N_h = \{3, 6, 10, 13, 17, 20, 23\}$, respectively. For $\alpha = 0.5$, positions of the NRMSE minimums correspond to the magnetic dipole models with voxels $\Delta a \times \Delta a \times \Delta h$ whose shape is closest to the cube (Δa^3), i.e., if N_a is given, then the number of slices ensuring the minimum of NRMSE is equal to $N_h = \lfloor h/\Delta a \rfloor$, where $\Delta a = a/N_a$, and $\lfloor \cdot \rfloor$ is the `floor` function.

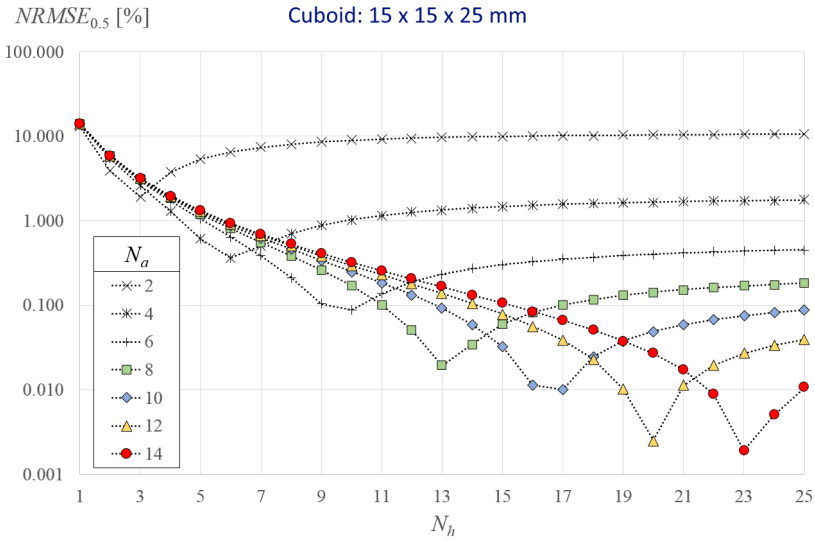

Fig. 4.24: NRMS errors of 0.5-MD models versus a number of slices N_h

Figure 4.25 shows the dependence of optimal parameter α_o on the total number of magnetic dipoles used in α_o-MD models. It can be seen that α_o corresponding to the optimal number of slices is less than $\alpha = 0.5$ for each N_a group and strives to 0.5 (the center of voxel) when the number of dipoles increases.

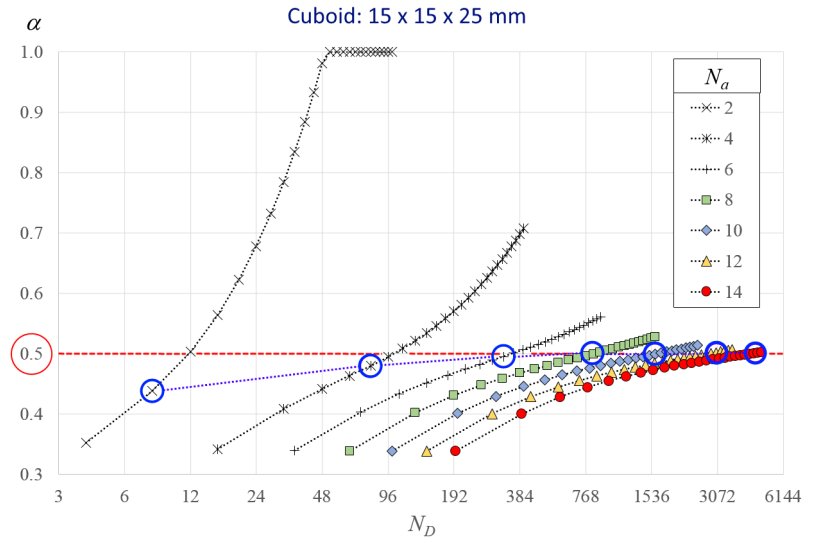

Fig. 4.25: The optimal parameter α_o versus the total number of magnetic dipoles in α_o-MD models (blue circles mark α_o corresponding to the optimal number of slices for each N_a group)

Figure 4.26 shows sample distributions of magnetic flux densities B_x and B_z in the vicinity of the magnet calculated for $y = 0$ and $z = -1\,\text{mm}$ (the distance to the PM equals $d = 2\,\text{mm}$, and $z_0 = h_0 = 1\,\text{mm}$ denotes the PM lift-off) for two optimal α_o-MD models: the first with $N_D = 2 \times 2 \times 2 = 8$ dipoles, and the second one with $N_D = 8 \times 8 \times 13 = 832$ dipoles ($B_y = 0$ at $y = 0$, due to symmetry). The magnetic

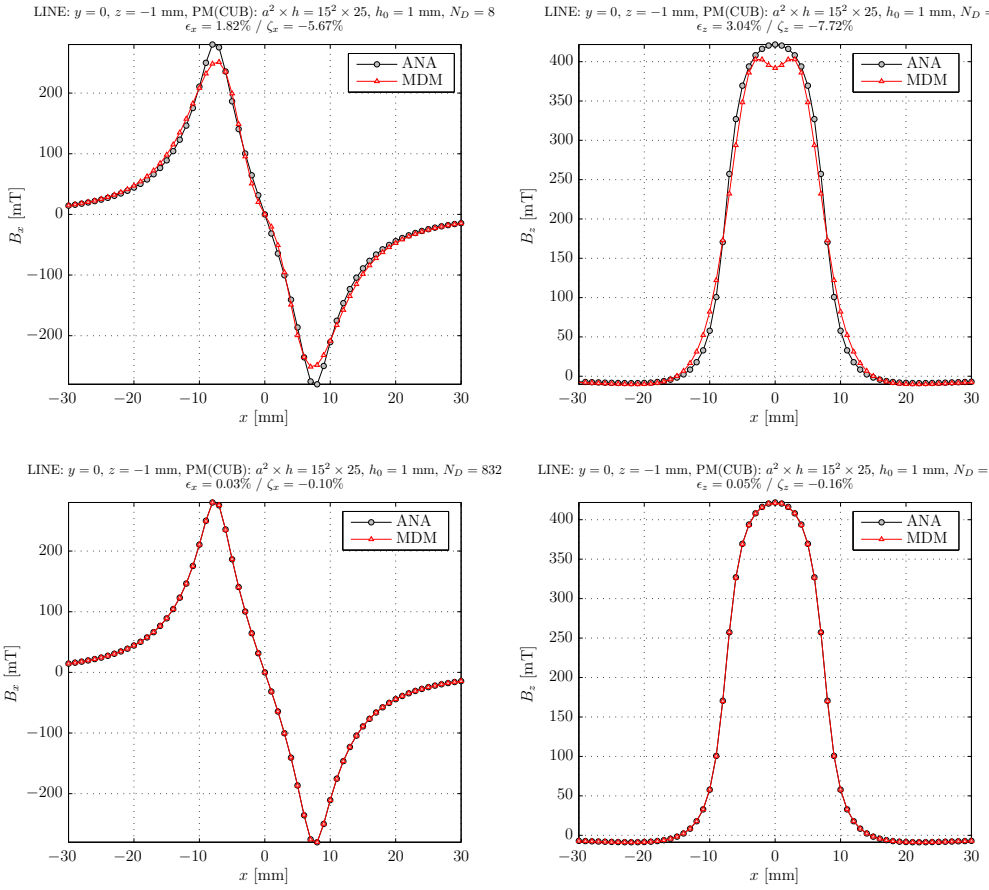

Fig. 4.26: Magnetic flux density distributions - the comparison of optimal α_o-MDM with the analytical model (*ANA*): (1) $N_D = 8$, $\alpha_o = 0.43842$, $NMRSE_{opt} = 1.52\%$ (*up*), (2) $N_D = 832$, $\alpha_o = 0.4992$, $NMRSE_{opt} = 0.02\%$ (*down*)

field far away from the PM is good approximated by both α_o-MD models. However, under the PM ($x \in < -7.5\,\text{mm}, 7.5\,\text{mm} >$), significant discrepancies of the first model ($N_D = 8$) comparing to the analytical solution can be observed. The maximum of B_x is smaller and B_z drops to a local minimum. The reason for this is the distance between dipoles in the α_o-MDM ($\Delta a = 7.5\,\text{mm}$) which is much greater than the distance of test points to the PM ($d = 2\,\text{mm}$). In this case, the closest magnetic dipole has the strongest influence on the magnetic field calculated at the actual test point. This effect, observed

as oscillations of magnetic field under the PM, is called a dipolar effect. If the distance between dipoles is small enough, e.g. for $N_D = 832$, $\Delta a = 1.875\,\text{mm}$, the dipolar effect is negligible. It should also be noted that for all cases, the NRMSE of B_z component is larger than the error of B_x component.

4.3.8. CYLINDRICAL PERMANENT MAGNET - RESULTS OF SIMULATIONS

The cylindrical PM of dimensions $2R \times H = 15\,\text{mm} \times 25\,\text{mm}$, located at the lift-off distance $z_0 = 1\,\text{mm}$ above $X0Y$ plane, and axially magnetized with the magnetization $\mu_0 M = 1.17\,\text{T}$ is investigated. A set of (α, β)-MD models specified by the number of concentric rings in one slice $N_R \in \{1:1:7\}$ and the number of slices $N_H \in \{1:1:25\}$ is studied. Optimal parameters α_o and β_o in (α, β)-MD models are determined using the same test region **G** as in the previous section. Results (NRMSE) are collected in groups using N_R as a leading constant parameter and N_H as a varying parameter.

Figure 4.27 shows NRMSE of (α_o, β_o)-MD models for optimal parameters α_o and β_o. Similar to rectangular permanent magnets, the minimum of NRMSE can be found for each N_R group. The optimal numbers of slices are equal to $N_H = \{2, 5, 8, 12, 15, 18, 23\}$ which corresponds to the following errors: $NMRSE_{opt} = \{2.19, 0.89, 0.36, 0.12, 0.05, 0.02, 0.01\}\%$.

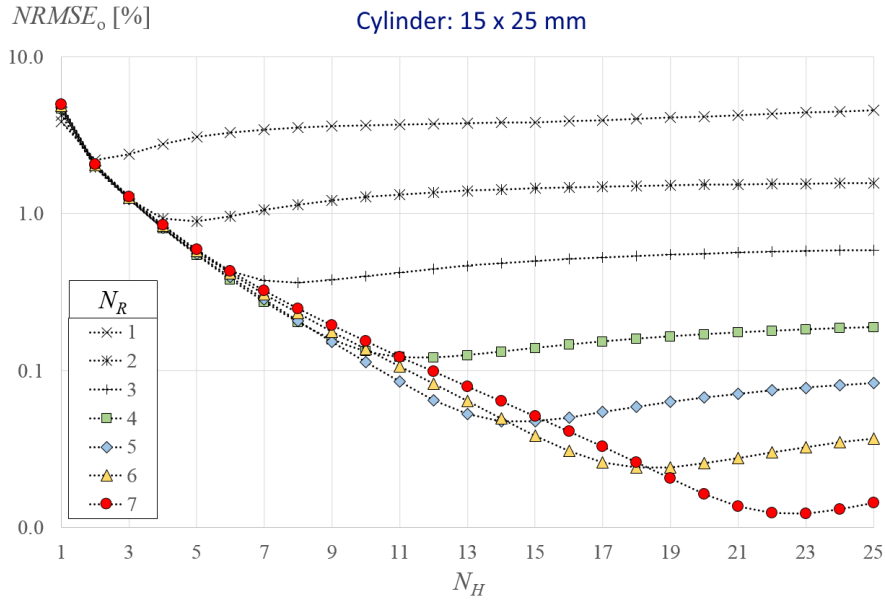

Fig. 4.27: NRMS errors of the optimal (α_o, β_o)-MD models versus a number of slices N_H

Figure 4.28 presents distributions of NRMS errors for $(0.5, 0.5)$-MD models with dipoles located at centers of voxels. The minimums of NRMSE for each N_R group are found for $N_H = \{3, 6, 9, 12, 14, 17, 20\}$ as $NRMSE_{0.5} = \{2.74,\ 0.97,\ 0.40,\ 0.13,\ 0.06,\ 0.05,\ 0.04\}\%$, respectively. The optimal number of slices for $(0.5, 0.5)$-MD models can be estimated using the following formula: $N_H = \lfloor H/\Delta r + \delta \rfloor$, where $\Delta r = R/N_R$, and δ is an arbitrary constant equals $\delta = 0.2$. It can be observed that in this case the number of slices is greater than N_H for the optimal α_o, β_o only for the first three N_R groups.

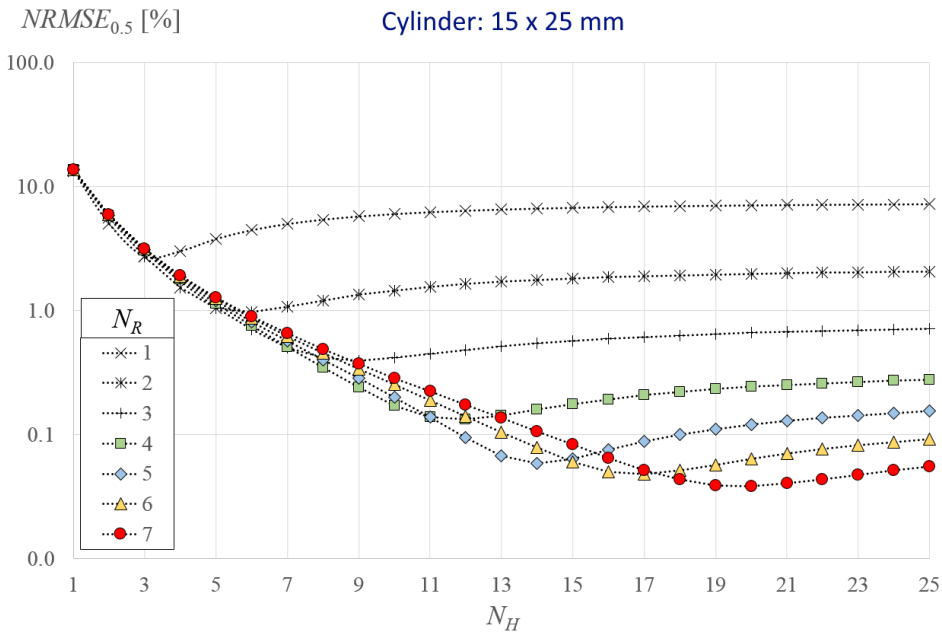

Fig. 4.28: NRMS errors of $(0.5, 0.5)$-MD models versus a number of slices N_H

The distribution of parameters α_o and β_o versus the total number of dipoles N_D is shown in Fig. 4.29. It can be observed that the optimal values of α_o as well as β_o strive to 0.5 when the total number of dipoles increases (blue circles). Generally, the errors of (α_o, β_o)-MD models are higher than for the models of rectangular permanent magnets with comparable number of magnetic dipoles, i.e., to achieve similar accuracy, the MDM with more dipoles has to be applied for a cylindrical permanent magnet.

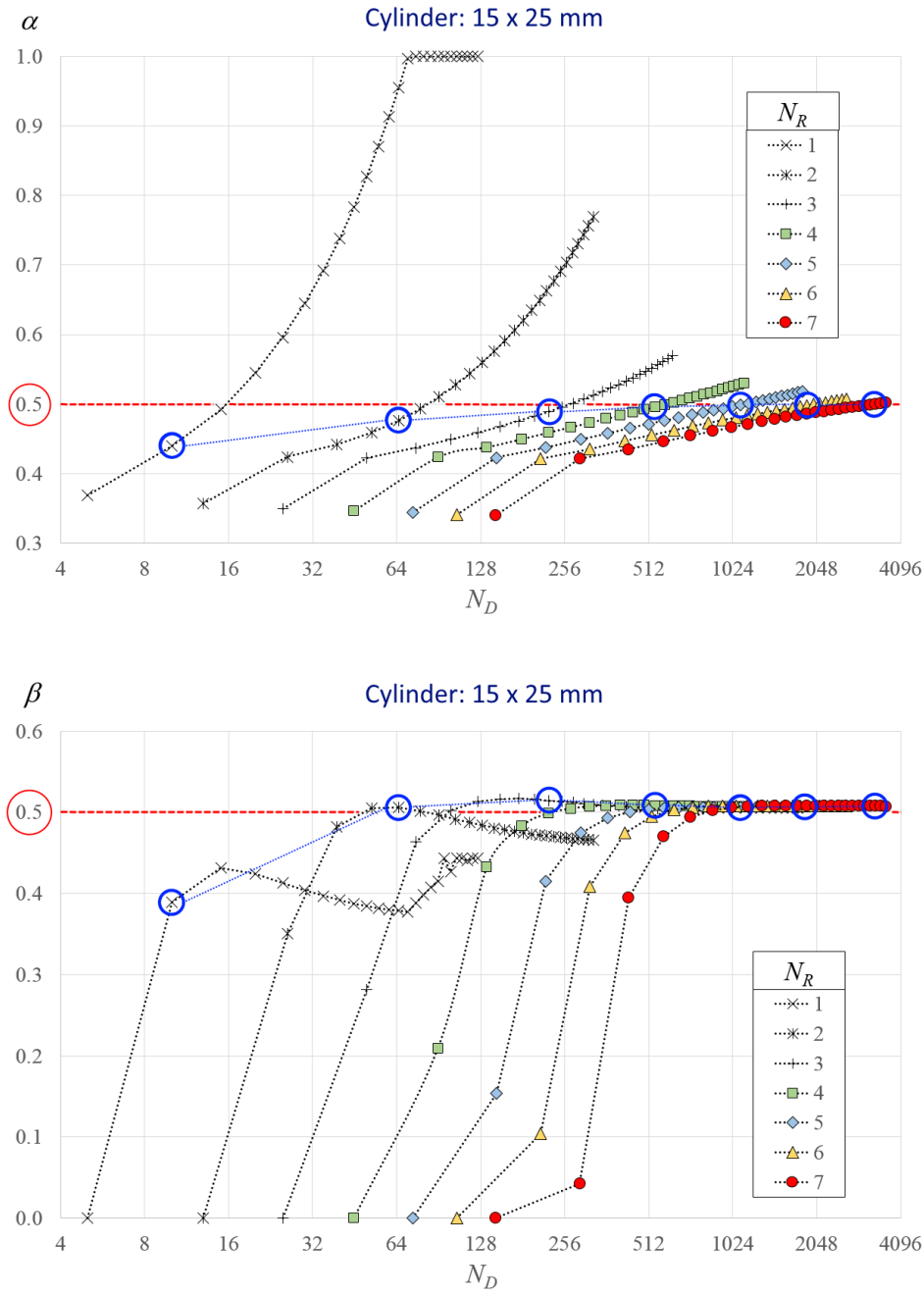

Fig. 4.29: The optimal parameters α_o, β_o versus the total number of magnetic dipoles N_D (blue circles mark α_o and β_o related to the optimal number of slices N_H for each N_R group)

Figure 4.30 presents sample distributions of magnetic flux density under the cylindrical PM ($2R \times H = 15\,\text{mm} \times 25\,\text{mm}$, lift-off $z_0 = h_0 = 1\,\text{mm}$) at $y = 0$ and $z = -1\,\text{mm}$ for the following (α_o, β_o)-MD models: (1) $N_D = 10$, $\alpha_o = 0.44007, \beta_o = 0.38922$, (2) $N_D = 1890$, $\alpha_o = 0.49802, \beta_o = 0.50779$. The corresponding normalized root mean square errors ($NMRSE_{opt}$) are equal to 2.19% and 0.02%, respectively.

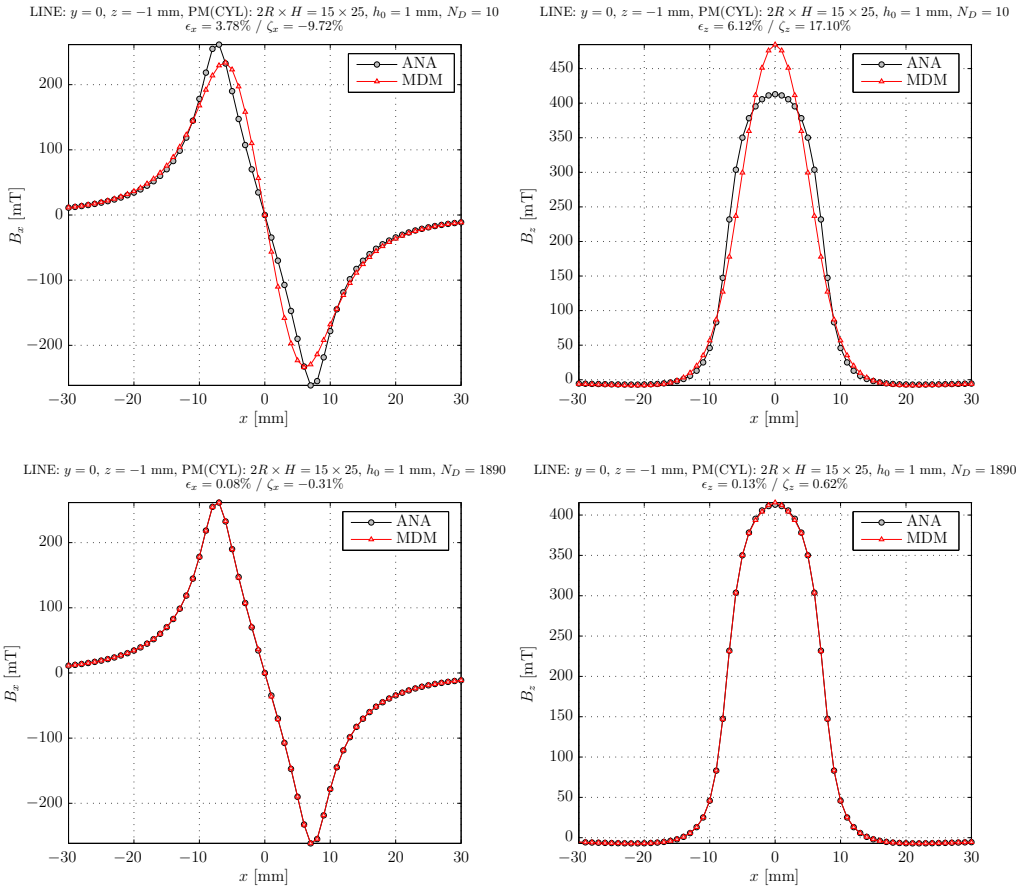

Fig. 4.30: Magnetic flux density distributions - the comparison of optimal (α_o, β_o)-MDM with the analytical model (ANA): (1) $N_D = 10$ (*up*), (2) $N_D = 1890$ (*down*)

4.3.9. RÉSUMÉ

In Section 4.3., modeling of 3D permanent magnets using magnetic dipoles models was presented. Two discrete models for modeling permanent magnets are introduced, namely: (1) α-MDM for the rectangular PM, and (2) (α, β)-MDM for the cylindrical PM. The procedure of finding optimal parameters α_o and β_o in the MDM is described in details. Additionally, analytical formulas for the magnetic flux density of rectan-

gular and cylindrical PM at any point outside the PM are given (based on [33, 137]). Simulation results are also presented and discussed.

4.4. CALCULATION OF FORCES IN 3D LET MODELS

4.4.1. PROBLEM DESCRIPTION

A 3D permanent magnet of arbitrary form (e.g. cylinder, cuboid, Halbach cylinder, etc.) is placed at a lift-off distance z_0 above a moving conducting plate ($L \times W \times D$, electrical conductivity σ_0): The plate contains a defect defined by $c_x \times c_y \times c_z$ located at depth d. Parameters c_x, c_y, and c_z enable to define defects of following shapes: cuboids, if all parameters are grater than 0, cylinders, if $c_y = 0$, and spheres, if $c_y = c_z = 0$, where c_x denotes a diameter of cylinder / sphere, respectively.

Figure 4.31 shows sample configuration of 3D LET model with a rectangular permanent magnet.

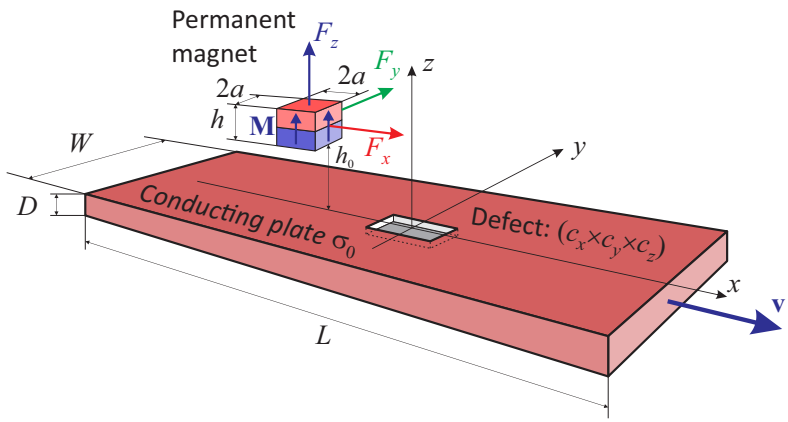

Fig. 4.31: Sample rectangular permanent magnet ($2a \times 2a \times h$) above a moving conducting plate ($L \times W \times D$) with a surface rectangular defect ($c_x \times c_y \times c_z, d = 0$)

The principal difference between 3D and 2D LET models lies in the fact that the third component of the Lorentz force F_y (side force) exerts on the PM if the PM is located outside the symmetry line of the 3D plate-defect configuration.

The conducting plate can be treated as a solid conductor with a constant, homogeneous electrical conductivity σ_0 or as an assembly of N conducting sheets of thickness $\Delta h = D/N$. The second model is especially useful for modeling experimental LET configurations [125, 138] where preparing LET setups with defects at various depths is much easier when stacked sheets are used. If thickness Δh of sheets is small enough and sheets are isolated from each other (e.g. using thin paper sheets) then an anisotropic model of electrical conductivity can be applied. In this case the electrical conductivity of stacked sheets can be described by a diagonal conductivity tensor $[\sigma] = \mathrm{diag}(\sigma_{xx}, \sigma_{yy}, \sigma_{zz})$, where $\sigma_{xx} = \sigma_{yy} = \sigma_0$ and $\sigma_{zz} = 0$.

4.4.2. LORENTZ FORCES FOR PLATES WITHOUT DEFECTS

Analytical calculations of Lorentz forces exerted on the PM located above the moving conducting plate without any defects are only possible if the width W and the length L of the analyzed plate are much greater than the dimensions of the PM, i.e., the plate can be treated as infinitely wide. It is also assumed that the permeability and the conductivity of the plate are constant and equal μ_0 and σ_0, respectively. The velocity v of the moving plate is also constant and is much less than the light velocity, i.e., the term of the displacement current in field equations can be omitted. Additionally, assuming that the PM is described by a constant magnetization vector $\mathbf{M}$, it can be substituted by an infinitely thin solenoid of length H_m with a surface current density $\mathbf{J}_M$, where $J_M = M$.

First, the Lorentz force exerted on the infinitely thin coil with current $I_0 = J_M \Delta z$ located at $z = z_0$ above the moving conducting plate of thickness D is calculated. Using approach presented in [114], the problem can be described in the coordinate system fixed to the coil (rest frame) by the following set of equations:

$$\nabla^2 \mathbf{H} = 0, \qquad \text{Region: I, II, IV} \tag{4.76}$$

$$\nabla^2 \mathbf{H} = \mu_0 \sigma_0 v \frac{\partial \mathbf{H}}{\partial x}, \qquad \text{Region: III} \tag{4.77}$$

$$\nabla \cdot \mathbf{H} = 0, \qquad \text{Region: all} \tag{4.78}$$

where regions I-IV are defined in Fig. 4.32.

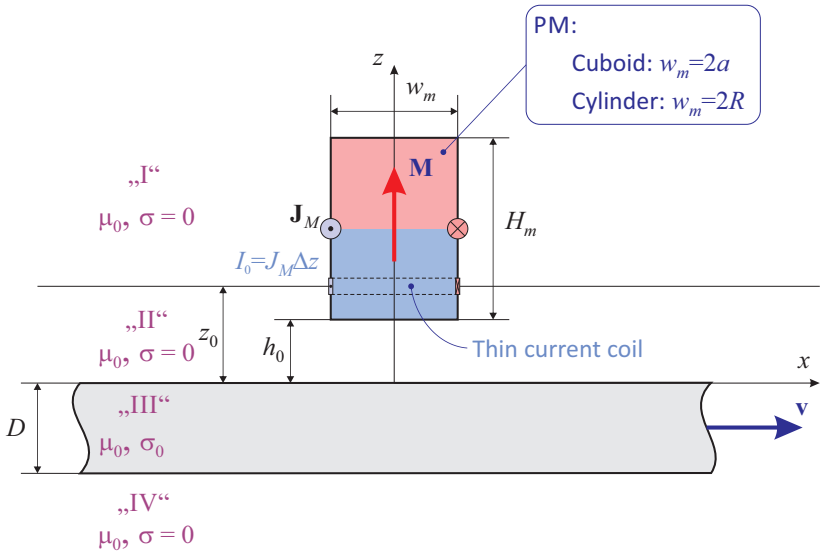

Fig. 4.32: Calculation setup for the permanent magnet above a moving conducting plate

For solving (4.76) - (4.78), 2D Fourier transform is applied:

$$\widehat{\mathbf{F}} = \widehat{\mathbf{F}}(k_x, k_y) = \int_{-\infty}^{\infty}\int_{-\infty}^{\infty} \mathbf{F}(\mathbf{r}) e^{-j(k_x x + k_y y)} dx dy \tag{4.79}$$

where $\mathbf{r} = x\mathbf{1}_x + y\mathbf{1}_y + z\mathbf{1}_z$, and k_x, k_y are transform variables. The inverse 2D Fourier transform is given by:

$$\mathbf{F}(\mathbf{r}) = \left(\frac{1}{2\pi}\right)^2 \int_{-\infty}^{\infty}\int_{-\infty}^{\infty} \widehat{\mathbf{F}}(k_x, k_y) e^{j(k_x x + k_y y)} dk_x dk_y \tag{4.80}$$

To simplify the notation, $\widehat{\mathbf{F}}(k_x, k_y)$ is further replaced with the symbol $\widehat{\mathbf{F}}$. After applying (4.79) to (4.76) - (4.78), the following equations are obtained

$$-(k_x^2 + k_y^2)\widehat{\mathbf{H}} + \frac{d^2\widehat{\mathbf{H}}}{dz^2} = 0, \qquad \text{Region: I, II, IV,} \tag{4.81}$$

$$-(k_x^2 + k_y^2)\widehat{\mathbf{H}} + \frac{d^2\widehat{\mathbf{H}}}{dz^2} = jk_x\mu_0\sigma_0 v\widehat{\mathbf{H}}, \qquad \text{Region: III,} \tag{4.82}$$

$$jk_x\widehat{H}_x + jk_y\widehat{H}_y + \frac{d\widehat{H}_z}{dz} = 0, \qquad \text{Region: all.} \tag{4.83}$$

The solution of (4.81) - (4.83) can be written as:

$$\widehat{\mathbf{H}}_1 = \widehat{\mathbf{H}}^{(i)} + \widehat{\mathbf{H}}^{(e)} = \widehat{\mathbf{H}}^{(i)} + \widehat{\boldsymbol{a}}e^{-kz}, \qquad \text{Region: I, II} \tag{4.84}$$

$$\widehat{\mathbf{H}}_2 = \widehat{\boldsymbol{b}}e^{-\alpha z} + \widehat{\boldsymbol{c}}e^{\alpha z}, \qquad \text{Region: III} \tag{4.85}$$

$$\widehat{\mathbf{H}}_3 = \widehat{\boldsymbol{d}}e^{kz}, \qquad \text{Region: IV} \tag{4.86}$$

where $\alpha^2 = j\mu_0\sigma_0 v k_x + k^2$, $k^2 = k_x^2 + k_y^2$, and $\widehat{\boldsymbol{a}}$, $\widehat{\boldsymbol{b}}$, $\widehat{\boldsymbol{c}}$, $\widehat{\boldsymbol{d}}$ are unknown complex constants defined as $\widehat{\boldsymbol{a}} = [\widehat{a}_x, \widehat{a}_y, \widehat{a}_z]^T$, $\widehat{\boldsymbol{b}} = [\widehat{b}_x, \widehat{b}_y, \widehat{b}_z]^T$, $\widehat{\boldsymbol{c}} = [\widehat{c}_x, \widehat{c}_y, \widehat{c}_z]^T$, $\widehat{\boldsymbol{d}} = [\widehat{d}_x, \widehat{d}_y, \widehat{d}_z]^T$, respectively. $\widehat{\mathbf{H}}_i = [\widehat{H}_{x,i}, \widehat{H}_{y,i}, \widehat{H}_{z,i}]^T$ denotes the resultant magnetic field in the i^{th} region ($i = 1, 2, 3$) while $\widehat{\mathbf{H}}^{(i)}$ is the primary (incident) magnetic field produced by the current coil in absence of the plate and $\widehat{\mathbf{H}}^{(e)}$ is the magnetic field produced by eddy currents induced in the moving conducting plate.

The Fourier transform of the primary magnetic field $\widehat{\mathbf{H}}^{(i)}$ of a thin wire coil located at $z = z_0$ and carrying a steady current I_0 can be found in regions I and II as

$$\text{Region I}: \quad \begin{cases} \widehat{\mathbf{H}}^{(i)}_{||,1} = -\frac{1}{2}\left(\mathbf{1}_z \times \widehat{\mathbf{J}}_s\right) e^{-k(z-z_0)} \\ \widehat{H}^{(i)}_{z,1} = j\dfrac{k_x}{k}\widehat{H}^{(i)}_{x,1} + j\dfrac{k_y}{k}\widehat{H}^{(i)}_{y,1} \end{cases} \tag{4.87}$$

$$\text{Region II}: \quad \begin{cases} \widehat{\mathbf{H}}^{(i)}_{||,2} = \frac{1}{2}\left(\mathbf{1}_z \times \widehat{\mathbf{J}}_s\right) e^{k(z-z_0)} \\ \widehat{H}^{(i)}_{z,2} = -j\dfrac{k_x}{k}\widehat{H}^{(i)}_{x,2} - j\dfrac{k_y}{k}\widehat{H}^{(i)}_{y,2} \end{cases} \tag{4.88}$$

where $\widehat{\mathbf{H}}_{||,n}^{(i)} = \widehat{H}_{x,n}^{(i)}\mathbf{1}_x + \widehat{H}_{y,n}^{(i)}\mathbf{1}_y$, $n = 1, 2$ and $\widehat{\mathbf{J}}_s$ is 2D Fourier transform of the coil with current. To complete formulas (4.87) and (4.88), it is necessary to find the 2D Fourier transform $\widehat{\mathbf{J}}_s$.

First, it is analyzed an infinitely thin rectangular coil $2a \times 2b$ with a current given as

$$\mathbf{J}_s(x,y) = I_0 \begin{bmatrix} \Pi\left(\dfrac{x}{2a}\right)\delta(y+b) - \Pi\left(\dfrac{x}{2a}\right)\delta(y-b) \\ \Pi\left(\dfrac{y}{2b}\right)\delta(x-a) - \Pi\left(\dfrac{y}{2b}\right)\delta(x+a) \end{bmatrix} \tag{4.89}$$

where $I_0 = M\Delta z$, $\delta(\cdot)$ is the Dirac function and $\Pi(\cdot)$ is the rectangle function [14] defined as:

$$\Pi(x) = \begin{cases} 1, & |x| < \frac{1}{2} \\ \frac{1}{2}, & |x| = \frac{1}{2} \\ 0, & |x| > \frac{1}{2} \end{cases} \tag{4.90}$$

The Fourier transform $\widehat{\mathbf{J}}_s$ of (4.89) is given by:

$$\widehat{\mathbf{J}}_s = \begin{bmatrix} \widehat{J}_{sx} \\ \widehat{J}_{sy} \end{bmatrix} = j4I_0 \sin(k_x a)\sin(k_x b) \begin{bmatrix} \dfrac{1}{k_x} \\ -\dfrac{1}{k_y} \end{bmatrix} \tag{4.91}$$

2D Fourier transform of an infinitely thin loop of radius R with a current defined as

$$\mathbf{J}_s(x,y) = I_0 \begin{bmatrix} -\delta(r-R)\sin\varphi \\ \delta(r-R)\cos\varphi \end{bmatrix} \tag{4.92}$$

can be calculated as

$$\widehat{\mathbf{J}}_s = \begin{bmatrix} \widehat{J}_{sx} \\ \widehat{J}_{sy} \end{bmatrix} = j2\pi R I_0 \mathrm{J}_1(kR) \begin{bmatrix} \dfrac{k_y}{k} \\ -\dfrac{k_x}{k} \end{bmatrix} \tag{4.93}$$

where $r^2 = x^2 + y^2$, $\sin\varphi = y/r$, $\cos\varphi = x/r$, and $\mathrm{J}_1(\cdot)$ is the first order Bessel function of the first kind [1]

$$\mathrm{J}_1(z) = \frac{j}{\pi}\int_0^{\pi} e^{-jz\cos\theta}\cos\theta d\theta \tag{4.94}$$

Unknown constants $\widehat{\boldsymbol{a}}$, $\widehat{\boldsymbol{b}}$, $\widehat{\boldsymbol{c}}$, $\widehat{\boldsymbol{d}}$ in (4.84) - (4.86) can be determined from the continuity conditions at $z = 0$ ($i = 2$) and $z = -D$ ($i = 3$):

$$\widehat{\mathbf{H}}_{t,i} = \widehat{\mathbf{H}}_{t,i+1} \tag{4.95}$$

$$\widehat{\mathbf{B}}_{n,i} = \widehat{\mathbf{B}}_{n,i+1} \tag{4.96}$$

The indexes t and n denote tangential and normal components of vectors $\mathbf{H}$ and $\mathbf{B}$, respectively. Additionally to (4.95) - (4.96), the condition $\nabla \times \mathbf{B}_{|z} = 0$ (z-component of $\nabla \times \mathbf{B}$) in the region III has to be taken into account because the induced eddy currents in the conducting plate flow only in XY-planes ($J_z = 0$). After a few elementary transformations, the constant $\widehat{\boldsymbol{a}}$ can be found as

$$\widehat{\boldsymbol{a}} = \begin{bmatrix} \widehat{a}_x = T(k,\beta)\ \widehat{H}^{(i)}_{x,2}\Big|_{z=0} = \frac{1}{2}T(k,\beta)\left(\mathbf{1}_z \times \widehat{\mathbf{J}}_s\right) e^{-kz_0} \\ \widehat{a}_y = \dfrac{k_y}{k_x}\widehat{a}_x \\ \widehat{a}_z = j\dfrac{k}{k_x}\widehat{a}_x \end{bmatrix} \tag{4.97}$$

where $T(k,\beta)$ is given by the expression

$$T(k,\beta) = \frac{(\beta^2 - 1)\tanh \beta k D}{2\beta + (1+\beta^2)\tanh \beta k D} \tag{4.98}$$

where $\beta = \alpha/k, k^2 = k_x^2 + k_y^2$, and $\alpha^2 = j\mu_0\sigma_0 v k_x + k^2$. The coefficient $T(k,\beta)$ can be treated as a "reflection coefficient" of the incident magnetic field "reflected" from the moving conducting plate [84, 85, 114]. Finally, using (4.88) and (4.97), the magnetic field $\widehat{\mathbf{H}}^{(e)}$ in regions I and II produced by eddy currents in the moving plate can be written as

$$\widehat{\mathbf{H}}^{(e)}_{||} = T(k,\beta)\ \widehat{\mathbf{H}}^{(i)}_{||,2}\Big|_{z=0} e^{-kz} = \frac{1}{2}T(k,\beta)\left(\mathbf{1}_z \times \widehat{\mathbf{J}}_s\right) e^{-k(z+z_0)} \tag{4.99}$$

$$\widehat{H}^{(e)}_z = -j\frac{1}{2}T(k,\beta)\left(\frac{k_x}{k}\widehat{J}_{sy}e^{-kz_0} - \frac{k_y}{k}\widehat{J}_{sx}e^{-kz_0}\right) e^{-kz} \tag{4.100}$$

The Lorentz force exerted on a thin coil above a moving conducting plate can be calculated using the following formula [85]:

$$\mathbf{F} = \mu_0 \int_{-\infty}^{\infty}\int_{-\infty}^{\infty} \mathbf{J}_s(\mathbf{r}) \times \mathbf{H}^{(e)}(\mathbf{r})\Big|_{z=z_0} dxdy \tag{4.101}$$

According Parseval's theorem [14], (4.99) - (4.100) are rewritten in Fourier domain as

$$\mathbf{F} = \frac{\mu_0}{4\pi^2}\int_{-\infty}^{\infty}\int_{-\infty}^{\infty} \widehat{\mathbf{J}}^*_s \times \widehat{\mathbf{H}}^{(e)}\Big|_{z=z_0} dk_x dk_y \tag{4.102}$$

After substitution (4.99) - (4.100) into (4.102), the following expressions are received

$$F_x = -j\frac{\mu_0}{8\pi^2}\int_{-\infty}^{\infty}\int_{-\infty}^{\infty} T(k,\beta)\left(\frac{k_x}{k}\left|\widehat{J}_{sy}\right|^2 - \frac{k_y}{k}\widehat{J}^*_{sy}\widehat{J}_{sx}\right) e^{-2kz_0} dk_x dk_y \tag{4.103}$$

$$F_y = 0 \tag{4.104}$$

$$F_z = \frac{\mu_0}{8\pi^2}\int_{-\infty}^{\infty}\int_{-\infty}^{\infty} T(k,\beta)\left(\left|\widehat{J}_{sx}\right|^2 + \left|\widehat{J}_{sy}\right|^2\right) e^{-2kz_0} dk_x dk_y \tag{4.105}$$

The side force F_y equals 0 due to the x-symmetry of the coil. Using the symmetry of $\widehat{\mathbf{J}}_s$ in the Fourier domain (see (4.91) and (4.93))

$$\begin{aligned}\widehat{J}_{sx}(k_x) &= \widehat{J}_{sx}(-kx), \qquad \widehat{J}_{sx}(k_y) = -\widehat{J}_{sx}(-k_y),\\ \widehat{J}_{sy}(k_x) &= -\widehat{J}_{sy}(-kx), \qquad \widehat{J}_{sy}(k_y) = \widehat{J}_{sy}(-k_y)\end{aligned}$$

Equations (4.103) - (4.105) can be simplified to the following form

$$F_x = \frac{\mu_0}{2\pi^2}\int_0^\infty\int_0^\infty \Im[T(k,\beta)]\left(\frac{k_x}{k}|\widehat{J}_{sy}|^2 - \frac{k_y}{k}\widehat{J}^*_{sy}\widehat{J}_{sx}\right)e^{-2kz_0}dk_xdk_y \tag{4.106}$$

$$F_z = \frac{\mu_0}{2\pi^2}\int_0^\infty\int_0^\infty \Re[T(k,\beta)]\left(|\widehat{J}_{sx}|^2 + |\widehat{J}_{sy}|^2\right)e^{-2kz_0}dk_xdk_y \tag{4.107}$$

To calculate Lorentz force $\mathbf{F}^{PM}$ exerted on the infinitely thin solenoid (Fig. 4.32), and thereby on the permanent magnet, it is necessary first to sum (integrate) at $z = 0$ the incident magnetic field contributions from infinitely thin coils evenly distributed along the solenoid. The result has the following form:

$$\widehat{\mathbf{H}}^{(i)}_{||,2}\Big|_{z=0} = \tfrac{1}{2}\left(\mathbf{1}_z \times \widehat{\mathbf{J}}_s\right)\frac{e^{-kh_0}}{k}\left(1 - e^{-kH_m}\right) \tag{4.108}$$

$$\widehat{H}^{(i)}_{z,2}\Big|_{z=0} = -j\frac{k_x}{k}\,\widehat{H}^{(i)}_{x,2}\Big|_{z=0} - j\frac{k_y}{k}\,\widehat{H}^{(i)}_{y,2}\Big|_{z=0} \tag{4.109}$$

Next, the magnetic field produced by induced eddy currents in the plate (4.99) - (4.100) has to be integrated along the solenoid length [84]. Finally, the following expressions for Lorentz forces exerted on a permanent magnet (possessing x-symmetry) above moving conducting plate are obtained:

$$F^{PM}_x = \frac{\mu_0}{2\pi^2}\int_0^\infty\int_0^\infty \Im[T(k,\beta)]\left(k_x|\widehat{J}_{sy})|^2 - k_y\widehat{J}^*_{sy}\widehat{J}_{sx}\right)\times$$
$$\times\,\frac{\left(1 - e^{-kH_m}\right)^2}{k^3}e^{-2kh_0}dk_xdk_y, \tag{4.110}$$

$$F^{PM}_y = 0 \tag{4.111}$$

$$F^{PM}_z = \frac{\mu_0}{2\pi^2}\int_0^\infty\int_0^\infty \Re[T(k,\beta)]\left(|\widehat{J}_{sx}|^2 + |\widehat{J}_{sy}|^2\right)\times$$
$$\times\,\frac{\left(1 - e^{-kH_m}\right)^2}{k^2}e^{-2kh_0}dk_xdk_y. \tag{4.112}$$

Formulas (4.110) and (4.112) are verified using the finite element method applied to similar configuration setup as for analytical method. Figures 4.33 and 4.34 show normalized Lorentz forces calculated using (4.110) - (4.112) and the FEM.

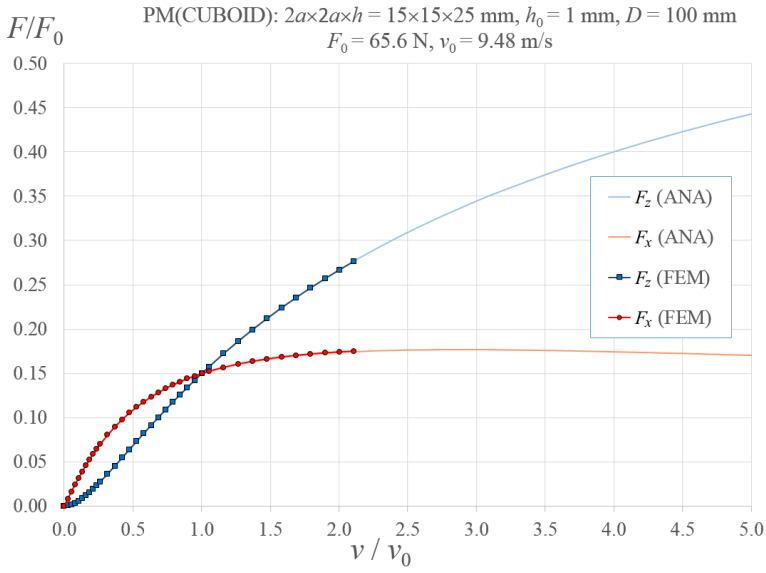

Fig. 4.33: Normalized Lorentz forces exerted on the rectangular PM ($2a \times 2a \times h$) located above a moving conducting plate: (ANA) - (4.110) - (4.112), (FEM) - finite element method

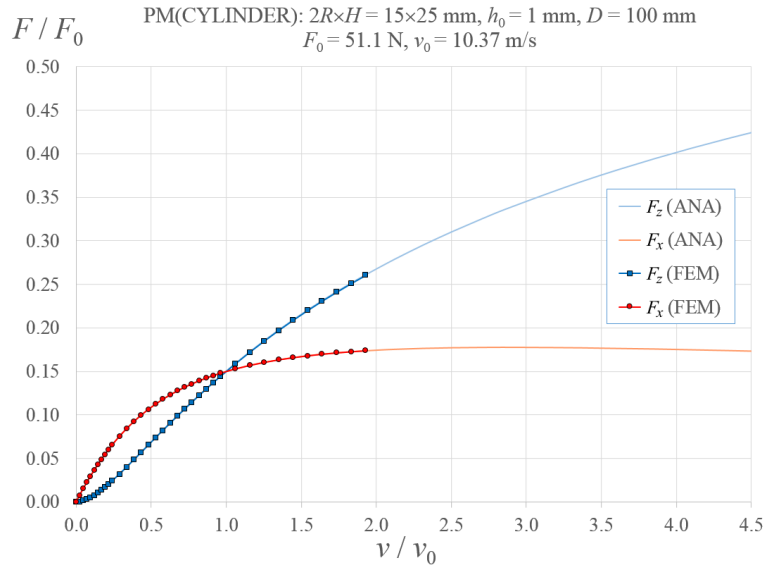

Fig. 4.34: Normalized Lorentz forces exerted on the cylindrical PM ($2R \times H$) located above a moving conducting plate: (ANA) - (4.110) - (4.112), (FEM) - finite element method

The forces are plotted versus normalized velocity v/v_0 for two permanent magnets defined as: (1) cuboid $2a \times 2a \times h = 15\,\text{mm} \times 15\,\text{mm} \times 25\,\text{mm}$, and (2) cylinder $2R \times H = 15\,\text{mm} \times 25\,\text{mm}$. The reference velocity v_0 corresponds to the condition $F_x = F_z$.

In both cases, the lift-off h_0 of the PM equals 1 mm and the magnetization $\mathbf{M}$ is defined as $\mathbf{M} = M\mathbf{1}_z$, where $M = B_r/\mu_0$ and B_r is the remanence equals 1.17 T. The electrical conductivity σ_0 and thickness D of the moving plate are equal to 30.61 MS/m and 100 mm, respectively.

As a reference force F_0, an asymptotic limit of (4.112) for $\sigma_0 v \to \infty$ is chosen:

$$F_0 = \frac{\mu_0}{2\pi^2} \int_0^\infty \int_0^\infty \left(|\widehat{J}_{sx}|^2 + |\widehat{J}_{sy}|^2 \right) \frac{\left(1 - e^{-kH_m}\right)^2}{k^2} e^{-2kh_0} dk_x dk_y \tag{4.113}$$

It can be observed a very good agreement between forces calculated analytically using (4.110) - (4.112) and obtained from FEM simulations. The normalized root mean deviation (NRMD) between ANA and FEM (defined similarly as (4.41)) is equal to 0.42% for both simulated cases.

The presented approach enables also to calculate induced eddy currents in the moving plate in easy way. Using $\mathbf{J} = \nabla \times \mathbf{H}_2$, the 2D Fourier transform of the eddy current density $\widehat{\mathbf{J}}$ takes the form

$$\widehat{\mathbf{J}} = \begin{bmatrix} \widehat{J}_x \\ \widehat{J}_y \end{bmatrix} = (1-\beta) \frac{1 - \frac{1-\beta}{1+\beta} e^{-2\beta k(D+z)}}{1 - \left(\frac{1-\beta}{1+\beta}\right)^2 e^{-2\beta kD}} e^{\beta kz} \left(1 - e^{-kH_m}\right) e^{-kh_0} \begin{bmatrix} \widehat{J}_{sx} \\ \widehat{J}_{sy} \end{bmatrix} \tag{4.114}$$

Next, applying symmetry properties of $\widehat{\mathbf{J}}_s$ in the Fourier domain, eddy current density in any point $\mathbf{r}$ of the plate is determined from the inverse 2D Fourier transform of the following form:

$$J_x(\mathbf{r}) = \frac{1}{\pi^2} \int_0^\infty \int_0^\infty \sin(k_y y) \left\{ \sin(k_x x) \Re[\widehat{J}_x] + \cos(k_x x) \Im[\widehat{J}_x] \right\} dk_x dk_y \tag{4.115}$$

$$J_y(\mathbf{r}) = \frac{1}{\pi^2} \int_0^\infty \int_0^\infty \cos(k_y y) \left\{ \sin(k_x x) \Im[\widehat{J}_y] - \cos(k_x x) \Re[\widehat{J}_y] \right\} dk_x dk_y \tag{4.116}$$

where $\mathbf{r} = x\mathbf{1}_x + y\mathbf{1}_y + z\mathbf{1}_z$.

Figures 4.35 and 4.36 show stationary eddy current distributions on the top surface ($z = 0$) of the plate moving with velocity $v = 10$ m/s. The distributions are calculated with help of (4.115) - (4.116) (ANA) using the same models as for force calculations. For comparison, results of FEM simulations for equivalent models are also presented. A very good agreement of both solutions can be observed.

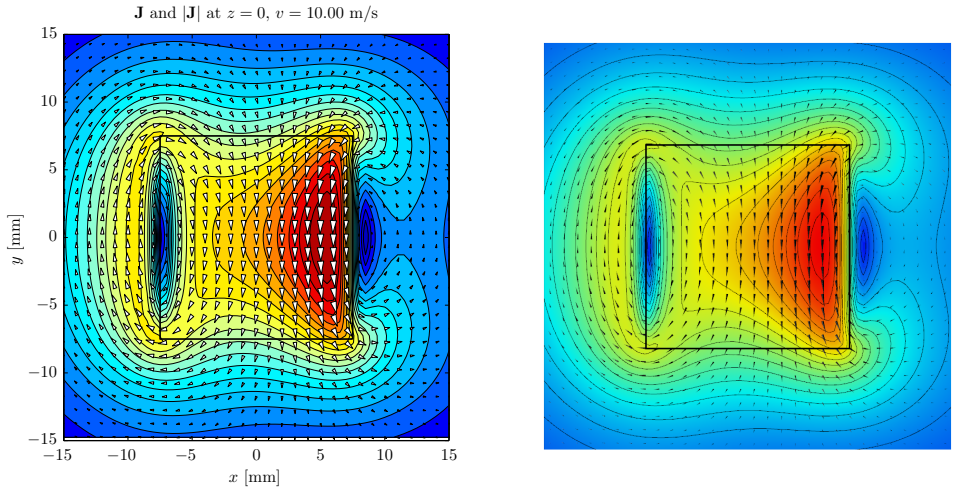

(a) ANA (b) FEM

Fig. 4.35: Permanent magnet (Cuboid): eddy currents density distribution on the top surface of the moving conducting plate ($z = 0$) for $\mathbf{v} = v\mathbf{1}_x$, $v = 10\,\mathrm{m/s}$

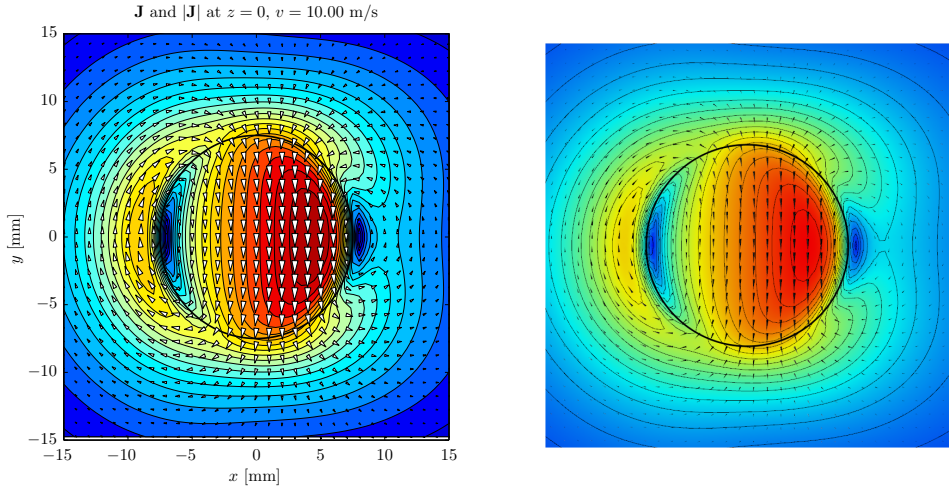

(a) ANA (b) FEM

Fig. 4.36: Permanent magnet (Cylinder): eddy currents density distribution on the top surface of the moving conducting plate ($z = 0$) for $\mathbf{v} = v\mathbf{1}_x$, $v = 10\,\mathrm{m/s}$

Figure 4.37 depicts eddy current distributions on the PM y-symmetry plane calculated with (4.115) - (4.116). In the plots only the distribution of J_y component is shown because $J_x = 0$ at $y = 0$.

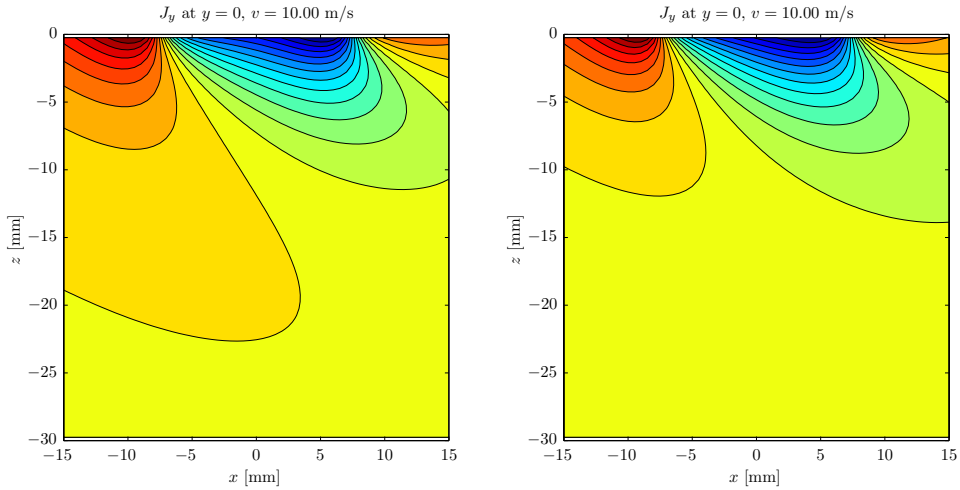

(a) Rectangular PM

(b) Cylindrical PM

Fig. 4.37: Eddy currents in the moving conducting plate on the y-symmetry plane of the permanent magnet ($y = 0$) for $\mathbf{v} = v\mathbf{1}_x$, $v = 10\,\mathrm{m/s}$

It should be noted that the distortion of induced eddy currents in the moving plate follows the direction of the plate velocity.

4.4.3. 3D DEFECT RESPONSE SIGNALS

Analytical calculations of response signals (defined in Section 4.2.2.) produced by 3D defects located in a moving plate under a fixed permanent magnet are only possible in an approximate way. The approximate method presented in [105] is a simple extension of the method described in Section 4.2. using a superposition of eddy currents induced in the plate without defect and in the virtual region covering the defect region for a slowly moving conducting plate. It uses a weak reaction approach for a description of electromagnetic fields and approximates the permanent magnet with a single magnetic dipole. It is assumed that the width and the length of the plate is much greater than the size of the PM and the plate itself is represented by a package of thin conducting sheets isolated from each other. The use of a package of sheets instead of a solid block greatly facilitates the preparation of the experiment where the same defect at various depths can be analyzed by a simple exchange of the appropriate sheets. The consequence of using isolated sheets is the assumption that the electrical conductivity of the plate can be modeled as an anisotropic one, i.e., it can be described by the diagonal conductivity tensor $[\sigma] = \mathrm{diag}(\sigma_{xx}, \sigma_{yy}, \sigma_{zz})$ with $\sigma_{zz} = 0$, and $\sigma_{xx} = \sigma_{yy} = \sigma_0$. Additionally, the defect is treated as an ideal one with the electrical conductivity equals 0. The paper [105] describes a defect reconstruction procedure in which only normalized defect response signals are used. However, if not-normalized absolute defect response signals

are considered, the significant errors of calculated ΔF_x and ΔF_z DRS profiles can be observed in comparison to the reference FEM solution.

Figure 4.38 shows sample DRS profiles in the vicinity of the defect calculated at $y = 0$ according to [105] for the following setup: the rectangular permanent magnet

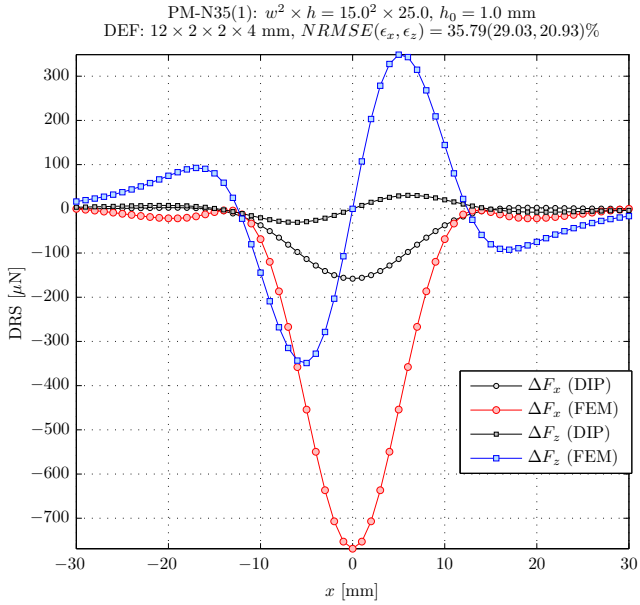

Fig. 4.38: Sample DRS profiles calculated using the single magnetic dipole model from [105]

$w^2 \times h = 15\,\text{mm} \times 15\,\text{mm} \times 25\,\text{mm}$ of remanence $B_r = 1.17\,\text{T}$ is hanged at a lift-off $h_0 = 1\,\text{mm}$ above the plate with a thickness of $D = 100\,\text{mm}$ and the electrical conductivity $\sigma_{xx} = \sigma_{yy} = \sigma_0 = 30.61\,\text{MS/m}$, $\sigma_{zz} = 0$, moving with the velocity $v = 1\,\text{cm/s}$ along the x-axis. The defect $c_x \times c_y \times c_z = 12\,\text{mm} \times 2\,\text{mm} \times 2\,\text{mm}$ is located at the depth $d = 4\,\text{mm}$ under the upper surface of the plate. The permanent magnet is modeled by a single magnetic dipole located locally at $[0.5w, 0.5w, 0.4181h]$ found with the procedure described in Section 4.3.6.. Current density voxels in a defect region are defined by $\Delta x = \Delta y = 1\,\text{mm}$, $\Delta z = 2\,\text{mm}$, i.e., the defect region is modeled by a regular one layer grid of rectangular voxels. The normalized root mean square error (NRMSE) defined by (4.41) - (4.44) is equal to 35.8% in this case. The NRMSE can be reduced when the PM is modeled by more magnetic dipoles using e.g. α-MDM (Section 4.3.3.).

Figure 4.39 shows DRS profiles calculated for the PM modeled with the optimal α-MDM consisting of $N_D = 1331$ magnetic dipoles. Although, the NRMSE is reduced ($NRMSE = 29.3\%$), the calculated DRS profiles are still far away from the reference FEM profiles. Further NRMSE reduction of DRS profiles calculated with the approach presented in [105] is not possible even by increasing the number of voxels in the defect region. In order to clarify this issue, the eddy current density distribution around the defect is calculated. In the analyzed problem, the eddy currents $\mathbf{J}$ induced in a large conductive metal plate without defect moving under the PM along x-axis flow only in

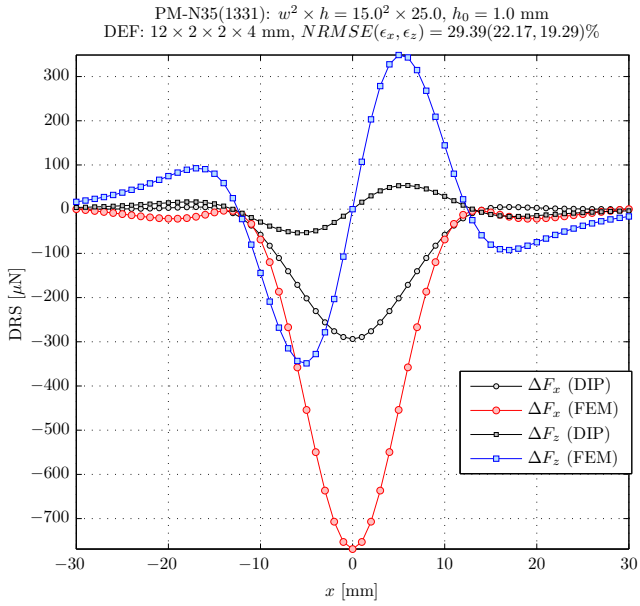

Fig. 4.39: DRS profiles calculated with α-MDM consisting of $N_D = 1331$ magnetic dipoles

XY-planes, i.d. z-component of $\mathbf{J}$ equals 0. In addition, the electrical conductivity of the plate is assumed to be anisotropic with $\sigma_{zz} = 0$. Therefore, the deformation of eddy currents caused by the defect is possible only in the XY-layer of thickness c_z coincident with the defect.

Figure 4.40 shows eddy current distributions in the defect layer in the vicinity of the defect found according to the approach presented in [105]. The distributions are plotted

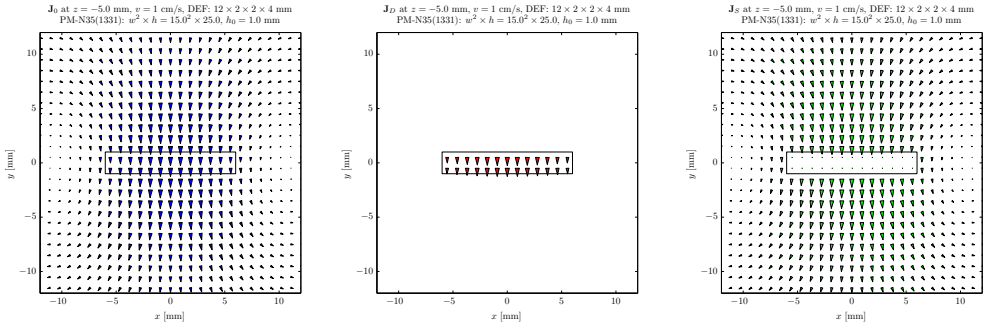

(a) $\mathbf{J}_0$ (b) $\mathbf{J}_D$ (c) $\mathbf{J}_0 - \mathbf{J}_D$

Fig. 4.40: Current density distributions in the layer with a defect for the moment when the PM is above the defect center ($x_m = 0$)

for the moment when the PM is just above the center of the defect ($x_m = 0$, x_m is the actual x-position of the PM coordinate system). $\mathbf{J}_0$ denotes the induced eddy current density in a moving plate in the absence of a defect. $\mathbf{J}_D$ is an artificial current density vector describing induced eddy currents in the region of conductivity $[\sigma]$ introduced in place of the defect. Eddy currents around the defect are described by the superposition of $\mathbf{J}_0$ and $\mathbf{J}_D$ as $\mathbf{J} = \mathbf{J}_0 - \mathbf{J}_D$. As it can be seen in Fig. 4.40c, this operation gives the eddy currents distribution which is not correct because the continuity $\nabla \cdot \mathbf{J} = 0$ of the current density near the defect is not fulfilled.

The correct eddy current distribution calculated by FEM is shown in Fig. 4.41. It can

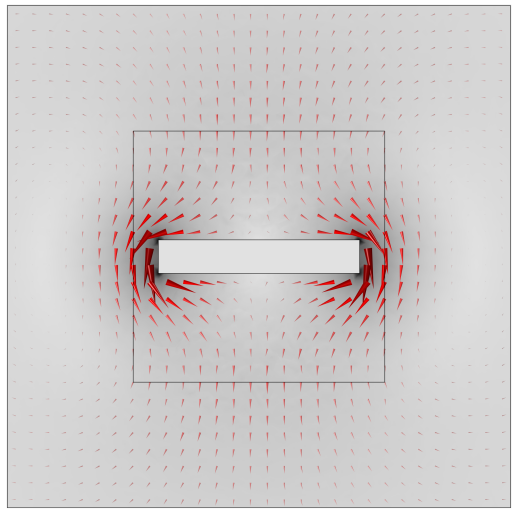

Fig. 4.41: Distribution of eddy currents near a defect calculated by FEM

be concluded that for the proper description of eddy currents in a moving conducting plate with a defect is not enough to subtract only the artificial eddy currents flowing in the region covering the defect from the distribution found in a plate without a defect because this operation does not take into account the impact of the defect on the eddy currents in the surrounding area. This explains also the relatively large errors of DRS profiles calculated with [105] approach.

In the following sections a new method based on a concept of an extended area approach (EAA) will be introduced. This new method enables to calculate DRS profiles with better accuracy. Before the introduction of the EAA, the analysis of the problem of finding a flow of electric current around a circular hole in a thin large conducting sheet is presented.

4.4.4. CIRCLE-SHAPED HOLE IN A THIN CONDUCTING SHEET

The flow of electric current in a thin very large conducting sheet is considered. The sheet is uniform with electrical conductivity $\sigma = \sigma_0$ except near the origin where a circle-shaped hole of radius R has been drilled (Fig. 4.42). Far away from the origin, the

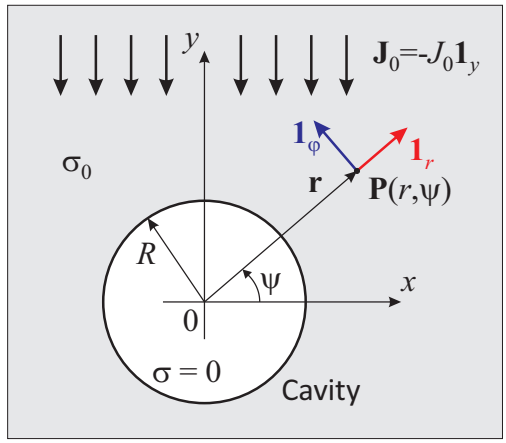

Fig. 4.42: Electric current in a thin conducting sheet with a circular hole

current density is uniform with $\mathbf{J} = \mathbf{J_0} = -J_0\mathbf{1}_y$. In the vicinity of the hole, the current is distorted because it has to flow around the hole. Introducing the electric scalar potential V as $\mathbf{E} = -\nabla\phi$, the current field problem can be described in cylindrical coordinates (r, ψ, z) by the following Laplace equation:

$$\nabla^2\phi = \frac{\partial^2\phi}{\partial r^2} + \frac{1}{r}\frac{\partial\phi}{\partial r} + \frac{1}{r^2}\frac{\partial^2\phi}{\partial\psi^2} = 0 \tag{4.117}$$

together with the boundary conditions

$$r = R: \quad J_n = 0, \qquad \frac{\partial\phi}{\partial r} = 0 \tag{4.118}$$

$$r \to \infty: \quad \mathbf{J} = -J_0\mathbf{1}_y, \quad V = \tfrac{1}{\sigma_0}J_0 r\sin\psi \tag{4.119}$$

The unique solution which satisfies Laplace equation (4.117) and boundary conditions (4.118) - (4.119) is given by

$$\phi = \phi_0 + \frac{J_0}{\sigma_0}r\left[1 + \left(\frac{R}{r}\right)^2\right]\sin\psi \tag{4.120}$$

where ϕ_0 is an arbitrary constant potential.

In cylindrical coordinates, the current density vector can be calculated as

$$\mathbf{J} = \sigma_0\mathbf{E} = -\sigma_0\nabla\phi = -\sigma\left(\frac{\partial\phi}{\partial r}\mathbf{1}_r + \frac{1}{r}\frac{\partial\phi}{\partial\psi}\mathbf{1}_\psi + \frac{\partial\phi}{\partial z}\mathbf{1}_z\right) \tag{4.121}$$

Having (4.120) in (4.121) is obtained

$$\mathbf{J} = -J_0\left[1 - \left(\frac{R}{r}\right)^2\right]\sin\psi\mathbf{1}_r - J_0\left[1 + \left(\frac{R}{r}\right)^2\right]\cos\psi\mathbf{1}_\psi \tag{4.122}$$

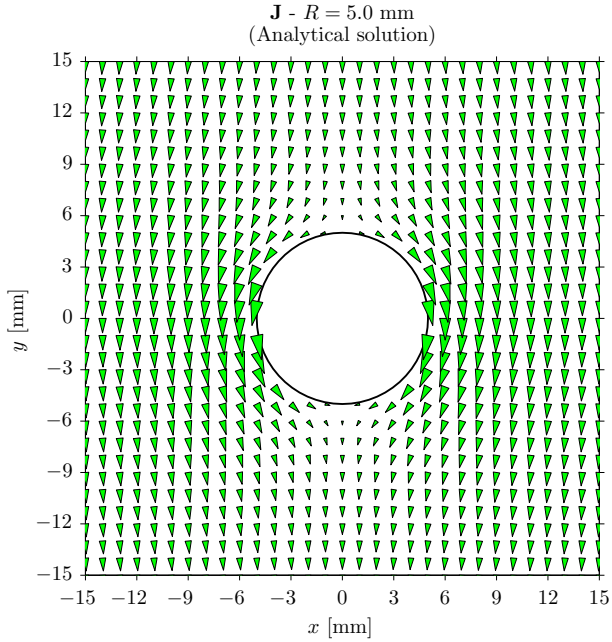

Fig. 4.43: Current density distribution in the vicinity of a circular hole

Sample current density distribution near the circle-shaped hole of radius $R = 5\,\text{mm}$ is shown in Fig. 4.43. Equation (4.122) can be divided into two parts, the primary input current $\mathbf{J}_0$ and the distortion current $\mathbf{j}$ introduced by the hole, as

$$\mathbf{J} = \mathbf{J}_0 - \mathbf{j} \tag{4.123}$$

with $\mathbf{j}$ given by

$$\mathbf{j} = \left(\frac{R}{r}\right)^2 \left(-J_0 \sin\psi \mathbf{1}_r + J_0 \cos\psi \mathbf{1}_\psi\right) \tag{4.124}$$

Using the vector identity

$$\mathbf{J}_0 = -J_0 \sin\psi \mathbf{1}_r - J_0 \cos\psi \mathbf{1}_\psi = \frac{\mathbf{J}_0 \cdot \mathbf{r}}{r^2}\mathbf{r} + (\mathbf{J}_0 \cdot \mathbf{1}_\psi)\mathbf{1}_\psi$$

the distortion current density in any point $\mathbf{r}$ outside the hole can be rewritten as

$$\mathbf{j} = \left(\frac{R}{r}\right)^2 \left(2\frac{\mathbf{J}_0 \cdot \mathbf{r}}{r^2}\mathbf{r} - \mathbf{J}_0\right) \tag{4.125}$$

A current dipole of the moment $\mathbf{p}$ placed in a large thin conducting plate of thickness δz at the origin of the coordinate system evokes in any point $\mathbf{r}$ of the plate a flow of electric current described by the current density vector $\mathbf{j}_p$ (see (4.32))

$$\mathbf{j}_p = \frac{1}{2\pi r^2 \delta z}\left(2\frac{\mathbf{p} \cdot \mathbf{r}}{r^2}\mathbf{r} - \mathbf{p}\right) \tag{4.126}$$

Introducing at the center of the hole an equivalent current dipole of the moment $\mathbf{p} = \mathbf{J}_0 \pi R^2 \delta z = \mathbf{J}_0 V_0$, (4.125) can be rewritten as

$$\mathbf{j} = \frac{1}{\pi r^2 \delta z}\left[2\frac{(\mathbf{J}_0 V_0)\cdot\mathbf{r}}{r^2}\mathbf{r} - \mathbf{J}_0 V_0\right] = \frac{1}{\pi r^2 \delta z}\left(2\frac{\mathbf{p}\cdot\mathbf{r}}{r^2}\mathbf{r} - \mathbf{p}\right) = 2\mathbf{j}_p \tag{4.127}$$

where V_0 is the volume of the hole.

Thus, it has been shown that a distortion current caused by a circular hole in a large thin conducting plate in which flows a uniform electric current can be expressed through the current density field produced by a single current dipole located at the center of the hole.

Figure 4.44 shows a sample distribution of a distortion current field in a vicinity of a circle-shaped hole in a thin metallic plate. The coefficient in front of $\mathbf{j}_p$ in (4.127) is named as a dipolar correction factor (DCF) χ_{DCF}, i.e., $\chi_{DCF} = 2$. Later, it will be shown that DCF depends on the shape of the hole drilled in the plate.

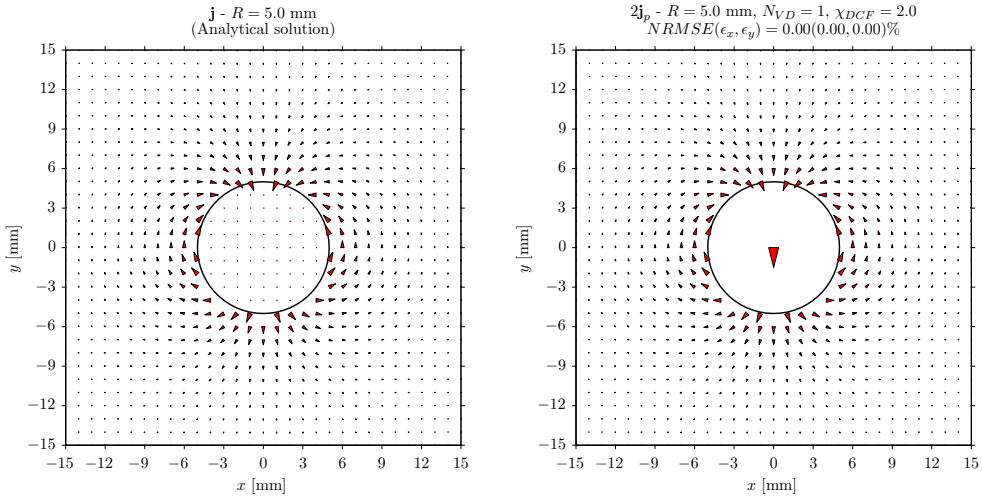

(a) Analytical solution - $\mathbf{j}$

(b) Equivalent dipole - $2\mathbf{j}_p$

Fig. 4.44: Distortion current near a hole in a large thin conducting plate

4.4.5. EXTENDED AREA APPROACH

Based on the results found in the previous section, a new semi-analytical approach for calculating the distortion current density near the hole in the thin conducting plate is introduced now. The approach is called the extended area approach (EAA).

It is considered the thin conducting plate of thickness δz parallel to $X0Y$ plane. First, the hole is substituted with a regular equidistant grid of N_{VD} voxels of volume $V_D = \Delta x \Delta y \delta z$, where Δx and Δy are grid densities in x- and y-directions. At the center of

each hole voxel $\mathbf{r}_i$, a current dipole of the moment $\mathbf{p}_i = \mathbf{j}_{D,i} V_D$ is placed, where $\mathbf{j}_{D,i}$ denotes the eddy current density vector at $\mathbf{r}_i$ induced by the primary magnetic field in the absence of the hole. The distortion current density at any point $\mathbf{r}$ in a large thin conducting plate outside the hole can be calculated according to

$$\mathbf{j}_E(\mathbf{r}) = \chi_{DCF} \frac{V_D}{2\pi\delta z} \sum_{i=1}^{N_{VD}} \left[2\frac{\mathbf{j}_{D,i} \cdot (\mathbf{r} - \mathbf{r}_i)}{|\mathbf{r} - \mathbf{r}_i|^4} (\mathbf{r} - \mathbf{r}_i) - \frac{\mathbf{j}_{D,i}}{|\mathbf{r} - \mathbf{r}_i|^2} \right] \tag{4.128}$$

where χ_{DCF} is the dipolar correction factor. Having the distortion current density $\mathbf{j}_E$ outside the hole and the "defect" current density $\mathbf{j}_D$ inside the hole, the resulting density $\mathbf{J}$ of currents flowing around the hole can be obtained using the following superposition

$$\mathbf{J} = \mathbf{J}_0 - \mathbf{j}_D - \mathbf{j}_E \tag{4.129}$$

where $\mathbf{J}_0$ is the current density in the plate without the hole.

To estimate a dipolar correction factor for holes of arbitrary shapes, distortion current distributions are analyzed for a series of elliptic holes defined as $c_x \times c_y$, where c_x and c_y denote the x- and y-axis of the elliptic hole. A distortion current outside an elliptic hole can be easy obtained in the elliptic-cylinder coordinate system (η, ψ, z) [95], where the coordinate iso-surfaces are respectively elliptic cylinders (η = const), hyperbolic cylinders (ψ = const), and planes (z = const). The relation between (η, ψ, z) and Cartesian coordinates (x, y, z) is given by:

$$\begin{cases} x = a \cosh\eta \cos\psi \\ y = a \sinh\eta \sin\psi \\ z = z \end{cases} \tag{4.130}$$

where $a = \frac{1}{2}\sqrt{c_x^2 + c_y^2}$. When a uniform excitation electric current in a thin conducting sheet flows opposite to the direction of the y-axis, the distortion current density $\mathbf{j}$ around the elliptic hole $c_x \times c_y$ located at the center of the coordinate system (see for comparison Fig 4.42) is described as follows [95]:

$$\mathbf{j} = \begin{bmatrix} j_x \\ j_y \end{bmatrix} = \frac{1}{2} J_0 \left(e^{2\eta_0} + 1 \right) \begin{bmatrix} -\dfrac{\sin\psi}{\cosh 2\eta - \cos 2\psi} \\ \dfrac{\sinh 2\eta}{\cosh 2\eta - \cos 2\psi} - 1 \end{bmatrix} \tag{4.131}$$

where $\eta_0 = \operatorname{artanh}(c_y/c_x)$ defines the elliptic contour of the hole. Analyzing distortion current distributions for various elliptic holes, it has been found that the dipolar correction factor χ_{DCF} can be approximated by the following expression

$$\chi_{DCF} \simeq 1 + \frac{c_x}{c_y} \tag{4.132}$$

To illustrate above, Fig 4.45 shows local relations between distortion currents for two sample elliptic holes calculated analytically using (4.131) and obtained with the EAA.

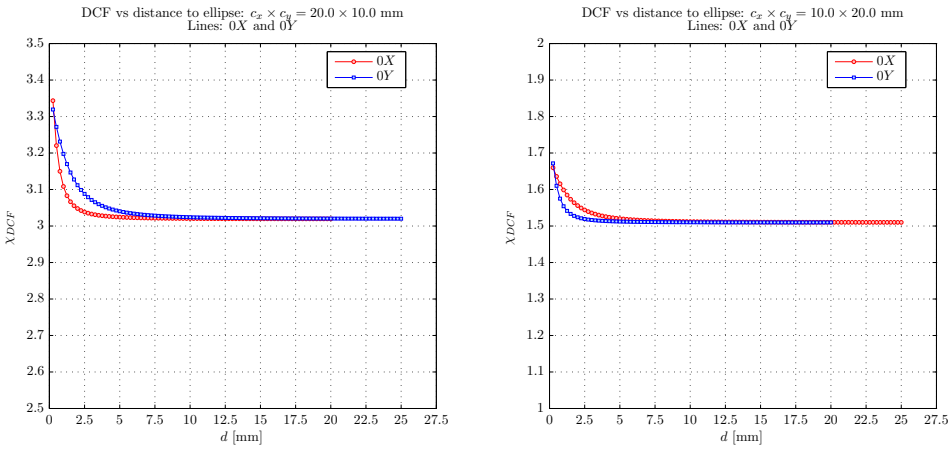

Fig. 4.45: Distribution of local dipolar correction factors

The relations are calculated along $0X$ and $0Y$ lines outside holes as a function of a distance d to the hole contour. Based on the above analysis, the DCF for an arbitrary hole with the outline given by $c_x \times c_y \times \delta z$ is generally defined as

$$\chi_{DCF} = 1 + \frac{c_x}{c_y} \tag{4.133}$$

In the case of circle-shaped holes, $c_x = c_y$ where c_x is equal to the diameter $2R$ of the circle, and $\chi_{DCF} = 2$ as it is shown in the previous section. For other shapes, i.e., elliptic or rectangular holes, c_x and c_y are the x- and y-axes of the ellipse or the length and the width of the rectangle, respectively. Although the DCF given by (4.133) is only an indicative factor it enables to model the distortion field around holes of various shapes with a sufficient accuracy.

Figure 4.46 shows sample current density distributions around holes of various shapes calculated with the EAA. In this case, normalized root mean square errors of the EAA for the circular and elliptic hole are equal to 2.47% and 1.98%, respectively.

In the presented examples, current distributions obtained from corresponding analytical solutions are used as a reference. In all cases, the density of voxel grids used in the EAA was the same and equal to $\Delta x = \Delta y = 1\,\text{mm}$. The $NRMSE$ of the EAA is reducing when the density of voxels in the hole is decreasing (more current dipoles in the hole area are placed), e.g. for $\Delta x = \Delta y = 0.25\,\text{mm}$, the $NRMSE$ equals 1.22% and 1.62% for the circular and the elliptical hole, respectively.

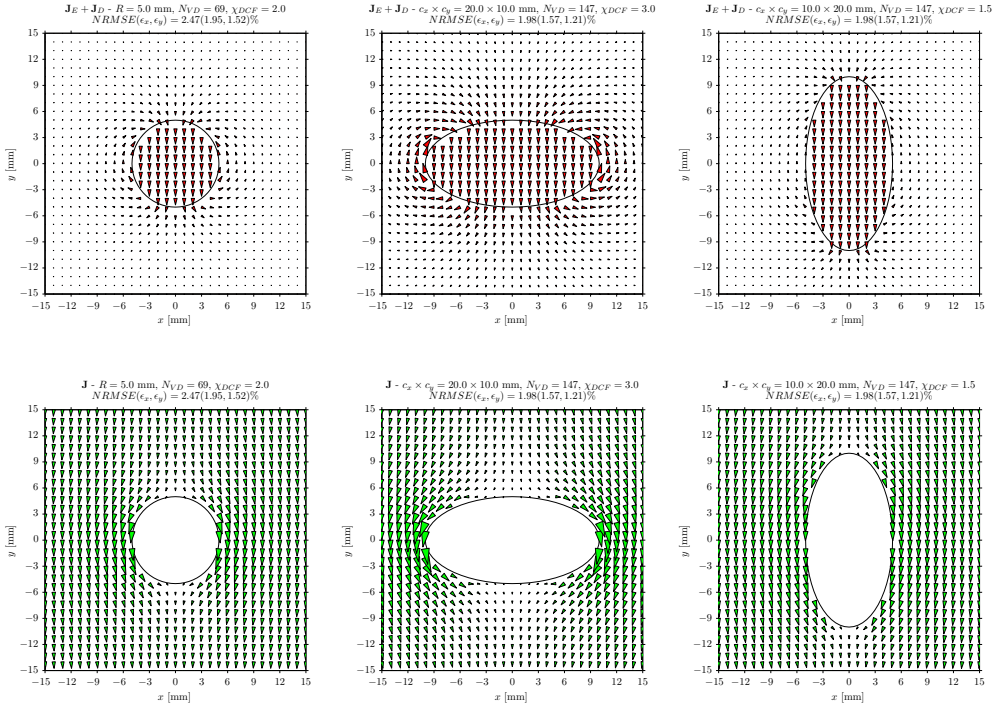

Fig. 4.46: Eddy current density distributions in a large thin conducting plate: (*up*) distortion and "defect" currents, (*down*) superimposed currents

4.4.6. DEFECT RESPONSE SIGNALS FOR DEFECTS IN ANISOTROPIC CONDUCTOR

Further, a conductive plate with a single ideal defect is analyzed. The plate is moving under the fixed permanent magnet with a constant velocity, sufficiently small that the secondary field produced by induced eddy currents in the plate does not influence the primary magnetic field produced by the PM. In that sense, the weak reaction approach can be applied to calculate 3D DRS profiles. The EAA can be directly used in these calculations if the plate is large and the electrical conductivity is anisotropic ($\sigma_{zz} = 0$). Assuming that the top surface of the plate coincides with $X0Y$ plane, the defect can be modeled by one or more XY layers of voxel grids (Fig. 4.47). Having in mind that the weak reaction approach is used, the EAA is applied to every voxel layer independently. The sum of DRSs calculated for each layer gives at the end the total defect response signal. To calculate DRS profile corresponding to one voxel layer, it is necessary to know a current density distribution in the moving plate without defect. To calculate this distributions, MD models of permanent magnets described in Section 4.3. are applied.

Before explaining how to calculate 3D DRS, generalized formulas for the magnetic field produced by an arbitrary oriented magnetic dipole and for eddy currents induced

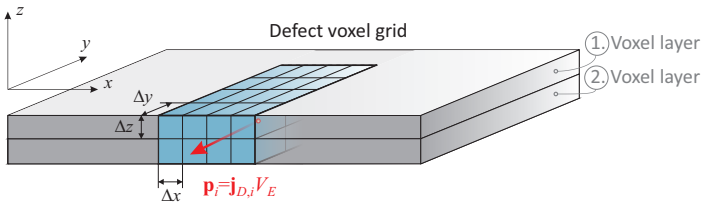

Fig. 4.47: Sample voxel grid covering the defect region

in a slowly moving conducting plate are briefly presented. The formulas enable to construct multi-dipole models (MDM) of complex PM arrangements such as Halbach permanent magnets [55] consisting of more than one magnetic part magnetized in various directions, e.g. cylindrical rods surrounded by segments or rings. The MDM consists of N_D magnetic dipoles located in a regular grid of voxels constructed as it was already shown in Section 4.3.. The moment $\mathbf{m}_i$ of the i^{th} magnetic dipole from the MDM can be determined using the PM magnetization vector $\mathbf{M} = M\mathbf{1}_M$ as $\mathbf{m}_i = MV_M\mathbf{1}_M$, where $V_M = V_0/N_D$ and V_0 is the volume of the PM. The orientation of $\mathbf{m}_i$ coincides with the direction of the magnetization vector $\mathbf{1}_M$. The magnetic flux density $\mathbf{b}_{ki} = \mathbf{b}_i(x_k, y_k, z_k) = [b_{x,i}, b_{y,i}, b_{z,i}]^T$ at the point $\mathbf{r}_k = [x_k, y_k, z_k]^T$ produced by an arbitrary oriented magnetic dipole $\mathbf{m}_i = [m_{x,i}, m_{y,i}, m_{z,i}]^T$ located at $\mathbf{r}_i = [x_i, y_i, z_i]^T$ can be described in the Cartesian coordinate system according to (4.53) as:

$$\mathbf{b}_{ki} = \frac{\mu_0}{4\pi}\begin{bmatrix} 3\frac{x_{ki}^2}{R_{ki}^5} - \frac{1}{R_{ki}^3} & 3\frac{x_{ki}y_{ki}}{R_{ki}^5} & 3\frac{x_{ki}z_{ki}}{R_{ki}^5} \\ 3\frac{x_{ki}y_{ki}}{R_{ki}^5} & 3\frac{y_{ki}^2}{R_{ki}^5} - \frac{1}{R_{ki}^3} & 3\frac{y_{ki}z_{ki}}{R_{ki}^5} \\ 3\frac{x_{ki}z_{ki}}{R_{ki}^5} & 3\frac{y_{ki}z_{ki}}{R_{ki}^5} & 3\frac{z_{ki}^2}{R_{ki}^5} - \frac{1}{R_{ki}^3} \end{bmatrix} \cdot \mathbf{m}_i^T \tag{4.134}$$

where

$$x_{ki} = x_k - x_i, \quad y_{ki} = y_k - y_i, \quad z_{ki} = z_k - z_i$$
$$R_{ki}^2 = r_{ki}^2 + z_{ki}^2, \quad r_{ki}^2 = x_{ki}^2 + y_{ki}^2$$

In the WRA, induced eddy currents $\mathbf{J}$ in a conducting object can be directly calculated using Ohm's law for moving conductors (4.20) because the influence of the secondary magnetic field produced by eddy currents on the primary field is neglected. Equation (4.20) can be written as

$$\mathbf{J} = \sigma_0(\mathbf{E} + \mathbf{v} \times \mathbf{B}) = \sigma_0(-\nabla\phi + \mathbf{v} \times \mathbf{B}) = -\sigma_0 \begin{bmatrix} \frac{\partial\phi}{\partial x} \\ \frac{\partial\phi}{\partial y} + vB_z \\ 0 \end{bmatrix} \tag{4.135}$$

where ϕ is the electric scalar potential fulfilling the Laplace equation $\nabla^2\phi = 0$, and $\nabla \cdot \mathbf{J} = 0$. For 3D LET problem, it can be shown that for an arbitrary magnetic dipole

located above the conducting plate moving along x-axis with constant velocity $\mathbf{v} = v\mathbf{1}_x$, induced eddy currents in the plate flow only in the planes parallel to the top surface of the plate [132], i.e., $J_z = 0$. For a large plate, the electric scalar potential $\phi_{ki} = \phi_i(x_k, y_k, z_k)$ at any point $\mathbf{r}_k = [x_k, y_k, z_k]^T$ in the plate corresponding to $\mathbf{m}_i$ can be directly determined from the condition

$$J_z = 0 \rightarrow \frac{\partial \phi_{ki}}{\partial z} = v b_{y,i} \tag{4.136}$$

where $b_{y,i}$ is the y-component of the magnetic flux density produced by the magnetic dipole $\mathbf{m}_i$ (see (4.134)). Finally, using the notation from [132], the eddy currents induced in the plate can be described as

$$\mathbf{J}_{ki} = \frac{\mu_0 \sigma_0 v}{4\pi} \begin{bmatrix} C_1 g_1 + C_3 g_3 & C_1 f_1 - C_3 f_3 & C_2 g_2 \\ -3C_1 f_1 - C_3 f_3 & -C_1 g_1 - C_3 g_3 & C_0 - C_2 f_2 \\ 0 & 0 & 0 \end{bmatrix} \cdot \mathbf{m}_i^T \tag{4.137}$$

where

$$\mathbf{J}_{ki} = \mathbf{J}_i(x_k, y_k, z_k) = [J_{x,i}, J_{y,i}, J_{z,i}]^T$$

$$f_1 = \frac{x_{ki}}{r_{ki}}, \quad f_2 = \frac{x_{ki}^2 - y_{ki}^2}{r_{ki}^2}, \quad f_3 = \frac{x_{ki}(x_{ki}^2 - 3y_{ki}^2)}{r_{ki}^3} \tag{4.138}$$

$$g_1 = \frac{y_{ki}}{r_{ki}}, \quad g_2 = 2\frac{x_{ki} y_{ki}}{r_{ki}^2}, \quad g_3 = \frac{y_{ki}(3x_{ki}^2 - y_{ki}^2)}{r_{ki}^3} \tag{4.139}$$

and

$$C_0 = \frac{3r_{ki}^2}{2R_{ki}^5} - \frac{1}{R_{ki}^3}, \quad C_1 = \text{sign}(z_{ki}) \frac{3r_{ki}|z_{ki}|}{4R_{ki}^5}, \quad C_2 = -\frac{3r_{ki}^2}{2R_{ki}^5} \tag{4.140}$$

$$C_3 = \text{sign}(z_{ki}) \left[\frac{|z_{ki}|}{R_{ki}^3} \left(\frac{3r_{ki}}{4R_{ki}^2} + \frac{1}{r_{ki}} \right) + \frac{2}{r_{ki}^3} \left(\frac{|z_{ki}|}{R_{ki}} - 1 \right) \right] \tag{4.141}$$

It can be observed that terms $C_1 f_1$, $C_1 g_1$, $C_3 f_3$, and $C_3 g_3$ in (4.137) become singular for $r_{ki} = 0$, i.e., for observation points $\mathbf{r}_k$ lying just under the magnetic dipole $\mathbf{m}_i$. To calculate eddy currents under the dipole, series expansions of C_1 and C_3 around $r_{ki} = 0$ have to be found

$$C_1|_{r \rightarrow 0} = \text{sign}(z_{ki}) \frac{3r}{4|z_{ki}|^4} \left(1 - \frac{5r^2}{2|z_{ki}|^2} \right) + \mathcal{O}(r^4) \tag{4.142}$$

$$C_3|_{r \rightarrow 0} = -\text{sign}(z_{ki}) \frac{15r^3}{8|z_{ki}|^6} + \mathcal{O}(r^4) \tag{4.143}$$

which gives at the end

$$\mathbf{J}_{ki}|_{r \rightarrow 0} = \frac{\mu_0 \sigma_0 v}{4\pi} \begin{bmatrix} 0 & 0 & 0 \\ 0 & 0 & -\frac{1}{|z_{ki}|^3} \\ 0 & 0 & 0 \end{bmatrix} \cdot \mathbf{m}_i^T \tag{4.144}$$

It should be noted that the formula (4.137) together with (4.144) is valid both for uniformly conductive plates and electrically anisotropic plates ($\sigma_{zz} = 0$).

Generally, 3D defect response signals are defined in the same way as in the case of 2D LET problems

$$\Delta\mathbf{F} = \mathbf{F} - \mathbf{F}_0 \tag{4.145}$$

where $\mathbf{F}$ and $\mathbf{F}_0$ are forces exerted on the PM above moving conducting plate with and without a defect, respectively. In the further analysis, it is assumed that the electric conductivity of the moving plate is anisotropic with $\sigma_{zz} = 0$. If only one ideal defect $c_x \times c_y \times c_z$ is located at the depth d in the large moving conducting plate $W \times L \times D$ then the 3D DRS profile for $x_n \in < x_1, x_2 >$ (Fig. 4.48) can be calculated using the EAA

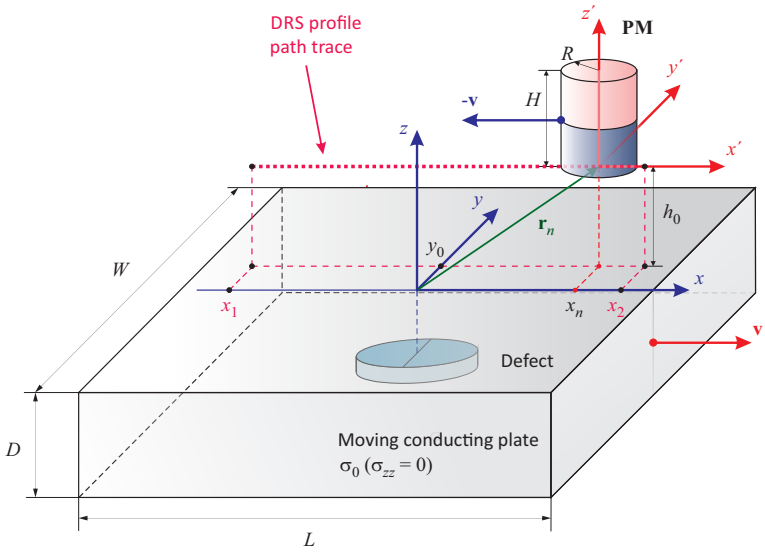

Fig. 4.48: LET configuration setup used in calculations of 3D DRS profiles

and is expressed as follows:

$$\Delta\mathbf{F}^{(n)} = \Delta\mathbf{F}(\mathbf{r}_n) = \int_{-\infty}^{\infty}\int_{-\infty}^{\infty}\int_{-d-c_z}^{-d} (\mathbf{j}_D^{(n)} + \mathbf{j}_E^{(n)}) \times \mathbf{B}^{(n)} dxdydz \tag{4.146}$$

where $\mathbf{r}_n = [x_n, y_0, h_0]^T$ describes the relative position between the PM and the plate coordinate systems, and $\mathbf{J}_E^{(n)}$ and $\mathbf{J}_D^{(n)}$ are distortion and "defect" current density vectors at $\mathbf{r}_n$, respectively.

To calculate 3D DRS profile numerically, the extended region $E_{xt} \times E_{xt} \times c_z$ around the defect $c_x \times c_y \times c_z$ is introduced. The size E_{xt} of the extended region is defined as

$$E_{xt} = (EXT + 1)\max(c_x, c_y) \tag{4.147}$$

where EXT is an arbitrary chosen scaling factor greater or equal 0. If $EXT = 0$ then the extended region does not exist and the model is reduced to the approach described in [105].

The extended region is substituted with $N_L = c_z/\Delta z$ XY-layers of regular grids of voxels each of volume $V_E = \Delta x \times \Delta y \times \Delta z$ (Fig. 4.49). Number of voxels outside and inside a defect is constant for each XY-layer and assigned to N_{VE} and N_{VD}, respectively.

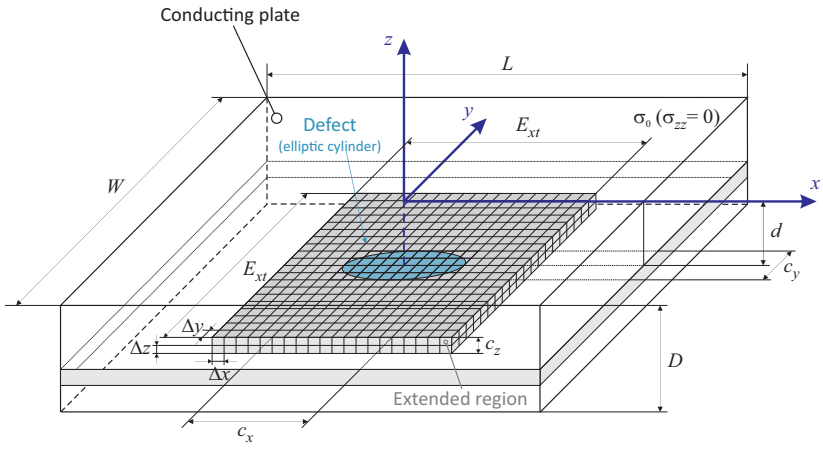

Fig. 4.49: Extended region ($EXT = 1$) around a sample ideal elliptic-cylindrical defect

The 3D DRS formula (4.146) takes the following discrete form:

$$\Delta\mathbf{F}^{(n)} \cong V_E \sum_{l=1}^{N_L} \left[\sum_{j=1}^{N_{VD}} \mathbf{j}_{D,j}^{l,(n)} \times \mathbf{B}_j^{l,(n)} + \sum_{i=1}^{N_{VE}} \mathbf{j}_{E,i}^{l,(n)} \times \mathbf{B}_i^{l,(n)} \right] \tag{4.148}$$

where $\mathbf{j}_{E,i}^{l,(n)}$, $\mathbf{B}_i^{l,(n)}$ are the distortion eddy current density and primary magnetic flux density at the center of the i^{th} voxel located at the l^{th} layer outside the defect, respectively. Vectors $\mathbf{j}_{D,j}^{l,(n)}$, $\mathbf{B}_j^{l,(n)}$ denote the "defect" eddy current density and primary magnetic flux density at the center of the j^{th} voxel in the l^{th} layer inside the defect.

The primary magnetic flux density $\mathbf{B}_k^{l,(n)}$ in the l^{th} layer at the point $\mathbf{r}_k$ outside/inside the defect is calculated using the MDM of the PM as

$$\mathbf{B}_k^{l,(n)} = \sum_{i=1}^{N_D} \mathbf{b}_{ki}^{l,(n)} \tag{4.149}$$

where N_D is the number of magnetic dipoles in the MDM and $\mathbf{b}_{ki}^{l,(n)}$ is given by (4.134) in which $\mathbf{r}_{ki} = \mathbf{r}_k - \mathbf{r}_i' - \mathbf{r}_n$ and $\mathbf{r}_i'$ is a local position of the i^{th} magnetic dipole in the MDM.

The "defect" eddy current density $\mathbf{j}_{D,k}^{l,(n)}$ at the point $\mathbf{r}_k$ inside the defect is a superposition of current density contributions $\mathbf{J}_{ki}^{l,(n)}$ (4.137) evoked by all magnetic dipoles from the MDM:

$$\mathbf{j}_{D,k}^{l,(n)} = \sum_{i=1}^{N_D} \mathbf{J}_{ki}^{l,(n)} \tag{4.150}$$

Having "defect" eddy current densities $\mathbf{j}_{D,k}^{l,(n)}$, distortion eddy currents $\mathbf{j}_{E,k}^{l,(n)}$ at $\mathbf{r}_k$ in the l^{th} layer of the extended region outside the defect can be calculated as

$$\mathbf{j}_{E,k}^{l,(n)} = \chi_{DCF} \frac{V_E}{2\pi\Delta z} \sum_{i=1}^{N_{VD}} \left[2 \frac{\mathbf{j}_{D,i}^{l,(n)} \cdot (\mathbf{r}_k - \mathbf{r}_i)}{|\mathbf{r}_k - \mathbf{r}_i|^4} (\mathbf{r}_k - \mathbf{r}_i) - \frac{\mathbf{j}_{D,i}^{l,(n)}}{|\mathbf{r}_k - \mathbf{r}_i|^2} \right] \tag{4.151}$$

where χ_{DCF} is the dipolar correction factor defined by (4.133).

The formula (4.148) together with (4.149) - (4.151) gives the complete way how to calculate 3D DRS coming up when an anisotropic conducting plate with a defect moves slowly under a fixed, arbitrary magnetized magnet system described by the MDM. The implementation of the above approach can be directly realized as a script in Matlab®. The script should be coded using vectorization features of Matlab® instead of classical loops for the realization of sums in (4.148) - (4.151). This significantly accelerates the code. However, even in the case of optimized code, its execution time strongly depends on the number of magnetic dipoles used in the MDM and thus it could be relatively time consuming for a very accurate MDM with the high number of N_D. Therefore, the possibility of eliminating MDM from DRS calculations has to be analyzed.

First, the MDM can be eliminated from (4.149) which describes the primary magnetic field produced by the permanent magnet by applying directly the analytical expressions presented in Section 4.3.5., i.e., (4.63) - (4.65) or (4.69) - (4.70) for rectangular or cylindrical permanent magnets, respectively.

The second possibility to accelerate the code is to use analytical expressions for $\mathbf{B}$ and $\mathbf{J}_D$ in (4.148). Unfortunately, it was not possible to find analytical formulas for induced eddy currents in a moving conducting plate produced by a cylindrical permanent magnet. Therefore, only the analytical solution for a rectangular PM above a moving plate is presented hereinafter.

The formulas (4.63) - (4.65) can be rewritten using expressions given in [42]. In this case, the magnetic flux density $\mathbf{B}(x,y,z)$ at any point $\mathbf{r} = [x,y,z]^T$ outside a rectangular permanent magnet can be given as

$$\mathbf{B}(x,y,z) = \frac{\mu_0 M}{4\pi} \begin{bmatrix} \sum_{k=1}^{2}\sum_{n=1}^{2} (-1)^{k+n} \ln\left[F_{nk}(x,y,z)\right] \\ \sum_{k=1}^{2}\sum_{m=1}^{2} (-1)^{k+m} \ln\left[H_{mk}(x,y,z)\right] \\ \sum_{k=1}^{2}\sum_{m=1}^{2}\sum_{n=1}^{2} (-1)^{k+m+n} \arctan\left[G_{nmk}(x,y,z)\right] \end{bmatrix} \tag{4.152}$$

where

$$F_{nk}(x,y,z) = \frac{R_{n1k}(x,y,z) + \Delta y_1}{R_{n2k}(x,y,z) + \Delta y_2} \tag{4.153}$$

$$G_{nmk}(x,y,z) = \frac{\Delta x_n \Delta y_m}{\Delta z_k R_{nmk}(x,y,z)} \tag{4.154}$$

$$H_{mk}(x,y,z) = \frac{R_{1mk}(x,y,z) + \Delta x_1}{R_{2mk}(x,y,z) + \Delta x_2} \tag{4.155}$$

and

$$R_{nmk}(x,y,z) = \sqrt{\Delta x_n^2 + \Delta y_m^2 + \Delta z_k^2},\ \Delta x_n = x - x_n,\ \Delta y_m = y - y_m,\ \Delta z_k = z - z_k$$

The parameters x_1, x_2, y_1, y_2, and z_1, z_2 describe the PM as it is shown in Fig. 4.50.

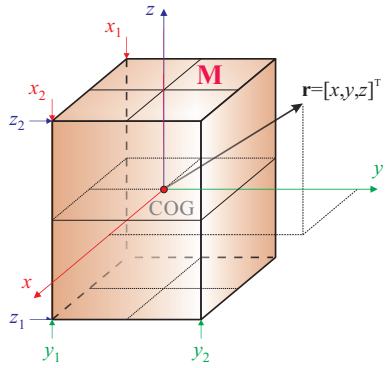

Fig. 4.50: Rectangular permanent magnet - setup for analytical calculations [42]

The electric scalar potential ϕ at any point $\mathbf{r} = [x,y,z]^T$ in the moving plate can be found using the WRA and (4.135) together with the condition (4.136) as

$$\phi(x,y,z) = \frac{\mu_0 M v}{4\pi} \sum_{k=1}^{2}\sum_{m=1}^{2}\sum_{n=1}^{2} (-1)^{k+m+n} \Big\{ \Delta x_n \ln\left[R_{nmk}(x,y,z) - \Delta z_k\right] + \\ + \Delta y_m \arctan \frac{\Delta x_n \Delta z_k}{\Delta y_m R_{nmk}(x,y,z)} - \Delta z_k \ln\left[R_{nmk}(x,y,z) + \Delta x_n\right] \Big\} \tag{4.156}$$

The eddy current density $\mathbf{J}$ in the plate is calculated from:

$$\mathbf{J}(x,y,z) = -\sigma_0 \begin{bmatrix} \dfrac{\partial \phi}{\partial x} \\ \dfrac{\partial \phi}{\partial y} + v B_z \\ 0 \end{bmatrix} \tag{4.157}$$

where B_z is given by (4.152) and gradient components are as follows:

$$\frac{\partial \phi}{\partial x} = \frac{\mu_0 M v}{4\pi} \sum_{k=1}^{2} \sum_{m=1}^{2} \left\{ (-1)^{k+m} \ln \frac{R_{2mk}(x,y,z) - \Delta z_k}{R_{1mk}(x,y,z) - \Delta z_k} + \right.$$
$$\left. + \sum_{n=1}^{2} \frac{(-1)^{k+m+n}}{R_{nmk}(x,y,z)} \left[\frac{\Delta y_m^2 \Delta z_k}{\Delta x_n^2 + \Delta y_m^2} + \frac{\Delta x_n^2}{R_{nmk}(x,y,z) - \Delta z_k} - \Delta z_k \right] \right\} \tag{4.158}$$

$$\frac{\partial \phi}{\partial y} = \frac{\mu_0 M v}{4\pi} \sum_{k=1}^{2} \sum_{m=1}^{2} \sum_{n=1}^{2} (-1)^{k+m+n} \left\{ \arctan \frac{\Delta x_n \Delta z_k}{\Delta y_m R_{nmk}(x,y,z)} + \right.$$
$$+ \frac{\Delta y_m}{R_{nmk}(x,y,z)} \left[\frac{\Delta x_n}{R_{nmk}(x,y,z) - \Delta z_k} - \frac{\Delta z_k}{R_{nmk}(x,y,z) + \Delta x_n} - \right.$$
$$\left. \left. - \frac{\Delta x_n \Delta z_k \left(\Delta x_n^2 + 2\Delta y_m^2 + \Delta z_k^2 \right)}{\left(\Delta x_n^2 + \Delta y_m^2 \right) \left(\Delta y_m^2 + \Delta z_k^2 \right)} \right] \right\} \tag{4.159}$$

In the case where **B** and $\mathbf{J}_D$ in (4.148) are expressed by (4.152) and (4.157), the approach is called the analytical EAA.

In the next section, some results of 3D DRS calculations performed with the EAA for various defects are presented.

4.4.7. SIMULATIONS OF 3D DRS WITH EXTENDED AREA APPROACH

Sample 3D defect response signals are calculated using the EAA for defects shown in Fig. 4.51.

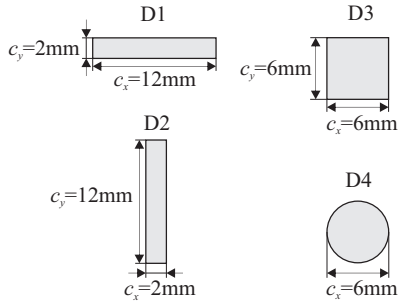

Fig. 4.51: Sample defects used in simulations with the electrically anisotropic plate ($c_z = 2\,\text{mm}$)

All sample defects were located at a depth of $d = 4\,\text{mm}$ and possess the same size $c_z = 2\,\text{mm}$. The size E_{xt} of the extended region was estimated according to (4.147) with the varying parameter EXT equals to 0(1)4. The density of a voxel grid replacing an extended region was constant and equal to $\Delta x \times \Delta y \times \Delta z = 1\,\text{mm} \times 1\,\text{mm} \times 2\,\text{mm}$, i.e., there was only one voxel layer covering the defect. Two permanent magnets (1) cuboid: $w^2 \times h = 15\,\text{mm} \times 15\,\text{mm} \times 25\,\text{mm}$, and (2) cylinder: $2R \times H = 15\,\text{mm} \times 25\,\text{mm}$ fixed at the lift-off $h_0 = 1\,\text{mm}$ above the moving conducting plate of thickness $D = 100\,\text{mm}$

are analyzed. Both magnets are Nd-Fe-B (Neodymium-Iron-Boron) magnets of grade N35 with the remanence (residual induction) B_r equals 1.17 T. The grade of Nd-Fe-B magnets corresponds to the maximum energy product BH_{max} expressed in CGS unit MGOe (Mega Gauss Oersted).

The plate of the anisotropic electrical conductivity $[\sigma] = \text{diag}(\sigma_0, \sigma_0, 0)$ with $\sigma_0 = 30.61\,\text{MS/m}$ moves along the x-axis with the speed $v = 1\,\text{cm/s}$. Defect response signals were calculated according to (4.148) using the analytical EAA for the rectangular PM (1) and the EAA with the optimal (α, β)-MDM consisting of 1365 magnetic dipoles for the cylindrical PM (2). The 3D DRS profiles $\Delta\mathbf{F}(\mathbf{r}_n)$ are calculated on a set of points $\mathbf{r}_n$, regularly distributed along x-line defined as: $y = y_0 = 0$, $z = h_0 = 1\,\text{mm}$, and $x = x_n$ where $x_n \in < -30\,\text{mm}, 30\,\text{mm} >$. The x-density of the profile points is set to $\delta x = 1\,\text{mm}$. Since DRS profile points lie on the XZ-symmetry plane of the considered defects the y-component of $\Delta\mathbf{F}^{(n)}$ is equal to 0 and the DRS profile is defined only by x- and z-component corresponding to the drag and the lift force exerted on the PM.

To quantify errors of DRS calculations with EAA, a normalized root mean square error ($NRMSE$) and a normalized maximum difference error ($NMDE$) are used. The errors are defined as:

$$NRMSE = \sqrt{\epsilon_x^2 + \epsilon_z^2}, \quad NMDE = \sqrt{\zeta_x^2 + \zeta_z^2} \tag{4.160}$$

where

$$\epsilon_c = \frac{\sqrt{\frac{1}{N}\sum_{n=1}^{N}\left[\Delta F_c^{(n)} - \Delta F_{c,FEM}^{(n)}\right]^2}}{\max\left[\Delta F_{c,FEM}^{(n)}\right] - \min\left[\Delta F_{c,FEM}^{(n)}\right]} 100\% \tag{4.161}$$

$$\zeta_c = \frac{\Delta F_c^{max}}{\max\left[\Delta F_{c,FEM}^{(n)}\right] - \min\left[\Delta F_{c,FEM}^{(n)}\right]} 100\% \tag{4.162}$$

$$\Delta F_c^{max} = \max_{n=1\ldots N}\left|\Delta F_c^{(n)} - \Delta F_{c,FEM}^{(n)}\right| \tag{4.163}$$

while index $c \in \{x, z\}$, N is the number of test points in a DRS profile $\Delta\mathbf{F}^{(n)}$, and a subscript FEM denotes a reference solution calculated by FEM.

Table 4.1 shows $NRMSE$ and $NMDE$ of DRS profiles calculated for defects $D1$-$D4$ in a conducting plate moving under the rectangular PM (1) using the analytical EAA with various sizes of the extended region (see (4.147)).

It can be observed that regardless of the shape of the defect both $NRMSE$ and $NMDE$ decrease when extended area increases. However, errors for the long defect $D1$ are much higher than for the other test defects. Increasing the density of voxel grids in the EAA does not improve DRS profiles in this case.

In order to reduce DRS errors for rectangular defects that are not squares, a modified DCF estimated from the so-called "equivalent ellipse" of equal area to the original rectangular defect is applied. The modified DCF χ_{DCF}^* takes the form

$$\chi_{DCF}^* = \frac{\pi}{4}\frac{c_x}{c_y} + 1 \tag{4.164}$$

Table 4.1: Normalized errors of 3D DRS - anisotropic plate

CUBOID[a]		*EXT*				
		0	1	2	3	4
NRMSE [%]	D1	29.28	12.97	11.74	11.40	11.08
	D2	24.76	4.62	3.42	3.42	3.62
	D3	11.95	9.32	6.89	4.51	3.21
	D4	12.18	9.40	7.29	5.00	4.00
NMDE [%]	D1	74.64	27.25	26.72	26.46	25.89
	D2	63.55	7.95	5.67	6.22	6.86
	D3	28.23	21.19	15.06	9.16	6.00
	D4	28.04	20.98	15.20	9.66	7.99

a PM-N35-CUBOID: $w^2 \times h = 15\,\text{mm} \times 15\,\text{mm} \times 25\,\text{mm}$, $h_0 = 1\,\text{mm}$, $v_0 = 1\,\text{cm/s}$, defect depth $d = 4\,\text{mm}$

Table 4.2 shows errors of DRS profiles for the defect $D1$ calculated with the modified DCF which reach now comparable values to the errors for the other test defects.

Table 4.2: Defect $D1$: errors after "equivalent ellipse" correction

*D*1	EXT			
	1	2	3	4
NRMSE [%]	8.92	6.38	5.36	4.81
NMDE [%]	17.49	11.78	10.06	9.22

The DRS profiles ΔF_x and ΔF_z for defects $D1$-$D4$ calculated with the EAA are presented in Fig. 4.52. The profiles for defects $D1$ and $D2$ are obtained using the modified DCF (4.164) while for defects $D3$ and $D4$ the standard DCF (4.133) is applied. For comparison, DRS profiles determined using only "defect" currents [105] are also plotted. DRS profiles for all test defects calculated with the EAA are definitely better than the profiles obtained using only "defect" currents ($NRMSE$ is less than 5%).

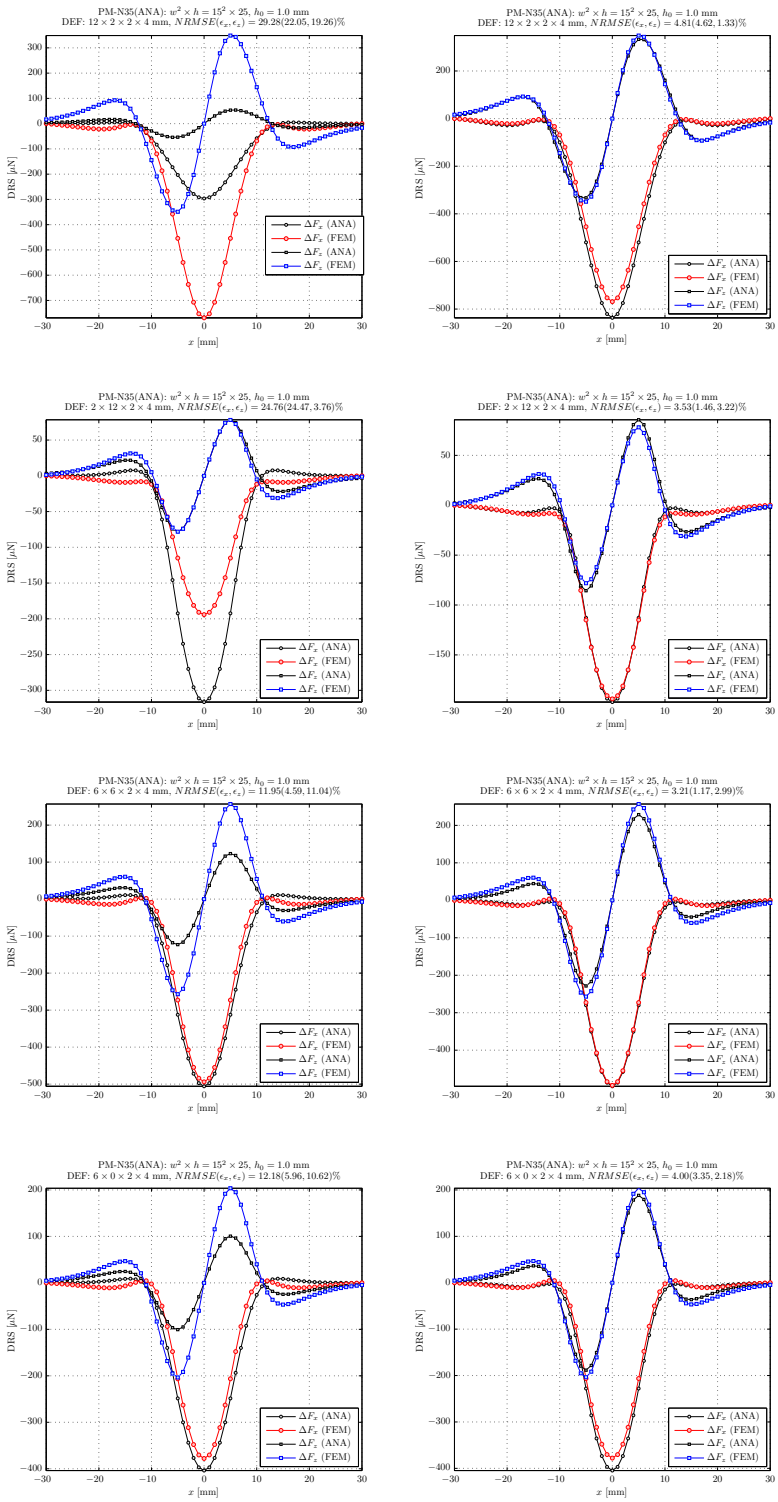

Fig. 4.52: DRS profiles for defects $D1$ - $D4$ (*up* - *down*) calculated for $EXT = 0/4$ (*left*/*right*)

The computation time T_{ANA} of DRS profiles simulations performed using the analytical EAA are also compared with the computation time T_{MDM} of DRS profiles obtained using the EAA with α-MDM for the corresponding rectangular PM. The α-MDM consists of 1331 magnetic dipoles with the optimal α equals 0.485071 which provides modeling of the magnetic flux density in the conducting plate of average error $NRMSE$ less than 0.15%. Computations of DRS profiles with the analytical EAA are over 30 times faster than calculations using the EAA with α-MDM, independently on the size of the applied extended region, e.g. for profiles consisting of 61 points and the extended region defined by $EXT = 4$, T_{ANA} found as average time of calculations performed for all test dipoles equals 2.54 s while the average T_{MDM} is equal to 95.1 s.

Additionally, induced eddy currents near analyzed test defects are calculated to illustrate the quality of the EAA. Figure 4.53 shows distributions of induced eddy currents flowing around defects $D1$-$D4$ at the moment when the PM is just above the center of the corresponding defect. The distributions are calculated with the analytical EAA at

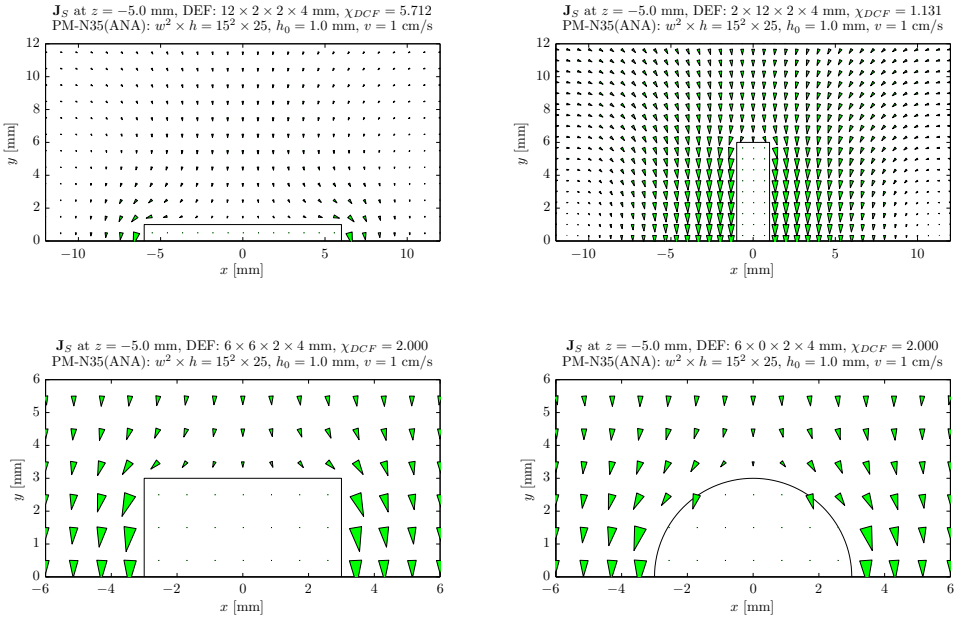

Fig. 4.53: Current density distributions around defects $D1$-$D4$ calculated with the EAA for $EXT = 4$ (PM is located above the defect center)

the XY-plane which is the mid-plane of the defect ($z = -5$ mm). Due to the symmetry of the problem, distributions are plotted only for $y > 0$. Cones represent the resultant eddy current density in centers of corresponding voxels used in the EAA. The resultant eddy currents are superposition of the currents in the moving plate without defect, the "defect" currents, and the currents in the extended region. It can be noticed that the

calculated current distributions are close to these which are expected (see for example Fig. 4.41).

Finally, the results of simulations performed with the cylindrical PM (2) located above the moving conducting plate are summarized in Table 4.3.

Table 4.3: Normalized errors of 3D DRS - anisotropic plate

CYLINDER[a]		EXT				
		0	1	2	3	4
NRMSE [%]	D1	28.45	8.28	6.08	5.27	4.82
	D2	22.19	4.94	4.57	4.64	4.79
	D3	11.73	8.64	6.04	3.82	2.68
	D4	11.93	8.60	6.28	4.16	3.31
NMDE [%]	D1	74.57	16.80	12.02	10.50	9.68
	D2	59.14	8.84	8.50	9.57	10.13
	D3	28.00	19.99	13.40	7.70	4.89
	D4	28.31	19.72	13.40	8.24	6.73

a PM-N35-CYLINDER: $2R \times H = 15\,\text{mm} \times 25\,\text{mm}$, $h_0 = 1\,\text{mm}$, $v_0 = 1\,\text{cm/s}$, defect depth $d = 4\,\text{mm}$

In this case, the PM is modeled by (α, β)-MDM consisting of 1365 magnetic dipoles, and the optimal (α, β) parameters equal $(0.508238, 0.488512)$ which results in an approximation of magnetic flux density in the plate with the average $NRMSE$ below 0.065%. Similarly, as in the case of the rectangular PM,the DRS profiles for defects $D1$ and $D2$ are obtained using the modified DCF in the EAA while for defects $D3$ and $D4$ the standard DCF is applied. The calculated $NRMSE$ and $NMDE$ errors for all test defects are similar as for the rectangular PM, i.e., less than 5% and 10%, respectively.

4.4.8. DEFECT RESPONSE SIGNALS FOR DEFECTS IN SOLID CONDUCTORS

So far, 3D DRS have been calculated for defects located in a moving large conducting plate described by an anisotropic electrical conductivity $[\sigma]$. The application of the EAA can be easily expanded on problems where a solid conducting plate is described by a homogeneous electrical conductivity σ_0. In this case, calculations of induced eddy currents in the moving conducting plate without defect can be performed in the same way as it is described in Section 4.4.6. because the distribution of eddy currents in the plate does not depend on the fact if the electrical conductivity is isotropic or anisotropic, i.e., in both cases, $J_{0,z} = 0$. Although "defect" eddy currents $\mathbf{j}_{D,k}^{(n)}$ remain the same as in the anisotropic case, the distortion currents in the extended region flow not only in the XY-planes but around the entire defect. This means that the extended region has

to be defined as a 3D surroundings of a defect and for distortion currents $\mathbf{j}_{E,k}^{(n)}$,instead of (4.151), the following formula has to be used

$$\mathbf{j}_{E,k}^{(n)} = \chi_{DCF}\frac{V_E}{4\pi}\sum_{i=1}^{N_{VD}}\left[3\frac{\mathbf{j}_{D,i}^{(n)}\cdot(\mathbf{r}_k-\mathbf{r}_i)}{|\mathbf{r}_k-\mathbf{r}_i|^5}(\mathbf{r}_k-\mathbf{r}_i)-\frac{\mathbf{j}_{D,i}^{(n)}}{|\mathbf{r}_k-\mathbf{r}_i|^3}\right] \tag{4.165}$$

where χ_{DCF} is a dipolar correction factor. It can be shown that $\chi_{DCF} = 3/2$ for spherical defects [95].

However, distortion currents calculated with (4.165) do not meet the boundary condition $\mathbf{1}_z \cdot \mathbf{j}_E = 0$ at the top surface of the plate ($z = 0$) where the jump of conductivity is observed. If the thickness of the conducting plate D can be assumed to be much greater than the depth and the maximum size of the defect, then the above boundary condition can be fulfilled by mirroring the "defect" currents $\mathbf{j}_{D,k}^{(n)}$ against the plane $z = 0$ (Fig. 4.54) and then taking into account the "mirrored" currents $\mathbf{j}_{M,k}^{(n)}$ in the distortion calculations.

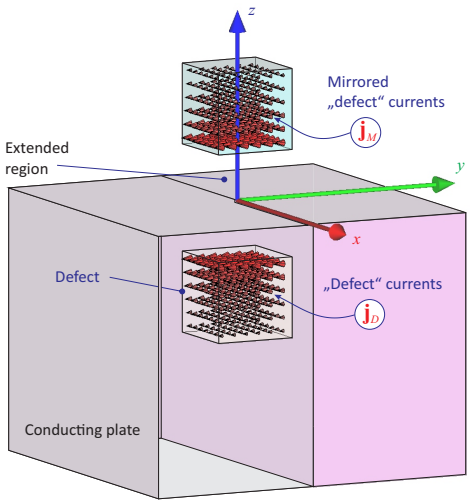

Fig. 4.54: The solid isotropic conducting plate with mirrored "defect" currents

Finally, the eddy currents at any point $\mathbf{r}_k$ in the extended region can be obtained as

$$\begin{aligned}\mathbf{j}_{E,k}^{(n)} = \chi_{DCF}\frac{V_E}{4\pi}\Bigg\{&\sum_{i=1}^{N_{VD}}\left[3\frac{\mathbf{j}_{D,i}^{(n)}\cdot(\mathbf{r}_k-\mathbf{r}_i)}{|\mathbf{r}_k-\mathbf{r}_i|^5}(\mathbf{r}_k-\mathbf{r}_i)-\frac{\mathbf{j}_{D,i}^{(n)}}{|\mathbf{r}_k-\mathbf{r}_i|^3}\right]+\\ &+\sum_{i=1}^{N_{VD}}\left[3\frac{\mathbf{j}_{M,i}^{(n)}\cdot(\mathbf{r}_k-\mathbf{r}_{M,i})}{|\mathbf{r}_k-\mathbf{r}_{M,i}|^5}(\mathbf{r}_k-\mathbf{r}_{M,i})-\frac{\mathbf{j}_{M,i}^{(n)}}{|\mathbf{r}_k-\mathbf{r}_{M,i}|^3}\right]\Bigg\}\end{aligned} \tag{4.166}$$

where $\mathbf{r}_{M,i}$ is the position of the i^{th} mirrored current dipole and $\mathbf{j}_{M,k}^{(n)} = \mathbf{j}_{D,k}^{(n)}$.

DRS profiles can be calculated using (4.148) with (4.166) instead of (4.151). To test the quality of DRS profiles calculated for defects in a solid conducting plate of homogeneous electrical conductivity $\sigma_0 = 30.61[MS/m]$ test defects shown in Fig. 4.55 are analyzed. Test defects are defined by a combination of parameters $c_x \times c_y \times c_z$ as follows: $D1$ (sphere) is described by its diameter ($c_x \times 0 \times 0$), $D2$ (cylinder) is described by the diameter and height ($c_x \times 0 \times c_z$), and $D3$ (cuboid) is given by the length, width, and height ($c_x \times c_y \times c_z$). Parameters c_i for all defects shown in Fig.4.55 are equal to 6 mm while the depth d of defects equals 4 mm. The density of the voxel grid used in the EAA is defined as $\Delta x \times \Delta y \times \Delta z = 1\,\text{mm} \times 1\,\text{mm} \times 1\,\text{mm}$.

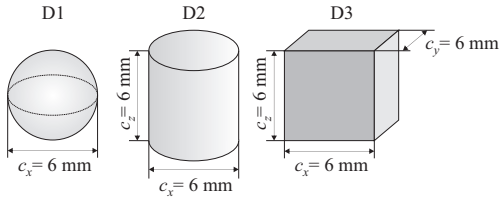

Fig. 4.55: Sample test defects simulated in the electrically isotropic conducting plate

In the LET system, the rectangular PM made of N35 material (remanence $B_r = 1.17\,\text{T}$) is applied. The PM of width 15 mm and height 25 mm is located at the lift-off $h_0 = 1\,\text{mm}$. The conducting plate $W \times L \times D = 400\,\text{mm} \times 400\,\text{mm} \times 100\,\text{mm}$ (important for FEM calculations) moves along the x-axis with the velocity $v = 1\,\text{cm/s}$.

Table 4.4 shows normalized errors ($NRMSE$ and $NMDE$ defined by (4.160)) of DRS profiles for defects $D1$-$D3$ calculated along x-line: $y = 0$, and $z = h_0$, where $x \in <\ -30\,\text{mm}, 30\,\text{mm} >$. The analytical EAA with $\chi_{DCF} = 3/2$ is applied using sequentially increasing extended regions ($EXT = 0 : 1 : 5$). As for the anisotropic case,

Table 4.4: Normalized errors of 3D DRS for defects in a solid plate

CUBOID[a]		EXT					
		0	1	2	3	4	5
NRMSE [%]	D1	17.04	11.08	8.31	5.36	3.82	2.88
	D2	16.10	11.52	8.95	6.00	4.40	3.29
	D3	15.54	11.24	8.36	5.49	4.07	3.26
NMDE [%]	D1	37.77	24.84	17.83	11.19	7.95	6.02
	D2	35.08	25.59	18.91	12.27	9.02	7.00
	D3	33.90	25.31	18.14	11.66	8.55	6.84

a PM-N35-CUBOID: $w^2 \times h = 15\,\text{mm} \times 15\,\text{mm} \times 25\,\text{mm}$, $h_0 = 1\,\text{mm}$, $v_0 = 1\,\text{cm/s}$, defect depth $d = 4\,\text{mm}$

if the extended region increases the reduction of errors can similarly be observed, i.e., $NRMSE$ and $NMDE$ are reduced below 3.5% and 7%, respectively.

Figures 4.56 - 4.57shows DRS profiles of all test defects calculated for $EXT = 0$ (no extended region) and $EXT = 5$, for comparison. It can be observed a very good agreement between the EAA ($EXT = 5$) and the reference FEM solutions. Additionally, distributions of eddy currents flowing around defects are plotted in Fig. 4.58.

In all test simulations, the same dipolar correction factor $\chi_{DCF} = 3/2$ determined from the analysis of a spherical cavity in a homogeneous current field is used. As it can be seen, this DCF works correctly also for other test defect shapes (cylinder, cube) because due to chosen defect dimensions they are quite close to a spherical defect.

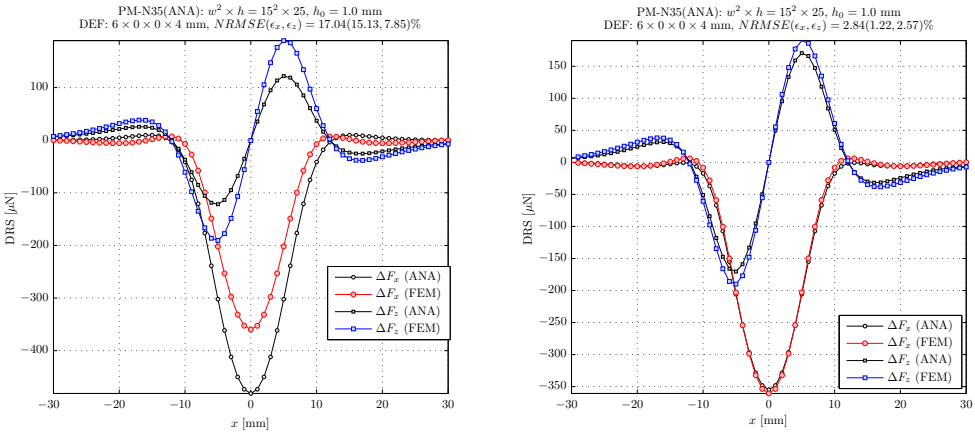

(a) Defect $D1$

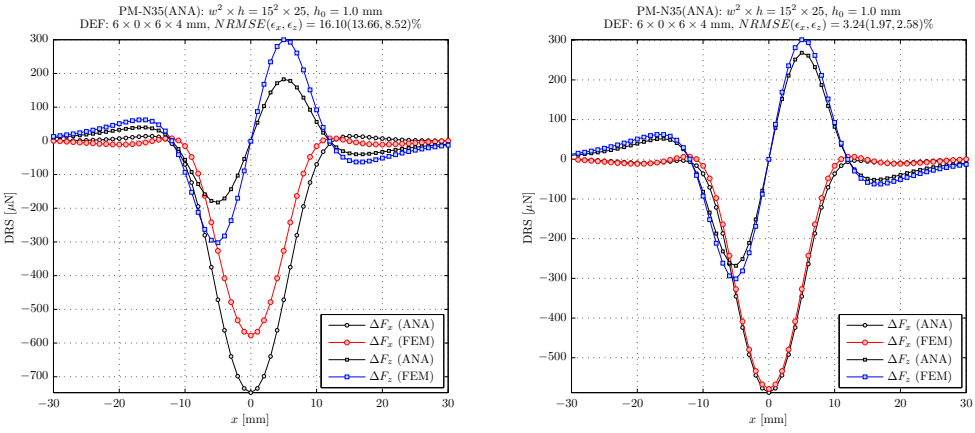

(b) Defect $D2$

Fig. 4.56: DRS profiles of defects $D1$-$D2$ in the solid plate calculated for $EXT = 0/5$ (*left*/*right*)

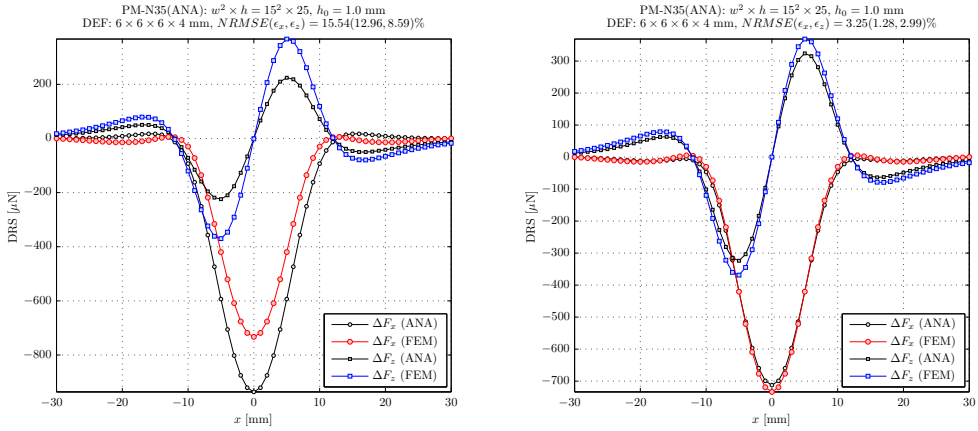

Fig. 4.57: DRS profiles of defect $D3$ in the solid plate calculated for $EXT = 0/5$ (*left*/*right*)

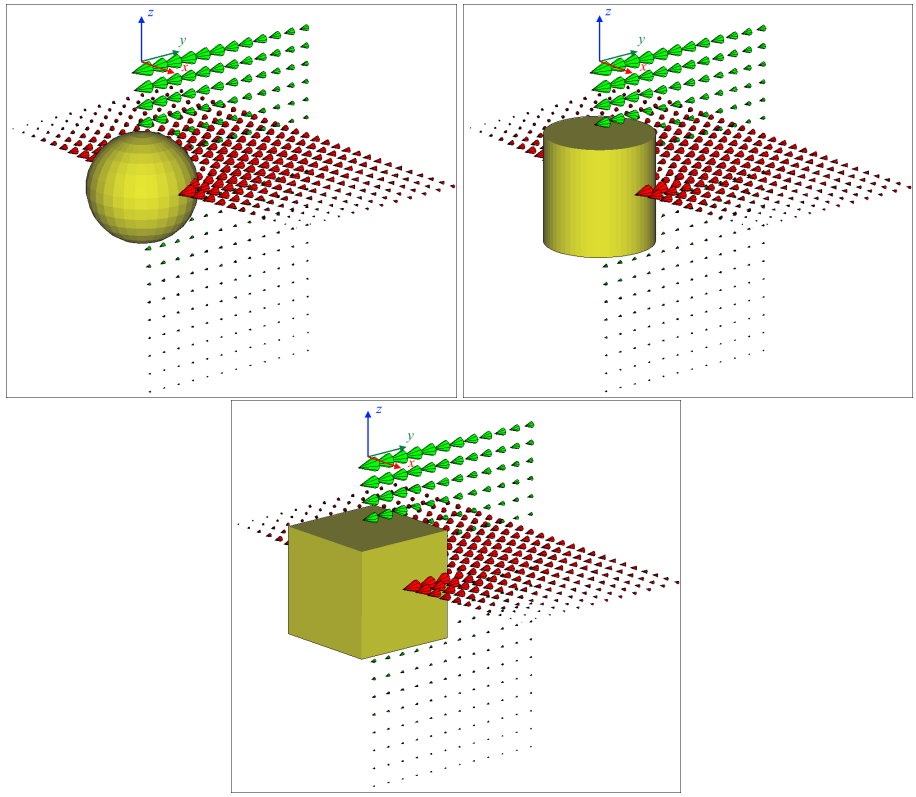

Fig. 4.58: Current density around defects $D1$-$D3$ on the defect symmetry plane for $y > 0$ calculated in the solid plate for $EXT = 5$ (the PM is above the center of defects)

To find the DCF for an arbitrary defect defined by the outline $c_x \times c_y \times c_z$ distortion currents around the idealized cavity in a form of oblate/prolate spheroid have to be analyzed [95]. The cavity is located in a conductor in which homogeneous flow of electric current is forced. The distribution of distortion currents can be found analytically using a separation of variables method in the appropriate coordinate system (oblate/prolate spheroidal CS) [74]. The local dipolar correction factors for defects of various shapes along the $0Y$ line are shown in Fig 4.59.

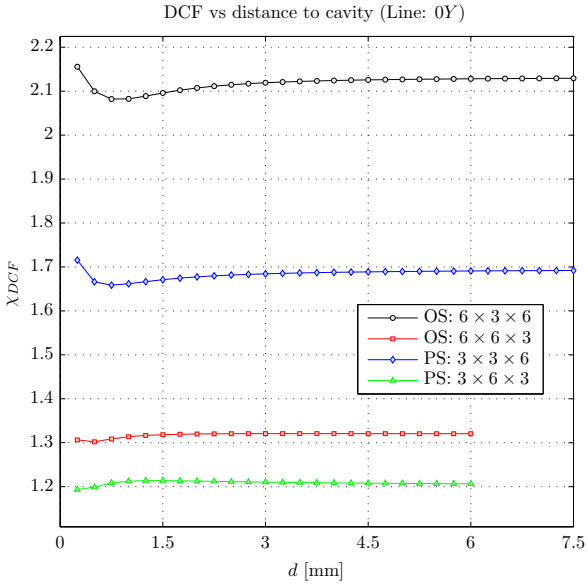

Fig. 4.59: Local dipolar correction factors for spheroidal cavities: (OS) oblate spheroid, (PS) prolate spheroid

The analysis of the presented results allows to find the following approximate formula for the dipolar correction factor in the EAA:

$$\chi_{DCF} = 1 + \frac{1}{4}\left(\frac{c_x}{c_y} + \frac{c_z}{c_y}\right) \tag{4.167}$$

Table 4.5 presents normalized root mean square errors of 3D DRS profiles calculated for rectangular test defects defined by $c_x \times c_y \times c_z$ using constant $\chi_{DCF} = 3/2$ and χ_{DCF} estimated from (4.167). It can be noted that the application of (4.167) reduces DRS errors by about 30% for all test defects.

Figure 4.60 presents DRS profiles for defects from the Table 4.5. A very good conformity can be observed between profiles received with the analytical EAA and the reference DRS calculated by FEM. However, it must be noted that the NRMSE of ΔF_z profiles is always higher than the error of x-DRS component.

Table 4.5: Various rectangular defects in a solid plate - normalized errors

Defect[a] $c_x \times c_y \times c_z$	χ_{DCF}	$NRMSE[\%]$	χ_{DCF} (4.167)	$NRMSE[\%]$
$3 \times 6 \times 3$	1.5	4.85	1.250	2.47
$6 \times 3 \times 3$	1.5	3.81	1.750	2.69
$6 \times 3 \times 6$	1.5	5.62	2.000	3.42
$6 \times 6 \times 3$	1.5	2.92	1.375	2.61

a PM-N35-CUBOID: $w \times w \times h = 15\,\text{mm} \times 15\,\text{mm} \times 25\,\text{mm}$, $h_0 = 1\,\text{mm}$, $v_0 = 1\,\text{cm/s}$, defect depth $d = 4\,\text{mm}$

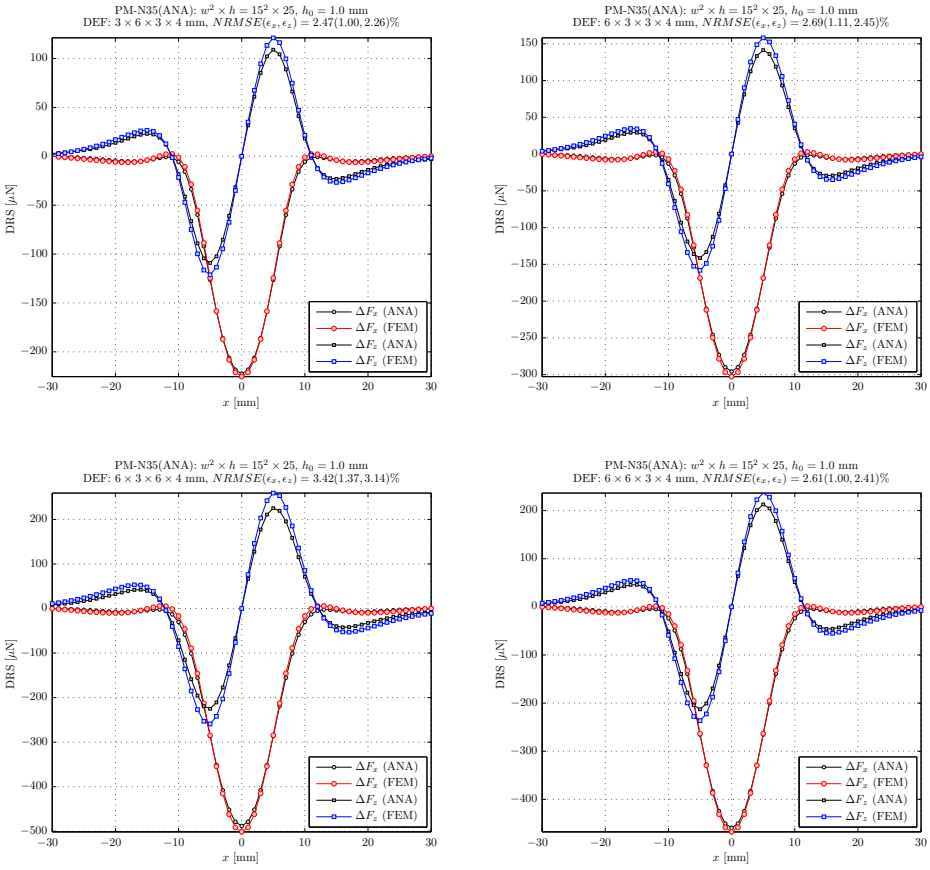

Fig. 4.60: DRS profiles of various rectangular defects in the solid plate calculated for $EXT = 5$

Finally, for the rectangular PM, comparing CPU times of the analytical EAA and the EAA where the α-MDM with 1331 magnetic dipoles is applied, it can be found that the analytical method is almost 40 faster than the MDM one. This comparison is independent on the applied extended region size and the used voxel grid density. For example, for the extended region $EXT = 5$ and the voxel grid density equals $1\,\text{mm} \times 1\,\text{mm} \times 1\,\text{mm}$, the average CPU time of finding 61 point defect response profiles is equal to 15.9 s and 632.1 s for the analytical and the MDM EAA implementation, respectively.

4.4.9. RÉSUMÉ

In Section 4.4., the drag and lift forces exerted on a rectangular/cylindrical PM above a large conducting plate moving with a constant velocity along the x-axis have been calculated using modification of the approach presented in [114]. Formulas for induced stationary eddy currents in the moving plate are also obtained. It has also been shown how to calculate defect response signals (DRS) of one defect located in a large conducting plate slowly moving under a permanent magnet. Using the weak reaction approach (WRA) and the new developed extended area approach (EAA) it was possible to find the DRS of the defect $c_x \times c_y \times c_z$ for large plates of any thickness D and the anisotropic electrical conductivity $[\boldsymbol{\sigma}]$, where $\sigma_{zz} = 0$ as well as for thick solid plates of homogeneous electrical conductivity σ_0. The introduced methods are illustrated by numerical simulations in which 3D DRS and induced eddy currents near a single defect are calculated. Simulations show that the proposed methods allow calculation of 3D DRS with the $NRMSE$ below 5% for all analyzed test defects.

4.5. SUMMARY

In this chapter Lorentz force eddy current testing (LET) method for systems where the source of magnetic field and the investigated conducting object are in relative movement has been presented. The purpose of this chapter was to present in details the use of analytical and semi-analytical methods for the calculation of 2D and 3D models of LET. Numerical Methods (FEM) and analysis of the problems of defects identification (inverse problems) have been deliberately omitted because they have been described elsewhere. At the beginning, two coordinate systems connected with the reference and the moving frame together with the corresponding magnetic field descriptions have been defined. Next, analytical methods of calculation of Lorentz forces for 2D LET models without and with defects have been described (starting from the dipole model and ending with a rectangular model of permanent magnet). Then, the dipole models of cylindrical and cuboidal 3D permanent magnets have been presented and discussed. The corresponding analytical formulas for the analyzed magnets enabling a calculation of the magnetic field at any point around the magnets were also included. Further, analytical approach to the calculation of the Lorentz forces acting on the 3D model of the permanent magnet (cylinder/cuboid) moving with a constant velocity above the conductive infinitely broad plate of given thickness has been described. Formula de-

scribing eddy currents induced in the conductive plate were also given. At the end, the semi-analytical method using an extended area approach for calculation of 3D response Lorentz force signals of defects located in anisotropic or solid conducting plates has been introduced. Discussion and results of simulations for various defects have also been included.

At the end of the summary, a list of associated publications (sorted by date) published by the team working together in the field of LET is presented: [17] LET idea, [153] 2D FEM simulations with moving source function, [18] 2D/3D simulations, [154] fast computation technique (FEM), [126] measurements, validation of numerical results, [140] FEM, 2D study, [139] modeling with logical expressions (FEM), [127] Lorentz force sigmometry, [145] Lorentz force sigmometry, [105] defects reconstruction, anisotropic block, [141] moving defect and moving magnet approaches, logical expressions (FEM), [9] drag force on a magnetic dipole, translating and rotating conducting cylinder, [143] defect depth and magnet lift-off studies, [142] weak reaction approach (FEM), [16] LET overview, [24] LET vs eddy current testing (ECT), [23] measurement, LET vs ECT, velocity and defect depth studies, [92] forward modeling with various permanent magnet models, [110] ECT probes, reverse engineering, [93] permanent magnet modeling.

So far, three doctoral dissertations were presented: [124] LET metrological implementation and verification, [138] LET numerical modeling, [104] Lorentz force evaluation, and the next three are in preparation.

Two patents directly related to the LET are also notified: [146] sigmometry, electrical conductivity measurements, and [144] differential sensor, inspection system.

5

POSTPROCESSING - 3D VISUALIZATION OF FIELDS AND OBJECTS

5.1. INTRODUCTION

Postprocessing is an important part of any numerical and analytical simulation. From one side, widely understanding, the term postprocessing in electromagnetic field analysis incorporates calculations of secondary parameters such as forces, inductances, capacitances, power losses, etc. based on potentials/fields quantities found in a simulation process. On the other hand, the primary goal of postprocessing is to convert the resulting large amounts of simulated data in an understandable form of presentation, e.g. in graphics and animations. This goal can be achieved using internal features of simulation programs (usually commercial), e.g. `ANSYS Maxwell` [4], `COMSOL Multiphysics` [26], `JMAG` [64], `MagNet` [87], `Opera` [102], etc., or with a separate program (commercial/free, e.g. `Geomview` [45], `GiD` [46], `GMV` [47], `Gpr` [50], `ParaView` [103], `Xd3d` [136], etc.) that has special functions and methods which enable visualization and interpretation of simulation results. Although the availability of postprocessing programs is relatively broad, they do not always fulfill the specific requirements of the user, such as, for example, import data in various formats, the implementation of specific functions to interpret the data, functioning on different platforms of operating systems, etc. This is the main reason why the program vv written by the author is introduced in this chapter. At the beginning, the main area of application of the program vv were biomagnetics problems [60, 159–163]. However, the range of applications of the vv program is not limited to the biomagnetic problems only but it can easily be extended on other areas of electromagnetic field analysis, see, eg. Chapters 2 - 4 where the majority of 3D figures are created with the vv-program.

5.2. DESCRIPTION OF VV PROGRAM

The vv is a console visualization program which enables to visualize in a graphic window various 3D objects like boundary/finite element meshes, sensors/electrodes structures together with scalar/vector fields. It is written in a standard C language and uses OpenGL [101] as a graphic library. In that sense, the vv is a system independent program because it can be compiled under MS-Windows as well as under Unix/Linux systems. The calling command of the vv-program has the following format:

```
vv [-option1 [-option2 ...]] file1 [file2 ... ]
```

where `file1` ... `fileN` denote input files with a description of objects which should be visualized and `option1` ... `optionN` are optional controlling parameters from the following list:

```
[-e]        do not show electrodes
[-G]        global scaling of dipoles
[-h]        print usage info
[-m<int>]   display FE mesh with material code <int>
[-M]        maximum mode for dipoles versus time
[-n]        print no name in saved window
[-T<value>] set threshold for displayed dipoles in [%]
[-w<dim>]   window size in pixels
```

Under MS-Windows, the user can use a helpful graphical user interface `vvgui` which makes it easy to use the program `vv`. Figure 5.1 shows the snapshot of `vvgui` main interface window.

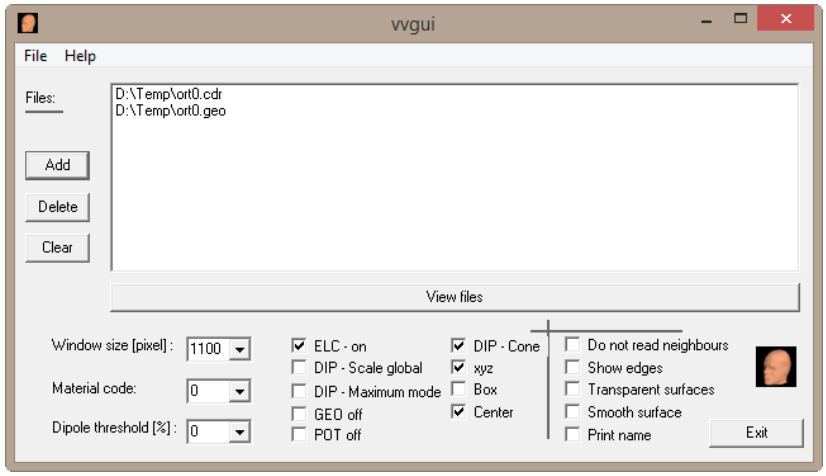

Fig. 5.1: Main window of `vvgui`- program

The `vvgui` enables to choose visualized files from any folder (`ADD` button) using the standard MS-Windows file selector. Because the files describing visualized objects can be located in different folders, using `vvgui` significantly simplifies completing visualized objects. The `vvgui` enables also to set some of `vv` starting options.

Most of the operations on the objects displayed in the graphical window of the vv-program is carried out with the mouse. Pressing and holding the left button and then moving the mouse enables rotation of objects. Pressing additionally `'Shift'` key allows the user to control zooming of displayed objects. Clicking the right button opens a small menu window where the user can control the behavior of visualized objects, e.g. making some of them inactive, set transparency, show edges of visualized meshes, etc. (Fig. 5.2).

Clicking the middle button (or the roller) enables to select elements in meshes used by the boundary element method (BEM). The element selection is necessary for some

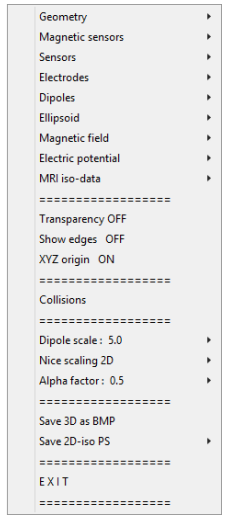

Fig. 5.2: Menu window used for changing execution parameters of the vv- program (activated by pressing the right mouse button)

vv operations, e.g. switching edges between selected elements or local refinement of meshes around chosen element. The selected element is marked with red color. Additionally, the full description of the selected element is printed at the vv console.

All other functions and features of vv are started by clicking a proper key on the keyboard. This activates, when necessary, a dialog on the vv console where some additional parameters can be defined. The complete list of available keys is shown below:

```
---------------------------------------------------------------------
GENERAL OPERATIONS:
---------------------------------------------------------------------
Home   - Reset actual position and zoom to start values
Arrows - Rotates objects 90Â° around main coordinate axes
PgUp   - Zoom objects +10%
PgDn   - Zoom objects -10%
Alt+b  - Show viewing BOX
Alt+e  - Show edges on backsides of objects ON/OFF
Alt+g  - Global scale of field ON/OFF
Alt+l  - Switch between local and global coordinate system
Alt+s  - Store actual view parameters of scene
Alt+u  - Use stored view parameters of scene
h      - Print help ...
I      - Switch ON/OFF spinning
N      - START/END record animation in files vv_xxx.png
O      - Set rotation angle
p      - Print active window in file (.png)
q      - QUIT/EXIT vv
r      - ROTATE active files around active axis
S      - SMOOTH mode ON/OFF (Phong shading ON/OFF)
s      - SCALE active files
T      - TRANSPARENCY ON/OFF
t      - TRANSLATE active files
x      - Set OX as active axis
y      - Set OY as active axis
z      - Set OZ as active axis
---------------------------------------------------------------------
```

```
---------------------------------------------------------------------
GEO-MESHES:
---------------------------------------------------------------------
6 - Change color of active GEO files
C - Define cut-planes
c - CUT-PLANES ON/OFF
d - Switch diagonals in neighbor elements
E - EDGES ON/OFF
F - Refine locally BE-mesh (use object curvature)
f - Refine locally BE-mesh (flat)
g - Define list of elements (geo)
L - Display list of elements ON/OFF
l - Reconnect elements using Lindholm test
m - Show elements with bad quality
n - Recalculate normals
o - Compare GEO with ideal sphere
R - Reduce number of BE-mesh nodes
---------------------------------------------------------------------
MRI-FILES:
---------------------------------------------------------------------
> - Next slice (MRI)
< - Previous slice (MRI)
a - Give actual slice positions (MRI)
---------------------------------------------------------------------
DIP/CDR-FILES (VECTOR FIELDS):
---------------------------------------------------------------------
Alt+a - Change color of arrows/cones
+     - Next time step
-     - Previous time step
A     - Ellipsoid axes ON/OFF
B     - Equivalent ellipsoids ON/OFF
b     - Show equivalent ellipsoids vector ON/OFF
D     - Generate test distributions for EqE and Dali procedures
e     - Calculate equivalent ellipsoids
H     - Define inside factor of equivalent ellipsoid
i     - Calculate focus region (Dali object)
k     - Calculate statistics of CDR
U     - Generate set of current dipoles (moving, radial/tangential)
u     - Generate current dipole tangential to the surface
X     - Calculate difference between axes of EQEs
---------------------------------------------------------------------
POT/FLX-FILES (SCALAR FIELDS):
---------------------------------------------------------------------
+ - Next time step
- - Previous time step
3 - Set new color palette (pot/flx)
j - Set step for iso-lines (pot/flx)
K - Subtract offset in scalar field (pot/flx)
v - Change color scale ON/OFF (pot/flx)
---------------------------------------------------------------------
EXPORT FUNCTIONS:
---------------------------------------------------------------------
5 - Export data in STL-format (stereolithography, ASCII)
W - Export active files in VRML-format
w - Export active files in ASCII-format
---------------------------------------------------------------------
```

Details of listed above available functions will be given in next sections.

5.3. VISUALIZATION OF 3D OBJECTS

The vv program can visualize various 3D objects, namely: surfaces defined as BEM meshes, volumes described by FEM meshes, isometric binary data received from a magnetic resonance imaging (MRI), and sets of sensors used in bioelectromagnetic measurements (sets of electrodes, magnetometers, gradiometers).

The format of visualized data is identified based on extensions used in data filenames. The following formats are recognized by vv:

```
.GEO  - 3D surface (ASA format)
.BND  - 3D surface (ASA format)
.PNT  - set of 3D points (ASA format)
.NPT  - set of 3D points (ASA format)
.BDx  - 3D surface (Curry format)
.Sxx  - 3D surface (Curry format)
.OFF  - 3D objects (Object Oriented File Format) (Geomview)
.GTS  - 3D surface (GNU Triangulated Surface Library format)
.NODE - volume - 3D FEM mesh (TETGEN format)
.ME3  - volume - 3D FEM mesh (FEM3D format)
.M3D  - volume - 3D FEM mesh (FEM3D format)
.GRD  - magnetic sensors - gradiometers (ASA format)
.RS3  - sensor geometry file (Curry format)
.ELC  - electric sensors (ASA format)
.MRI  - magnetic resonance isometric binary data (ASA format)
```

where x denotes any digit.

ASA™[5] is a highly flexible EEG/ERP/ECG (ElectroEncephaloGraphy/ Event Related Potentials/ ElectroCardioGraphy) and MEG/MCG (MagnetoEncephaloGraphy/ MagnetoCardioGraphy) analysis package with a variety of source reconstruction, signal analysis and MRI processing features.

The Curry software [30] is the most advanced and comprehensive tool for multimodal neuroimaging. Curry combines functional data such as EEG and MEG with structural data from MRI and CT (Computer Tomography) to optimize source reconstruction.

Geomview [45] is an interactive 3D viewing program for Unix using OOGL (Object Oriented Graphics Library) file formats for description of 3D objects.

TetGen [122] is a program which generates good quality and adaptive tetrahedral meshes of any 3D polyhedral domains suitable for finite element or finite volume methods.

FEM3D is a finite element program for calculation of some 3D electrodynamic problems based on [51].

GNU stands for *GNU's Not Unix* and describes the complete Unix -like software system [48]. It differs from Unix by being free (not commercial) software and containing no Unix code.

Figure 5.3 shows sample one compartment BEM models of brain and torso with activated SMOOTH option (Phong shading with interpolated surface normals, [119]) and Show EDGES option switched off (brain model) and on (torso model).

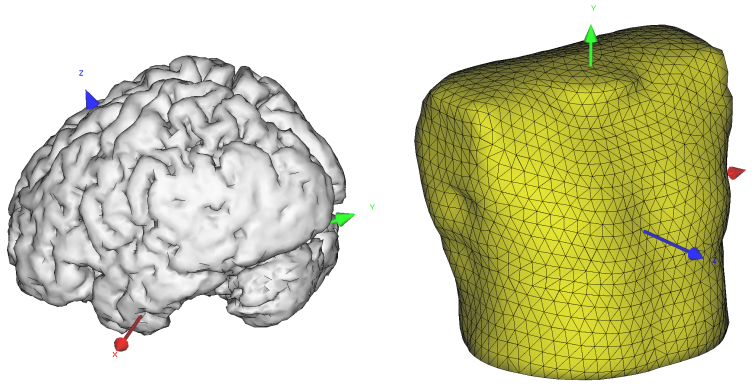

(a) Brain model (grey matter) (b) Torso model

Fig. 5.3: Sample BEM meshes with activated `SMOOTH` option. Option `Show EDGES` is switched on for torso model

The `vv` program can also visualize complex compartment models. In Fig. 5.4, the complex multi-compartment BEM model of torso consisting of thorax, lungs, heart, and ventricles is shown. The BEM model is created from MRI scans. Figure 5.4a presents objects when the `TRANSPARENCY` option is on while Fig. 5.4b shows the same objects with `CUT PLANES` option applied. The user can define up to 6 cut planes perpendicular

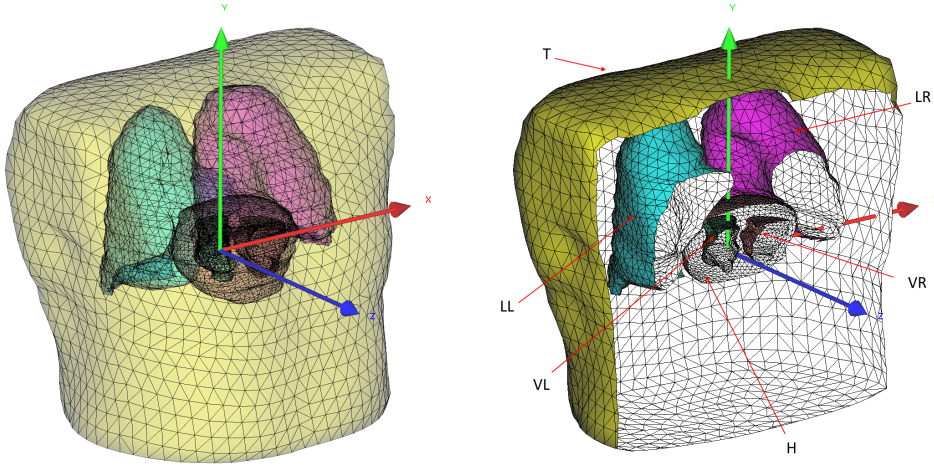

(a) `TRANSPARENCY` option is on (b) XY-cut plane, $z = 30\,\mathrm{mm}$

Fig. 5.4: Multi compartment BE-model of torso created from MRI scans (T - thorax, LL/LR - lung left/right, H - heart, VL/VR - ventricle left/right)

to the main coordinate axes. The other possibility of viewing complex compartment models is so called "onion" approach where the user deactivates some objects (Fig. 5.5).

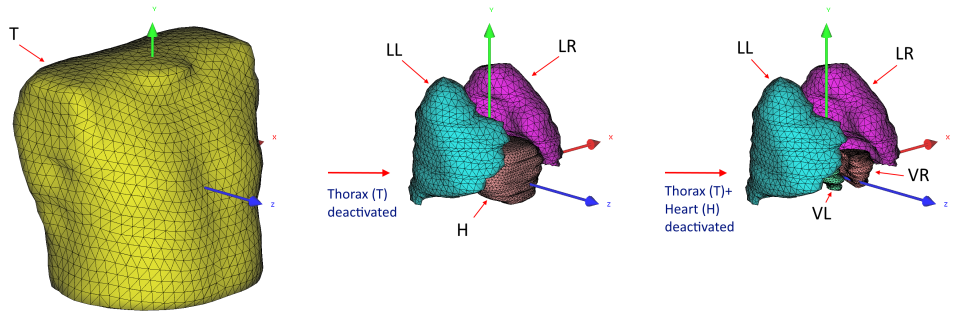

Fig. 5.5: Multi compartment BEM model - "onion" approach

The vv program enables to perform some operations on 3D surface triangular meshes, i.e., a simple reduction of global mesh nodes and local mesh refinements. For creation new BEM meshes (reduced/refined), the vv uses a simple triangle quality criterion [86] to find connections between mesh elements. Considering a triangle ABC with edges of length a, b, c and the semi-perimeter $s = (a + b + c)/2$, the quality q of the triangle ABC is defined as:

$$q = 8\frac{(s-a)(s-b)(s-c)}{abc} \tag{5.1}$$

The maximum of q equals 1 and corresponds to an equilateral triangle.

For a pair of triangles sharing a common edge, the optimal connection of triangles [86] can be defined as a connection with the maximum of a joint quality factor q_{12} given as:

$$q_{12} = 2\frac{q_1 q_2}{q_1 + q_2} \tag{5.2}$$

where q_1 and q_2 are the individual quality factors of analyzed triangles.

Figure 5.6 shows sample reduction of BE mesh of torso model performed by vv which removes some nodes and elements from the original mesh and creates a new reduced BE mesh. The reduced model consists of $N_E = 1950$ triangular elements which is almost twice less than the number of elements of the original mesh.

However, it must be noted that the average quality Q_a of the reduced mesh is worse than the average quality of the original mesh. Before the reduction process can be started, the user has to choose the compartment which should be reduced. This can be done by clicking the middle mouse button/roller over the object to select. The selection is marked by changing the actual color of the closest element to `red` color (Fig. 5.6a).

Sometimes, the user would like to perform calculations with higher accuracy in a certain region. In this case, it becomes helpful to perform a local refinement of the

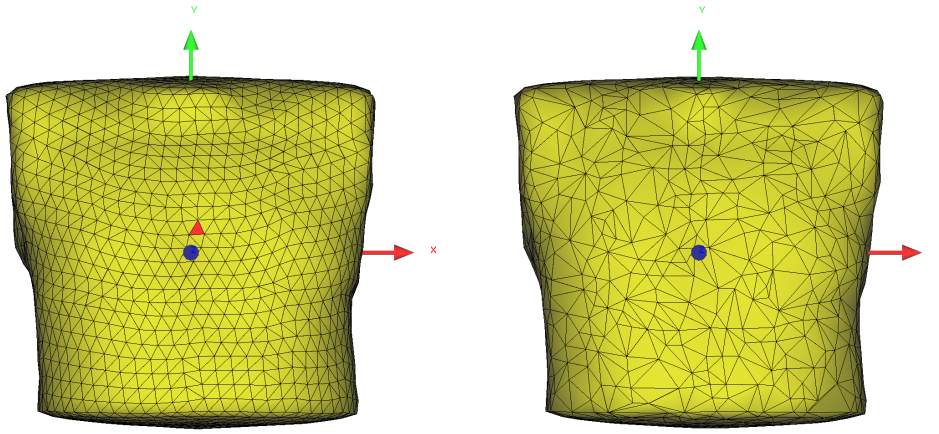

(a) Original mesh: $N_E = 3654$, $Q_a = 92.7\%$ (b) Reduced mesh: $N_E = 1950$, $Q_a = 76.5\%$

Fig. 5.6: Sample reduction of BE-mesh for thorax model

boundary element mesh. The `vv` program offers two BE-mesh refinement procedures: a simple one (key: `'f'`), in which positions of additional nodes are calculated as average positions of nodes belonging to the corresponding elements and more advanced one (key: `'F'`), where the curvature of the object is taken into account for the estimation of new nodes.

As for the mesh reduction function, at the beginning, the user has to select a compartment for which the refinement should be carried out. The selection is realized by pressing the middle button of the mouse. Using the actual mouse cursor position, the closest element of the BE-mesh and the compartment are selected. The active selection is shown by changing the color of the selected element to `red`. The selected mesh element is treated as a center of the refinement region. The refinement procedure refines all elements from the selected compartment located in the sphere of radius R. The user defines the radius of the refinement sphere at the `vv` console. The modified BE-mesh can be saved using `vv`-export keys: `'w'`, `'W'`, and `'5'`, which enable to export active objects, i.e., the objects which are actually present in the `vv`-view window, in `ASCII`, `VMRL`, or `STL` format, respectively. The `VMRL` format (Virtual Reality Meta Language) is a standard file format for representing 3D interactive vector graphics, designed specially for using in the World Wide Web (WWW) environment. The `STL` format (STereoLithography) is a file format native to the stereolithography software which is supported by many CAD software packages.

Figure 5.7 presents sample results of local advanced refinement for brain and torso models. The refinement procedure has been used twice for both models with corresponding refinement radii equal 50 mm and 25 mm for the brain model and 100 mm and 50 mm for the torso model, respectively. In both cases, the average mesh quality

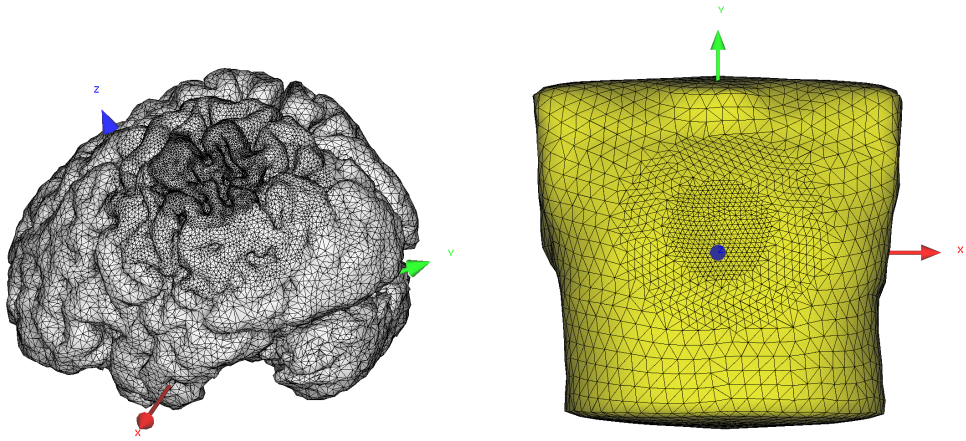

(a) Brain model (b) Torso model

Fig. 5.7: Sample refinements of BE-meshes

remains almost unchanged, i.e., $Q_a|_{\text{before/after}} = 87.4\%/86.8\%$ and $92.6\%/92.6\%$ for the brain and the torso model, respectively.

Figure 5.8a shows MRI scans of a physical thorax phantom visualized on 3 mutually perpendicular planes [15]. The vv program enables to visualize MRI isometric

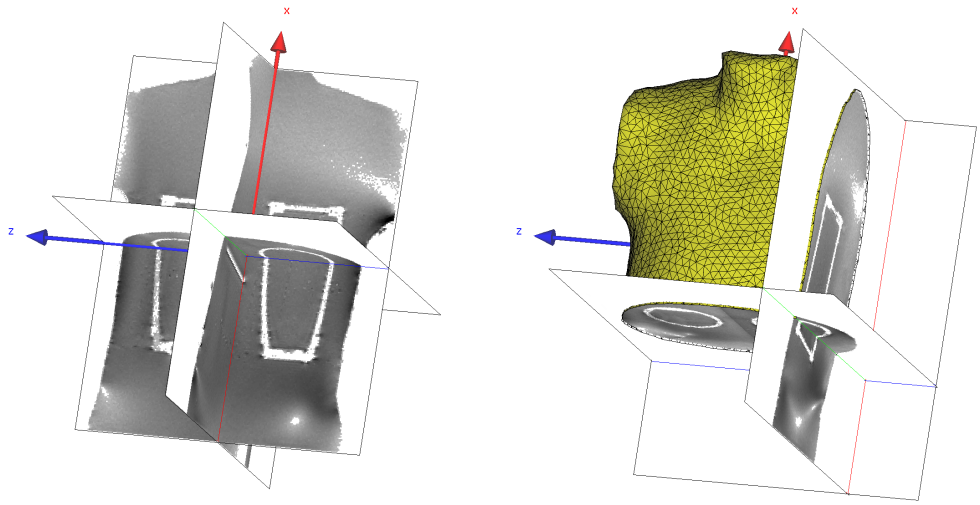

(a) MRI scans (b) MRI scans combined with BE-model

Fig. 5.8: Visualization of MRI scans of artificial thorax model

data stored in a binary file containing one byte per voxel of optional items (file extension: `.mri` - raw ASA format). Positions of planes along active axis (chosen by key: `'x'/'y'/'z'`) can be controlled by keys `'>'/'<'`. Figure 5.8b presents the same MRI scans combined with the BEM model of thorax. The BEM model is displayed using 2 clipping planes (key: `'C'`) defined by the plane normal vector and the distance to the center of the system:

- Plane 1: $\mathbf{n} = [0, 0, 1]$, $z_d = -100\,\text{mm}$,
- Plane 2: $\mathbf{n} = [1, 0, 0]$, $x_d = -100\,\text{mm}$.

The `vv` program can also visualize various systems of magnetic sensors (file extensions: `.rs3/ .grd` - Curry/ASA format) and electrodes (file extension: `.elc`). Electrodes are presented in a form of small grey balls while magnetic sensors (magnetometers/-gradiometers) are drawn as simplified coil configurations (e.g. thin solid disks, rectangular thin coils, etc.). Figure 5.9 presents the Neuromag-122 system and the configuration of magnetic sensors around sample BEM model of a test person head. The Neuromag-122 MEG system was built by the company Neuromag Ltd., Helsinki (Finland) in 1989 (Fig. 5.9a). It was the first developed whole head MEG device (helmet system) [3]. It consists of 122 planar off-diagonal first-order gradiometers located at 61 measurement points with the average separation of 4 cm [56] (Fig. 5.9b).

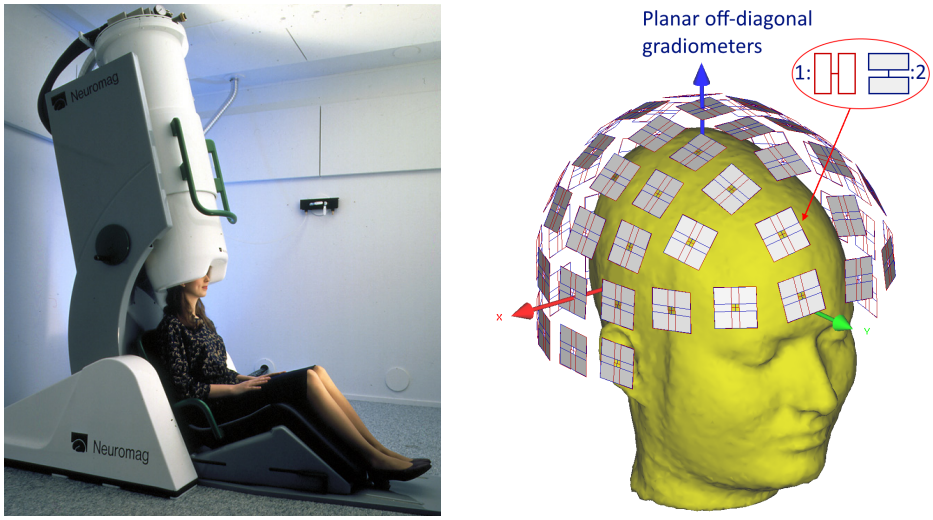

(a) Neuromag-122 (b) 122 Planar gradiometers

Fig. 5.9: Neuromag-122 whole head MEG system (helmet shaped) [3]

Figure 5.10 shows the Philips (the Netherlands) twin dewar (a large thermos-like container) biomagnetometer system with 2×31 symmetrical first order axial gradiometers [34] for operation inside a shielded room [3]. The system can be used for the MEG/MCG recording. Additionally, up to 62 channels of EEG/ECG signals can be recorded.

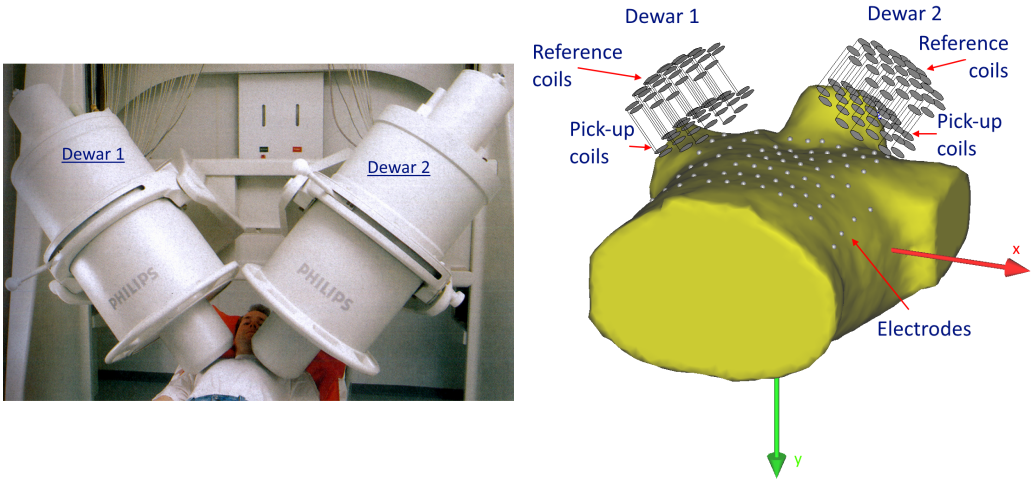

(a) Twin dewar system

(b) 2×31 axial gradiometers

Fig. 5.10: Philips twin dewar biomagnetometer system (MCG/ECG session) [3]

5.4. VISUALIZATION OF SCALAR AND VECTOR FIELDS

There are two ways to visualize scalar fields distributions in `vv`. In both ways, a pair of files must be read, one file with the field values and the second one with the description of sensors. In the first way, scalar field values (e.g. the electric potential) are given in the file with the extension `[.pot]` while sensors (electrodes) are defined in the file with the extension `[.elc]`. In the second way, field values (e.g., the magnetic flux density component/magnitude) are given in the file with the extension `[.flx]` and sensors have to be defined in the file with the extension `[.grd]`. In addition to the positions of the sensors, the sensors file must also contain a grid of links between them. In both ways, the file with field values can contain data for one or more time steps. Introduction of two ways to describe scalar fields in the visualization procedure is due to the specificity of biomagnetic applications where there is a need to distinguish electric from magnetic sensor configurations. Figure 5.11 shows sample instantaneous distributions of the electric potential V and the magnetic flux density B recorded during EEG/MEG session together with the BEM model of the subject's head. The electric potential has been registered using 32 electrodes mounted on the subject's scalp. The magnetic flux density has been measured using only one dewar of the Philips system with 31 magnetic channels. The presented distributions correspond to the moment when the electric potential reaches maximum. The user can choose the moment of the displayed field by pressing key `'+'/'-'` which increases/decreases the actual time about one time step. The maximum/minimum values of actually visualized fields are printed in the console window. The distance between isolines in field plots can be modified using key `'j'`.

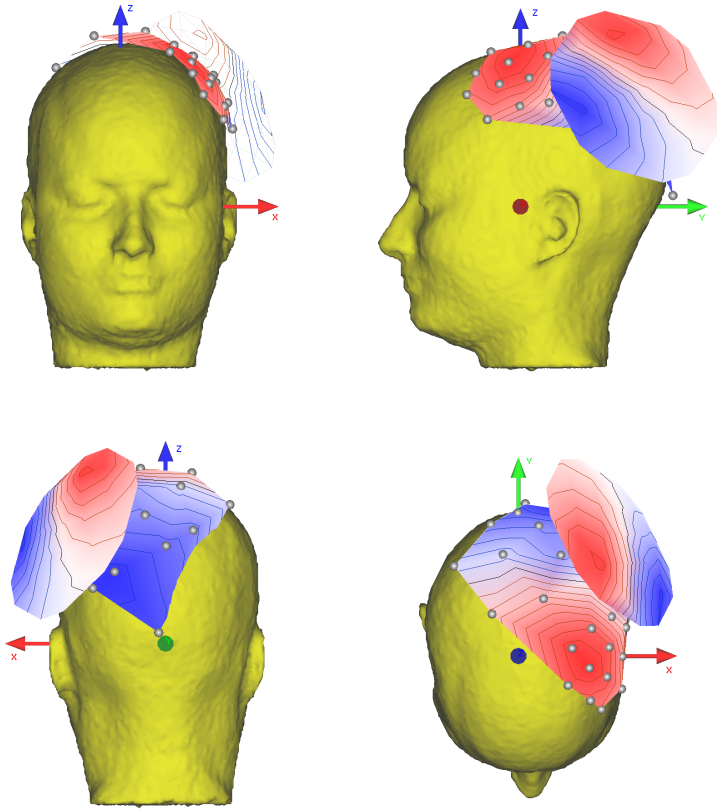

Fig. 5.11: Instantaneous electric potential V and magnetic flux density B (one dewar of the Philips system) recorded during EEG/MEG session. Min/max values of V/B: $[-3.74, 4.53]\mu V/[-311.8, 258.4]fT$. Distance between contour lines: $\Delta V = 0.5\,\mu V$, $\Delta B = 50\,fT$

Because files with field values and sensors are simple ASCII files with self-explaining keywords, both ways of scalar field visualization can easily be adapted to other applications, see eg. Chapter 3 or 4.

Figure 5.12 presents a cylindrical cell leading direct current (DC) with two oscillating conducting fluids for the moment when the interface between fluids described by the mode η_{13} reaches the maximum elevation. Contour plot of the interface elevation is created using data stored in a pair of files with `[.pot]-` and `[.elc]-` extensions.

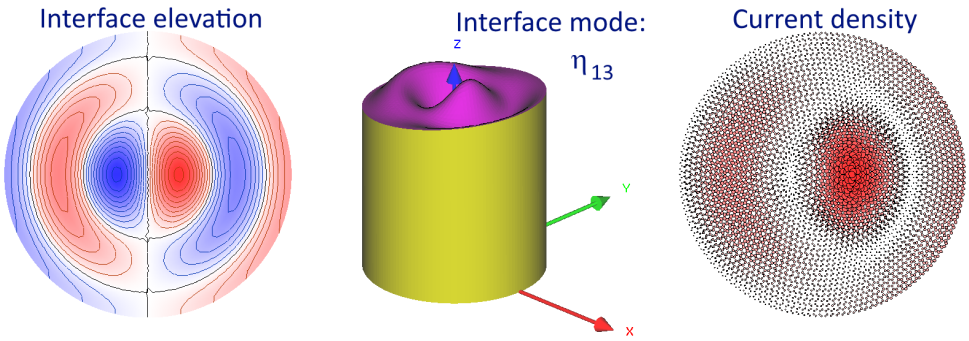

Fig. 5.12: Cylindrical cell with two oscillating conducting fluids - interface mode η_{13}. Interface elevation (*left*) and current density near interface projected on $X0Y$-plane (*right*)

Figure 5.13 shows distributions of radial and axial magnetic flux density components around the above cylindrical cell leading DC current for the maximum elevation of the interface. In this case both approaches are used. The field on the cylindrical surface is plotted using `[.pot] + [.elc]` files while the field on the evolved surface (plane) is displayed using `[.flx] + [.grd]` files.

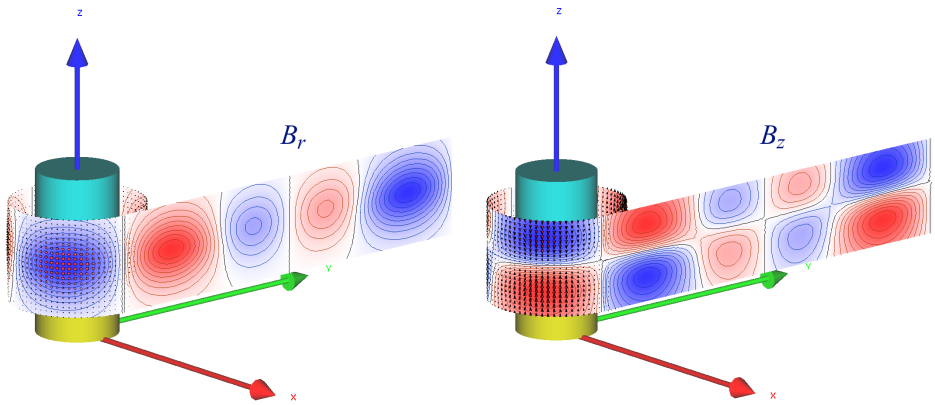

Fig. 5.13: Distribution of radial and axial magnetic flux density components around cylindrical conducting cell for the maximum elevation of the interface (mode η_{13})

Discrete vector fields (eg., current density field, magnetic flux density distribution, etc.) defined on a set of spatial points can be visualized in the `vv` with the help of 3D arrows or cones (Fig. 5.14). The tail of 3D arrow/cone base is located at the corresponding vector field position. Arrows/cones show local direction of the field while their size is proportional to the magnitude of the field at the location point. The format of the file, in which vector field is stored, is recognized by the `vv` using the file extension, i.e., `[.dip]` - `ASA` format, `[.cdr]` - `Curry` format, or `[.jd3]` - `FEM3D` format.

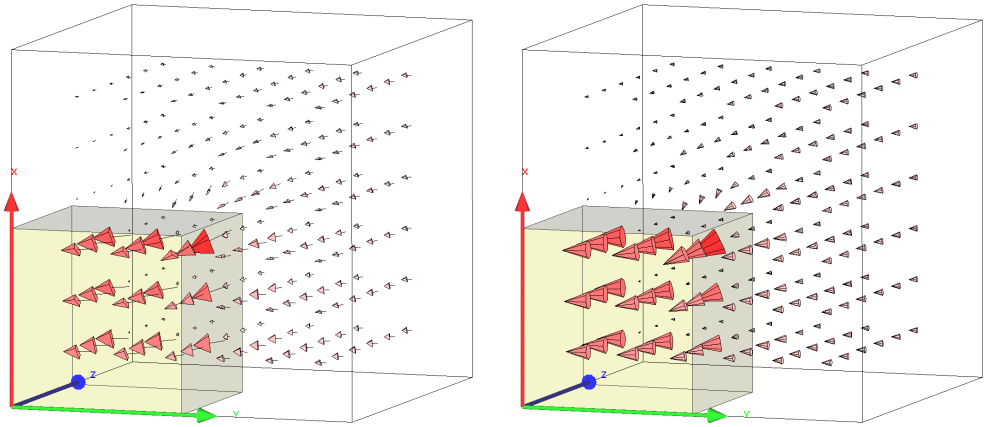

(a) 3D arrows (b) Cones

Fig. 5.14: Vector field visualization - 3D arrows versus cones

The implementation of ASA format is the most general. It allows work with time dependent vector fields, i.e., transient field values stored at several time steps per only one set of field positions or stored as several compound sets of field values and positions together, for movement simulations. The other two formats assure vv functionality for static vector fields only. In the case of time dependent fields, the switching between time moments is done by pressing '+'/'-' key.

5.5. ADVANCED TOOLS IN VV

Despite of functions described in the previous sections, some additional advanced tools are implemented in the vv program. These tools are helpful in the interpretation of large data sets (equivalent ellipsoid, Dali object), the preparation of animated objects (movies), or the generation of test vector fields.

To prepare animated objects, the user has to activate a spinning mode in the current viewing scene by pressing the key 'I'. When the spinning mode is activated, moving the mouse with pressed left button results in spinning/rotating objects around the axis determined from the tracked positions of the mouse. Pressing 'I' once more deactivates the spinning mode. Move the mouse faster/slower results in faster/slower spinning of active objects. If the user would like to save the spinning scene, he can press the key 'N' which starts recording serial snapshots of the vv graphic window. The snapshots are stored in files with automatically generated names 'vv_nnn.png', where 'nnn' are the numbers of successive pictures. Pressing 'N' once more stops the recording. Figure 5.15 presents a few snapshots recorded during spinning of a sample L-object.

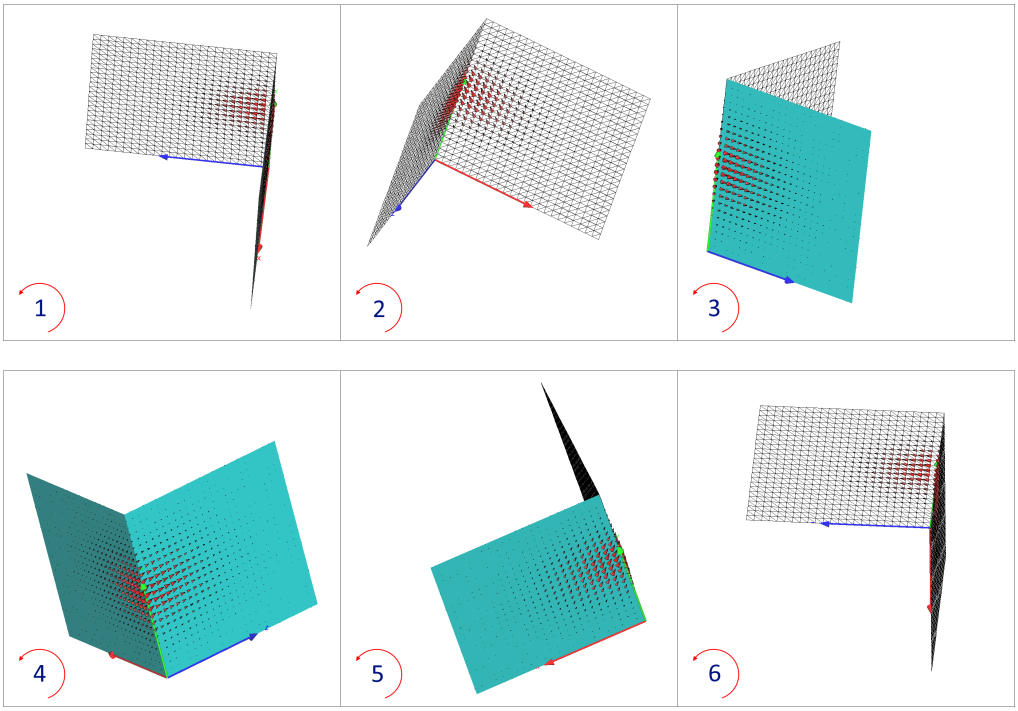

Fig. 5.15: Sequential snapshots of L-object spinning around free axis

Pressing the key `'D'` generates test distributions of vector fields defined on sample predefined surfaces, like: rectangle (plane), two perpendicular rectangles (L-shape), three perpendicular rectangles (corner), or in a cuboidal volume (cube). The distributions can be uniform or can be concentrated around a predefined center. The number of centers as well as the concentration damping (according to the Gauss distribution) are defined by the user. Figure 5.16 presents examples of test distributions generated by vv.

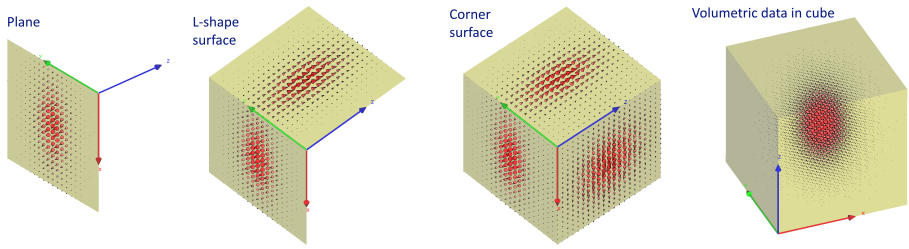

Fig. 5.16: Sample test concentrated vector field distributions on a plane, L-shape and corner surfaces, and in a cube

The test objects created by vv can be saved in ASCII files by pressing the key 'w'. In this case, all actually viewed objects are stored in separate files with appropriate extensions in the folder from which the vv has been started or in the home vv folder.

The equivalent ellipsoid tool (EqE), introduced in [163] and [161], is a tool which can be used for the interpretation of large sets of discrete vector fields data, e.g. current dipoles distributions, current density distributions received from reconstructions in biomagnetical or non-destructive testing problems. Usually, a parametrization of such distributions to facilitate statistical comparisons between data sets (from different individuals or from one individual in different conditions or times) is desirable. An equivalent ellipsoid is defined as 3D ellipsoidal object fitted to a vector field distribution region in which the magnitude of the field is above a certain threshold (in the following called supraliminal y distribution). The equivalent ellipsoid is defined by three orthogonal semi-axes ($\mathbf{a} = a\mathbf{e}_1$, $\mathbf{b} = b\mathbf{e}_2$, $\mathbf{c} = c\mathbf{e}_3$), where $\mathbf{e}_i$ denotes the i^{th} unit vector of the local ellipsoid coordinate system. The user has to define the threshold T_h used for the determination of the most important region in the analyzed distribution. The vv program delivers some statistical information about the analyzed distribution together with some suggestions about the threshold definition. Sample statistics for a set of current dipoles is given below:

```
-----------------------------------------------------------------------
 Maximum                = 1.200000 [Am]
 Minimum                = 0.000000 [Am]
 Mean/Max               = 14.12 [%]
 Variance/(Max*Max)     = 2.80 [%]
 Standard deviation/Max = 16.73 [%]
 Average deviation/Max  = 12.74 [%]
 Skewness               = 1.60 (x39.83)
 Kurtosis               = 2.75 (leptokurtic)
-----------------------------------------------------------------------
 ...> Thresholds:
-----------------------------------------------------------------------
 SD/Max                 = 16.73 %
 (Max - SD)/Max         = 83.27 %
 (Mean + SD)/Max        = 30.86 %
 (Mean + Max)/2Max      = 57.06 %
 Power50%               = 45.00 %
 (Max2 - SD2)/Max2      = 89.90 %
 (Mean2 + SD2)/Max2     = 14.90 %
 (Mean2 + Max2)/2Max2   = 52.40 %
-----------------------------------------------------------------------
```

where the skewness is a measure of the asymmetry of the distribution about its mean value, and the kurtosis is a measure of the "peakness" of the distribution, and *Power50%* denotes the threshold for the supraliminal distribution with 50% of total power calculated as a sum of squared magnitudes over all points in the distribution.

Depending on the distribution, the user has to decide if the data should be partitioned or not to find some concentration regions (clusters) in the distribution. To find partitioning clusters, the vv uses Partition Around Medoids (PAM) algorithm described in [67]. The PAM is based on the search for k representative objects among all objects of the data sets. The representative objects are called medoids of the clusters (centroids). The PAM chooses data points as medoids and works with an arbitrary matrix of distances between data points associating each data point to the closest medoid. Distances

can be calculated using any valid distance metric (in the VV Euclidean metric is used). The algorithm works iteratively so long as no changes in the medoids are observed.

Having representative clusters, the center of gravity (COG) $\mathbf{p}_{COG}^{(k)}$ for each cluster is calculated as

$$\mathbf{p}_{COG}^{(k)} = \frac{1}{Q^{(k)}} \sum_{i=1}^{N^{(k)}} q_i^{(k)} \mathbf{p}_i^{(k)}, \quad Q^{(k)} = \sum_{i=1}^{N^{(k)}} q_i^{(k)} \tag{5.3}$$

where $N^{(k)}$ is the number of field points in the k^{th} cluster, and $q_i^{(k)}$ is the current density magnitude at the point $\mathbf{p}_i^{(k)}$.

The equivalent ellipsoid for k^{th}-cluster is calculated using the Principal Component Analysis (PCA) based on the singular value decomposition (SVD) of the 3×3 covariance matrix $[\mathbb{C}]$ constructed from the distances between the vector field points and the COG:

$$[\mathbb{C}] = \frac{1}{N^{(k)} - 1} \sum_{i=1}^{N^{(k)}} [\mathbf{p}_i^{(k)} - \mathbf{p}_{COG}^{(k)}]^T \cdot [\mathbf{p}_i^{(k)} - \mathbf{p}_{COG}^{(k)}] \tag{5.4}$$

The eigenvectors received from SVD define unit directions $\mathbf{e}_i^{(k)}$ of the k^{th} equivalent ellipsoid while the eigenvalues $\lambda_i^{(k)}$ sorted in descending order are used for the estimation of the initial values of ellipsoid semi-axes $[a_0^{(k)}, b_0^{(k)}, c_0^{(k)}]^T$:

$$\left[a_0^{(k)}, b_0^{(k)}, c_0^{(k)}\right]^T = \left[\sqrt{\left|\lambda_1^{(k)}\right|}, \sqrt{\left|\lambda_2^{(k)}\right|}, \sqrt{\left|\lambda_3^{(k)}\right|}\right]^T \tag{5.5}$$

Then, each vector field position is associated with a small volume V_{vox} around it, called voxel. Voxel is defined as an elementary cube centered around the field position. The length of voxel edge d_{vox} is set to the average of minimum distances between the field position and its neighbors calculated for all N points in the distribution:

$$\begin{aligned} \forall i, j \in \{1 \dots N\} : d_i &= \min_{i \neq j} \left|\mathbf{p}_j - \mathbf{p}_i\right| \\ d_{vox} &= \frac{1}{N} \sum_{i=1}^{N} d_i \end{aligned} \tag{5.6}$$

To assess the quality of the k^{th} equivalent ellipsoid, the goodness factor $G_0^{(k)}$ is defined as follows:

$$G_0^{(k)} = \frac{N_I^{(k)}}{N^{(k)}} \frac{N_I^{(k)} V_{vox}}{\frac{4}{3}\pi a^{(k)} b^{(k)} c^{(k)}} \frac{\sum_{i=1}^{N_I^{(k)}} \left[Q_i^{(k)}\right]^2}{\sum_{i=1}^{N^{(k)}} \left[Q_i^{(k)}\right]^2} 100\% \tag{5.7}$$

where $N_I^{(k)}$ is the number of field points inside the ellipsoid and $a^{(k)}$, $b^{(k)}$, $c^{(k)}$ are semi-axes of the ellipsoid. The low value of $G_0^{(k)}$ indicates that more partitioned clusters might be required. If the length of the smallest semi-axis c_0 is shorter than half the voxel edge, i.e., the distribution is located on the plane like surface, then c_0 is arbitrary set to $0.5d_{vox}$. In this case, instead of (5.7), the following modified formula is applied:

$$G_0^{(k)} = \frac{N_I^{(k)}}{N^{(k)}} \frac{N_I^{(k)} d_{vox}^2}{\pi a^{(k)} b^{(k)}} \frac{\sum_{i=1}^{N_I^{(k)}} \left[Q_i^{(k)}\right]^2}{\sum_{i=1}^{N^{(k)}} \left[Q_i^{(k)}\right]^2} 100\% \tag{5.8}$$

The size of the equivalent ellipsoid is determined using growing up procedure (ballooning technique) with $[a_0^{(k)}, b_0^{(k)}, c_0^{(k)}]^T$ as start values. The procedure works until the ellipsoid covers all field points in the cluster while the ratio of the semi-axes is kept constant. In every ballooning step, the goodness factor is calculated and at the end the semi-axes corresponding to the maximum goodness factor are chosen as axes of the equivalent ellipsoid.

Figure 5.17 shows equivalent ellipsoids constructed for noisy test volumetric vector data with four dominant concentration centers (Gauss damped) generated in the cube 120 mm × 120 mm × 120 mm. The distance between field points equals $d_{vox} = 5$ mm. The partitioning has been calculated for 4 clusters using the threshold $T_h = 45[\%]$ which corresponds to the *Power50* threshold suggested by VV.

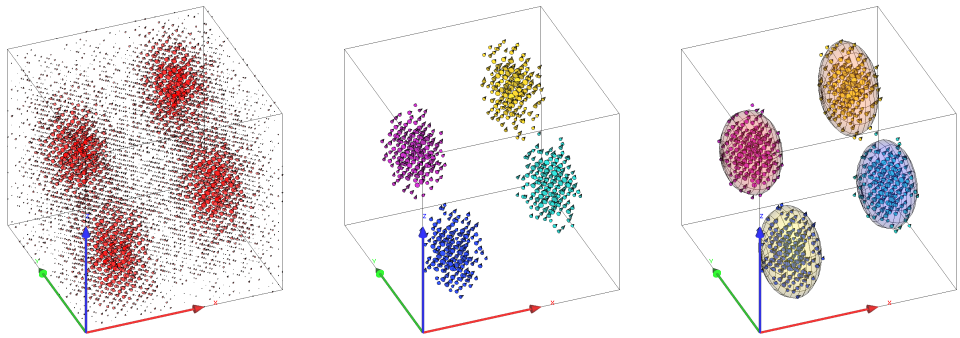

(a) Test noisy data (b) Partitioned clusters (c) Equivalent ellipsoids

Fig. 5.17: Equivalent ellipsoids for noisy test volumetric data with four concentration centers

Table 5.1 presents details of obtained ellipsoids. The parameter N_I is the ellipsoid inside factor defined as the number of field points located inside the ellipsoid to the number of all points of the corresponding cluster. The column G_0 presents the maximum of the ellipsoid goodness for which the ellipsoid is constructed. It can be observed that for all ellipsoids the inside factor is high, i.e., almost all field points are located inside ellipsoids. The goodness of all equivalent ellipsoids is over 50%. The relative

Table 5.1: Equivalent ellipsoids for test noisy data

EqE	Center	Semi-axes	N_I	G_0	P
	$[mm]$	$[mm]$	[%]	[%]	[%]
1	[25.2, 24.7, 24.6]	[23.4, 18.4, 14.4]	90.8	56.9	11.6
2	[25.3, 74.9, 50.6]	[21.1, 18.5, 14.3]	84.2	53.5	11.7
3	[74.8, 25.5, 50.4]	[22.9, 17.8, 13.4]	85.8	54.4	11.0
4	[74.9, 74.8, 74.8]	[23.4, 18.0, 13.6]	84.6	50.0	11.7

power P is relatively uniformly distributed between ellipsoids. By adding P- power of all the ellipsoids, an approximately threshold *Power50*, the start threshold in the EqE-reconstruction procedure is obtained.

The second example presents the application of equivalent ellipsoids to interpretation of current density distributions reconstructed on a cerebral cortex of a patient with pharmacological induced migraine (nitroglycerin spray). The 31 channels DC MEG has been measured using the Philips one dewar biomagnetometer system [34]. The system has recorded one hour of continuous data with a sampling rate of 40 Hz ($0 - 15$ Hz bandwidth). Artifact rejection has been performed on the basis of the magnetic reference sensors. Large amplitude waves have been identified in the raw data and have been used for the source reconstruction using the minimum norm estimation with a one compartment BEM model of the patient head. The source model consists of 17480 current density vectors located on the segmented brain surface. The average closest mutual distance of current density vectors equals 3.2 mm.

Figure 5.18 shows the interpretation of the reconstructed current density using only one equivalent ellipsoid obtained for the threshold $T_h = 57.8\%$. The threshold T_h has

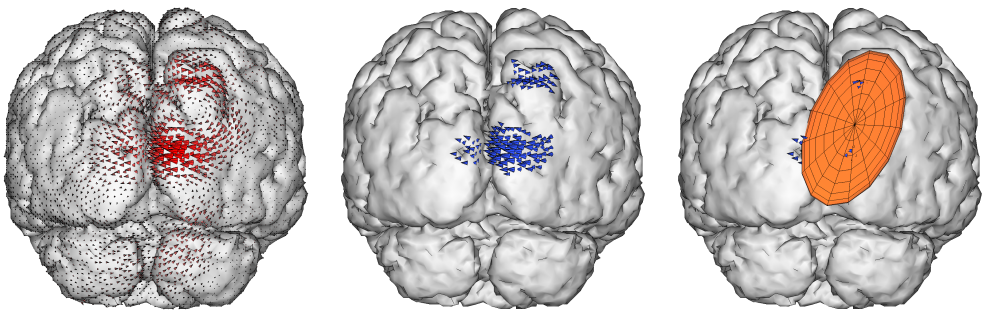

(a) Source model (b) $T_h = 57.8\%$ (c) Equivalent ellipsoid

Fig. 5.18: Current density distribution on a cerebral cortex surface and equivalent ellipsoid constructed for threshold $T_h = 57.8\%$

been chosen using the formula: $100\% - 4\sigma$, where $\sigma = 10.55\%$ is the standard deviation calculated for the analyzed distribution. The semi-axes $[a, b, c]$ of the calculated EqE are equal to [40.1 mm, 20.9 mm, 4.6 mm]. Although the inside ellipsoid factor is high ($N_I = 88.4\%$), the goodness of the EqE is low ($G_0 = 8.7\%$). The reason for this is the complicated shape of the cortex surface on which the reconstructed current density distribution is located. In order to improve the data interpretation more partitioning clusters have to be used. The partitioning with 3 and 4 centers has been tested (Fig. 5.19a and Fig. 5.19b). Visual inspection shows that using 4 centers results in better clusters separation than for 3 centers where one of the clusters contains also points lying on the adjacent wall of the cortex surface. Equivalent ellipsoids for the partitioning with 4 clusters are shown in Fig. 5.19c.

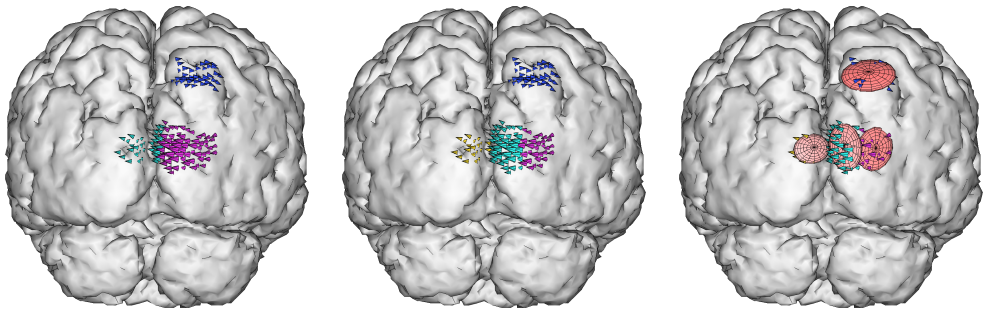

(a) 3 clusters (b) 4 clusters (c) Equivalent ellipsoids

Fig. 5.19: Current density distribution reconstructed on a cerebral cortex surface and equivalent ellipsoids for 3 and 4 clusters found for threshold $T_h = 57.8\%$

Details of found equivalent ellipsoids are given in Table 5.2. The estimated voxel size obtained as the average closest mutual distance of field points in the analyzed distribution equals $d_{vox} = 2.43$ mm.

Concluding, it can be said that the interpretation of real data is not straightforward. Although the equivalent ellipsoid is a robust tool and helps significantly to interpret

Table 5.2: Equivalent ellipsoids for sample neurological data

EqE	Semi-axes	N_I	G_0	P
	$[mm]$	[%]	[%]	[%]
1	[12.6, 9.4, 2.7]	90.7	35.2	5.3
2	[11.5, 8.6, 1.2]	86.7	38.2	4.2
3	[11.6, 7.6, 2.5]	75.6	33.1	6.9
4	[9.6, 7.0, 2.5]	100.0	41.2	2.2

large distributions of vector data, it requires intensive user interaction especially for data spread out on complex curved surfaces.

Let a sample data distribution with one concentration center be given on the L-shape surface as in Fig. 5.20. Using one cluster partitioning in the EqE-procedure results in

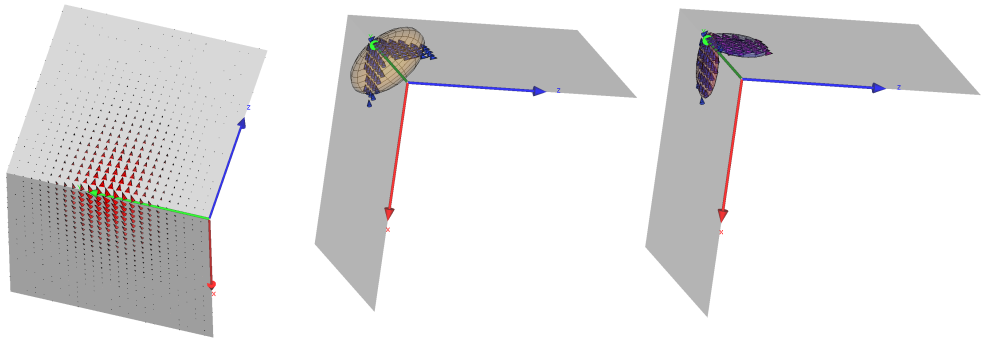

(a) L-shape distribution (b) $G_0 = 17.9\%$ (c) $G_0 = 77.8\%$ / 83.1%

Fig. 5.20: Sample data on the L-shape surface with one concentration center. Equivalent ellipsoids for partitioning using 1 and 2 clusters and threshold $T_h = 50\%$

construction of the equivalent ellipsoid with a very low goodness ($G_0 = 17.9\%$). For the proper data interpretation, i.e, to fit equivalent ellipsoids better to data on the L-shape surface, the partitioning with 2 clusters has to be applied.

To overcome problems with the interpretation of data located on complicated surfaces, the Dali object introduced in [160] can be applied. The idea of creating the Dali object was inspired by the well known painting of Salvador Dali "*The persistence of memory*" (Fig. 5.21).

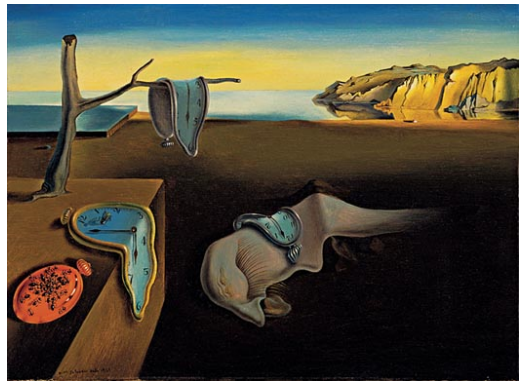

Fig. 5.21: "*The persistence of memory*", Salvador Dali (1931), MoMA, New York

To create Dali object, first, the user has to define the threshold T_h for marking the most representative region in the analyzed distribution (similarly to the EqE-procedure).

Next, the partitioning into suitable number of clusters around concentration centers has to be performed. The Dali tool uses for partitioning the following algorithm: (1) the position of the maximum field value in the thresholded distribution is searched, (2) around this position, using surface neighborhood information, a simply connected mesh of triangles is created, forming the first cluster, (3) all points in the found cluster are marked as active, (4) the procedure checks if all points in the distribution are active, if not, the procedure starts with (1) to look for the next cluster using only not marked positions. Dali objects are constructed for each found cluster separately in a

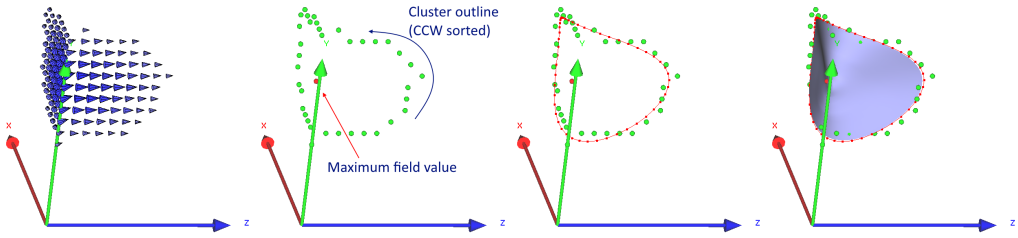

(a) Vector field in cluster (b) Outline points (c) Fourier points (d) Dali object

Fig. 5.22: Construction of the Dali object for a cluster located on the L-shape surface

few steps. Using the surface neighborhood information, the unsorted cluster outline is created (Fig. 5.22b). Then, the outline points are sorted using counter clockwise (CCW) direction and are connected to produce a closed polygon. Having the outline polygon, the parametric Fourier representation is found [96] (Fig. 5.22c). At the end, the Dali object represented by a surface spanned over the found Fourier points is constructed (Fig. 5.22d).

The parametric Fourier representation is calculated as follows. Let $\mathbf{P}(t)$, $t \in [0,1]$ be a closed 3D piecewise linear polygon with vertices $\mathbf{p}_i \in R^3$, $i = 0, \ldots, M$ and $\mathbf{p}_0 = \mathbf{p}_M$. For every point $\mathbf{p}_i$, the following symbols are defined

$$\Delta t_i = \|\mathbf{p}_i - \mathbf{p}_{i-1}\|, \quad T = \sum_{i=1}^{M} \Delta t_i = 1, \quad t_i = \sum_{j=1}^{i>0} \Delta t_j, \quad t_0 = 0 \tag{5.9}$$

The N-harmonic parametric representation (PFR^N) of closed 3D polygon is defined as

$$\mathbf{P}(t) = \mathbf{a}_0 + \sum_{k=1}^{N} (\mathbf{a}_k \cos 2\pi kt + \mathbf{b}_k \sin 2\pi kt) \tag{5.10}$$

where coefficients $\mathbf{a}_0$, $\mathbf{a}_k$, $\mathbf{b}_k$ are given by [75]

$$\mathbf{a}_0 = \sum_{i=1}^{M} \frac{\mathbf{p}_i + \mathbf{p}_{i-1}}{2} (t_i - t_{i-1}) \tag{5.11}$$

$$\mathbf{a}_k = \frac{2}{(2\pi k)^2} \sum_{i=1}^{M} \frac{\mathbf{p}_i - \mathbf{p}_{i-1}}{t_i - t_{i-1}} (\cos 2\pi k t_i - \cos 2\pi k t_{i-1}) \tag{5.12}$$

$$\mathbf{b}_k = \frac{2}{(2\pi k)^2} \sum_{i=1}^{M} \frac{\mathbf{p}_i - \mathbf{p}_{i-1}}{t_i - t_{i-1}} (\sin 2\pi k t_i - \sin 2\pi k t_{i-1}) \tag{5.13}$$

The first example presents Dali objects created for a sample artificial distribution shown in Fig. 5.20 using the threshold $T_h = 50\%$. Figure 5.23 shows Dali objects created for 1, 2, and 5 spatial harmonics used in the parametric Fourier representation.

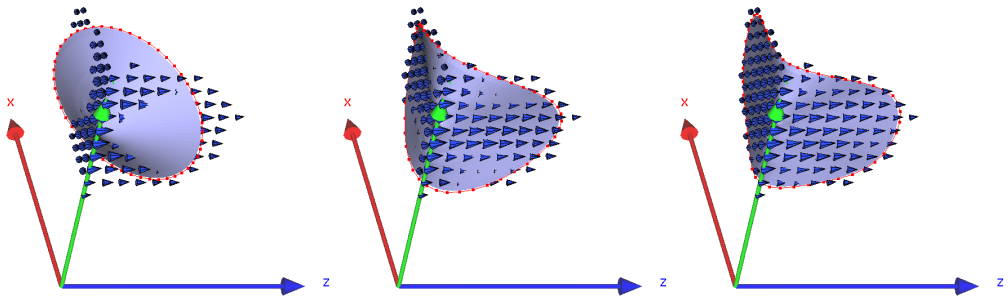

(a) PFR^1 (b) PFR^2 (c) PFR^5

Fig. 5.23: Dali objects for the L-shape distribution with one concentration center using $n = 1, 2,$ and 5 spatial harmonics

It can be observed that increasing the number of used spatial harmonics results in better fitting of the Dali object to the distribution. The relative surface areas of calculated Dali objects are equal to: $S_N/S_{CDD} = 86.0\%$, 97.2%, and 99.2% for the PRF with 1, 2, and 5 spatial harmonics, respectively. The parameter S_{CDD} denotes the area of simply connected triangular mesh spanned over the cluster. In multi subject studies, semi-axes of the equivalent ellipsis calculated from the first spatial harmonic of the found PFR can be used as interpretation parameters for evaluation of the quality of various distributions [159].

The second example presents results for a realistic data [160]. The measurements have been taken in a magnetically shielded room (AK3b, Vacuumschmelze, Hanau, Germany) at the Biomagnetic Center in Jena, Germany. The magnetic field has been recorded with the Philips twin dewar biomagnetometer system (2×31 channels) [34]. The magnetocardiogram of a patient with non-sustained ventricular tachycardia developed after anterior left ventricular myocardial infarction has been measured. The subject has been lying in a supine position and the two dewars have been positioned above the thorax so that they covered the magnetic field maximums. Signals have been

recorded for 600 s at a sampling rate of 1000 Hz. To stabilize the baseline, an analog high pass filter (first order with the cutoff frequency $f_c = 0.036$ Hz) has been applied to the analog signals. A two step averaging procedure as described in [62] in order to improve the signal-to-noise ratio has also been applied. A noise level of 50 fT has been estimated for both dewars. The last 40 ms of the bi-directional 30 Hz highpass filtered depolarization signals (late potentials, *LP*) have been used for inverse computations (Fig. 5.24).

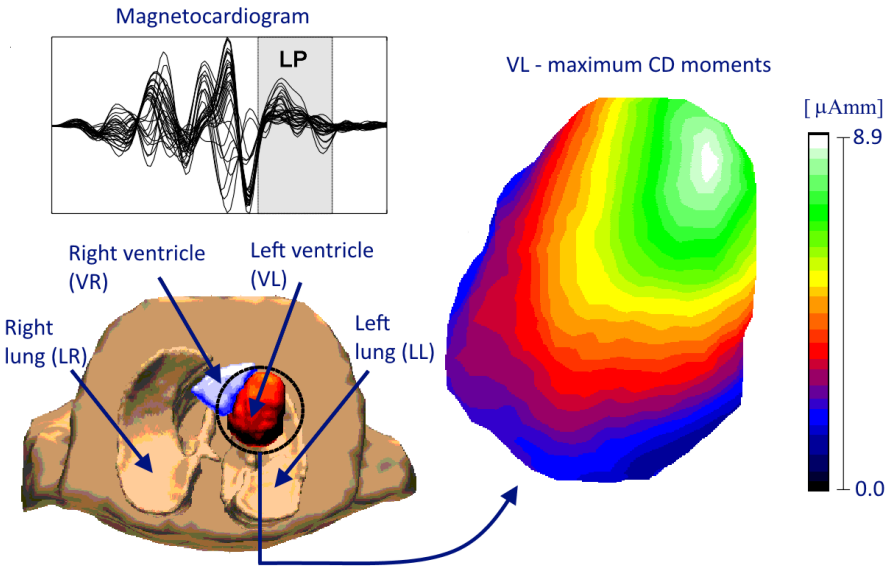

Fig. 5.24: Diaphragmal view on the 3D magnetic resonance torso image and magnetic late potentials of heart signals (analyzed time interval is marked with gray). Zoomed color shaded left ventricle (VL) shows maximum current dipoles moments during the *LP* interval

3D MRI data set of the chest of the patient has been also registered. The BEM model consisting of the left and right lungs as well as the outer torso surface has been applied for the magnetic field computations (forward model). Surfaces of lungs have been eroded by 3 mm in order to avoid numerical problems arise when the distance between the left ventricle (*lv*) and the lungs [59] is too small. The surface of the left ventricle has been segmented using the MRI data set and is subsequently used as the source domain. The source space consists of 1022 current dipoles distributed on the *lv*-surface with an average spacing of 4.7 mm. The ratio of the electrical conductivity of the torso and lungs is equal to 5. Moments of the current dipoles have been determined using the minimum L_2-norm least squares algorithm [39] for all time steps.

Figure 5.25 shows the obtained distribution of reconstructed current dipoles on the *lv*-surface for a moment of *LP*-time interval when the maximum of current dipoles reaches the global maximum.

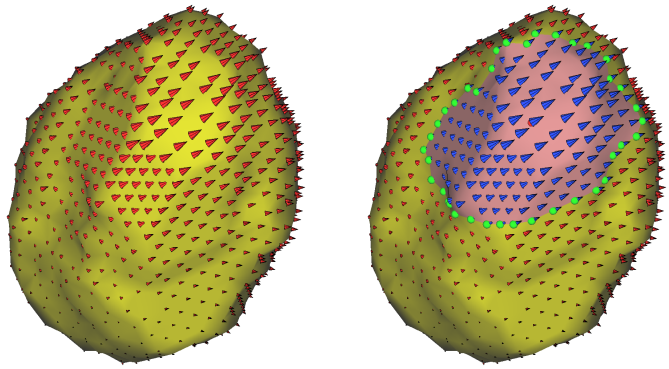

(a) Current dipoles (b) $T_h = 63\%$

Fig. 5.25: Left ventricle - (a) reconstructed current dipoles, (b) the most representative cluster

Figure 5.26 presents the Dali object constructed for a dominant activity in the *lv*-source space using the threshold $T_h = 63\%$ which corresponds to *Power50%* indicator. The current dipole with the maximum moment is found at point [27.3 mm, 31.2 mm,

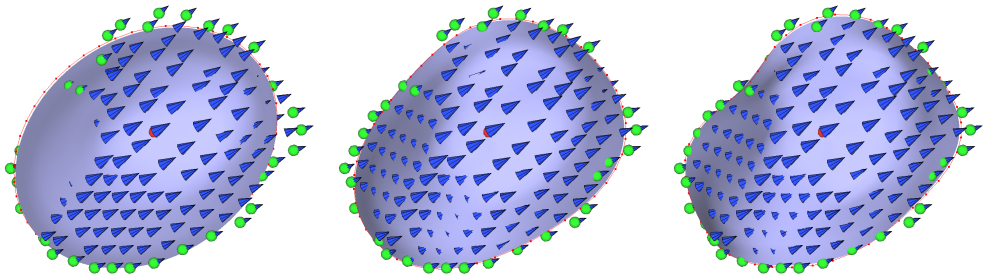

(a) PFR^1 (b) PFR^3 (c) PFR^5

Fig. 5.26: Left ventricle - Dali objects constructed for *Power50%* cluster ($T_h = 63\%$) and the PFR with $n = 1, 3$, and 5 spatial harmonics

22.5 mm] where the coordinates are given in a local coordinate system located at the center of gravity of the left ventricle. The center of gravity of the outline current dipoles at [17.3 mm, 21.4 mm, 16.5 mm] is determined for the *Power50%*- cluster and is located at a distance of 15.2 mm from the maximum current dipole. The Dali object is obtained using 1, 3, and 5 spatial harmonics in the parametric Fourier representation. The semi-axes of the equivalent ellipsis are equal to $[a, b] = [21.7\,\text{mm}, 23.1\,\text{mm}]$. The semi-axes can be used as comparative parameters in a statistical analysis of current spread activity on the left ventricle. The relative surface area of the Dali object for PFR^1, PFR^3, and PFR^5 are equal to $S_{1...3}/S_{CDD} = 93.6\%, 96.1\%$, and 96.8%, respectively.

5.6. SUMMARY

In this chapter, the postprocessing program vv for 3D visualization of various objects has been presented. Scalar and vector discrete fields, BEM/FEM meshes stored in many formats, electric and magnetic sensors of various measuring systems, and MRI scans can be visualized.

Several different objects can be simultaneously displayed in the vv- graphic window. For the convenience of the user, the vv is equipped with a graphical interface (`vvgui`) which allows easy selection of files as well as setting of principle vv options. The vv is an interactive program which can be controlled by mouse and/or by pressing a proper key on a keyboard.

Together with 3D objects, the vv can present scalar fields on 3D surfaces associated with systems of sensors. Vector fields are presented in 3D space as 3D arrows or cones.

Additionally, several simple and advanced functions are implemented in the vv. The list of most important vv- functions includes: export of viewed objects in several formats, print snapshots of the actual graphic window, spinning viewed scene for recording animations, generation of test data, the equivalent ellipsoid and the Dali object tools. The last two functions are important for an interpretation of large data and in statistical comparisons between data sets from different experiments/simulations or from one experiment under other conditions or time.

The vv is without any restrictions free software with full access to the source C code which makes the program easy to adopt to any windows system and to extend its capabilities with new features.

REFERENCES

[1] Abramowitz M., Stegun I.A.: *Handbook of Mathematical Functions: with Formulas, Graphs, and Mathematical Tables*. Dover Books on Mathematics, New York, USA, 1965. 137

[2] Akoun G., Yonnet J.-P.: 3D analytical calculation of the forces exerted between two cuboidal magnets. *IEEE Transactions on Magnetics*, vol. 20, no. 5 (1984), 1962–1964. 119

[3] Andrä W., Nowak H.: *Magnetism in Medicine. A Handbook*, 1st ed. John Wiley & Sons, Berlin, 1998. 182, 183

[4] ANSYS: ANSYS Maxwell - field simulation FEM software. http://www.ansys.com. 173

[5] ASA: ASA - EEG/ERP and MEG analysis software package. http://www.ant-neuro.com/products/asa. 177

[6] Avriel M., Wilde D.: Optimally proof for the symmetric Fibonacci search technique. *Fibonacci Quarterly*, vol. 4, no. 3 (1966), 265–269. 87

[7] Bancel F.: Magnetic nodes. *Journal of Physics D: Applied Physics*, vol. 32, no. 17 (1999), 2155–2161. 119

[8] Bandelier B., Rioux-Damidau F.: Modelling of magnetic fields using nodal or edge variables. *IEEE Transactions on Magnetics*, vol. 26, no. 5 (1990), 1644–1646. 3, 11

[9] Boeck T., Zec M., Thess A.: Electromagnetic drag on a magnetic dipole caused by a translating and rotating conducting cylinder. *Journal of Engineering Mathematics*, vol. 88, no. 1 (2014), 177–195. 172

[10] Bossavit A.: Two dual formulations of the 3-D eddy-currents problem. *COMPEL: The Int. Journal for Computation and Mathematics in Electrical and Electronic Engineering*, vol. 4, no. 2 (1985), 103–116. 11

[11] Bossavit A.: A rationale for 'edge-elements' in 3-D fields computations. *IEEE Transactions on Magnetics*, vol. 24, no. 1 (1988), 74–79. 11

[12] Bossavit A.: Whitney forms: a class of finite elements for three-dimensional computations in electromagnetism. *IEE Proceedings A: Physical Science, Measurement and Instrumentation, Management and Education, Reviews*, vol. 135, no. 8 (1988), 493–500. 1, 3

[13] Bossavit A., Verite J.-C.: The TRIFOU code: Solving the 3-D eddy-currents problem by using H as state variable. *IEEE Transactions on Magnetics*, vol. 19, no. 6 (1983), 2465–2470. 3, 11

[14] Bracewell R.N.: *The Fourier Transform & Its Applications*, 3rd ed. McGraw-Hill Publishing Company, 2000. 90, 137, 138

[15] Brauer H., Haueisen J., Ziolkowski M., Tenner U., Nowak H.: Reconstruction of extended current sources in a human body phantom applying biomagnetic measuring techniques. *IEEE Transactions on Magnetics*, vol. 36, no. 4 (2000), 1700–1705. 47, 181

[16] Brauer H., Porzig K., Mengelkamp J., Carlstedt M., Ziolkowski M., Toepfer H.: Lorentz force eddy current testing: A novel NDE - technique. *COMPEL - The Int. Journal for Computation and Mathematics in Electrical and Electronic Engineering*, vol. 33, no. 6 (2014), 1965–1977. 172

[17] Brauer H., Ziolkowski M.: Eddy current testing of metallic sheets with defects using force measurements. *Serbian Journal of Electrical Engineering*, vol. 5, no. 1 (2008), 11–20. 172

[18] Brauer H., Ziolkowski M.: Lorentz force eddy current testing - A simulation study. In *Proc. of XV Int. Symposium on Theoretical Engineering (ISTET)* (Luebeck, Germany, 2009), 227. 172

[19] Brauer H., Ziolkowski M., Dannemann M., Kuilekov M., Alexeevski D.: Forward simulations for free boundary reconstruction in magnetic fluid dynamics. *COMPEL: The Int. Journal for Computation and Mathematics in Electrical and Electronic Engineering*, vol. 22, no. 3 (2003), 674–688. 100

[20] Brauer H., Ziolkowski M., Kuilekov M.: An improved technique for interface shape identification in magnetic fluid dynamics. *COMPEL: The Int. Journal for Computation and Mathematics in Electrical and Electronic Engineering*, vol. 24, no. 3 (2005), 849–857. 100

[21] Brauer H., Ziolkowski M., Kuilekov M., Men S., Resagk C.: Surface current reconstruction using magnetic field tomography. *IEEE Transactions on Magnetics*, vol. 40, no. 2 (2004), 1398–1401. 100

[22] Brown M.: Scalar potentials in multiply connected regions. *International Journal for Numerical Methods in Engineering*, vol. 20, no. 4 (1984), 665–680. 27

[23] Carlstedt M., Porzig K., Uhlig R.P., Zec M., Ziolkowski M.: Application of Lorentz force eddy current testing and eddy current testing on moving nonmagnetic conductors. *International Journal of Applied Electromagnetics and Mechanics*, vol. 45, no. 1-4 (2014), 519–526. 172

[24] Carlstedt M., Porzig K., Ziolkowski M., Uhlig R.P., Brauer H., Toepfer H.: Comparison of Lorentz force eddy current testing and common eddy current

testing - Measurements and simulations. In *Electromagnetic Nondestructive Evaluation*, Capova K., Udpa L., Janousek L., Rao B.P.C., Eds., vol. XVII. IOS Press, Amsterdam, 2014, 218–225. 172

[25] Coley D.A.: *Introduction to Genetic Algorithms for Scientists and Engineers*. World Scientific Pub. Co., 1999. 78

[26] COMSOL: COMSOL Multiphysics - Multiphysics Software Product Suite. http://www.comsol.de. 60, 173

[27] Conway J.T.: Exact solutions for the magnetic fields of axisymmetric solenoids and current distributions. *IEEE Transactions on Magnetics*, vol. 37, no. 4 (2001), 2977–2988. 119

[28] Crowley C.W., Silvester P.P., Hurwitz H.: Covariant projection elements for 3D vector field problems. *IEEE Transactions on Magnetics*, vol. 24, no. 1 (1988), 397–400. 6

[29] Csendes Z., Weiss J., Hoole S.R.H.: Alternative vector potential formulations of 3-D magnetostatic field problems. *IEEE Transactions on Magnetics*, vol. 18, no. 2 (1982), 367–372. 32

[30] Curry: Curry SCAN 7 Neuroimaging Suite - Signal Processing, Basic and Advanced Source Analysis of EEG/EP/ERP data. http://compumedicsneuroscan.com. 177

[31] Davidson P.A.: Magnetohydrodynamics in material processing. *Annual Revue of Fluid Mechanics* vol. 31 (1999), 273–300. 47

[32] Davidson P.A.: An energy analysis of unstable, aluminium reduction cells. *European Journal of Mechanics B/ Fluids*, vol. 13, no. 1 (1994), 15–32. 47, 57

[33] Derby N., Olbert S.: Cylindrical magnets and ideal solenoids. *American Journal of Physics*, vol. 78, no. 3 (2010), 229–235. 119, 125, 134

[34] Dössel O., David B., Fuchs M., Krueger J., Luedeke K.M., Wischmann H.A.: Modular 31-channel SQUID system for biomagnetic measurements. *IEEE Transactions on Applied Superconductivity*, vol. 3, no. l (1993), 1883–1886. 182, 191, 195

[35] Dyachenko A., Korotkevich A., Zakharov V.: Weak turbulent Kolmogorov spectrum for surface gravity waves. *Physical Review Letters*, vol. 92, no. 13 (2004), 134501.1–4. 54

[36] Eisenstat S.C., Gursky M.C., Schultz M.H., Sherman A.H.: Yale Sparse Matrix Package. II. The Nonsymmetric Codes. Tech. Rep. 114, Yale University, Dept. of Computer Science, New Haven City, USA, 1977. 62

[37] Eisenstat S.C., Gursky M.C., Schultz M.H., Sherman A.H.: Yale sparse matrix package I: The symmetric codes. *International Journal for Numerical Methods in Engineering*, vol. 18, no. 8 (1982), 1145–1151. 62

[38] Frigo M., Johnson S.G.: FFTW: The Fastest Fourier Transform in the West. Tech. rep., MIT, Lab. for Computer Science, Cambridge, USA, 1997. 72

[39] Fuchs M., Wagner M., Köhler T., Wischmann H.A.: Linear and nonlinear current density reconstructions. *Journal of Clinical Neurophysiology*, vol. 16, no. 3 (1999), 267–295. 196

[40] Fujisaki K., Wajima K., Ohki M.: 3D magnetohydrodynamics analysis method for free surface molten metal. *IEEE Transactions on Magnetics*, vol. 36, no. 4 (2000), 1325–1328. 47

[41] Furlani E.P.: A three-dimensional field solution for axially-polarized multipole disks. *Journal of Magnetism and Magnetic Materials*, vol. 135, no. 2 (1994), 205–214. 119

[42] Furlani E.P.: *Permanent Magnet and Electromechanical Devices: Materials, Analysis, and Applications*. Academic Press, San Diego, London, 2001. 103, 123, 157, 158

[43] Furlani E.P., Reznik S., Kroll A.: A three-dimensional field solution for radially polarized cylinders. *IEEE Transactions on Magnetics*, vol. 31, no. 1 (1995), 844–851. 119

[44] Garrett M.W.: Calculation of fields, forces, and mutual inductances of current systems by elliptic integrals. *Journal of Applied Physics*, vol. 34, no. 9 (1963), 2567–2573. 119

[45] Geomview: Geomview - interactive 3D viewing program for Unix. http://www.geomview.org. 173, 177

[46] GiD: GiD - universal, adaptive and user-friendly pre and postprocessor for numerical simulations in science and engineering. http://www.gidhome.com. 173

[47] GMV: GMV - General Mesh Viewer. http://www.generalmeshviewer.com. 173

[48] GNU: GNU operating system - manifest. https://www.gnu.org/gnu/manifesto.html. 177

[49] Goldberg D.E.: *Genetic Algorithms in Search, Optimization, and Machine Learning*. Addison-Wesley Longman, Bonn, 1989. 69, 78, 81

[50] Gpr: Gpr - general purpose postprocessor for FEM and FDM post files. http://www.matemagic.it/Gpr.htm. 173

[51] Gramz M., Ziolkowski M.: *SONMAP v.2.0. System Oprogramowania Numerycznych Metod Analizy Pól*, vol. 358. Wydawnictwo Naukowe Politechniki Szczecińskiej, Szczecin, Poland, 1988. 2, 62, 177

[52] Gramz M., Ziolkowski M.: *Obliczanie trójwymiarowych pól elektromagnetycznych. Część I: Analiza trójwymiarowych zagadnień brzegowych metodą elementów skończonych*, vol. 444. Wydawnictwo Naukowe Politechniki Szczecińskiej, Szczecin, Poland, 1991. 1, 19

[53] Gratkowski S., Ziolkowski M.: On the accuracy of a 3-D infinite element for open boundary electromagnetic field analysis. *Archiv für Elektrotechnik*, vol. 77, no. 2 (1994), 77–83. 24, 26

[54] Green M.A.: Modeling the behavior of oriented permanent magnet material using current doublet theory. *IEEE Transactions on Magnetics*, vol. 24, no. 2 (1988), 1528–1531. 119

[55] Halbach K.: Design of permanent multipole magnets with oriented rare earth cobalt material. *Nuclear Instruments and Methods*, vol. 169, no. 1 (1980), 1–10. 153

[56] Hämäläinen M.S.: Functional localization based on measurements with a whole-head magnetometer system. *Brain Topography*, vol. 7, no. 4 (1995), 283–289. 182

[57] Harrold C., Simkin J.: Cutting multiply connected domains. *IEEE Transactions on Magnetics*, vol. 21, no. 6 (1985), 2495–2498. 27

[58] Hasebe S., Kano Y.: About treatment of gauge of a in 3-D magnetostatic analysis. *IEEE Transactions on Magnetics*, vol. 23, no. 5 (1987), 3305–3307. 32

[59] Haueisen J., Böttner A., Funke M., Brauer H., Nowak H.: Der Einflußder Randelementediskretisierung auf die Vorwärtsrechnung und das inverse Problem in Elektroencephalographie und Magnetoencephalographie. *Biomedizinische Technik*, vol. 42, no. 9 (1997), 240–248. 196

[60] Haueisen J., Ziolkowski M., Leder U.: Time varying current density distributions in the human heart and brain. *Visualization and Imaging in Transport Phenomena, Annals of the New York Academy of Sciences*, vol. 972 (2002), 133–138. 173

[61] Hoole S.R.H., Rios R., Yoganathan S.: Vector potential formulations and finite element trial functions. *International Journal for Numerical Methods in Engineering*, vol. 26, no. 1 (1988), 95–108. 32

[62] Huck M., Haueisen J., Hoenecke O., Fritschi T., Leder U., Nowak H.: QRS amplitude and shape variability in magnetocardiograms *Pacing and Clinical Electrophysiology : PACE*, vol. 23, no. 2 (2000), 234–242. 196

[63] Jackson J.D.: *Classical Electrodynamics*, 3rd ed. John Wiley & Sons, New York, 1998. 101

[64] JMAG: JMAG : Simulation Technology for Electromechanical Design. https://www.jmag-international.com. 173

[65] Kacprzak D., Ziolkowski M., Gustafsson M., Taylor M.: Magnetic field profile of an aluminum reduction cell and Lorentz force formation. In *Proc.of 12th Int. IGTE Symposium on Numerical Field Calculation in Electrical Engineering* (Graz, Austria, 2006), 301–304. 100

[66] Kanai Y., Abe T., Sengoku M., Iijima T., Iizuka M., Mukasa K.: New formulation of finite-element method with gauge condition for three-dimensional magnetic field analysis. *IEEE Transactions on Magnetics*, vol. 24, no. 6 (1988), 3123–3125. 35, 37

[67] Kaufman L., Rousseeuw P.J.: *Finding groups in data: An introduction to cluster analysis*. John Wiley & Sons, Inc., Hoboken, New Jersey, 2005. 188

[68] Kiefer J.: Sequential minimax search for a maximum. *Proceedings of the American Mathematical Society*, vol. 4, no. 3 (1953), 502–506. 87

[69] Knoepfel H.E.: *Magnetic Fields. A Comprehensive Theoretical Treatise for Practical Use*. John Wiley & Sons, New York, 2000. 103, 104

[70] Kost A., Vix M.: Berechnung ebener Felder in bereichsweise homogenen Dielektrika mit weitgehend allgemeiner Trennfläche. *Archiv für Elektrotechnik*, vol. 70, no. 2 (1987), 145–150. 57

[71] Kotiuga P.R.: On making cuts for magnetic scalar potentials in multiply connected regions. *Journal of Applied Physics*, vol. 61, no. 8 (1987), 3916–3918. 27

[72] Kotiuga P.R.: Toward an algorithm to make cuts for magnetic scalar potentials in finite element meshes. *Journal of Applied Physics*, vol. 63, no. 8 (1988), 3357–3359. 27

[73] Kotiuga P.R., Silvester P.P.: Vector potential formulation for three-dimensional magnetostatics. *Journal of Applied Physics*, vol. 53, no. 11 (1982), 8399–8401. 32

[74] Kraiger M., Schnizer B.: Potential and field of a homogeneous magnetic spheroid of arbitrary direction in a homogeneous magnetic field in Cartesian coordinates. *COMPEL: The Int. Journal for Computation and Mathematics in Electrical and Electronic Engineering*, vol. 32, no. 3 (2013), 936–960. 169

[75] Kuhl F.P., Giardina C.R.: Elliptic Fourier features of a closed contour. *Computer Graphics and Image Processing*, vol. 18 (1982), 236–258. 195

[76] Kuilekov M.: *Magnetic field tomography on electrically conducting fluids*. Dissertation, Technische Universität Ilmenau, Germany, 2008. 69

[77] Kuilekov M., Ziolkowski M., Brauer H.: Application of genetic algorithms to an inverse field problem in magnetic fluid dynamics. *Serbian Journal of Electrical Engineering*, vol. 1, no. 1 (2003), 1–13. 100

[78] Kuilekov M., Ziolkowski M., Brauer H.: Precise reconstruction of the interface between two conducting fluids in a simple cylindrical model. In *Proc. of 6th Int. Conference on Computation in Electromagnetics (CEM)* (Aachen, Germany, 2006), 139–140. 100

[79] KUILEKOV M., ZIOLKOWSKI M., BRAUER H.: Regularization technique applied to the reconstruction of the interface between two conducting fluids. *Int. Journal of Applied Electromagnetics and Mechanics*, vol. 26 (2007), 257–264. 100

[80] KURENKOV A., THESS A., ZIKANOV O., SEGATZ M., DROSTE C., VOGELSANG D.: Stability of aluminum reduction cells with mean flow. *Magnetohydrodynamics*, vol. 40, no. 2 (2004), 203–212. 100

[81] KURENKOV O.: *Reconstruction and stability analysis of interfaces between electrically conducting fluids*. Dissertation, Technische Universität Ilmenau, Germany, 2005. 50

[82] LAMB H.: *Hydrodynamics*, 6th ed. Cambridge University Press, London, New York, 1993. 50

[83] LANDAU L.D., LIFSHITZ E.M.: *Fluid Mechanics*, 2nd ed. Pergamon Press, Oxford, 1987. 50, 51

[84] LANGERHOLC J.: Torques and forces on a moving coil due to eddy currents. *Journal of Applied Physics*, vol. 44, no. 4 (1973), 1587–1594. 138, 139

[85] LEE S.W., MENENDEZ R.C.: Force on current coils moving over a conducting sheet with application to magnetic levitation. *Proceedings of the IEEE*, vol. 62, no. 5 (1974), 567–577. 138

[86] LINDHOLM D.: Automatic triangular mesh generation on surfaces of polyhedra. *IEEE Transactions on Magnetics*, vol. 19, no. 6 (1983), 2539–2542. 179

[87] MAGNET: MagNet 2D/3D - Electromagnetic Field Simulation Software. http://www.infolytica.com. 173

[88] MATLAB: *MATLAB and Simulink - Release Notes R2012a*. The MathWorks, Inc., 2012. 60

[89] MEN S., RESAGK C., BRAUER H., ZIOLKOWSKI M., KUILEKOV M.: Reconstruction of interface between two electrically conducting fluids from magnetic field measurements. In *Proc. of Joint 15th Riga and 6th Pamir Int. Conference on Fundamental and Applied MHD* (Riga Jurmala, Latvia, 2005), vol. 2, 329–332. 100

[90] MEN S., RESAGK C., KUILEKOV M., ZIOLKOWSKI M., BRAUER H.: 2D measurements of magnetic field near an oscillating interface between two fluids carrying an electrical current. *Steel Research International*, vol. 78 (2007), 433–437. 100

[91] MEN S., RESAGK C., ZIOLKOWSKI M., KUILEKOV M., BRAUER H.: Measurement of magnetic flux density on a rotating distorted electrolyte - metal interface. *Measurement Science and Technology*, vol. 15, no. 7 (2004), 1323–1326. 100

[92] MENGELKAMP J., PORZIG K., CARLSTEDT M., ZIOLKOWSKI M., BRAUER H., HAUEISEN J.: Forward solution for Lorentz force evaluation with different models of the permanent magnet. In *Proc. of 9th IET International Conference on Computation in Electromagnetics (CEM)* (London, UK, 2014), vol. 1, 1–2. 172

[93] Mengelkamp J., Ziolkowski M., Weise K., Carlstedt M., Brauer H.: Permanent magnet modeling for Lorentz force evaluation. *IEEE Transactions on Magnetics*, DOI: 10.1109/TMAG.2015.2392082 (2015), 1–20 (in press). 172

[94] Mohammed O., Davis W., Popovic B., Nehl T., Demerdash N.: On the uniqueness of solution of magnetostatic vector-potential problems by three-dimensional finite-element methods. *Journal of Applied Physics*, vol. 53, no. 11 (1982), 8402–8404. 32

[95] Moon P., Spencer D.E.: *Field Theory For Engineers*. D. Van Nostrand Company, Inc., Toronto, London, New York, 1961. 150, 165, 169

[96] Müller K., Klinger A.: Surface interpolation from cross sections. In *Focus on Scientific Visualization*, Hagen H., Müller H., Nielson G., Eds. Springer, Berlin, 1993, 139–189. 194

[97] Mur G., de Hoop A.: A finite-element method for computing three-dimensional electromagnetic fields in inhomogeneous media. *IEEE Transactions on Magnetics*, vol. 21, no. 6 (1985), 2188–2191. 3, 11

[98] Nakata T., Takahashi N., Fujiwara K., Okada Y.: Improvements of the T-Omega method for 3-D eddy current analysis. *IEEE Transactions on Magnetics*, vol. 24, no. 1 (1988), 94–97. 27

[99] Nelder J.A., Mead R.: A simplex method for function minimization. *The Computer Journal*, vol. 7, no. 4 (1965), 308–313. 126

[100] Nyquist H.: Certain topics in telegraph transmission theory. *Proceedings of the IEEE*, vol. 90, no. 2 (2002), 280–305. 71

[101] OpenGL: OpenGL - The Industry Standard for High Performance Graphics. https://www.opengl.org. 173

[102] Opera: Opera - general-purpose multiphysics finite element software suite. http://operafea.com. 173

[103] ParaView: ParaView - open-source, multi-platform data analysis and visualization application. http://www.paraview.org. 173

[104] Petković B.: *Assessment of linear inverse problems in magnetocardiography and Lorentz force eddy current testing*. Dissertation, Technische Universität Ilmenau, Germany, 2013. 172

[105] Petković B., Haueisen J., Zec M., Uhlig R.P., Brauer H., Ziolkowski M.: Lorentz force evaluation: a new approximation method for defect reconstruction. *NDT & E International*, vol. 59 (2013), 57–67. 101, 143, 144, 145, 146, 156, 161, 172

[106] Petruska A.J., Abbott J.J.: Optimal permanent-magnet geometries for dipole field approximation. *IEEE Transactions on Magnetics*, vol. 49, no. 2 (2013), 811–819. 118

[107] PINCHUK A.R., CROWLEY C.W., SILVESTER P.P.: Spurious solutions to vector diffusion and wave field problems. *IEEE Transactions on Magnetics*, vol. 24, no. 1 (1988), 158–161. 44

[108] PISSANETZKY S.: Solution of three-dimensional, anisotropic, nonlinear problems of magnetostatics using two scalar potentials, finite and infinite multipolar elements and automatic mesh generation. *IEEE Transactions on Magnetics*, vol. 18, no. 2 (1982), 346–350. 23

[109] PISSANETZKY S.: *Sparse Matrix Technology*. Academic Press, London, 1984. 62, 63

[110] PORZIG K., CARLSTEDT M., ZIOLKOWSKI M., BRAUER H.: Reverse engineering of ECT probes for nondestructive evaluation of moving conductors. *Annual Review of Progress in Quantitative Nondestructive Testing*, vol. 1581, no. 1 (2014), 1519–1525. 172

[111] PRESS W.H., TEUKOLSKY S.A., VETTERLING W.T., FLANNERY B.P.: *Numerical Recipes: The Art of Scientific Computing*, 3rd ed. Cambridge University Press, New York, 2007. 93, 126

[112] RAKOTOARISON H.L., YONNET J.-P., DELINCHANT B.: Using Coulombian approach for modeling scalar potential and magnetic field of a permanent magnet with radial polarization. *IEEE Transactions on Magnetics*, vol. 43, no. 4 (2007), 1261–1264. 119

[113] RAVAUD R., LEMARQUAND G., LEMARQUAND V., DEPOLLIER C.: Analytical calculation of the magnetic field created by permanent-magnet rings. *IEEE Transactions on Magnetics*, vol. 44, no. 8 (2008), 1982–1989. 119

[114] REITZ J.R., DAVIS L.C.: Force on a rectangular coil moving above a conducting slab. *Journal of Applied Physics*, vol. 43, no. 4 (1972), 1547–1553. 135, 138, 171

[115] RESAGK C., MEN S., ZIOLKOWSKI M., KUILEKOV M., BRAUER H.: Magnetic field tomography on two electrically conducting fluids. *Measurement Science and Technology*, vol. 17, no. 8 (2006), 2136–2140. 100

[116] SCHWARZ H.R.: *Finite Element Methods (Computational Mathematics and Applications)*. Academic Press, London, 1988. 21

[117] SELVAGGI J.P., SALON S., KWON O.-M., CHARI M.V.K., DEBORTOLI M.: Computation of the external magnetic field, near-field or far-field, from a circular cylindrical magnetic source using toroidal functions. *IEEE Transactions on Magnetics*, vol. 43, no. 4 (2007), 1153–1156. 119

[118] SHANNON C.E.: Communication in the Presence of Noise. *Proceedings of the IEEE*, vol. 86, no. 2 (1998), 447–457. 71

[119] SHREINER D.: *OpenGL programming guide: the official guide to learning OpenGL, versions 3.0 and 3.1*, 7th ed. Addison-Wesley Professional, 2010. 177

[120] Sikora R., Gawrylczyk K.M., Gramz M., Gratkowski S., Ziolkowski M.: Magnetic field computation in the end-region of electric machines using various boundary conditions on iron surfaces. *IEEE Transactions on Magnetics*, vol. 22, no. 3 (1986), 204–207. 27

[121] Simkin J., Trowbridge C.W.: On the use of the total scalar potential on the numerical solution of fields problems in electromagnetics. *International Journal for Numerical Methods in Engineering*, vol. 14, no. 3 (1979), 423–440. 23

[122] TetGen: TetGen: A Quality Tetrahedral Mesh Generator. http://wias-berlin.de/software/tetgen/. 177

[123] Thess A., Votyakov E.V., Kolesnikov Y.: Lorentz force velocimetry. *Physical Review Letters*, vol. 96, no. 16 (2006), 164501.1–4. 101

[124] Uhlig R.P.: *Identification of material defects in metallic materials using Lorentz force eddy current testing - fundamentals, metrological implementation and verification*. Dissertation, Technische Universität Ilmenau, 2013. 172

[125] Uhlig R.P.: *An experimental validation of Lorentz force eddy current testing*. Universitätsverlag Ilmenau, 2014. 134

[126] Uhlig R.P., Zec M., Ziolkowski M., Brauer H.: Lorentz force eddy current testing: Validation of numerical results. *Proccedings of Electrotechnical Institute*, vol. 251 (2011), 135–145. 172

[127] Uhlig R.P., Zec M., Ziolkowski M., Brauer H., Thess A.: Lorentz force sigmometry: A contactless method for electrical conductivity measurements. *Journal of Applied Physics*, vol. 111, no. 9 (2012), 094914.1–7. 101, 172

[128] Urankar L.: High accuracy field computation of magnetized bodies. *IEEE Transactions on Magnetics*, vol. 21, no. 6 (1985), 2169–2172. 119

[129] van Welij J.: Calculation of eddy currents in terms of H on hexahedra. *IEEE Transactions on Magnetics*, vol. 21, no. 6 (1985), 2239–2241. 3

[130] Vandevender W.H., Haskell K.H.: The SLATEC mathematical subroutine library. *ACM SIGNUM Newsletter*, vol. 17, no. 3 (1982), 16–21. 62

[131] Verite J.-C.: Application of a 3-D eddy current code (TRIFOU) to non-destructive testing. *COMPEL: The Int. Journal for Computation and Mathematics in Electrical and Electronic Engineering*, vol. 3, no. 3 (1984), 167–178. 11

[132] Votyakov E.V., Thess A.: Interaction of a magnetic dipole with a slowly moving electrically conducting plate. *Journal of Engineering Mathematics*, vol. 77, no. 1 (2012), 147–161. 154

[133] Wall M.: GAlib : A C ++ Library of Genetic Algorithm Components. Tech. Rep. 8, MIT, Cambridge, MA, USA, 1996. 78

[134] Webb J.P.: Efficient generation of divergence-free fields for the finite element analysis of 3D cavity resonances. *IEEE Transactions on Magnetics*, vol. 24, no. 1 (1988), 162–165. 44

[135] Woodson H.H., Melcher J.R.: *Electromechanical Dynamics (Part I: Discrete Systems)*. John Wiley & Sons, New York, London, 1968. 103

[136] Xd3d: Xd3d - simple scientific visualization tool. http://www.cmap.polytechnique.fr/~jouve/xd3d/. 173

[137] Yang Z., Johansen T., Bratsberg H., Helgesen G., Skjeltorp A.: Potential and force between a magnet and a bulk Y1Ba2Cu3O7-δ superconductor studied by a mechanical pendulum. *Superconductor Science and Technology*, vol. 3, no. 12 (1990), 591–597. 119, 123, 124, 134

[138] Zec M.: *Theory and numerical modelling of Lorentz force eddy current testing*. Dissertation, Technische Universität Ilmenau, 2013. 106, 112, 134, 172

[139] Zec M., Uhlig R.P., Ziolkowski M., Brauer H.: Lorentz force eddy current testing: Modelling of permanent magnets in dynamic simulation using logical expressions. In *IET 8th Int. Conference on Computation in Electromagnetics (CEM)* (Wrocław, Poland, 2011), 1–2. 172

[140] Zec M., Uhlig R.P., Ziolkowski M., Brauer H.: Lorentz force eddy current testing: Two-dimensional numerical study. *Proceedings of Electrotechnical Institute*, vol. 252 (2011), 55–66. 172

[141] Zec M., Uhlig R.P., Ziolkowski M., Brauer H.: Finite element analysis of non-destructive testing eddy current problems with moving parts. *IEEE Transactions on Magnetics*, vol. 49, no. 8 (2013), 4785–4794. 172

[142] Zec M., Uhlig R.P., Ziolkowski M., Brauer H.: Fast technique for Lorentz force calculations in non-destructive testing applications. *IEEE Transactions on Magnetics*, vol. 50, no. 2 (2014), 133–136. 106, 127, 172

[143] Zec M., Uhlig R.P., Ziolkowski M., Brauer H.: Three-dimensional numerical investigations of Lorentz force eddy current testing. In *Electromagnetic Nondestructive Testing*, Rebello J.M.A., Kojima F., Chady T., Eds., vol. XVI. IOS Press, Amsterdam, 2014, 83–93. 172

[144] Zec M., Uhlig R.P., Ziolkowski M., Brauer H.: Differential sensor, inspection system and method for the detection of anomalies in electrically conductive materials, WO 2014/037388, 13.03.2014, Int. Patent Application. 172

[145] Zec M., Uhlig R.P., Ziolkowski M., Brauer H., Thess A.: Lorentz force sigmometry. *Journal of Iron and Steel Research, International*, vol. 19, Supplement 1 (2012), 123–126. 172

[146] Zec M., Uhlig R.P., Ziolkowski M., Brauer H., Thess A.: Verfahren und Anordnung zur Bestimmung der elektrischen Leitfähigkeit eines Werkstoffes, DE 10 2011 056 650, 20.02.2014, German Patent. 172

[147] Zienkiewicz O.C., Lyness J., Owen D.: Three-dimensional magnetic field determination using a scalar potential–A finite element solution. *IEEE Transactions on Magnetics*, vol. 13, no. 5 (1977), 1649–1656. 21

[148] Zienkiewicz O.C., Taylor R.L.: *The Finite Element Method Set*, 6th ed. Butterworth-Heinemann, London, 2005. 21

[149] Ziolkowski M., Brauer H.: Electrode shape influence on the magnetic field distribution in interface reconstruction problems. In *Proc. of XII Int. Symposium on Electromagnetic Fields (ISEF)* (Baiona, Spain, 2005), vol. 1, 1–6. 100

[150] Ziolkowski M., Brauer H.: Influence of feed-wire on magnetic field measurements with MFT-system. In *Proc. of 7th Int. Conference on Applied Electromagnetics (PES)* (Nis, Serbia and Montenegro, 2005), O2–5(1–2). 100

[151] Ziolkowski M., Brauer H.: Cross-correlation in identification of interface shape between two conducting fluids. In *Proc. of 12th Int. IGTE Symposium on Numerical Field Calculation in Electrical Engineering, (CD Edition)* (Graz, Austria, 2006), Verlag der Technischen Universität Graz, 467–470. 69, 93, 97

[152] Ziolkowski M., Brauer H.: Calibration of magnetic field sensors in a MFT system. *IEEE Transactions on Magnetics*, vol. 44, no. 6 (2008), 1626–1629. 100

[153] Ziolkowski M., Brauer H.: Validation of force calculations in Lorentz force eddy current testing. In *Proc. of 13th IGTE Symposium on Numerical Field Calculation in Electrical Engineering* (Graz, Austria, 2008), Graz University of Technology, 364–368. 172

[154] Ziolkowski M., Brauer H.: Fast computation technique of forces acting on moving permanent magnet. *IEEE Transactions on Magnetics*, vol. 46, no. 8 (2010), 2927–2930. 112, 172

[155] Ziolkowski M., Brauer H., Kuilekov M.: Interface identification in magnetic fluid dynamics. *Serbian Journal of Electrical Engineering*, vol. 1, no. 1 (2003), 61–69. 100

[156] Ziolkowski M., Brauer H., Kuilekov M.: Comparison of semi-analytical and FEM solutions in a certain magnetic fluid dynamics problem. *COMPEL: The Int. Journal for Computation and Mathematics in Electrical and Electronic Engineering*, vol. 24, no. 2 (2005), 418–426. 68

[157] Ziolkowski M., Brauer H., Kuilekov M.: Identification of dominant modes in the interface between two conducting fluids. *IEEE Transactions on Magnetics*, vol. 42, no. 4 (2006), 1083–1086. 69, 87

[158] Ziolkowski M., Brauer H., Kuilekov M., Resagk C., Men S.: Reconstruction of the interface between two conducting fluids with modified genetic algorithms. In *Computer Engineering in Applied Electromagnetism (ISEF)*, Wiak S., Krawczyk A., Trlep I., Eds. Springer, Heidelberg, 2005, 111–116. 100

[159] Ziolkowski M., Haueisen J.: Visualization of 3-D multi-focal current density reconstructions. In *Electromagnetic Fields in Electrical Engineering (ISEF)*. IOS Press, Amsterdam, 2002, 158–161. 173, 195

[160] Ziolkowski M., Haueisen J., Leder U.: Visualization procedures for volume and surface current density distributions in cardiac regions. *Int. Journal of Bioelectromagnetism*, vol. 2, no. 2 (2000), 1–10. 193, 195

[161] Ziolkowski M., Haueisen J., Leder U.: Postprocessing of 3-D current density reconstruction results with equivalent ellipsoids *IEEE Transactions on Biomedical Engineering*, vol. 49, no. 11 (2002), 1379–84. 188

[162] Ziolkowski M., Haueisen J., Nowak H., Brauer H.: Visualization of current density distributions in biomagnetic inverse problems. In *Proc. of IX Int.Symposium on Electromagnetic Fields in Electrical Engineering (ISEF)* (Pavia, Italy, 1999), 501–504.

[163] Ziolkowski M., Haueisen J., Nowak H., Brauer H.: Equivalent ellipsoid as an interpretation tool of extended current distributions in biomagnetic inverse problems. *IEEE Transactions on Magnetics*, vol. 36, no. 4 (2000), 1692–1695. 173, 188

NOWOCZESNE METODY W ANALIZIE WYBRANYCH PROBLEMÓW POLA ELEKTROMAGNETYCZNEGO

W monografii przedstawiono wyniki kilkunastu lat badań autora prowadzonych w Katedrze Elektrotechniki Teoretycznej i Informatyki na Wydziale Elektrycznym Politechniki Szczecińskiej (obecnie Zachodniopomorskiego Uniwersytetu Technologicznego w Szczecinie) oraz w FG Theoretische Elektrotechnik, Technische Universität Ilmenau (Niemcy). Monografia składa się z pięciu rozdziałów, w których opisano niektóre metody stosowane w analizie problemów pola elektromagnetycznego.

Rozdział 1 jest poświęcony metodzie elementów skończonych (MES). Wychodząc z założenia, że czytelnik zna podstawy metody elementów skończonych, nie opisano samej metody, a skupiono się na przedstawieniu pewnej klasy funkcji kształtu, która może być zastosowana w MES, a mianowicie wektorowych funkcji kształtu dla prostopadłościennego elementu skończonego. Ich realizacja węzłowa, krawędziowa i ścienna została szczegółowo opisana i przedyskutowana.

W rozdziale 2 przedstawiono analizę ogólnego trójwymiarowego zagadnienia pola magnetostatycznego, wykorzystującą MES z różnymi sformułowaniami opisującymi pole magnetyczne. W pierwszej części omówiono analizę pola magnetycznego z wykorzystaniem potencjałów skalarnych. Następnie opisano modelowanie trójwymiarowych uzwojenień z prądem. Przedyskutowano też wykorzystanie wektorowego potencjału magnetycznego $\mathbf{A}$ oraz bezpośredniego opisu, za pomocą wektora natężenia $\mathbf{H}$, w analizie pól magnetostatycznych. W ostatniej części rozdziału przedstawiono realizację sformułowań $\mathbf{A}/\mathbf{H}$ z rozdzielonymi składowymi w metodzie elementów skończonych wykorzystującej elementy krawędziowe.

W rozdziale 3 zajęto się problemem rekonstrukcji powierzchni granicznej pomiędzy dwoma swobodnie oscylującymi, niemieszalnymi, elektrycznie przewodzącymi płynami, przez które przepływa wymuszony prąd stały. Na początku opisano system do identyfikacji powierzchni granicznej, wykorzystujący pomiary pola magnetycznego wokół walcowego zbiornika z płynami (koncepcja tomografii magnetycznej). Następnie przedstawiono metody obliczania pola magnetycznego wokół zbiornika z oscylującymi płynami wytwarzanego przez przepływający przez nie prąd elektryczny. Sformułowano i przeanalizowano problem identyfikacji dominującej harmonicznej w oscylującej powierzchni granicznej. Podano i przedyskutowano metody identyfikacji wykorzystujące prosty algorytm genetyczny, technikę wyszukiwania bezpośredniego oraz współczynnik korelacji wzajemnej.

W rozdziale 4 opisano metody analityczne i semianalityczne użyteczne przy modelowaniu układów wiroprądowego badania materiałow z wykorzystaniem pomiaru siły Lorentza (LET). Na początku przeanalizowano dwuwymiarowe modele LET. Podano sposoby obliczania siły Lorentza oddziałującej na magnes trwały umieszczony nad przewodzącą płytą przesuwaną ze stałą prędkością. Dodatkowo opisano metodę uwzględniania defektów oraz skończonej długości płyty w obliczaniu siły Lorentza.

Następnie przedstawiono koncepcję magnetycznych dipoli do optymalnego modelowania walcowych i prostopadłościennych magnesów trwałych. Ostatnią część rozdziału poświęcono trójwymiarowym układom LET. Przedstawiono w niej semianalityczną metodę modelowania pojedynczego defektu w przewodzącej ruchomej płycie (anizotropowej lub izotropowej), wykorzystującej tzw. obszar rozszerzony defektu.

Rozdział 5 poświęcono zagadnieniom wizualizacji obiektów i pól skalarnych / wektorowych w przestrzeni trójwymiarowej. Na przykładzie programu vv przedstawione zostały różne techniki wizualizacji oraz interaktywnej interpretacji obiektów i pól. Omówiono szczegółowo technikę równoważnych elipsoid stosowaną w analizie niejednorodności w polach wektorowych. Opisano również nową klasę obiektów, tzw. obiektów Dalego, które mogą być wykorzystywane do interpretacji pól wektorowych zdefiniowanych na powierzchniach 3D.

ISBN 978-83-7663-198-1